UAB

Universitat Autònoma de Barcelona

Advanced Synthesis and Characterization of Noble Metal Nanoparticles

Jordi Piella Bagaria

Doctoral Thesis

Supervisor

Prof. Dr. Víctor F. Puntes

Tutor

Prof. Dr. Jordi Pascual

Memòria presentada per optar al grau de Doctor per la

Universitat Autònoma de Barcelona

Programa de doctorat en Ciència de Materials

Bellaterra, setembre de 2018

Preface

The present PhD Thesis summarizes my work at the Inorganic Nanoparticle Group of the Catalan Institute of Nanoscience and Nanotechnology (ICN2) carried out between the years 2012 and 2018. According to the decision of the PhD Commission, this thesis is presented as a compendium of publications.

All publications are listed below in order of their appearance in the thesis:

Publication 1. J. Piella, N.G. Bastús and V. Puntes, Size-Controlled Synthesis of Sub-10-nanometer Citrate-Stabilized Gold Nanoparticles and Related Optical Properties, *Chemistry of Materials* **2016**, *28,* 1066-1075.

Publication 2. N.G. Bastús, F. Merkoçi, J. Piella and V. Puntes, Synthesis of Highly Monodisperse Citrate-Stabilized Silver Nanoparticles of up to 200 nm: Kinetic Control and Catalytic Properties, *Chemistry of Materials* **2014**, *26*, 2836-2846.

Publication 3. N.G. Bastús, J. Piella and V. Puntes, Quantifying the Sensitivity of Multipolar (Dipolar, Quadrupolar, and Octapolar) Surface Plasmon Resonances in Silver Nanoparticles: The Effect of Size, Composition, and Surface Coating, *Langmuir* **2016**, *32,* 290-300.

Publication 4. J. Piella, F. Merkoçi, A. Genç, J. Arbiol, N.G. Bastús and V. Puntes, Probing the surface reactivity of nanocrystals by the catalytic degradation of organic dyes: the effect of size, surface chemistry and composition, *Journal of Materials Chemistry A* **2017**, *5*,11917-11929.

Publication 5. J. Piella, N. G. Bastús and V. Puntes, Size-Dependent Protein-Nanoparticle Interactions in Citrate-Stabilized Gold Nanoparticles: The Emergence of the Protein Corona, *Bioconjugate chemistry* **2017**, *28,* 88-97.

Each publication is preceded by a section that contains an introduction to the topic and a summary of the results. As the reader will notice, in these sections I give my opinion of some research directions and ideas that were not included in the publications because of their subjective nature.

The following quote is dedicated to all of them.

"We are like dwarves perched on the shoulders of giants, and thus we are able to see more and farther than the latter. And this is not at all because of the acuteness of our sight or the stature of our body, but because we are carried aloft and elevated by the magnitude of the giants."

<div align="right">Bernard of Chartres (by John of Salisbury, Metalogicon, 1159)</div>

Table of contents

List of Abbreviations

4-NP:	4-Nitrophenol, *p*-nitrophenol
4-Hx:	4-Hydroxylaminophenol
AFM:	Atomic Force Microscopy
BSA:	Bovine Serum Albumin
cCCM:	Complete Cell Culture Medium
CTAB:	Cetyltrymethylammonium bromide
DLS:	Dynamic Ligth Scattering
DMEM:	Dulbecco's Modified Eagle Medium
FBS:	Fetal Bovine Serum
GA:	Gallic Acid
HD	Hydrodynamic Diameter (DLS measurements)
IB:	Intraband (transitions)
ICP-MS:	Inductively Coupled Plasma Mass Spectroscopy
LSPR:	Localized Surface Plasmon Resonance
MUA:	Mercaptoundecanoic Acid
NC:	Nanocrystal*
NP:	Nanoparticle
NP-PC:	Nanoparticle Protein Corona
PBS:	Phosphate Buffer Saline
PC:	Protein Corona
PEG:	Polyethylene Glycol
PG:	Pyrogallol
PVP:	Polyvinylpyrrolidone
QD:	Quantum Dot
ROS:	Reactive Oxygen Species
RT:	Room Temperature
SAM:	Self-Assembled Monolayer
SC:	Trisodium Citrate
SERS:	Surface Enhanced Raman Spectroscopy
SPR:	Surface Plasmon Resonance*
TEM:	Transmission Electron Microscopy
TMAOH:	Tetramethylammonium Hydroxyde
UV-vis:	Ultraviolet-visible (spectroscopy)
XRD	X-ray diffraction
Z-pot:	Zeta Potential (ζ-potential)

*In Publication 4, nanoparticles are referred to as nanocrystals.

**LSPR and SPR are used indistinctly in the thesis

Thesis Overview

The aim of this dissertation is to provide a framework for the design, synthesis, characterization and surface modification of colloidal gold and silver nanoparticles (NPs). The thesis consists on different chapters that, except of Chapter 1, include the corresponding published article in its original form. They are ordered following a logic sequence that starts by the synthesis of Au and Ag NPs, followed by the characterization of their optical and catalytic properties, and finally the exposure of the NPs to cell culture media.

Chapter 1 is a general introduction to colloidal NPs that summarize some important aspects related to their synthesis, regulation, characterization and reactivity. The aim of this chapter is to provide and illustrative overview of current research directions and challenges in the use of these novel nanomaterials for various applications.

Chapter 2 presents a seeded-growth based strategy for the aqueous synthesis of highly monodisperse colloids of spherical Au NPs with diameters below 10 nm. One advantage of the method is the use of sodium citrate as the main surfactant, which can be easily replaced by other molecules when surface functionalization is required The optimal synthetic conditions are described and discussed, in particular those that lead to the homogeneous formation of the particles: seed to precursor ratio, temperature and pH. The method overcomes traditional limitations in the size control syntheses of these NPs, usually restricted to diameters larger than 10 nm, and extends the available size-range from 3.5 nm up to 200 nm. The chapter includes the corresponding published articles *Size-Controlled Synthesis of Sub-10-nanometer Citrate-Stabilized Gold Nanoparticles and Related Optical Properties* (**Publication 1**) with a detailed characterization of the obtained samples.

Chapter 3 is similar to Chapter 2 but for the case of Ag NPs. The method overcomes traditional limitations in the aqueous syntheses of Ag NPs that have frequently resulted in polydisperse samples with poor size control. The chapter includes the corresponding published article *Synthesis of Highly Monodisperse Citrate-Stabilized Silver Nanoparticles of up to 200 nm: Kinetic Control and Catalytic Properties* (**Publication 2**) with a detailed characterization of the obtained samples.

Chapter 4 looks at the optical properties of the synthetized Au and Ag NPs in greater depth, with special emphasis on size-dependent effects. Thus, the evolution with size of the NP's characteristic surface plasmon resonance is described in a detail not previously reported. Changes in the particle optical response due to surface modifications with different and commonly used surfactants is also described. The chapter includes the article *Quantifying the Sensitivity of Multipolar (Dipolar, Quadrupolar, and Octapolar) Surface Plasmon Resonances in Silver Nanoparticles: The Effect of Size, Composition and Surface Coating* (**Publication 3**).

Chapter 5 is an extended study related to the effects of size and surface state on catalytic activity and reactivity of Au and Ag NPs. The chosen model reaction for the study is the catalytic reduction of 4-nitrophenol to 4-aminophenol, which can be easily monitored by UV-vis spectroscopy. The work is summarized in the article *Probing the surface reactivity of nanocrystals by the catalytic degradation of organic dyes: the effect of size, surface chemistry and composition* (**Publication 4**).

Chapter 6 presents a detailed characterization of the process of protein corona formation on the surface of various Au NPs after exposure to serum proteins. The effect of the curvature radius on protein adsorption is discussed. Results are summarized in the article *Size-Dependent Protein-Nanoparticle Interactions in Citrate-Stabilized Gold Nanoparticles: The Emergence of the Protein Corona* (**Publication 5**).

Finally, **Appendix A** highlights some important considerations when seeking reproducible and reliable results in the field of nanotechnology. It can be understood as the Materials and Methods section, with the main difference that it is presented as a general discussion relevant to all nanomaterials, including NPs. The reason is that each article presented in the thesis already contain a specific and dedicated Materials and Methods section. Moreover, it has been claimed that the reproducibility of research published in nanoscience journals is as low as 10-30 %, a worrying assertion for the long-term credibility of scientific results.

Chapter 1:

Introduction

Nanoparticle research is a fascinating branch of science. Their strongly size-related properties offer innumerable opportunities for surprising discoveries. However, the same unprecedented behaviour that endows nanoparticles with their great potential for innovative technological applications, also poses great challenges for scientists. Some of these challenges are the design of highly controllable and reproducible syntheses and the development of precise characterization tools and handling protocols that may differ from those of conventional materials. In this chapter, some important aspects of nanoparticle research, mostly in the form of colloidal dispersions, are discussed to provide an illustrative overview of current research directions and challenges in this rapidly developing field.

1.1. The fascinating world of nanoparticle research

The fascination with nanoparticle (NP) research is founded on the observation of unusual effects related to their small size, the so-called quantum size effects [1, 2]. Metal and semiconducting NPs just of a few nanometers in diameter, and thus with sizes somewhere between single atoms/molecules and bulk materials, show pronounced size- and shape- dependent electronic and optical properties. These properties stem from their hybrid electronic structure which contains aspects of both discrete energy levels as in atoms or molecules and the band structure seen in bulk matter. Although some of these phenomena have been applied in materials technology for several hundreds of years, their quantized nature was first recognized in the 1980s, in Ekimov-Efros's description of the size-dependent electronic excitation of various semiconductors nanocrystals (CdS, CdSe, CuCl and CuBr), later termed quantum dots, and Louis Burs's paper on electron-electron and electron-hole interactions in small crystallites of CdS [3].

Among the reported quantum-effects, one of the most spectacular is presented in NPs made of noble metals, such as Au and Ag NPs, which confers on the resultant colloids characteristic colours that have captivated scientists for centuries [4]. For instance, colloids of small spherical Au NPs are of a wine-red colour while those of Ag are yellow. These interesting optical features stem from their unique interaction with light at the nanoscale. In the presence of the oscillating electromagnetic field of the light, the free electrons of these metal NPs undergo collective oscillations with respect to the metal lattice. The peculiarity of Ag and Au NPs over their bulk counterparts is that this process is confined in a very small volume and the electron oscillations can be resonantly exited at a specific frequency of the visible spectrum, termed the localized surface plasmon resonance (LSPR) [5]. A momentary electric field is generated on the surface of the NP as a result of the oscillations, which can extend into a dielectric medium over nanometer length scale and hence gives rise to an enhancement of several orders of magnitude of the incident field under resonances conditions. As a result of these unique optical features, Au and Ag NPs have become the subject of substantial research, with an extensive range of applications including biological imaging, electronics, and materials science [5].

Another fascinating quantum-size effect of NPs was reported by *Haruta* in 1987 [6]. When deposited on metal oxide supports, Au NPs smaller than 10 nm were found to be very effective in converting toxic carbon monoxide into carbon dioxide at room temperature. This is because at considerably smaller size regimes, i.e., below 10 nm, the metallic character of these NPs is substantially lost and they start to exhibit molecular-like transitions under ambient conditions. Consequently, in the form of NPs, materials apparently inert, such as noble metals, can serve as excellent catalysts for a variety of chemical reactions, including hydrogenation, CO oxidation, selective oxidation, and nucleophilic additions [7].

Furthermore, NPs are a particularly versatile class of materials. Their reactive surfaces and high surface to volume ratio offers a unique opportunity to conjugate ligands, such as oligonucleotides, proteins, and antibodies containing functional groups, for example, thiols, mercaptans, phosphines, and amines, which have demonstrated strong mutual affinity. The realization of such (bio)nanoconjugates, coupled with quantum size-effects (e.g. the LSPRs of Au NPs, the superparamagnetism of iron oxide NPs, and the enhanced heat transfer of metallic and semiconductor NPs, etc), are of special interest in medicine for a new generation of diagnostic and imaging agents and drugs to detect and treat various diseases [8, 9].

These and other recent observations of size effects, which now extends over a wide variety of NPs and applications, have opened up a new and exciting possibility to tailor the chemical and physical properties of a material without forcing scientists to necessarily develop completely new materials compositions. Variation of size, shape and assembly just does the job if they can be controlled in a rational way. Consequently, advanced synthesis routes that offer not only control over the composition, as typically required for traditional bulk syntheses, but also control of particle size, size distribution, shape and surface chemistry have become essential on the way to study and apply the size-dependent properties of nanomateirals.

1.2. Nanoparticles as reagents in chemical synthesis

Colloidal NPs are self-assembled in solution by the nucleation and further growth of atomic or molecular precursors [10]. Thanks to recent advances in synthetic techniques, it is now possible to think about the control of almost any aspect of NPs: from chemistry to morphology, dispersion, atomic distribution and their physicochemical properties. The exceptionality of these new materials is reflected in singularities at the electromagnetic level, translated into optical, electrical, magnetic and catalytic advanced properties [8, 11]. For example, by successively combining layers of nanometric thick magnetic materials with conductors without magnetism in the same NP, it is possible to achieve giant magnetoresistance [12].

Preparation of NPs is neither the exclusive result of modern research nor is it restricted to man-made materials. NPs exist in nature and their use can be traced back to ancient times [13]. Simple examples of naturally occurring NP appear in natural processes of mineralization and include a large variety of inorganic compounds, such as novel metals (Ag reduced by humic acid), semiconductors (PbS resulting from oils and clay mixtures) and oxides (Fe_3O_4 in volcanos, which in turn catalyses the formation of carbon nanotubes during eruption) [14-16]. These natural NPs have a variety of morphologies and compositions due to different mechanisms of nucleation, growth and aggregation. Nanomaterials can also be found perfectly integrated into biological structures. For example, biogenic NPs occur naturally in many organisms ranging from bacteria to protozoa and to animals, playing a critical role in cellular adaptation and metabolism. One classical example of biogenic NPs, for instance, is the magnetosomes found in magnetotactic bacteria that live in the muddy bottoms of ponds and lakes [17]. Studies in auriferous soil have also shown that the resident microbiota can reduce Au and Ag salts and accumulate them in the form of NPs [18]. These and other examples of NPs from natural and biological origin can be found in the work of Banfield and Zhang [19].

Engineered NPs differ from naturally occurring NPs in two main aspects (**Figure 1.1**). First, their surface is protected with different molecules in such a way that they can
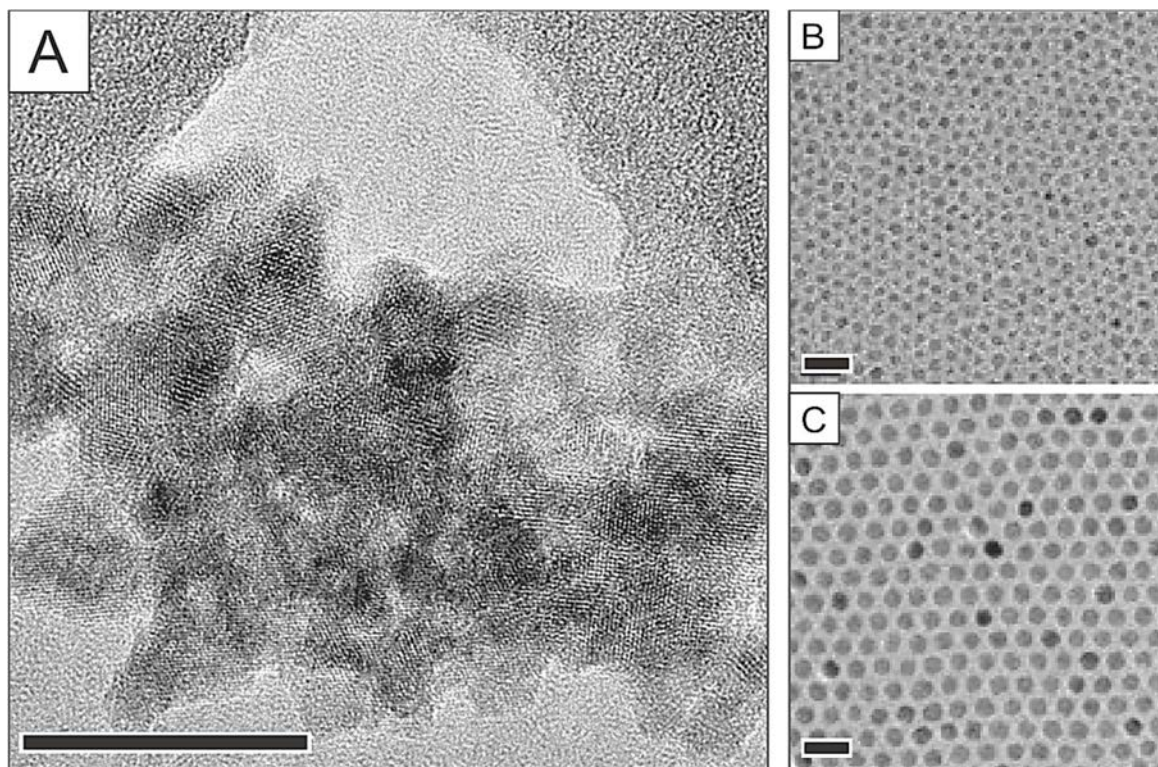
Figure 1.1. Differences between natural and engineered nanoparticles. A) TEM image of an aggregate composed by 3-5 nm iron oxide NPs found in red soils from Brazil. B, C) TEM images of 6 and 10 nm iron oxide NPs synthesized in the laboratory. Scale bar is 10 nm. Partially adapted from [20].

remain stable and individually dispersed for relatively long periods, in contrast to the large aggregates of NPs usually found in nature. Second, engineered NPs are highly monodisperse with a low degree of structural and morphological dispersity, what qualifies them to be considered somehow as molecular entities. These two characteristics were originally achieved in a small set of materials in the 19th and 20th centuries [21]. Thus, the first level of synthetic control acquired was the composition or nature of the NPs. Then, with the seminal work of Frens in 1973 [22], came size control (from 1980) [22-24] and shape control (from 2000) [25-28] leading to a second generation of NPs with a larger variety of morphologies. This second generation is fully assumed currently in the field of nanotechnology, with NPs having practically *ad libitum* size and a variety of shapes from spheres to rods, octahedrons, triangles, cubes and to the more recent hollow NPs, in which all the material is practically at the surface [29-33]. Finally, a third generation of NPs is emerging that includes a set of multicomponent hybrid structures composed of differentiated domains and functionalized surfaces [34] (**Figure 1.2**).
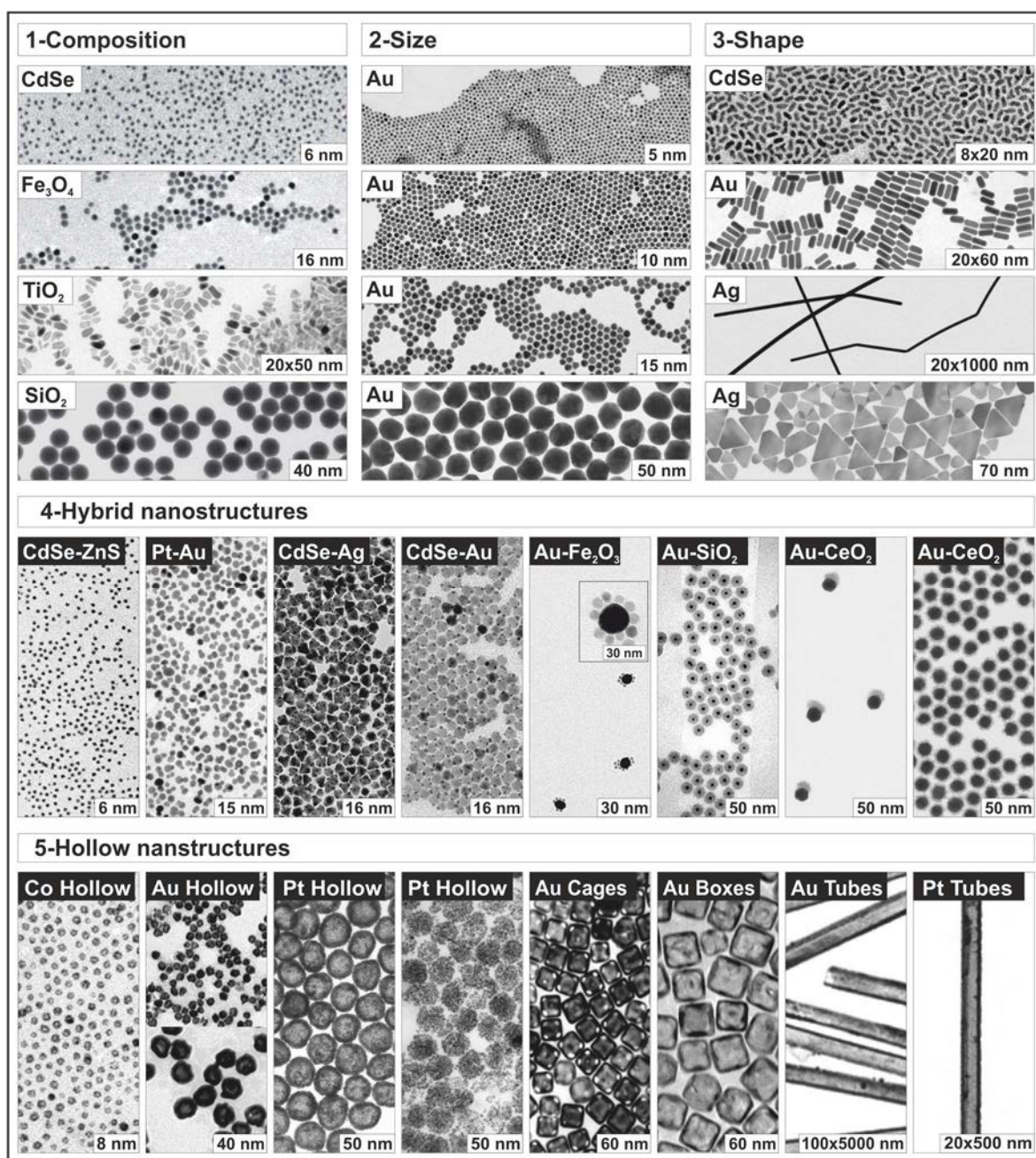
Figure 1.2. Different degrees of control achieved in the colloidal synthesis of nanoparticles. Representative TEM images of NPs (inorganic) produced by our group at the ICN2. Partially adapted from [34].

To achieve these high degrees of control is a great challenge and requires the mastering of a variety of synthetic strategies, some of which are still in a primary stage of development. Basically, the main breakthrough relies on utilizing the NPs as reagents and scaffolds, similar to those used historically in synthetic chemistry. With this change of paradigm, particles are no longer the product as they become the starting point for obtaining nanomaterials with increasing structural complexity and properties.
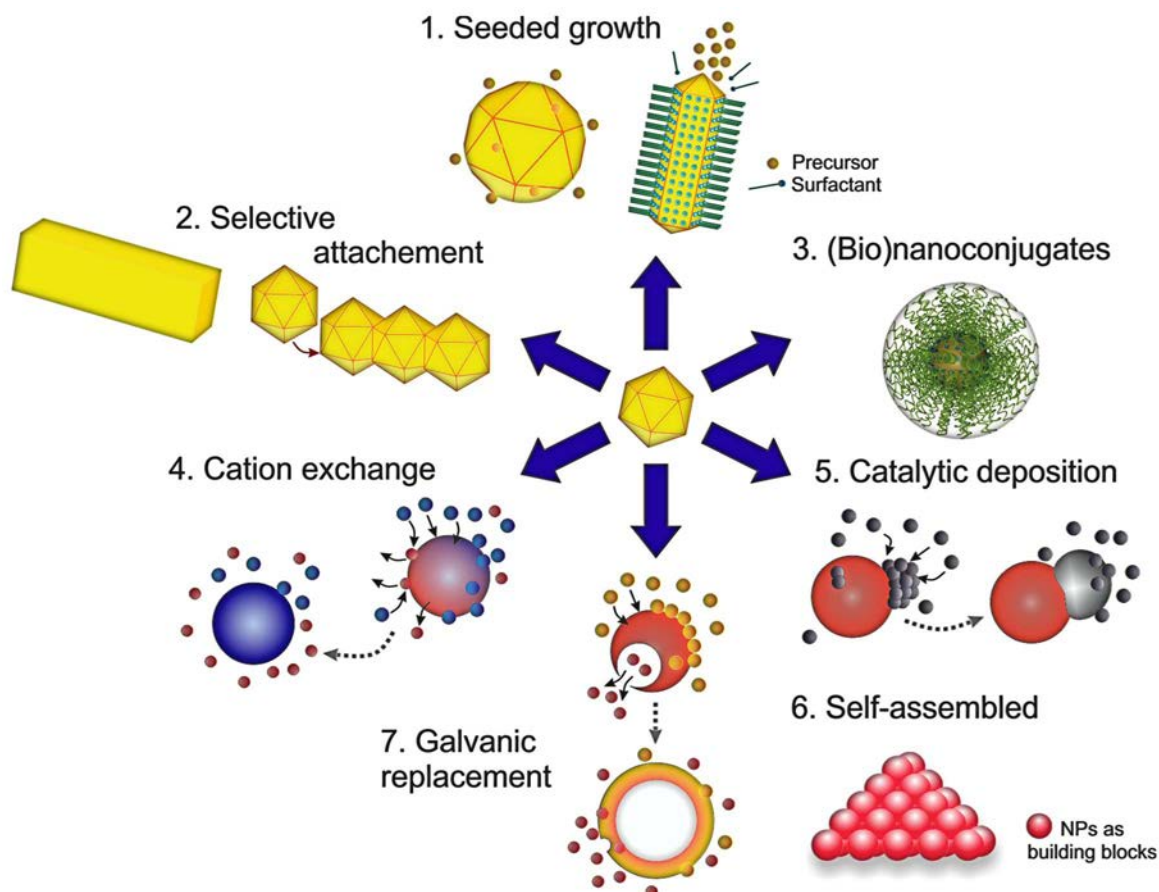
Figure 1.3. Recently developed strategies for the synthesis of complex nanoparticles by wet chemical routes. Most of the strategies consist on transforming previously synthesized NPs into more complex nanostructures.

Among the different methods of preparing NPs, the chemical synthesis in a solution system is probably the most employed route, which has the intrinsic advantages of producing more uniform and stable samples compared to other synthetic approaches [35]. Currently existing strategies for increasing NP complexity in solution systems can be categorized as follow (**Figure 1.3**):

(i)   seed-mediated growth, used to control the size and shape of NPs by slow addition of precursors onto preformed NPs used as "seeds" [29, 31];

(ii) similarly, the combination of competing reducers to simultaneously adjust the generation of seeds and their subsequent growth in one-pot [31, 36, 37];

(iii) the use of organic chemistry principles to functionalize NPs with biomolecules and generate NP-bioconjugates [38];

(iv) the use of cation exchange for controlling the chemical composition and crystalline phase of semiconductor nanocrystals [39];

(v)   the use of NPs as catalysers for the formation of hybrid nanomaterials via mineralization and growth of new materials on their surfaces [40];

(vi)   the use of NPs as building blocks, like LEGO bricks, and their self-assembly into larger superstructures [41];

(vii)   the pioneer combination of previously known galvanic corrosion and the kirkendall effect for the transformation of solid NPs into hollow nanostructures [33, 42].

These examples illustrate the adoption of hierarchical principles in the synthesis of NPs, wherein new functions and properties recursively emerge as additional layers of structural complexity are progressively incorporated into the NPs. For example, a combination of competing reducers and seeding-growth strategies has been successfully implemented in **Chapters 2, 3** to synthesize spherical Au and Ag NPs with great control of particle size and size dispersity. This achievement has been used to describe some of the size-dependent properties of these NPs under unprecedented resolution (see **Chapters 4-6**). However, advancing the design of NPs with more complex architectures and functionalities is not exempt from additional challenges. Ultimately, the most useful particles may be the most difficult to define and regulate.

1.3. Addressing the challenges in the adoption of engineered nanoparticles for emerging applications

Engineered NPs have hold great promise for imparting novel material properties and advances in a large number of fields; from improved catalytic reactions in the automobile industry to diagnosis and treatment of diseases. It is curious then that although there are many proof-of-concepts studies in the research literature, the use of these materials in new applications still remains rather limited, even though advances in synthetic techniques have lead to low cost NP production. A major barrier against the adoption of NPs for emerging applications stem from the challenge of finding a proper description for a material that is highly susceptible to experiment physicochemical transformations and whose novel properties change with size, morphology and surface state, and strongly depend on the surrounding media [43]. This, in turn, informs the characterization challenge, as determination of any attribute of the NPs requires the development of

dedicated protocols rather than the adoption of standard methodologies [44]. This uncertainty in the definition and characterization of NPs has resulted in a waste of inventoried resources and created a number of regulatory issues that are expected to increase with the development of more complex nanomaterials (**Figure 1.4**).
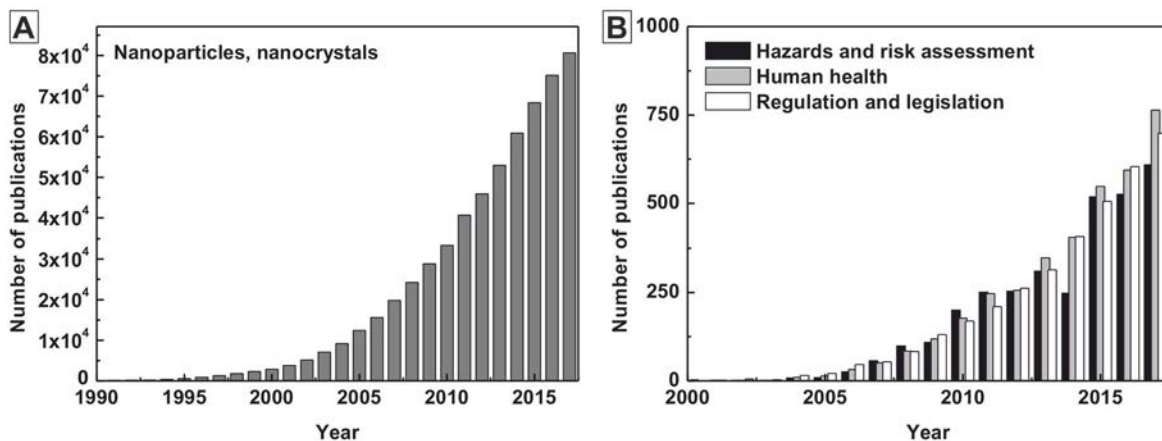
Figure 1.4. Publications addressing regulation of nanoparticles. (A) All publications identified by the Web of Science containing the search topic (nanoparticles AND nanocrystals) by year. (B) Additionally containing regulatory topics.

A difficult question that must be solved before nanomaterial products can enter the mainstream market is how we define and thus regulate this category of materials. The EU defines an engineered NP as any intentionally produced particle that has a characteristic dimension from 1 to 100 nm and has properties that are not shared by non-nanoscale particles of the same composition [45]. This encompasses a disparate group of materials, ranging from macro assemblies composed of highly monodisperse nanoparticles to polydisperse and poorly defined powders. Moreover, it is rather anecdotic to define a NP by its size when there are still inconsistencies in defining the size of a NP: crystalline size, hydrodynamic size, TEM size, etc (see **Appendix A**). Even in the optimal case of highly monodisperse spherical NPs, the amount of material present in a product or administered to a patient may be dosed on the basis of surface area, mass or number count, each relevant depending on the application.

Beyond size discussion, another important feature that distinguishes engineered NPs from other particulate matter is their degree of monodispersity. In this sense, when NPs are described as molecular entities or "artificial atoms" it is not only because of their reduced size and size/shape dependent properties, but also due to their high degree of monodispersity (as in the case of biological macromolecules and their structure-activity

relationship). Without entering into a discussion about the physical limit of monodispersity, i.e. which standard deviation threshold with respect to the mean size determines that a collection of NPs should be considered monodisperse, from a practical point of view, two NPs can be considered monodisperse if they respond undiscernibly to a determined test using current characterization techniques (such as electron microscopies, XRD diffraction, UV–vis spectroscopy, dynamic light scattering, BET surface analysis, etc). It is worth noting that in the field samples with size distributions equal to or below 10% have been traditionally considered as monodisperse.

Last but not least, in order to provide an accurate description of the concept of NP, it is important to note again that once produced many of them are truly nanometric, but they tend to aggregate rapidly into micro- or macrometric particles, thus losing their nanoscale properties [46]. This fact has been undeservedly neglected in discussions about the regulation of nanomaterial. In the majority of applications, an engineered NP must be understood as a dense collection of atoms (core) that display different properties with respect to other formats of the same material together with a stabilization layer (inorganic or organic shell), which prevents its agglomeration or aggregation into something bigger.

In this regard, it is obvious that regulatory challenges go beyond the definition that we use to describe NPs. There is a great deal of debate within the scientific community as to which definition is acceptable from a research or regulatory standpoint. Some argue that there should not be a one-size-fits-all definition used in regulation, rather an approach based on the appearance of novel size-dependent properties, which are mostly reported for well-dispersed particles below 30 nm [43]. Thus, new fundamental physics or theories beyond those encompassed by colloidal chemistry are restricted to a small set of NPs with atypical surface structure and reactivity. These NPs can enhance processes that would not be expected by larger particles of the same chemical composition and display a characteristic kinetic behaviour [47, 48]. However, for the same reason the unique kinetic behaviour of these NPs may be associated with potential nanotoxicity. In this regards, there is not yet a consensus regarding the potential hazards of NPs on organisms in natural environments, while the use of NPs in various scientific researchers and medical applications continues [49].

Another important issue to consider when dealing with NPs is how they should be treated or disposed of as waste [50, 51]. There is currently abundant literature on this topic and a number of reviews have been published. For example, Bystrzejewska-Piotrowska *et al.* [52] pointed out that any approach proposed for the treatment of nanowaste requires understanding of all the properties of the nanowaste (i.e. chemical, but also physical and biological).

In conclusion, the regulatory challenges of NPs, including those of definition, reproducibility and characterization must be addressed in order to facilitate the introduction of these nanomaterials into the market, evaluate their potential toxicity and simplify regulatory labelling. This is particularly the case with upcoming complex multifunctional hybrid nanomaterials, whose development is currently based on the use of NPs as reagents, scaffolds and building blocks, which makes regulation even more challenging and necessary for the future of this promising technology.

1.4. The reactivity of colloidal nanoparticles

The development of functional colloidal NPs has increased exponentially over the past decades offering a toolbox for use in a wide range of applications, such as materials science, catalysis, biology and medicine [53]. This applicability relies principally on their unique electronic structure which results in novel properties. However, as the size of a particle is reduced and the percentage of atoms at the surface starts to be significant, its reactivity becomes increasingly altered. Thus, in very small particles (<30 nm), the low coordination of atoms at the surface can decrease the melting temperature, decrease oxidation potentials and increase the kinetics of some reactions [54, 55]. This is extremely useful, e.g. for catalysis applications allowing reactions at the active sites of their surfaces, but, at the same time, the high fraction of unsaturated atoms may also lead to some instabilities which can promote processes of material degradation such as corrosion and sintering [56]. Thus, boosting the applicability of NPs requires an understanding of how these materials react (evolve and behave) in the different media where they are introduced.

NPs are thermodynamically unstable and quickly transform in order to reduce their excess surface energy, either growing via aggregative and sintering related processes,

dissolving in the form of ions or passivating their surfaces with adsorbed molecules [57, 58]. This condition is particularly relevant in biological and medical systems where the effect of NPs, that is, their potential toxicity, biodistribution, and biocompatibility, as well as their fate in the environment, depend on the extent of these processes [59, 60]. Indeed, it has been proposed that the higher toxicity of unstable preparations of NPs may not be due to the material *per se* but to their rapid transformation in solution; e.g. aggregation into final micro- or macrometric sizes [60] and the leaching of toxic ionic species [61]. Given these effects, when conducting studies involving NPs for safety or medicine, as for many others, it is essential to understand the changes that take place with their insertion into different media and the way NPs are presented to that. This is one of the reasons that motivated the research described in last Chapter 6 of the present thesis. Along with this study, different aspects associated with the reactivity of NPs (size, chemical compositions, surface coating), are discussed.

In general, the reactivity of a NP is a function of each part of its structure (**Figure 1.5**). The core determines its physicochemical properties while the surface chemistry dictates the interfacial interactions with the surrounding medium. Thus, NPs with the same core material can interact distinctly depending on the nature of the molecules at their surface (sometimes referred to as surfactants, ligands, dispersants or stabilizing agents). Finally, it is important to consider the interactions between NPs in a colloidal solution. NPs are not isolated entities; on the contrary, they are in a constant Brownian movement which forces their collisions towards an aggregated state.

1.4.1. Reactivity and morphology

Core size plays a relevant role in the reactivity of NPs and the reasons are clear and easily defined. In bulk materials, surface atoms contribute only to a relatively small fraction (only a few per cent) of the total number of atoms, while in NPs all the atoms lay close to or at the surface [57, 58]. Besides, in NPs the curvature radii is so high that these atoms have lower coordination numbers and higher energy than bulk atoms and, as a result, structural changes (for example crystal lattice contractions or deformation, the appearance of defects or changes in morphology) occur to stabilize them. These unique nanoscale features affect the intrinsic properties and reactivity of the NPs. An example
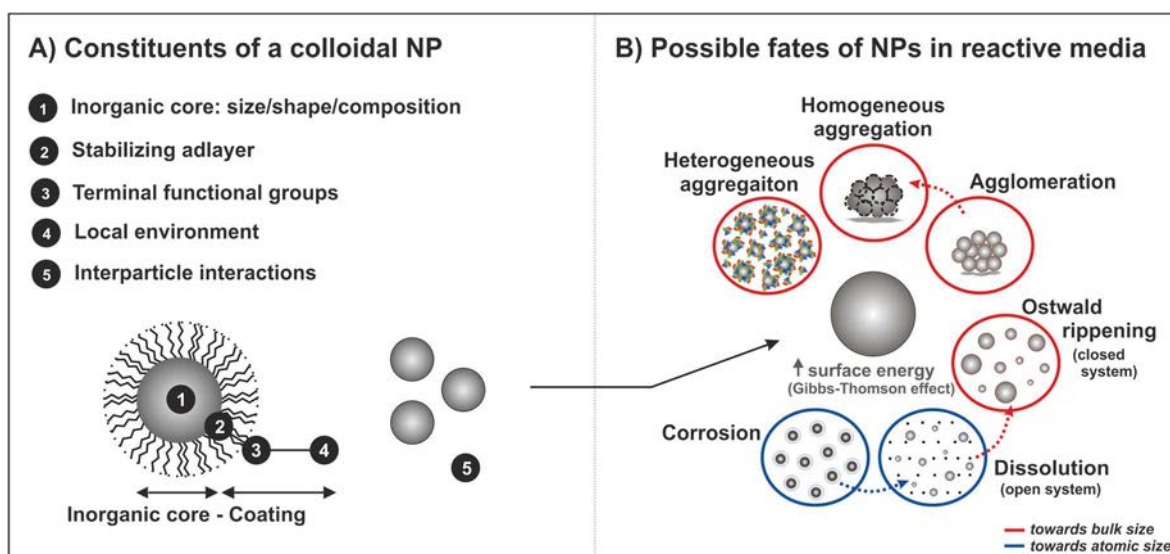
Figure 1.5. **Reactivity of colloidal inorganic nanoparticles.** (A) The critical factors determining the reactivity of a NP are: 1) size, shape and composition of the inorganic core; 2) the type of stabilizing molecules, 3) including their terminal functional groups; and 4) the interaction with ions (electrical double layer) and other molecules in solutions, as well as, with 5) other NPs. (B) Due to the high surface energy of NPs, they are susceptible to different degradation processes when exposed to reactive media.

is the size-dependent thermal properties of nanocrystals: the melting point of Au NPs decreases as their diameter decreases from 20 to 2 nm, with an exponential drop for sizes below 5 nm [54]. The normalized heat fusion behaves in a similar way, whereas it is assumed to be constant in classical thermodynamics. This is attributed to an increase fraction of lattice defects and irregularities in the crystalline structure of these NPs.

Other considerations in regard to the size of NPs are not necessarily related to unique nanoscale properties (intrinsic properties) but typically results from their small size (extrinsic properties). Thus, considering a colloidal solution of NPs with a fixed mass, as the particle size decreases 10 times, the particle concentration increases by a factor of 1000 (**Figure 1.6**). A larger number of smaller NPs results in a larger total surface area, and hence the reactivity of the system increases [62, 63]. This enhancement of reactivity, which can be either beneficial or disadvantageous depending on the intended use of NPs, has been a source of controversy when studying, e.g., the toxicity of NPs as a function of their size; attributing the higher toxicity of small NPs to a nanoscale effect instead of attributing it to a mere consequence of increasing the total surface area of the system.

A

Particle diameter (nm)	Total number atoms	Total number surface atoms	Surface atoms / Total atoms (%)	Surface area (nm²)
1	76	76	100	3.1
2	610	303	50.2	12.5
5	9541	1897	19.7	78.5
10	76332	7591	9.9	314
20	610658	30364	4.9	1256
50	9541533	189779	1.9	7859
100	76103500	757600	1.0	31416
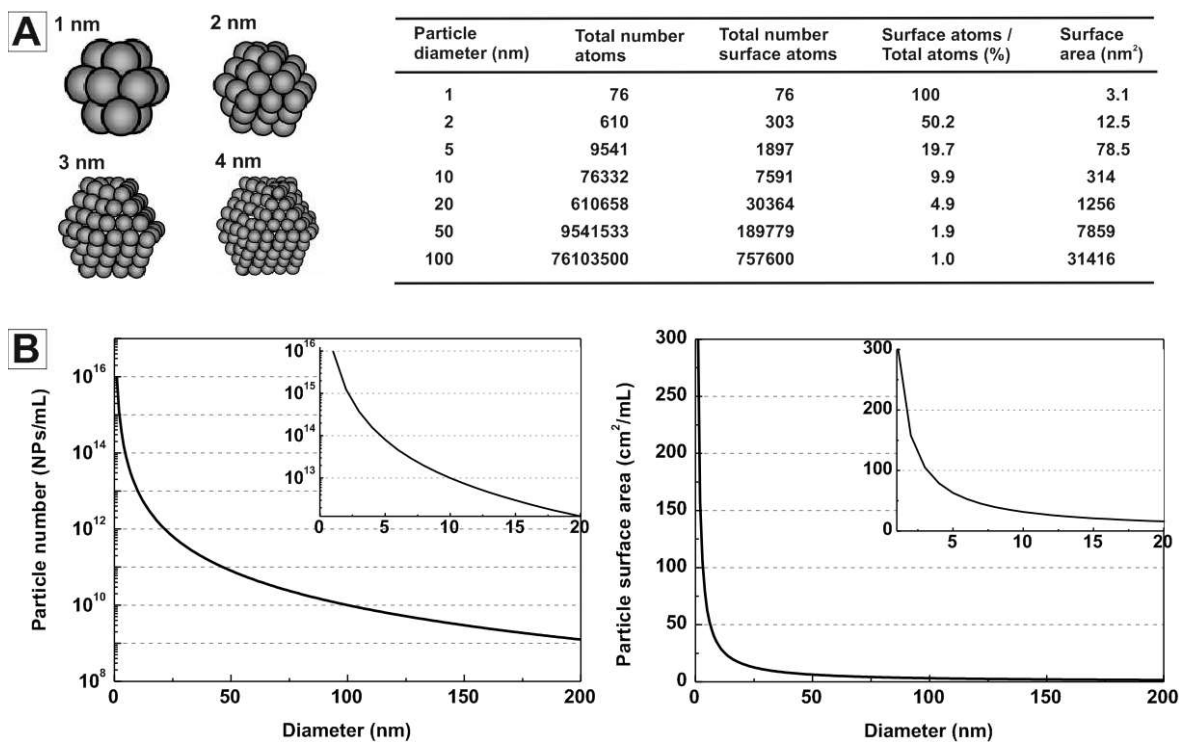
Figure 1.6. Core and surface atoms distribution in spherical gold nanoparticles. (A) Atomic distribution in icosahedral Au NPs of 1-4 nm in diameter.(B) Particle number, left, and total particle surface area, right, for a colloidal solution containing 1 g/L of Au. Partially adapted from [57].

Similar considerations apply to the shape of NPs. As explained above, NP reactivity is directly associated with surface atoms, whose number and degree of coordination is determined not only by particle size but also by the distribution of atoms within the surface (**Figure 1.7**). Atoms in flat surfaces, which have a higher degree of coordination than spheres, have a lower reactivity compared to the atoms on vertices and edges present in the anisotropic shapes. Moreover, anisotropic shapes expose different crystal faces. In fact, shape control is usually achieved by the selective interaction of surfactant molecules with a particular crystallographic facet, preventing it from growth in this direction [64].

Due to these size- and shape- effects, NPs have been extensively investigated for their implications in catalysis [7]. Especially interesting is the case of Au NPs, which, although considered chemically inert, have been found to be a very effective catalyst for sizes below 5 nm for CO oxidation. Rather than to the exact number of atoms at the surface, this improved catalytic activity is attributed to the number of edges and corners and the exposure of certain crystallographic planes as particle size decreases [65]. Size and shape also have important implications in the surface functionalization of NPs. The

Particle diameter (nm)	Total number atoms	Sphere		Cube		Rod		Disk	
		Surface atoms / Total atoms (%)	Surface area (nm²)	Surface atoms / Total atoms (%)	Surface area (nm²)	Surface atoms / Total atoms (%)	Surface area (nm²)	Surface atoms / Total atoms (%)	Surface area (nm²)
10	76080	9.4	314	10.6	354	13.5	451	29.2	971
20	608642	4.7	1256	5.3	1416	6.8	1804	14.5	3886
30	2054169	3.1	2826	3.5	3187	4.5	4059	9.7	8743
50	9512937	1.9	7850	2.1	8854	2.7	11274	5.8	24287
70	26095556	1.35	15394	1.5	17364	1.9	22109	4.2	47629
100	76080340	0.94	31400	1.06	35419	1.35	45097	2.9	97151
200	608828006	0.47	125600	0.53	141676	0.67	180386	1.46	388686

The number of total atoms in each row is kept constant and the percentage of surface atoms is calculated for each geometry.

Figure 1.7. Core and surface atoms distribution in gold nanoparticles with different shapes. (A) Atomic distribution in Au NPs with different geometries. Rod particles have a cubic section with a long length 10 times larger than the short length and disk particles have a diameter 10 times larger than their thickness. Adapted from [57].

surface curvature affects the structure (e.g. secondary structure of peptides) and organization of molecules attached at the particle surface [66], with packaging densities significantly lower for small NPs than for their larger counterparts [67]. The strength of the chemical bond is also affected by the surface curvature and exposed crystalline faces. As a consequence, the stability of this adlayer, and that of the NPs, is modified for small NPs [68].

1.4.2. Degradation, corrosion and dissolution

Another important consequence of size- and shape- effects, high surface-to-volume ration and low atomic surface coordination of NPs is their constant exposure to degradation processes, which chemically transforms them and/or reduces them to their constituents, either by chemical reactions with the surrounding media or simply because these are thermodynamically/kinetically favourable.

In this context, it is well-known that some NPs can dissolve in certain dispersing media, either by oxidative and non-oxidative pathways. This is the case for Ag, zinc oxide, iron oxide or cerium dioxide NPs among others [69-71]. The extent of dissolution depends on the crystal solubility within a given environment, the concentration gradient between the particle and the solution, the specific surface area, the presence of organic matter and the aggregation state. Thus, it is intuitive that for a given mass the dissolution kinetics is proportional to specific surface area, with faster dissolution predicted for small

NPs than for larger NPs. This ability to control the kinetics of the dissolution process is of special interest in applications and/or therapies where controlled delivery of ions is required, such as in the production of biogas in anaerobic digesters [71]. What is often ignored in the case of NPs is that from a thermodynamic point of view, the crystal solubility constant becomes size dependent and may differ from that obtained for bulk materials with the same composition, particularly for those NPs smaller than 20-30 nm [43]. As a consequence, they can dissolve in saturating conditions. This phenomenon is referred to as the Gibbs–Thomson effect and in NPs it manifests as Ostwald ripening, where NPs spontaneously dissolve and recrystallize in solution because of concentration gradients of reacting species. The result is a change in the average size, size distribution and morphology of the NPs with time [59].

Corrosion is another ubiquitous characteristic of NPs, in particular for those composed by metals, in which the metallic core is converted into its ionic state or oxide form by electrochemical surface reactions [72]. NPs are especially vulnerable to corrosion and oxidative environments because of the higher energy and chemical instability of surface atoms. Thus, when exposed to different environments, corrosion changes the properties of the NPs, for instance, by transforming a magnetic conductor material (magnetite) to magnetic insulator (maghemite) or non-magnetic insulator (hemathite), where the reactivity and properties of the conducting and non-conducting materials significantly differ [73]. In the case of Ag NPs, they are often mistakenly considered as noble metals while in most biological environments they are probably a mixture of pure silver at the core of the NPs surrounded by an oxide layer present at the surface [74]. In some conditions, where the oxidized products are soluble, corrosion may leads to complete dissolution of the original NPs [70, 75]. This is especially relevant, not only on the metabolization and expulsion of NPs from the body when used in nanomedicine, but also to their regulation; if NPs are persistent, they should be regulated as a device, such as implants, whereas if they are metabolized and expulsed, they should be regulated as a drug.

1.4.3. Toxicity and ion release

The importance of the chemical stability of metal and metal oxide NPs on their integrity and toxicity *in vitro* has been demonstrated recently [76]. Chemical unstable NPs and

nanostructured implants that oxidize and dissolve in biological media release ions that may be toxic for the organism. In this regard, NPs that show a higher solubility in cellular growth media, such as ZnO, CdSe and Ag NPs, are those that tend to also present the strongest toxicity, e.g. to mammalian cells, when compared with NPs with lower solubility, such as TiO_2 and Au NPs [77-79]. In other cases, the oxidation reaction during corrosion can be toxic in itself, modifying the redox biochemistry activity of the surrounding biological media and leading to an oxidative stress both *in vivo* and *in vitro* [80].

The increased production of NPs, their use in nanomedicine and their possible environmental impact have certainly contributed in the assessment of degradation and persistency of these materials. But even when the chemical composition and the size-effects and the surrounding medium of the NPs are considered, there are other factors that determine the chemical stability and reactivity of NPs. Several studies have shown how the encapsulation of NPs in micelles or their functionalization with self-assembled monolayers (SAM) of molecules can prevent their corrosion. Thus, apart from the composition and morphology of the core material, the surface coating (intended or unintended) cannot be ignored when assessing the reactivity of NPs.

1.4.4. Reactivity and surface chemistry

Once synthesized, NPs have to be stabilized. As mentioned previously, atoms at the surface of a NP are quite unsettled: they do not benefit from the protection of the highly co-ordinated atoms in the bulk nor do they dispose the high mobility of small molecular species to dissipate energy. The only way that NPs have to reduce the excess of surface energy is through chemical reactions, resulting in fast degradation processes, or via particle aggregation, which reduces the available surface area at the expenses of the nanoscale physicochemical properties. Therefore, control of the surface state of NPs is needed for their efficient use in reactive environments (different from synthesis environments), such as the biological ones. This is commonly achieved through addition of different molecules that attach on the NP surface and reduce the surface energy. Conjugation, initially used to passivate and stabilize NPs, can also be used as an interface for functionalization, providing the chemical and biological moieties that will determine the behaviour and fate of the NPs, e.g. inside the body, by promoting or avoiding

opsonisation.[81, 82] Thus, the requirements for NP surface modifications are: (i) controlled colloidal stability (aggregation, sedimentation and stickiness) [70, 83]; (ii) controlled interaction with the surrounding medium (protein coating, absence of inmunogenity, targeting, etc) [82, 84, 85]; and (iii) controlled chemical reactivity (integrity and persistency in the working environment) [70, 86]. These requirements have to be accomplished simultaneously since different processes can happen at the same time, and there might be competition between them. In fact, it is commonly observed that NPs become unstable in biological media and that they corrode while aggregating and being coated by proteins, with the resulting material having a large tendency to precipitate [87].

Coatings used for NPs may not be persistent and can be metabolized, exposing the inorganic core. Employed coating molecules usually bind to the NP surface by their reactive (terminal) groups, such as thiols, amines and carboxylic groups, with different and specific affinities. As a consequence, it is necessary to be aware of the surfactant exchange possibilities: If the media is rich in new species that bind more strongly than those already present at the NP surface, a ligand exchange process can take place. This is the case of Au NPs coated with amines or carboxilic acids that are further exposed to thiol molecules [88]. In fact, it has even been observed that Au NPs coated with thiol molecules may undergo a ligand exchange process if other thiols are present in solution at similar or higher concentrations [89]. Other studies have shown that the surface coating can be weathered either by exposition to oxygen-rich environments or by ultraviolet (UV) irradiation [78, 90], which leads to nonreversible aggregation of the NPs. In more sophisticated situations, as in the case of alloys presenting different types of surface atoms, the different metals may spontaneously segregate forming a core-shell structure depending on the coating molecules (atoms with lower surface tension migrates outwards [91]). These examples illustrate the importance of the surface coating in the structure and ultimate behaviour of NPs, even when they exhibit the same core.

1.4.5. Protein corona

Surface coating modifications are not always intended. One interesting case is the modification of NP surfaces when exposed to biological fluids and their non-specific binding to media proteins [92] (**Figure 1.8**). This process, known as NP's protein corona

(PC), is one of the most significant surface alterations and may, in turn, strongly influence the biocompatibility and biodistribution of the NPs. As early as 2004, it was reported that the presence of proteins in physiological media affected the entry and intracellular localization of NPs in cells, and thus modulated their potential biological effects and toxicity [93]. Later on, the formation of a PC on top of the NP surface was observed to control biodistribution, uptake and biological response, transforming them from innocuous to toxic, or vice versa. Indeed, once the PC is formed, it is this that the cell actually "sees", rather than the NP surface [94].
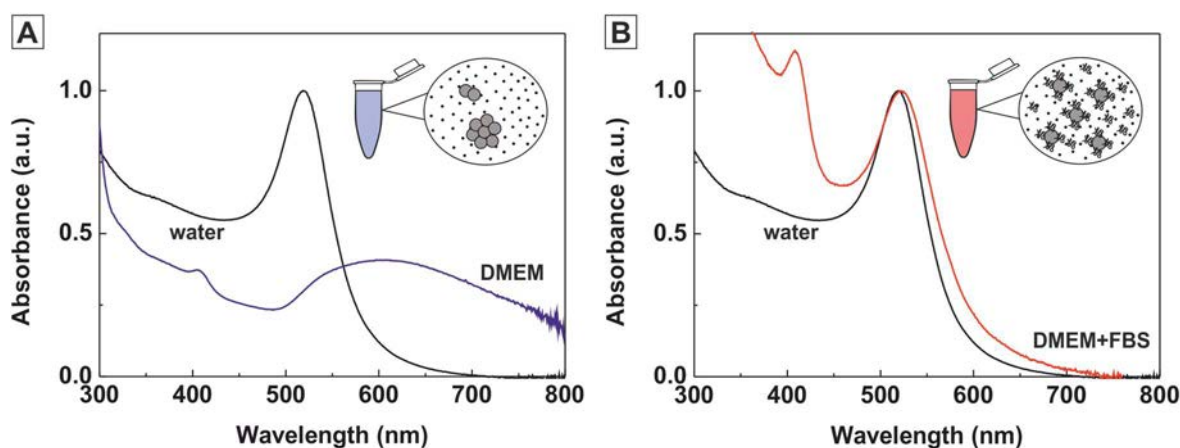
Figure 1.8. Effect of proteins on the colloidal stability of nanoparticles dispersed in biological media. Extinction spectra of Au NPs of 10 nm dispersed in water (black), DMEM (blue) and DMEM supplemented with fetal bovine serum (red). In the absence of proteins, Au NPs aggregate due to the high ionic strength of most biological media which screen the electrostatic repulsion between particles. This aggregation process is known to damp and broaden the characteristic extinction peak of the Au NPs (A). Conversely, in the presence of proteins, particles remain stable and the extinction peak is preserved (B).

The formation of the PC is a dynamic process governed by the Vroman effect: a competitive time-dependent adsorption of a complex mixture of proteins (as serum) by a finite number of surface sites [95]. Thus, the highest mobility and abundant proteins arrive first and are later (it may take several hours) replaced by less mobile proteins with a higher affinity for the surface. Therefore, after exposition to cell culture media, the PC of the NPs evolves in a time-dependent manner from a *soft corona*, a transient agglomeration of proteins on the NP surface, to a *hard corona*, a stable and permanent protein coating [92, 96]. This evolution is dependent on the serum as well as on NP size and surface chemistry and must be considered when assessing NP-biological interactions [92, 96-98]. For example, when NPs are intravenously injected they may take hours to reach the target site, by which time a fully *hard corona* has already formed on the surface,

whereas direct injection may present the NPs into the target site with the corona still in the *soft* form, which may have different effects.

The increasing number of publications relating to PC formation, which includes the study of different materials such as Au [92, 96], Ag, Fe_2O_3, CoO, CeO_2 [99], FePt and CdSe/ZnS [100] and the biological implications of the process highlights the increasing interest on the topic (see **Chapter 6**). In this regard, it is important to note that the formation of the PC adds a new layer of complexity to NPs and their characterization. Even in the simple case of well-dispersed spherical NPs, they are composed of at least three different layers: the inorganic core, the engineered surface coating and the corona of adsorbed biological molecules. A fourth layer could even be added if considering the local environment (temperature, pH, ion concentration) around the NP [101]. Because each of these components may have different fates and degrade individually, some authors claim that NPs should no longer be considered as homogeneous entities but complex heterostructures [102]. From this perspective, previous considerations about the characterization and reactivity of NPs should be drastically reviewed.

1.4.6. Reactivity and aggregation

Finally, it is important to consider the interaction between NPs in colloidal solutions and their effect on the final reactivity of the NPs. Full utilization of physico-chemical properties of NPs require well-dispersed individual particles in non-physical contact. Therefore, a significant effort has been made to obtain isolated NPs over long periods of time, which is usually achieved by conjugating the surface with different molecules that provide either electrostatic repulsion, e.g. allowing the formation of a double electrical layer of inorganic ions around the NPs, or steric stabilization, e.g.th9e conjugation of large organic or biological molecules [103]. In fact, this is one of the critical differences between synthetized and previously existing NPs, since natural and un-intentional occurring NPs tend to be in the form of aggregates.

There are several factors that cause the aggregation of colloidal NPs, for instance, the initial concentration of NPs, their chemical nature and the ionic strength of the medium [103], The degree of aggregation has relevant consequences on the final behaviour of the nanometric material. For example, TiO2NPs used for sunscreens are

usually composed of large agglomerates of micrometric domains [58]. Although these agglomerates are still effective sun blockers, the optical properties and light absorption of the constituent NPs are less efficient than when individually dispersed. Similarly, the optical properties of noble metal NPs are also affected by the aggregation state. Thus, when Au NPs aggregates their surface plasmon resonance is strongly attenuated and the peak position red-shifts. As a consequence, the colloidal solution changes its colour from red to purple. This feature has allowed the use of Au NPs as sensors, such as in the colorimetric detection of single-straded oligonucleotides targets by using DNA-functionalized Au NPs probes [104].

However, despite few exceptions, aggregation is an unwanted process if it cannot be controlled in a rational way, because not only are the properties of the NPs strongly deteriorated but they also usually present a higher toxicity. Indeed, aggregation is one of the main sources of controversy in the assessment of toxicity, safety and the therapeutic use of NPs, with different observed effects for similar NPs, ranging from acute toxicity to beneficial results [105]. At the source of these discrepancies, is the diversity of the materials employed in the different studies, which are presented under the same name. For instance, most research regarding NP toxicity has been performed with commercially available samples supplied in dry aggregated form. These are different materials from those produced by wet chemistry routes in specialized laboratories, where the NPs are always kept isolated and well dispersed. Additionally, most NPs are prone to aggregation when dispersed into buffers and biological fluids, such as complete cell culture medium or serum, due to the high ionic strength and corrosive effect of these mediums [92]. For example, He *et al.* [106] showed how intratracheal instilled CeO2 NPs into Wistar rats aggregated and formed sediments in the bronchoalveolar medium. Consequently, the actual objects that cells encounter may behave very differently from that initially designed and produced.

Functionalized NPs follow a similar fate unless coated with large highly mobile molecules that provide steric repulsion and control NP interaction. Thus, preincubation of NPs in the serum or functionalization of NPs with PVP or PEG molecules has been a traditional way to produce colloidally stable NPs in physiological media. It is important to note that molecules such as PEG can be absorbed on the surface of the NP in a flat or radial configuration, and it is only in the latter case that they stabilized the NPs against

aggregation [107]. Neither does the presence of proteins in solution that can adsorb in the surface of the NPs ensure their stability. The competition between aggregation induced by high ionic concentration and stabilization by protein absorption is well correlated to the relative amounts of both (ions and proteins) in the media and the kinetics of the processes [96, 107]. Thus, if NPs are added to the protein solution, there is always an excess of proteins that ensures that all NP surface can be passivated without the need for sharing proteins, which therefore aggregation is avoided. However, if proteins are added to a NP solution, in a very short times, there are few proteins and many NPs trying to absorb them, resulting in large protein-NP aggregates.

1.5. Future perspectives

There is growing recognition in the research community of the challenges presented by NPs, i.e. their definition, reproducible synthesis and efficient and safe use. To face these challenges interdisciplinary integration is of paramount importance. Applications of nanotechnologically designed objects still suffer from gaps between the different disciplines, particularly those destined for biological applications. On the one hand, chemists, physicists and engineers create new advanced materials of sophisticated functionality on a daily basis, but their understanding of biology is usually limited. As a results, they use precisely engineered NPs while ignoring key biological facts, e.g., that reagents used in the synthesis may be present in the final solution and must therefore be biocompatible to truly determine NP effects. On the other hand, in biological contexts, the effects of NPs on cells are typically investigated with relatively undefined samples with large polydispersity, limited colloidal stability, unknown surface chemistry, and large aggregate size. In these cases it is not always possible to determine the cause of the deleterious effect of the NPs. For this reason, appropriate and adapted protocols for the synthesis and characterization of NPs along with studies on the factors that determine their reactivity and chemical stability in different media is needed, otherwise conclusions will be weak.

1.6. References

[1] W.P. Halperin, Quantum size effects in metal particles, Reviews of Modern Physics 58 (1986) 533-606.

[2] A.P. Alivisatos, Semiconductor clusters, nanocrystals, and quantum dots, Science 271 (1996) 933-937.

[3] A.I. Ekimov, *et al.*, QUANTUM SIZE EFFECT IN SEMICONDUCTOR MICROCRYSTALS, Solid State Communications 56 (1985) 921-924.

[4] E.P. P., T.J. Meurig, Gold in a Metallic Divided State—From Faraday to Present-Day Nanoscience, Angewandte Chemie International Edition 46 (2007) 5480-5486.

[5] M.A. Garcia, Surface plasmons in metallic nanoparticles: fundamentals and applications (vol 44, 283001, 2011), Journal of Physics D-Applied Physics 45 (2012).

[6] M. Haruta, *et al.*, NOVEL GOLD CATALYSTS FOR THE OXIDATION OF CARBON-MONOXIDE AT A TEMPERATURE FAR BELOW 0-DEGREES-C, Chemistry Letters (1987) 405-408.

[7] D. Astruc, *et al.*, Nanoparticles as recyclable catalysts: The frontier between homogeneous and heterogeneous catalysis, Angewandte Chemie-International Edition 44 (2005) 7852-7872.

[8] B. Pelaz, *et al.*, Diverse Applications of Nanomedicine, ACS Nano 11 (2017) 2313-2381.

[9] I. Ojea-Jimenez, *et al.*, Engineered Inorganic Nanoparticles for Drug Delivery Applications, Current Drug Metabolism 14 (2013) 518-530.

[10] N.T.K. Thanh, *et al.*, Mechanisms of Nucleation and Growth of Nanoparticles in Solution, Chemical Reviews 114 (2014) 7610-7630.

[11] D.V. Talapin, *et al.*, Prospects of Colloidal Nanocrystals for Electronic and Optoelectronic Applications, Chemical Reviews 110 (2010) 389-458.

[12] S.X. Wang, G. Li, Advances in giant magnetoresistance biosensors with magnetic nanoparticle tags: Review and outlook, IEEE Trans. Magn. 44 (2008) 1687-1702.

[13] F.J. Heiligtag, M. Niederberger, The fascinating world of nanoparticle research, Materials Today 16 (2013) 262-271.

[14] N. Akaighe, *et al.*, Humic Acid-Induced Silver Nanoparticle Formation Under Environmentally Relevant Conditions, Environmental Science & Technology 45 (2011) 3895-3901.

[15] C. Buzea, *et al.*, Nanomaterials and nanoparticles: Sources and toxicity, Biointerphases 2 (2007) MR17-MR71.

[16] A. Dominika Dybowska, *et al.*, Naturally occurring clay nanoparticles in Latosols of Brazil central region: detection and characterization, EGU General Assembly Conference Abstracts 17 (2015) 8056.

[17] R. Blakemore, MAGNETOTACTIC BACTERIA, Science 190 (1975) 377-379.

[18] F. Reith, D.C. McPhail, Effect of resident microbiota on the solubilization of gold in soil from the Tomakin Park Gold Mine, New South Wales, Australia, Geochimica et Cosmochimica Acta 70 (2006) 1421-1438.

[19] J.F. Banfield, H. Zhang, Nanoparticles in the Environment, Reviews in Mineralogy and Geochemistry 44 (2001) 1-58.

[20] J. Park, *et al.*, One-Nanometer-Scale Size-Controlled Synthesis of Monodisperse Magnetic Iron Oxide Nanoparticles, Angewandte Chemie International Edition 44 (2005) 2872-2877.

[21] J. Kreuter, Nanoparticles—a historical perspective, International Journal of Pharmaceutics 331 (2007) 1-10.

[22] G. Frens, Controlled Nucleation for the Regulation of the Particle Size in Monodisperse Gold Suspensions, Nature Physical Science 241 (1973) 20.

[23] M. Brust, *et al.*, Synthesis of thiol-derivatised gold nanoparticles in a two-phase Liquid-Liquid system, Journal of the Chemical Society, Chemical Communications (1994) 801-802.

[24] C.B. Murray, *et al.*, Synthesis and characterization of nearly monodisperse CdE (E = sulfur, selenium, tellurium) semiconductor nanocrystallites, Journal of the American Chemical Society 115 (1993) 8706-8715.

[25] V.F. Puntes, *et al.*, Colloidal nanocrystal shape and size control: the case of cobalt, Science 291 (2001) 2115-2117.

[26] X. Peng, *et al.*, Shape control of CdSe nanocrystals, Nature 404 (2000) 59.

[27] Y.G. Sun, Y.N. Xia, Shape-controlled synthesis of gold and silver nanoparticles, Science 298 (2002) 2176-2179.

[28] T.S. Ahmadi, *et al.*, Shape-Controlled Synthesis of Colloidal Platinum Nanoparticles, Science 272 (1996) 1924-1925.

[29] N.G. Bastús, *et al.*, Kinetically Controlled Seeded Growth Synthesis of Citrate-Stabilized Gold Nanoparticles of up to 200 nm: Size Focusing versus Ostwald Ripening, Langmuir 27 (2011) 11098-11105.

[30] N.G. Bastús, *et al.*, Synthesis of Highly Monodisperse Citrate-Stabilized Silver Nanoparticles of up to 200 nm: Kinetic Control and Catalytic Properties, Chemistry of Materials 26 (2014) 2836-2846.

[31] J. Piella, *et al.*, Size-Controlled Synthesis of Sub-10-nanometer Citrate-Stabilized Gold Nanoparticles and Related Optical Properties, Chemistry of Materials 28 (2016) 1066-1075.

[32] J. Patarroyo, *et al.*, One-pot polyol synthesis of highly monodisperse short green silver nanorods, Chemical Communications 52 (2016) 10960-10963.

[33] E. González, *et al.*, Carving at the Nanoscale: Sequential Galvanic Exchange and Kirkendall Growth at Room Temperature, Science 334 (2011) 1377-1380.

[34] N.G. Bastus, *et al.*, Exploring New Synthetic Strategies for the Production of Advanced Complex Inorganic Nanocrystals, Zeitschrift Fur Physikalische Chemie-International Journal of Research in Physical Chemistry & Chemical Physics 229 (2015) 65-83.

[35] J. Park, *et al.*, Synthesis of monodisperse spherical nanocrystals, Angewandte Chemie-International Edition 46 (2007) 4630-4660.

[36] S.I. Lim, *et al.*, Exploring the Limitations of the Use of Competing Reducers to Control the Morphology and Composition of Pt and PtCo Nanocrystals, Chemistry of Materials 22 (2010) 4495-4504.

[37] A. Sperling Ralph, *et al.*, One-Pot Synthesis of Cationic Gold Nanoparticles by Differential Reduction, Zeitschrift für Physikalische Chemie, 2017, pp. 7.

[38] I. Ojea-Jiménez, *et al.*, Facile Preparation of Cationic Gold Nanoparticle-Bioconjugates for Cell Penetration and Nuclear Targeting, ACS Nano 6 (2012) 7692-7702.

[39] B.J. Beberwyck, *et al.*, Cation Exchange: A Versatile Tool for Nanomaterials Synthesis, The Journal of Physical Chemistry C 117 (2013) 19759-19770.

[40] S.I. Lim, *et al.*, Pt nanocrystal evolution in the presence of Au(iii)-salts at room temperature: spontaneous formation of AuPt heterodimers, Journal of Materials Chemistry 21 (2011) 11518-11523.

[41] E.V. Shevchenko, *et al.*, Structural diversity in binary nanoparticle superlattices, Nature 439 (2006) 55.

[42] L. Russo, *et al.*, Time- and Size-Resolved Plasmonic Evolution with nm Resolution of Galvanic Replacement Reaction in AuAg Nanoshells Synthesis, Chemistry of Materials (2018).

[43] M. Auffan, *et al.*, Towards a definition of inorganic nanoparticles from an environmental, health and safety perspective, Nature Nanotechnology 4 (2009) 634-641.

[44] D.R. Baer, *et al.*, Surface characterization of nanomaterials and nanoparticles: Important needs and challenging opportunities, Journal of Vacuum Science & Technology A 31 (2013).

[45] H. Rauscher, *et al.*, Regulatory Aspects of Nanomaterials in the EU, Chemie Ingenieur Technik 89 (2017) 224-231.

[46] B. Faure, *et al.*, Dispersion and surface functionalization of oxide nanoparticles for transparent photocatalytic and UV-protecting coatings and sunscreens, Science and Technology of Advanced Materials 14 (2013).

[47] V. Puntes, Nanoparticle interaction with biomolecules: How it shapes the nano-effects on immunity, Toxicology Letters 280 (2017) S38-S38.

[48] V. Puntes, Design and pharmacokinetical aspects for the use of inorganic nanoparticles in radiomedicine, British Journal of Radiology 89 (2016).

[49] G.J. Oostingh, *et al.*, Problems and challenges in the development and validation of human cell-based assays to determine nanoparticle-induced immunomodulatory effects, Particle and Fibre Toxicology 8 (2011) 8.

[50] M. Busquets-Fite, *et al.*, Exploring release and recovery of nanomaterials from commercial polymeric nanocomposites, Nanosafe 2012: International Conferences on Safe Production and Use of Nanomaterials2013.

[51] A. Sanchez, *et al.*, Ecotoxity of, and remediation with, engineered inorganic nanoparticles in the environment, Trac-Trends in Analytical Chemistry 30 (2011) 507-516.

[52] G. Bystrzejewska-Piotrowska, *et al.*, Nanoparticles: Their potential toxicity, waste and environmental management, Waste Management 29 (2009) 2587-2595.

[53] J. Conde, *et al.*, Revisiting 30 years of biofunctionalization and surface chemistry of inorganic nanoparticles for nanomedicine, Front Chem 2 (2014).

[54] T. Castro, *et al.*, Size-dependent melting temperature of individual nanometer-sized metallic clusters, Physical Review B 42 (1990) 8548-8556.

[55] J.-D. Cafun, *et al.*, Absence of Ce3+ Sites in Chemically Active Colloidal Ceria Nanoparticles, ACS Nano 7 (2013) 10726-10732.

[56] G.V. Lowry, *et al.*, Transformations of Nanomaterials in the Environment, Environmental Science & Technology 46 (2012) 6893-6899.

[57] N.G. Bastus, *et al.*, The Reactivity of Colloidal Inorganic Nanoparticles, 2012.

[58] N.G. Bastus, *et al.*, Reactivity of engineered inorganic nanoparticles and carbon nanostructures in biological media, Nanotoxicology 2 (2008) 99-112.

[59] E. Casals, *et al.*, Reactivity of inorganic nanoparticles in biological environments: insights into nanotoxicity mechanisms, Journal of Physics D: Applied Physics 45 (2012) 443001.

[60] E. Casals, *et al.*, Distribution and potential toxicity of engineered inorganic nanoparticles and carbon nanostructures in biological systems, Trac-Trends in Analytical Chemistry 27 (2008) 672-683.

[61] J.R. Morones, *et al.*, The bactericidal effect of silver nanoparticles, Nanotechnology 16 (2005) 2346-2353.

[62] G. Oberdorster, Toxicology of ultrafine particles: in vivo studies, Philosophical Transactions of the Royal Society of London Series a-Mathematical Physical and Engineering Sciences 358 (2000) 2719-2739.

[63] G. Oberdorster, *et al.*, Acute pulmonary effects of ultrafine particles in rats and mice, Research report (Health Effects Institute) (2000) 5-74; disc. 75-86.

[64] B. Nikoobakht, M.A. El-Sayed, Preparation and Growth Mechanism of Gold Nanorods (NRs) Using Seed-Mediated Growth Method, Chemistry of Materials 15 (2003) 1957-1962.

[65] B. Hvolbæk, *et al.*, Catalytic activity of Au nanoparticles, Nano Today 2 (2007) 14-18.

[66] S. Goy-López, *et al.*, Physicochemical Characteristics of Protein–NP Bioconjugates: The Role of Particle Curvature and Solution Conditions on Human Serum Albumin Conformation and Fibrillogenesis Inhibition, Langmuir 28 (2012) 9113-9126.

[67] H.D. Hill, *et al.*, The Role Radius of Curvature Plays in Thiolated Oligonucleotide Loading on Gold Nanoparticles, ACS Nano 3 (2009) 418-424.

[68] J.-S. Lee, *et al.*, DNA-Induced Size-Selective Separation of Mixtures of Gold Nanoparticles, Journal of the American Chemical Society 128 (2006) 8899-8903.

[69] P. Borm, *et al.*, Research Strategies for Safety Evaluation of Nanomaterials, Part V: Role of Dissolution in Biological Fate and Effects of Nanoscale Particles, Toxicological Sciences 90 (2006) 23-32.

[70] X. Li, *et al.*, Aggregation Kinetics and Dissolution of Coated Silver Nanoparticles, Langmuir 28 (2012) 1095-1104.

[71] E. Casals, *et al.*, Programmed Iron Oxide Nanoparticles Disintegration in Anaerobic Digesters Boosts Biogas Production, Small 10 (2014) 2801-2808.

[72] J.L. Elechiguerra, *et al.*, Corrosion at the Nanoscale: The Case of Silver Nanowires and Nanoparticles, Chemistry of Materials 17 (2005) 6042-6052.

[73] F.J. Lázaro, *et al.*, Magnetic characterisation of rat muscle tissues after subcutaneous iron dextran injection, Biochimica et Biophysica Acta (BBA) - Molecular Basis of Disease 1740 (2005) 434-445.

[74] Y. Han, *et al.*, Effect of Oxidation on Surface-Enhanced Raman Scattering Activity of Silver Nanoparticles: A Quantitative Correlation, Analytical Chemistry 83 (2011) 5873-5880.

[75] J. Liu, R.H. Hurt, Ion Release Kinetics and Particle Persistence in Aqueous Nano-Silver Colloids, Environmental Science & Technology 44 (2010) 2169-2175.

[76] M. Auffan, *et al.*, Chemical stability of metallic nanoparticles: A parameter controlling their potential cellular toxicity in vitro, Environmental Pollution 157 (2009) 1127-1133.

[77] T.J. Brunner, *et al.*, In Vitro Cytotoxicity of Oxide Nanoparticles: Comparison to Asbestos, Silica, and the Effect of Particle Solubility, Environmental Science & Technology 40 (2006) 4374-4381.

[78] A.M. Derfus, *et al.*, Probing the Cytotoxicity of Semiconductor Quantum Dots, Nano Letters 4 (2004) 11-18.

[79] C. Kirchner, *et al.*, Cytotoxicity of Colloidal CdSe and CdSe/ZnS Nanoparticles, Nano Letters 5 (2005) 331-338.

[80] G. Oberdorster, *et al.*, Nanotoxicology: an emerging discipline evolving from studies of ultrafine particles, Environmental health perspectives 113 (2005) 823-839.

[81] J. Comenge, *et al.*, Detoxifying Antitumoral Drugs via Nanoconjugation: The Case of Gold Nanoparticles and Cisplatin, Plos One 7 (2012).

[82] B. Pelaz, *et al.*, Surface Functionalization of Nanoparticles with Polyethylene Glycol: Effects on Protein Adsorption and Cellular Uptake, ACS Nano 9 (2015) 6996-7008.

[83] I. Ojea-Jimenez, *et al.*, Stability of polymer encapsulated quantum dots in cell culture media, Nanosafe 2012: International Conferences on Safe Production and Use of Nanomaterials2013.

[84] N.G. Bastus, *et al.*, Homogeneous conjugation of peptides onto gold nanoparticles enhances macrophage response, ACS Nano 3 (2009) 1335-1344.

[85] S. Makama, *et al.*, Properties of silver nanoparticles influencing their uptake in and toxicity to the earthworm Lumbricus rubellus following exposure in soil, Environmental pollution (Barking, Essex : 1987) 218 (2016) 870-878.

[86] Q. Xu, *et al.*, Impact of Surface Polyethylene Glycol (PEG) Density on Biodegradable Nanoparticle Transport in Mucus ex Vivo and Distribution in Vivo, ACS Nano 9 (2015) 9217-9227.

[87] N. Tran, The life of nanoparticles in contact with biological media and entities, Departament de Física, Universitat Autònoma de Barcelona, 2015, pp. 144.

[88] G.H. Woehrle, *et al.*, Thiol-Functionalized, 1.5-nm Gold Nanoparticles through Ligand Exchange Reactions: Scope and Mechanism of Ligand Exchange, Journal of the American Chemical Society 127 (2005) 2172-2183.

[89] A.M. Smith, *et al.*, Quantitative Analysis of Thiolated Ligand Exchange on Gold Nanoparticles Monitored by 1H NMR Spectroscopy, Analytical Chemistry 87 (2015) 2771-2778.

[90] F. Rancan, *et al.*, Cytotoxicity and photocytotoxicity of a dendritic C(60) mono-adduct and a malonic acid C(60) tris-adduct on Jurkat cells, Journal of photochemistry and photobiology. B, Biology 67 (2002) 157-162.

[91] M. Olivier, *et al.*, NiFe Nanoparticles: A Soft Magnetic Material?, Small 3 (2007) 451-458.

[92] E. Casals, *et al.*, Time Evolution of the Nanoparticle Protein Corona, Acs Nano 4 (2010) 3623-3632.

[93] J. Rejman, *et al.*, Size-dependent internalization of particles via the pathways of clathrin- and caveolae-mediated endocytosis, The Biochemical journal 377 (2004) 159-169.

[94] I. Lynch, *et al.*, What does the cell see?, Nature Nanotechnology 4 (2009) 546.

[95] S.M. Slack, T.A. Horbett, The Vroman Effect, Proteins at Interfaces II, American Chemical Society1995, pp. 112-128.

[96] J. Piella, *et al.*, Size-Dependent Protein-Nanoparticle Interactions in Citrate-Stabilized Gold Nanoparticles: The Emergence of the Protein Corona, Bioconjugate Chemistry 28 (2017) 88-97.

[97] M. Lundqvist, *et al.*, Nanoparticle size and surface properties determine the protein corona with possible implications for biological impacts, Proceedings of the National Academy of Sciences of the United States of America 105 (2008) 14265-14270.

[98] G. Maiorano, *et al.*, Effects of cell culture media on the dynamic formation of protein-nanoparticle complexes and influence on the cellular response, ACS Nano 4 (2010) 7481-7491.

[99] E. Casals, *et al.*, Hardening of the Nanoparticle-Protein Corona in Metal (Au, Ag) and Oxide (Fe3O4, CoO, and CeO2) Nanoparticles, Small 7 (2011) 3479-3486.

[100] C. Röcker, *et al.*, A quantitative fluorescence study of protein monolayer formation on colloidal nanoparticles, Nature Nanotechnology 4 (2009) 577.

[101] C. Pfeiffer*, et al.*, Interaction of colloidal nanoparticles with their local environment: the (ionic) nanoenvironment around nanoparticles is different from bulk and determines the physico-chemical properties of the nanoparticles, Journal of the Royal Society, Interface 11 (2014) 20130931.

[102] N. Feliu*, et al.*, In vivo degeneration and the fate of inorganic nanoparticles, Chemical Society Reviews 45 (2016) 2440-2457.

[103] J.K. Jiang*, et al.*, Characterization of size, surface charge, and agglomeration state of nanoparticle dispersions for toxicological studies, Journal of Nanoparticle Research 11 (2009) 77-89.

[104] F. Xia*, et al.*, Colorimetric detection of DNA, small molecules, proteins, and ions using unmodified gold nanoparticles and conjugated polyelectrolytes, Proceedings of the National Academy of Sciences of the United States of America 107 (2010) 10837-10841.

[105] E. Casals*, et al.*, Intrinsic and Extrinsic Properties Affecting Innate Immune Responses to Nanoparticles: The Case of Cerium Oxide, Frontiers in Immunology 8 (2017).

[106] X.A. He*, et al.*, Lung deposition and extrapulmonary translocation of nano-ceria after intratracheal instillation, Nanotechnology 21 (2010).

[107] J. Comenge, V.F. Puntes, The role of PEG conformation in mixed layers: from protein corona substrate to steric stabilization avoiding protein adsorption, ScienceOpen Research 0 (2015) 1-10.

Chapter 2:

Synthesis of metal nanoparticles with controllable sizes I: The case of gold

Gold has fascinated alchemists and later chemists for centuries. It is not then a coincidence that the synthesis of gold nanoparticles (Au NPs) has a long history, probably longer than any other NP synthesis. From the seminal work of Faraday in 1857, to the citrate method developed by Turkevich in 1951 and the more recent seeded growth techniques, the synthesis of Au NPs has advanced to such an extent that nowadays it is possible to obtain Au NPs with a large variety of sizes and shapes. However, size control of Au NPs smaller than 10 nm in diameter still represents a difficult challenge, mainly because the seeded growth approach has been traditionally difficult to apply to NPs with such small sizes. In this chapter, and related publication, the synthesis of sub-10 nm Au NPs by a seeded growth strategy is presented. The method has the advantage of being done in water and resulting in biocompatible and functionalizable Au NPs stabilized by citrate.

2.1. An introduction to the synthesis of gold nanoparticles

Metal nanoparticles (metal NPs) have attracted the interest of scientists for many years. In particular, Au NPs have been intensively studied because of their size- and shape-dependent physicochemical properties, which are of enormous interest for basic research, with applications in photonics, catalysis, electronics, and biomedicine [1]. Indeed, more than 100,000 publications have appeared on Au NPs to date and there are already several companies that commercialize them [2]. Accordingly to the knowledge acquired so far, to harvest the novel properties and high performance of NPs, a uniform size distribution is required [3]. Consequently, over the past decades, much effort has been conducted into developing strategies and techniques for synthetizing highly monodisperse Au NPs with controlled size and shape.

From a scientific point of view, the first step forward the controlled synthesis of Au NPs was pioneered by Michael Faraday in 1857, when he observed that the reduction of an aqueous solution of chloroaurate ($AuCl_4^-$) using phosphorus in carbon disulfide produced a pure form of deep-red-coloured gold, termed sol at that time (the word *colloid* was coined from the French word *colle* by Graham in 1861 and thus it was nonexistent at the time of Faraday's work) [4]. This is considered one of the major step in the development of nanotechnology. Following Faraday, much progresses in the rational preparation of Au NPs was achieved in the second half of the last century (**Scheme 2.1**). The invention of the electron microscope in 1931, which overcame the limitations of optical microscopes and enabled size and shape of NPs to be directly characterized, and the increasing interest of the petrochemical industry for the development of more efficient catalysts were probably the main reasons for the larger number of reported methods. Thus, the first breakthrough came 100 years after Faraday's seminal work, in 1957, with Turkevich's citrate method [5], and the later revision by Frens in 1973 [6]. The importance of these works is reflected in the fact that, more than 60 years later, the Turkevich method is still widely used by the scientific community for producing aqueous colloids of Au NPs. This was followed in 1981 by Schmid's group, who introduced the concept of Au quantum dots after synthesizing Au55-phosphine cluster [7]. Then, in 1993, Mulvaney and Giersing developed a thiolate based synthesis [8] and, in 1994, Brust-Schiffrin published their widely used biphasic method to produce
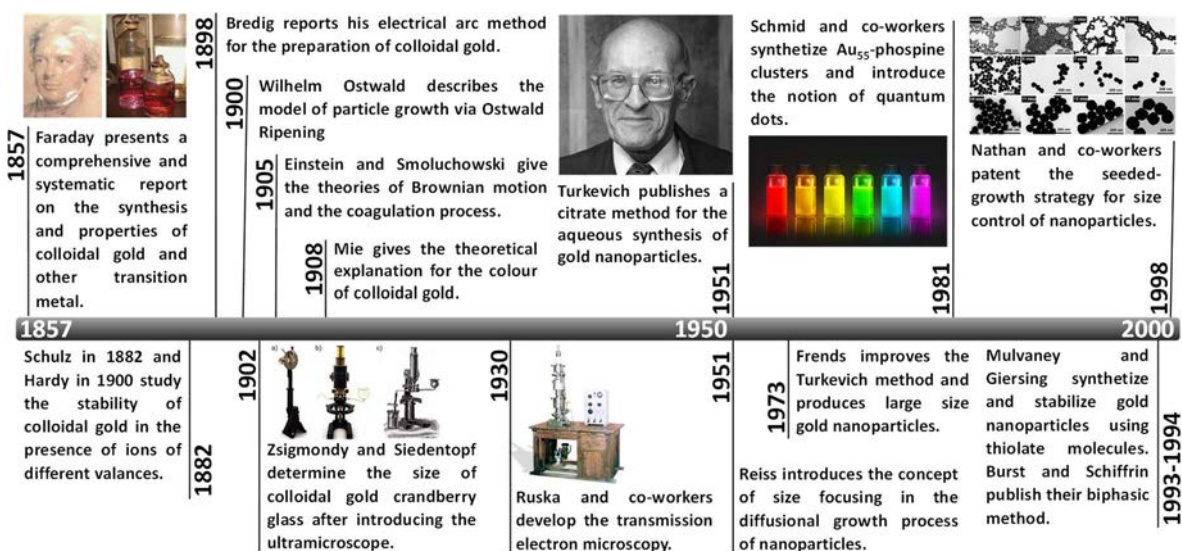
Scheme 2.1. Main breakthroughs in the modern history of gold nanoparticle synthesis.

thiolate stabilized Au NPs [9]. In 1998, Natan and co-workers developed the seeded growth strategy for size control [10] and finally, in 2001, Murphy introduced the synthesis of Au nanorods after growing anysotropically spherical Au NPs and initiated the research into shape control [11]. Most of the synthetic strategies used currently in the synthesis of Au NPs and other nanostructures are sophistications of these pioneering methods, which now extend to a large variety of materials, including metals, metal oxides and alloys.

As illustrated by the above mentioned works, Au NPs are usually prepared in colloidal form in an aqueous or non-aqueous solution where a dissolved gold precursor (typically a gold salt) is chemically reduced to gold atoms (**Figure 2.1**). Due to the low solubility of gold atoms, they aggregate in form of small clusters that subsequently grow into NPs. This process is often performed in the presence of a stabilizing agent, which
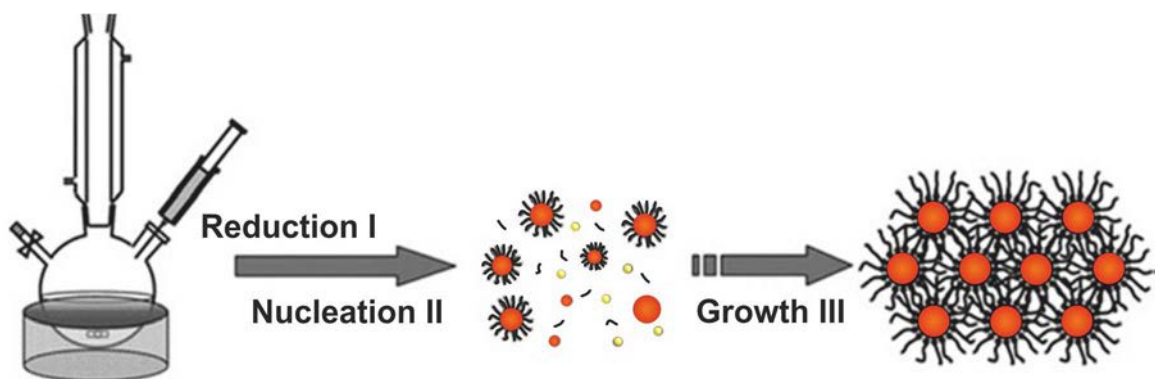

Figure 2.1. Colloidal synthesis of gold nanoparticles. Schematic representation of the wet chemical reduction method. Red/yellow spheres represent the NPs/precursor. Partially adapted from [3].

provides repulsive forces via an electrostatic stabilization (such as citrate ions) or a steric stabilization (as for polymers such as PVP) of the resultant NPs. The choice of the reducing agent, reaction time and capping material is determinant of the final morphology of the Au NPs, as well as, of their stability and potential biological, catalytic and optical features.

2.2. Size control and the seeded growth strategy

The basic idea for the formation of monodisperse NPs in solution was introduced by LaMer and his collages back to the 1950s [12, 13] (**Figure 2.2**). According to the model of LaMer, the preparation of highly uniform NPs requires, in succession, a sudden increase in supersaturation and a short burst nucleation of small clusters (nuclei) that fast depletes the monomer from the solution and prevents additional nucleation during the subsequent growth of these nuclei into the final. Otherwise, if nucleation persists throughout the particle-formation process, the growth histories of the NPs will differ greatly from one to another, and consequently the final size distribution will extend to a wide range. Thus, the model of LaMer interpreted for the synthesis of monodisperse NPs is a concept of separating nucleation and growth [3, 14-16]. Additionally, as stated by Reiss in 1951 [17], if the growth process only depends on the diffusion rates, smaller NPs will then grow faster in the presence of larger NPs, resulting in a self-regulating mechanism called "size focusing effect". In the case of Au NPs, this description has been overtaken by other more sophisticated models that are able to better predict the number of NPs, size and size distribution [18-20]. For example, an intermediate aggregative step, where the early formed highly reactive Au NPs aggregate and coalesce upon collision, has been recently used to explain the tendency of many Au NPs to show multiple twined crystalline structures (**Figure 2.2B**). Despite these limitations, the principles introduced by LaMer and Reiss are still vivid in most Au NP syntheses, rationalizing conventional approaches for kinetically controlling particle size, i.e. extending or restricting the growth process by adjusting the strength of the reducer and the flux of monomer supply.

Inspired by the principles of nucleation and particle growth of LaMer, Natan and co-workers first patented a seeded growth strategy in 1998 which led to an unprecedented control of Au NP size [10, 21, 22] and overcame most limitations of previous methods
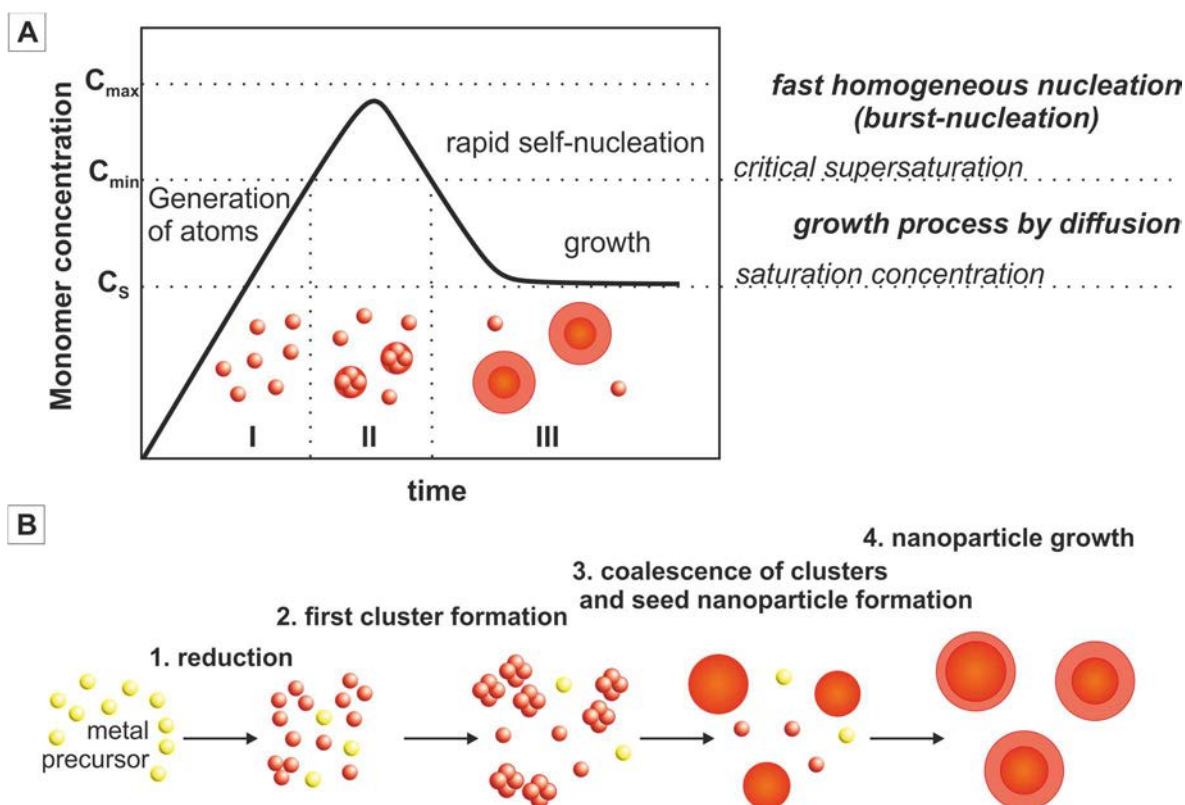
Figure 2.2. Gold nanoparticle formation process. (A) Nucleation-growth model of LaMer. Au atoms generated by chemical reduction (I) are essentially insoluble in liquid and, therefore, gradually aggregate in clusters called nuclei (II). The number and size of the nuclei depends on many parameters in the precipitation reaction, including the concentration and redox potential of the reactants, temperature and the nature and concentration of the surfactants. The formation of these nuclei results in a fast depletion of metal atoms from the solution below a critical concentration. At this stage no new nuclei are formed but the diffusion of atoms onto them may continue, a process known as growth by diffusion, forming the final NPs (III). Reiss[17] deduced that if the diffusional growth is only dependent on the monomer flux, smaller NPs will then grow faster in the presence of larger NPs, leading to a size focusing (narrowing of size distribution). (B) Model including growth by coalescence proposed by Polte [20]. The early formed nuclei are thermodynamically stable but not colloidal stable, thus they coalescence into larger clusters (seed nanoparticles), which already have stable sizes and consists of some hundreds of atoms.

(e.g. the increasing polydispersity of large particles obtained by the one-pot method of Frens [6]). In their experiments, Au NPs between 20-100 nm were prepared by adding pre-synthesized Au NPs used as seed into a growth solution containing a gold salt (HAuCl$_4$) and a mild reducing agent, such as hydroxylamine. In the absence of seed particles, the gold salt was not reduced, but when present in solution the reduction reaction was catalysed on the particle surface resulting in the possibility of growing them. As the growth step was separated from the nucleation step, the number of particles and the amount of precursor in solution could be easily adjusted in such a way that the system was maintained at relatively low supersaturated conditions and a homogeneous particle

growth was promoted. This work was improved by other groups, including Murphy's group [23], Han's group [24] and Liz-Marzan's group [25], who obtained highly monodisperse spherical Au NPs of various diameters by using ascorbic acid as a mild reducing agent and CTAB as a stabilizer. These groups also noticed that in the presence of external agents such as specific surfactants and ions, Au NPs could grow anysotropically [11]. For example, the presence of iodine ions adsorbs on gold seeds to suppress the growth along the Au(111) directions, leading to the formation of Au{111}-faced triangular nanoprisms [26]. However, as more sophisticated methods were developed for improved control of particle size and shape, the need for using CTAB and/or other toxic surfactants and reagents for a homogeneous growth of the Au NPs restricted their potential applications compared with those initially synthesized by Turkevich and Frens, where non-toxic reagents were employed (citrate, tetrachloraureate and water). As a consequence, over the last decade many research groups started looking back and revisiting Turkevich's synthesis.

2.3. The "classical" citrate reduction method

When it comes to the synthesis of Au NPs, probably the most convenient and widely used method is the so-called citrate route, which was introduced by Turkevich in 1951 and later improved by Frens in 1973 [5, 6]. The synthesis is done in water and involves a reduction of a gold salt ($HAuCl_4$) by citrate ions, which acts as both a stabilizer and reducing agent. The resultant dispersion exhibits a characteristic ruby red colour due to the presence of spherical and narrowly dispersed Au NPs of 15-20 nm in diameter. The main advantage of this protocol is the formation of colloidal stable Au NPs that are biocompatible (no toxic reagents, solvents nor surfactants are employed). Additionally, the use of a citrate as a capping agent is very convenient due to its easy post-synthesis treatment since it can be replaced by other capping agents bearing an appropriate functionality to the NPs.

Recently, several research groups revisited the Turkevich-Frens method in order to promote the convenient use of citrate-stabilized Au NPs. Indeed, it is amazing that more than 50 years after the publication of the work of Turkevich, still new mechanistic aspects of this reaction are revealed. In particular, the mechanism of Au^{3+} reduction by citrate

ions were examined in detail by these groups [27-36], which includes the formation of intermediate species [28], their pH dependence [31-33], and the effect of temperature [34], citrate to Au precursor ratio [32, 35] and the sequence of reagents addition [37] on the final particles size. On this basis, narrowly dispersed Au NPs with sizes ranging from 10 to 40 nm were synthesized by systematically varying these parameters.

Nevertheless, a major advance was probably achieved by our group in 2011. After the control of some reaction parameters, including temperature, solution pH, Au precursor to seed particle concentration, and citrate concentration, Bastús *et al.* [38] were able to obtain Au NPs from 10 to 200 nm in diameter by a kinetically controlled step-by-step seeded growth process without the need of additional reducing and stabilizing agents apart from citrate, thus merging the citrate method with the seeded-growth approach. Thanks to this and other similar works [39], it is now possible to synthesize biocompatible and functionalizable citrate stabilized Au NPs from 10 nm up to any desired size with a high degree of monodispersity without giving up biocompatibility and surface accessibility (**Figure 2.3**).
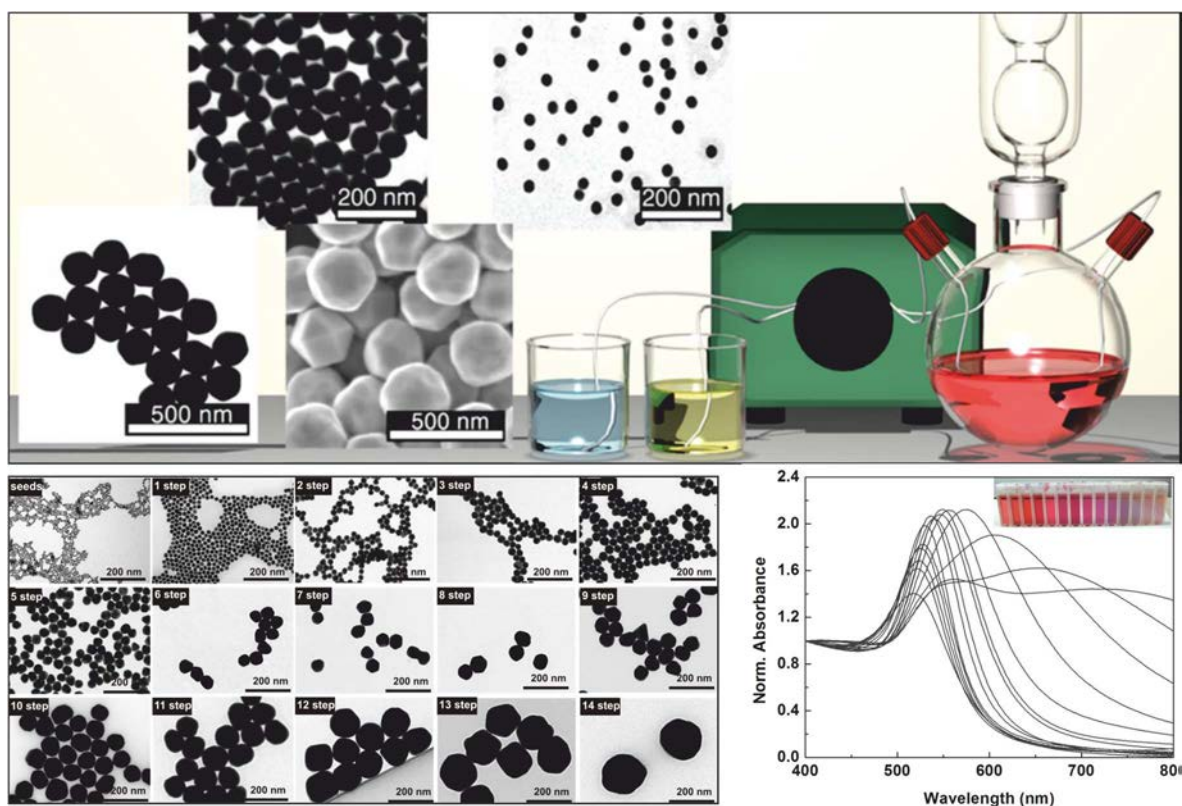

Figure 2.3. Citrate-capped Au NPs with diameters from 10 to 200 nm obtained using seeded growth strategies in water. On the bottom-right there is the corresponding extinction spectra of the obtained colloids together with representative images. Adapted from [38] and [39].

2.4. Limitations in the synthesis of sub-10 nm gold nanoparticles

One of major limitations of citrate based syntheses of Au NPs is that the size is down limited to 10 nm, since the weak reducing power of the citrate is not able to create the supersaturation conditions needed for the formation of a large number of small NPs. However, sub-10 nm Au NPs with tuneable surfaces are appealing materials. In this regime, the percentage of surface atoms starts taking over bulk atoms, and their atomic coordination at the surface decreases, increasing their catalytic properties and resulting in large variations in the particles responses and reactivity (i.e., plasmon shifts, corrosion, dissolution and stability) [30, 40]. Furthermore, these Au NPs are especially attractive for biomedical applications and nanomedicine since many body barriers fall in the sub-10-nm regime therefore determining NP biodistribution, accumulation in tissues, excretion, and interaction with proteins.[41, 42] As a result much effort was focused in the production of biocompatible sub-10 nm Au NPs.

Our group conducted a remarkable revision of the citrate method for the production of very small sizes (less than 10 nm) [37]. This revision involved modification of the order of addition of the reagents, the so called reverse addition [37, 43], which is carried out by fast injecting a concentrated solution of gold precursor to a boiling solution of citrate. The strategy takes advantage of the thermal decomposition of the citrate to the more reactive dicarboxiacetone that faster reduce the gold precursor, thereby producing a higher degree of supersaturation in solution that results in a larger number of smaller NPs. However, it offers a very limited size control. As a consequence, the synthesis of small Au NPs was based on using (i) an excess of a strong reducing agent, i.e. sodium borohydride, in the presence of (ii) strong capping agent, i.e. phosphines, that typically arrests a limited amount of reactant in micelles and quench further particle growth. Size-control is then achieved via thermodynamic and stoichiometric means by controlling the type and concentration of the strong capping agents, which, in turns, have been commonly reported to be toxic when internalized by organisms. In this context, the question was how to obtain reproducible control over particle size distribution in the small size regime similar to that obtained by Bastús *et al.* for large NPs, that is without restricting surface accessibility and biocompatibility.

The article presented in this chapter, "Size-controlled Synthesis of Sub-10 nm Gold Nanoparticles and Related Optical Properties", describes a kinetically controlled seeded growth protocol for the production of aqueous colloidal dispersions of Au NPs in the sub-10 nm range [44]. The main advance of the protocol lies in the combined use of two reducing agents, traces of a strong one (tannic acid) and an excess of a weak one (citrate), that enables a decrease in the initial size of the Au NPs from 10 nm down to 3.5 nm. Further step-by-step growth of these particles is achieved by subsequent injections of gold precursor while adjusting the reaction conditions to avoid new nucleation and ensure a homogeneous growth. As a result, highly monodisperse Au NPs with nanometre size resolution between 3.5 and 10 nm are obtained, although there is no reason why larger sizes could not be easily produced by increasing the number of growing steps. The unprecedented size resolution offered by this protocol represents a step forward in the synthesis of small Au NPs and it is of particular importance in the study of the size dependent optical and catalytic properties of these NPs.

2.5. Results: Size-controlled synthesis of sub-10 nm gold nanoparticles

An interesting approach to overcome the drawbacks in the citrate synthesis of small Au NPs is the use of a second stronger reducer in conjunction with citrate to promote a faster reduction of the gold ions and thus a higher degree of supersaturation during nucleation. The result is a larger number of smaller NPs. To our knowledge, and despite the numerous studies highlighting the importance of kinetically controlling the growth of NPs, our group pioneered the exploration of the differential reducing performance of two competing agents. The first paper was published in respect to the synthesis of Pt nanocrystals in organic solvents [45]. The results confirmed that it is possible to precisely accelerate the reduction of a fraction of the precursor molecules at a desired moment during the nucleation-growth process and to obtain particles of smaller sizes.

2.5.1. Tannic acid as an additional reducing agent in the synthesis of Au seeds

Among different strong reducers, such as NaBH$_4$ or ascorbic acid, we found tannic acid (TA), a plant derived polyphenolic compound, to be a particularly interesting candidate

for the synthesis of Au NPs [46, 47]. TA was first successfully used in conjunction with citrate in the preparation of Au NPs by Mühlpford in 1981 and later by Slot and Geuze in 1985 [48]. The main advantage relies on its biocompatibility. Indeed, tannin derivate molecules have been widely studied for their antioxidant, antimutagenic and anticancarciogenic properties among other attributes [46]. The reducing properties of these molecules drive from the numerous phenolic groups in their structure that take part in the redox reaction by forming quinone and donating electrons. The donated electrons then reduce metal ions to form corresponding metal NPs (**Scheme 2.2**).
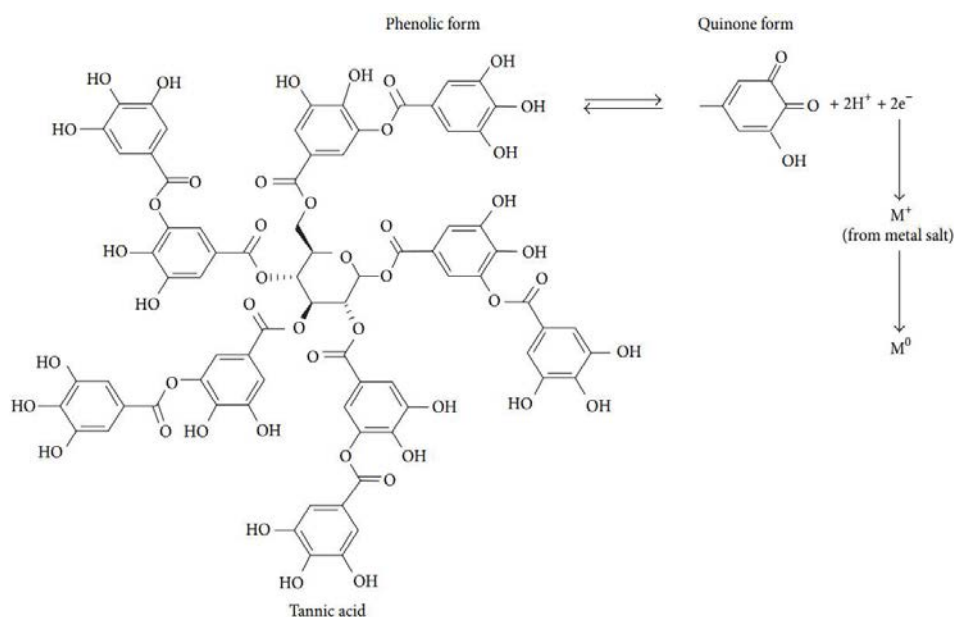
Scheme 2.2. Mechanism of tannic acid based reduction of metal salts. The phenolic groups in the TA are oxidized to quinones with the subsequent reduction of the metal ions. Adapted from [46].

Initially, the effect of TA in the synthesis of Au NPs was tested under different conditions of pH, temperature and TA concentration while the concentration of gold precursor and sodium citrate (SC) were maintained constant at values commonly used in similar methods (**Figure 2.4**). The addition of traces of TA resulted in an overall decrease in particle size. For example, when the concentration of TA was increased from 0.167 to 167 μM a controlled reduction of the diameter of the Au NPs from 10 to 3.3 nm was achieved. This trend can be rationalized as follows: the fast reduction of a fraction of Au^{3+} by TA induces an initial burst nucleation of small particles which decrease the Au^{3+} concentration below the nucleation limit, leaving the remaining fraction available for the particle growth. In this growth stage, citrate acts as both a stabilizer and a weak reducing agent. Following this idea, the fraction of the Au^{+3} reduced by TA determines the number
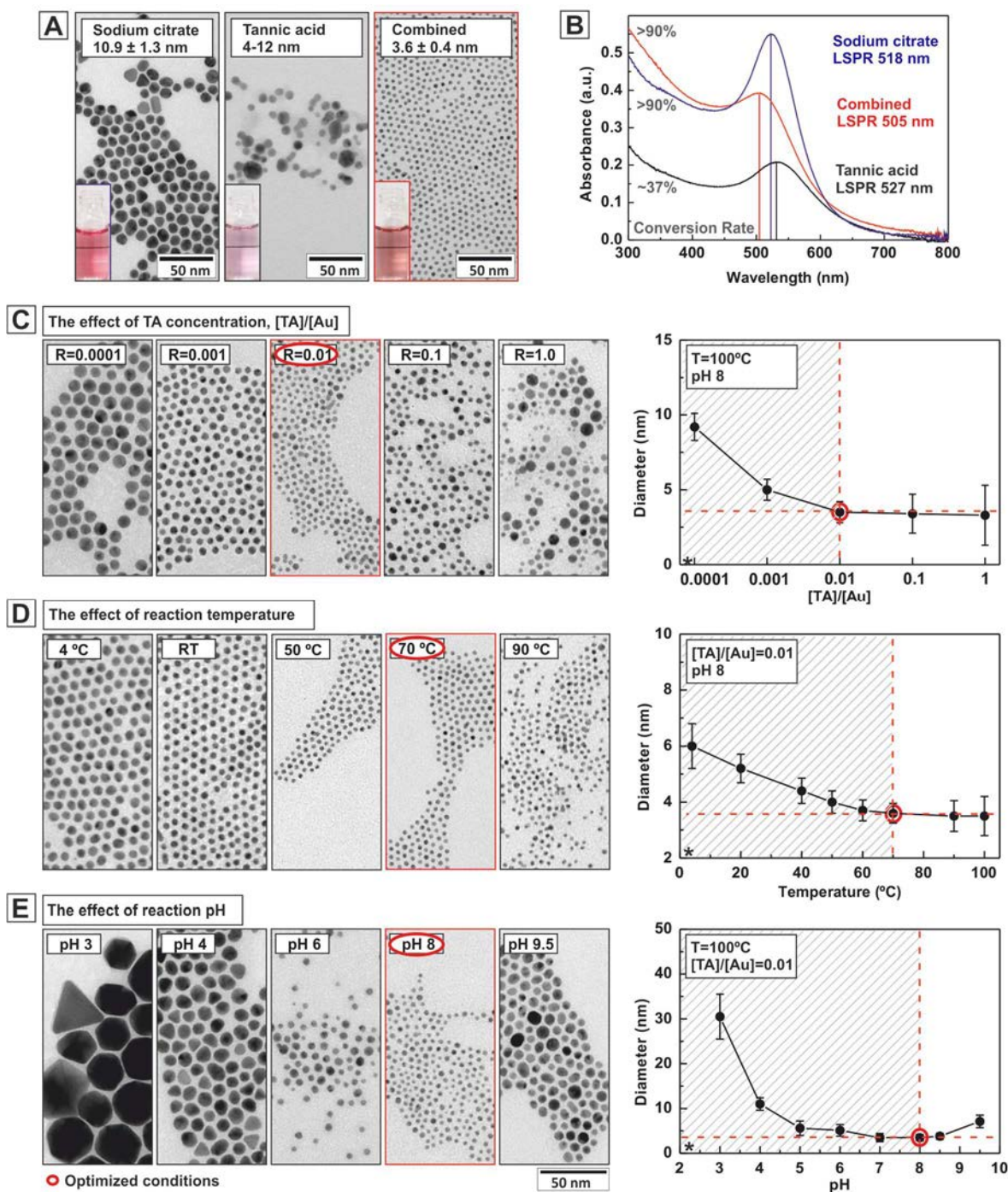
Figure 2.4. Effect of tannic acid, temperature and pH on the synthesis of gold nanoparticles. In a typical synthesis, an aqueous solution of $HAuCl_4$ (1 mL, 25 mM) was injected into a stirred solution of milli-Q-water (150 mL) containing a mixture of SC (2.2 mM) and TA (1.67 µM). (A-B) Representative TEM images and corresponding extinction spectra of Au NPs synthesized using SC (100 ºC, blue line), TA (100 ºC, black line) or a combination of SC and TA (70 ºC, red line). (C) Evaluation of the effect of TA. (D) Evaluation of the effect of reaction temperature. (E) Evaluation of the effect of reaction pH. The reaction pH was adjusted with citric acid and K_2CO_3. Depending on the reaction conditions, it took from few seconds (high TA concentration) to a couple of days (temperature 4 ºC) for the solution to turn first purple and then red. (*) Bars in the graphs are indicative of the sample polydispersity expressed in standard deviation of mean particle size.

of Au NPs in a matter of seconds, and these are then grown by the citrate in the reaction mixture, which slowly reduces the remaining Au^{+3} catalysed on the particle surface in a matter of few minutes. As a result, the number and size of the Au NPs is determined by the relative ratio of both reducers. An analogous idea can be applied to the size evolution that was observed after systematic increase in the reaction temperature. High temperatures favours nucleation over growth of the NPs and thus the particle size decrease. In contrast, slight variations in the solution pH resulted in critical effects on the size, shape and polydispersity of the Au NPs. It is well known that pH determines the hydrolysis of gold species in solution and the protonation/deprotonation state of citrate ions, which in turn affect the reaction mechanism and stability of the system [32]. In summary, these results confirmed the suitability of using competing reducing to properly balance nucleation and growth of Au NPs by adjusting the amount of the weak and strong reducers.

2.5.2. Is the size of 3.5 nm a down limit for citrate-stabilized Au NPs?

Interestingly, the smallest Au NPs obtained with highly monodisperse size distributions were around 3.5 nm in diameter. This is more or less in the same range as the smallest Au NPs reported using other protocols, where strong reducers are used, such as $NaBH_4$, and citrate acts purely as a stabilizer. The reasons for this size limit is something not fully understood but we believe that it may be related to colloidal stability rather than to thermodynamic or kinetic issues. An interesting discussion on this issue can be found in the recent work of Polte *et al.* [20] Thus, citrate molecules are probably unable to prevent high concentrated Au NPs from aggregation and coalescence when these are smaller than 3 nm due to their greater reactivity and the weak interaction of the citrate with gold surfaces. As a consequence, there is a point at which increasing the nucleation rate of the reaction, either by increasing the concentration of TA in solution or the temperature, is not accompanied by an effective reduction in particle size but by an increase in sample polydispersity; mainly because the high concentration of formed nuclei and the total depletion of monomer in solution favours particle growth via aggregative and coalescence pathways rather than growth by monomer diffusion. In this sense, we believe 3.5 nm to be a universal small size limit in the synthesis of Au NPs stabilized by citrate, at least, at the most commonly working Au concentrations (0.1-1 mM).

2.5.3. Growth of gold nanoparticle from 3.5 to 10 nm with nanometric size resolution

With the aim of acquiring further control on the size of the Au NPs in the small size regime, including size resolution, a step by step seeded growth process was developed. As discussed previously, the main advantage of this strategy is that the growth of the NPs is separated from the nucleation process and can be adjusted accordingly. The chosen Au NPs used as initial seeds were of 3.5 nm in diameter, synthesized at 70 ºC in an electron substeichiometric amount of TA with respect to the Au precursor, thus ensuring the total consumption of the TA before the end of the reaction. Successive injections of the Au precursor to the seed particles were then performed as depicted in **Figure 2.5**.
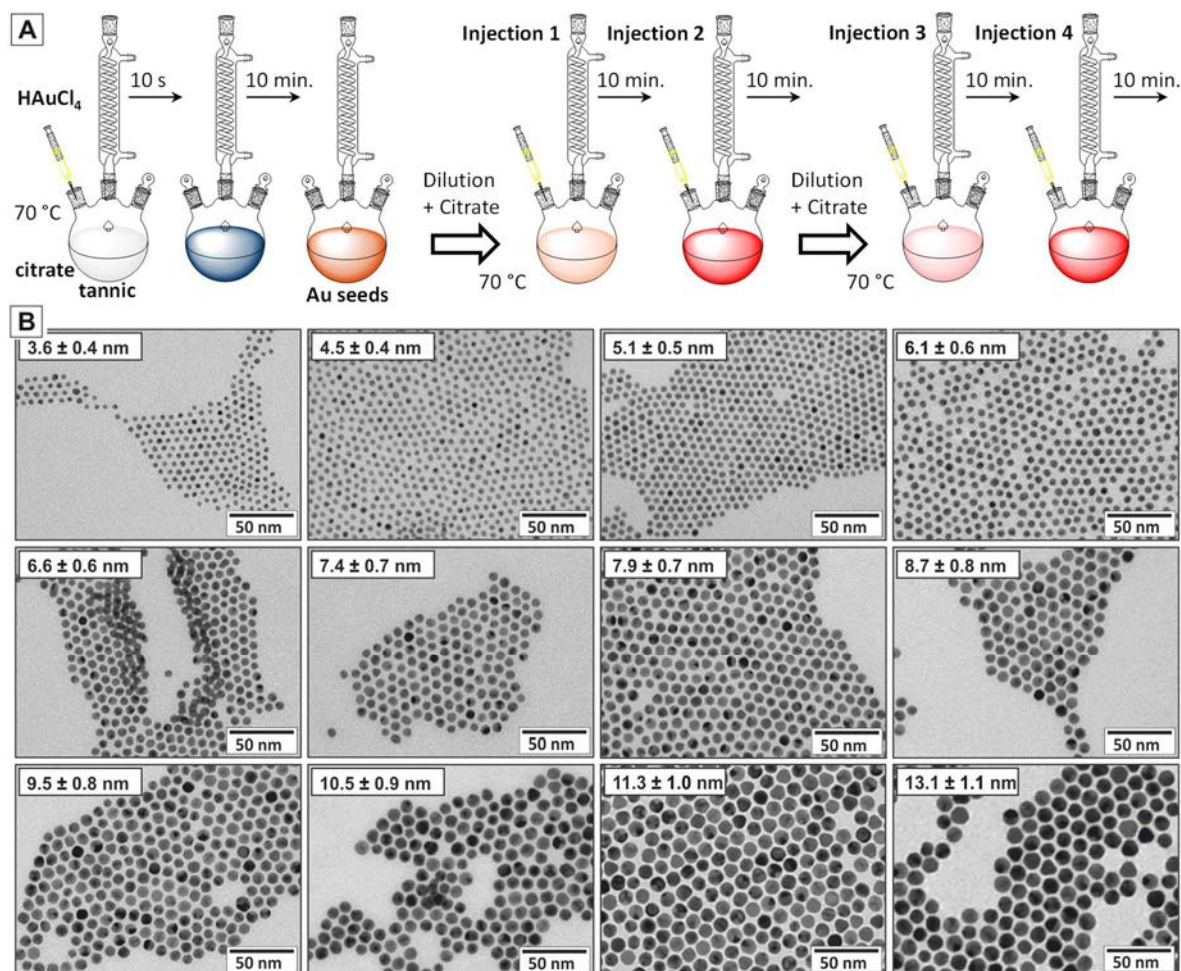
Figure 2.5. **Seeded growth synthesis of gold nanoparticles.** (A) Scheme of the synthetic protocol. (B) TEM images of seed Au NPs, top-left, and those obtained after each injection. The particle size increased from $3.6.8 \pm 0.4$ nm to $13.1.4 \pm 1.1$ nm, and the particle concentration decreased from $\sim 7.0 \times 10^{13}$ to $\sim 4.5 \times 10^{12}$ NPs/mL. Experimental procedure is described in more detail in **Publication 1**.

In order to ensure a homogeneous growth the following kinetic parameters were adjusted: 1) only sodium citrate (weak reducer) was added during subsequent growing steps; 2) the reaction temperature was maintained at 70 ºC, low enough to avoid new nucleation in the absence of TA; 3) Au precursor was added in successive and small quantities to avoid a high supersaturation degree of monomer in solution, which could cause new nucleation; and 4) a dilution step of the reaction mixture was performed after every two injections of the gold precursor to progressively reduce the number of NPs in solution and maintain a steady growth. This dilution step was also used to prevent an increase in solution's ionic strength after several gold precursor and citrate additions, which would compromise colloidal stability. Finally, it is worth noting that at the described conditions the solution remained at pH 5-7, a value that properly balance Au NP stability and Au precursor reactivity [31]. Representative TEM images of the Au NPs are shown in **Figure 2.5B**, proving a homogenous growth with nm size resolution.

2.6. Additional research

The size control described previously is particularly interesting in studies on the size-dependent properties of small Au NPs. Some of these studies were performed and the results collected as part of various publications that are discussed in the thesis (**Publications 1, 3-5**). For example, the controlled growth of Au NPs was used to describe some size dependencies in the localized surface plasmon resonance (LSPR) of these NPs measured by UV-vis spectroscopy (**Figure 2.6**). LSPRs are of special relevance in many applications of Au NPs, including photonics, photocatalysis, chemical and biological sensing and Raman scattering detection. Because LSPRs are strongly dependent on the morphology and surrounding environment of the NPs, they can be additionally used to assess the state of the NPs in colloidal solutions. A detailed description of the LSPR of the synthetized Au NPs can be found in the related **Publication 1**. Theoretical aspects of the LSPRs can also be found in **Chapter 4**.

Other experiments were conducted with the aim of assessing the possibility of performing the synthesis of small Au NPs at room temperature. This is of crucial importance: the development of protocols able to be done under truly green conditions, which not only consists of using biocompatible reagents but also under sustainable
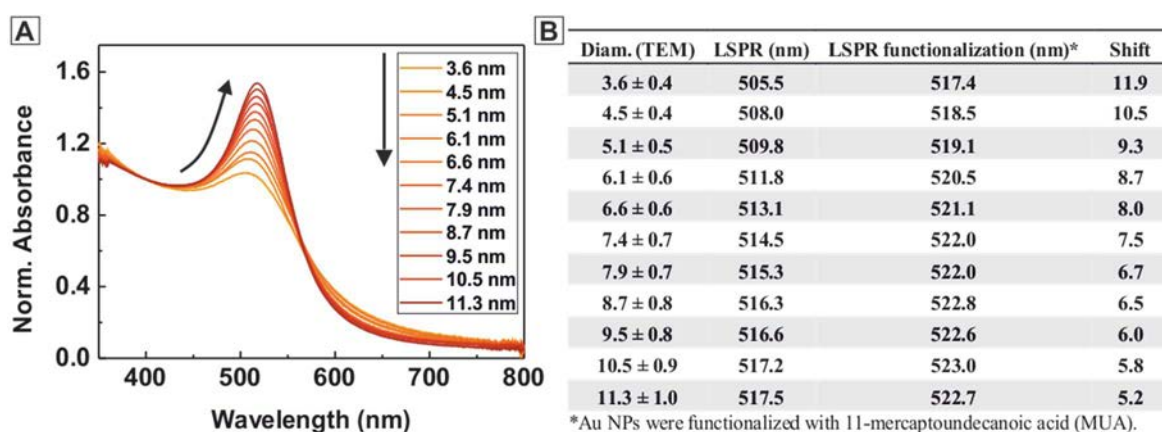
Diam. (TEM)	LSPR (nm)	LSPR functionalization (nm)*	Shift
3.6 ± 0.4	505.5	517.4	11.9
4.5 ± 0.4	508.0	518.5	10.5
5.1 ± 0.5	509.8	519.1	9.3
6.1 ± 0.6	511.8	520.5	8.7
6.6 ± 0.6	513.1	521.1	8.0
7.4 ± 0.7	514.5	522.0	7.5
7.9 ± 0.7	515.3	522.0	6.7
8.7 ± 0.8	516.3	522.8	6.5
9.5 ± 0.8	516.6	522.6	6.0
10.5 ± 0.9	517.2	523.0	5.8
11.3 ± 1.0	517.5	522.7	5.2

*Au NPs were functionalized with 11-mercaptoundecanoic acid (MUA).

Figure 2.6. **Optical properties of sub-10 nm gold nanoparticles.** (A) Extinction spectra normalized at 400 nm of the synthesized Au NPs showing well defined LSPR bands. (B) LSPR peak position before and after particle functionalization with a self-assembled monolayer of 11-mercaptoundecanoic acid (MUA). Higher sensitivity of small Au NPs towards surface modifications was traduced in larger shifts in the position of the LSPR peak (right column of table B).

energy consumption, is a prerequisite for the extensive production and use of NPs. In this regard, the synthetic conditions were optimized for the production of small Au NPs at room temperature in one-pot (**Figure 2.7**). Preservation of the high quality of the Au NPs and narrowness of the size distribution is evidenced in the superlattice self-assembly formed once the Au NPs were deposited on a TEM grid (**Figure 2.7A, B**). It is worth pointing that the diameter of the particles (5 nm) was slightly larger than that obtained at 70 ºC (3.5 nm) for equal concentration of TA.

Phenol based molecules other than TA were also tested for the synthesis. Gallic acid (GA) and pyrogallol (PG) were chosen as model molecules for being the structural units of TA and generally of many polyphenols. The absence of relevant differences in the size and size distribution of the Au NPs (**Figure 2.7C, D**) as well as in the kinetics of the formation process (**Figure 2.7E**), and thus the option of choosing the strong reducer, was attributed the result of the compensative effect by the SC, which stabilizes the particles and allows for a full conversion of the gold precursor. Therefore, there is apparently no reason why this protocol could not be extended to other polyphenol based molecules, or even other reducers, independently on their structure as far as the reducing power is satisfied. Indeed, we successfully reproduced the synthesis by using commercial tea leaves.

Figure 2.7F evidences the slow formation of the Au NPs at room temperature, which took more than 2 h under detailed conditions. To our knowledge, the synthesis of
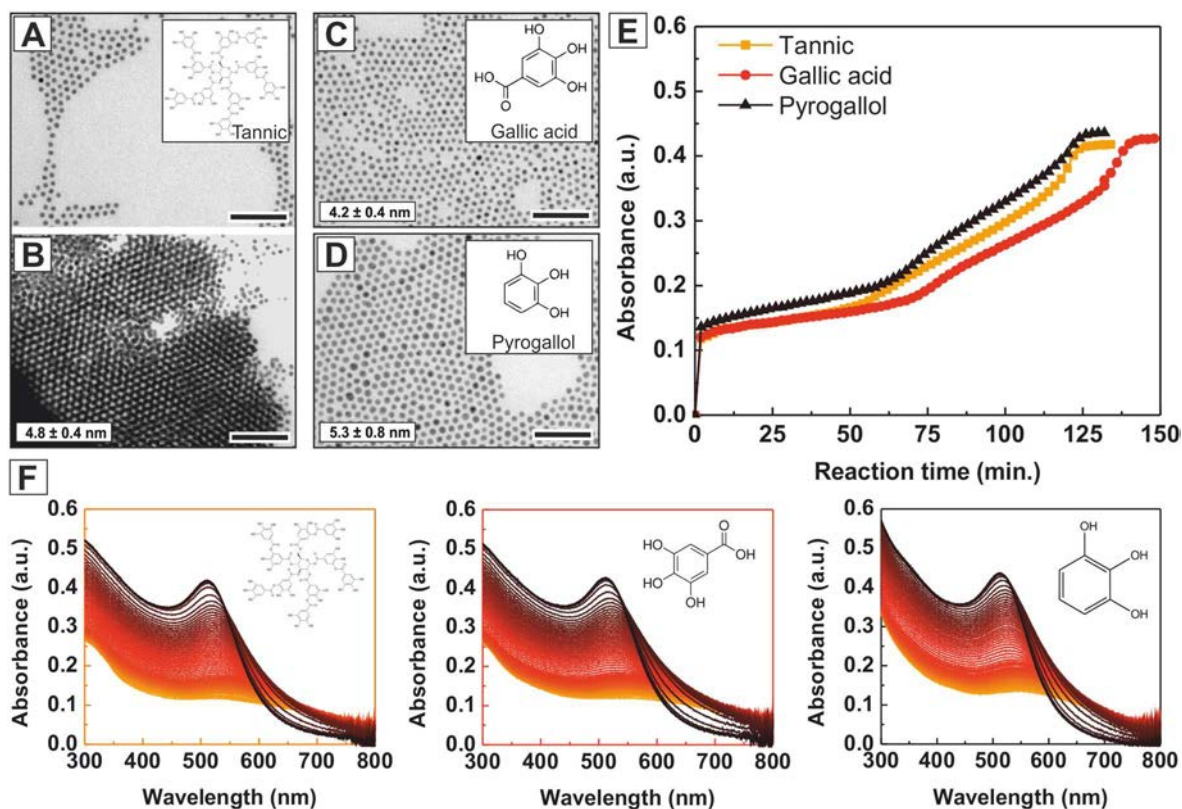
Figure 2.7. Synthesis of gold nanoparticles at room temperature. In a typical synthesis, an aqueous solution of HAuCl₄ (1 mL, 25 mM) was injected into a stirred solution of mili-Q water (150 mL) containing a mixture of SC (2.2 mM), TA (1.67 μM) and K₂CO₃ (1 mM). (A, B) Representative TEM images of the Au NPs after being conjugated with MUA for a proper deposition on the TEM grid. The formation of supperlattices is indicative of a high degree of monodispersity. Au NPs obtained using (C) GA (16.7 μM) and (D) PG (16.7 μM) instead of TA. (E) Time-dependent LSPR peak intensity during the reaction and (F) time-dependent extinction spectra at intervals of 2 min.

such small Au NPs (5 nm) in such large reaction times (>1 h) has not been previously reported. As an illustrative example, in the classical Turkevich method, the solution takes approximately 10 min. to turn read and the resultant Au NPs are significantly larger and polydisperse (10-15 nm). The reason of these observations is that the number of NPs is already determined at the very beginning of the reaction by the fraction of gold precursor reduced by the strong reducer and, therefore, the final particle size is not dependent of the time needed to consume the remaining Au precursor by the weak reducer. A slow reaction is of special importance for two main reasons: 1) it allows an easy in-situ monitoring of the reaction and thus provides deeper insights into the mechanism of particle formation and 2) a slow reaction is easy scalable since mass gradients during initial mixing of the precursors are avoided. These two points, as well as the nanometric step-by-step growth of the Au NPs at room temperature, are currently the subject of ongoing research.

Finally, characterization of Au NPs of such small sizes entailed some additional and unexpected challenges. **Figure 2.8** shows the tendency of the small Au NPs to sinter and merge when exposed to the electron beam of a TEM microscope. Interestingly, this was strongly dependent on the size of the Au NPs, affecting to a larger extent the particles with smaller sizes compared with the larger ones, giving insights into the size-dependent melting temperature of this material at the nanoscale. This is also being investigated in more detail.
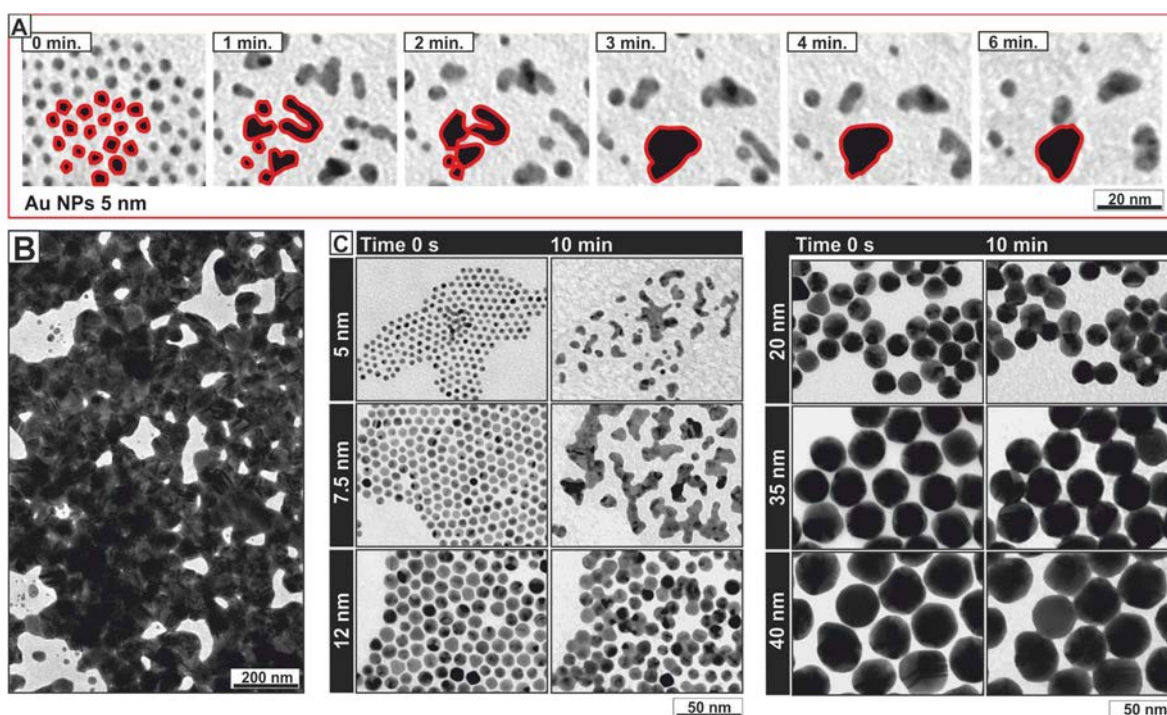
Figure 2.8. Sintering of gold nanoparticles. (A) Evolution of 5 nm Au NPs deposited on a carbon coated TEM grid after exposure to a microscope electron beam (JEOL 1010 operating at 80 kV). (B) Representative TEM image of a region with a dense concentration (multilayer) of Au NPs after 10 min under the electron beam. (C) Representative TEM images of Au NPs of different diameters before and after exposure to the electron beam. The small Au NPs were synthetized following the protocol herein described while the large Au NPs were synthetized using Bastús' protocol [38].

2.7. Conclusions

In this chapter a synthetic strategy for the production of sub-10 nm Au NPs in water has been presented. Resultant particles are highly monodisperse, biocompatible and easily functionalizable. Furthermore, the size control achieved by optimizing some key parameters of the reaction represents a step forwards in the study of the size dependent properties of these NPs. Ongoing research is being done in this direction.

2.8. References

[1] R. Sardar, *et al.*, Gold Nanoparticles: Past, Present, and Future, Langmuir 25 (2009) 13840-13851.

[2] A. Shiohara, *et al.*, Recent approaches toward creation of hot spots for SERS detection, Journal of Photochemistry and Photobiology C: Photochemistry Reviews 21 (2014) 2-25.

[3] J. Park, *et al.*, Synthesis of monodisperse spherical nanocrystals, Angewandte Chemie-International Edition 46 (2007) 4630-4660.

[4] M. Faraday, The Bakerian Lecture: Experimental Relations of Gold (and Other Metals) to Light, Philosophical Transactions of the Royal Society of London 147 (1857) 36.

[5] J. Turkevich, *et al.*, A STUDY OF THE NUCLEATION AND GROWTH PROCESSES IN THE SYNTHESIS OF COLLOIDAL GOLD, Discussions of the Faraday Society (1951) 55-&.

[6] G. Frens, Controlled Nucleation for the Regulation of the Particle Size in Monodisperse Gold Suspensions, Nature Physical Science 241 (1973) 20.

[7] G. Schmid, *et al.*, Au55[P(C6H5)3]12CI6 — ein Goldcluster ungewöhnlicher Größe, Chemische Berichte 114 (1981) 3634-3642.

[8] M. Giersig, P. Mulvaney, Preparation of ordered colloid monolayers by electrophoretic deposition, Langmuir 9 (1993) 3408-3413.

[9] M. Brust, *et al.*, Synthesis of thiol-derivatised gold nanoparticles in a two-phase Liquid-Liquid system, Journal of the Chemical Society, Chemical Communications (1994) 801-802.

[10] K.R. Brown, M.J. Natan, Hydroxylamine seeding of colloidal Au nanoparticles in solution and on surfaces, Langmuir 14 (1998) 726-728.

[11] J.N. R., *et al.*, Seed-Mediated Growth Approach for Shape-Controlled Synthesis of Spheroidal and Rod-like Gold Nanoparticles Using a Surfactant Template, Advanced Materials 13 (2001) 1389-1393.

[12] V.K. Lamer, NUCLEATION IN PHASE TRANSITIONS, Industrial and Engineering Chemistry 44 (1952) 1270-1277.

[13] V.K. Lamer, R.H. Dinegar, THEORY, PRODUCTION AND MECHANISM OF FORMATION OF MONODISPERSED HYDROSOLS, Journal of the American Chemical Society 72 (1950) 4847-4854.

[14] C.B. Murray, *et al.*, Synthesis and characterization of monodisperse nanocrystals and close-packed nanocrystal assemblies, Annual Review of Materials Science 30 (2000) 545-610.

[15] Y. Xia, *et al.*, Shape-Controlled Synthesis of Metal Nanocrystals: Simple Chemistry Meets Complex Physics?, Angewandte Chemie International Edition 48 (2009) 60-103.

[16] R. Viswanatha, D.D. Sarma, Growth of Nanocrystals in Solution, Nanomaterials Chemistry2007.

[17] H. Reiss, THE GROWTH OF UNIFORM COLLOIDAL DISPERSIONS, Journal of Chemical Physics 19 (1951) 482-487.

[18] N.T.K. Thanh, *et al.*, Mechanisms of Nucleation and Growth of Nanoparticles in Solution, Chemical Reviews 114 (2014) 7610-7630.

[19] H. You, J. Fang, Particle-mediated nucleation and growth of solution-synthesized metal nanocrystals: A new story beyond the LaMer curve, Nano Today 11 (2016) 145-167.

[20] J. Polte, Fundamental growth principles of colloidal metal nanoparticles - a new perspective, CrystEngComm 17 (2015) 6809-6830.

[21] K.R. Brown, *et al.*, Seeding of Colloidal Au Nanoparticle Solutions. 2. Improved Control of Particle Size and Shape, Chemistry of Materials 12 (2000) 306-313.

[22] K.R. Brown, *et al.*, Hydroxylamine Seeding of Colloidal Au Nanoparticles. 3. Controlled Formation of Conductive Au Films, Chemistry of Materials 12 (2000) 314-323.

[23] N.R. Jana, *et al.*, Seeding Growth for Size Control of 5−40 nm Diameter Gold Nanoparticles, Langmuir 17 (2001) 6782-6786.

[24] K. Kwon, *et al.*, Controlled Synthesis of Icosahedral Gold Nanoparticles and Their Surface-Enhanced Raman Scattering Property, The Journal of Physical Chemistry C 111 (2007) 1161-1165.

[25] J. Rodríguez-Fernández, *et al.*, Seeded Growth of Submicron Au Colloids with Quadrupole Plasmon Resonance Modes, Langmuir 22 (2006) 7007-7010.

[26] M. Grzelczak*, et al.*, Shape control in gold nanoparticle synthesis, Chemical Society Reviews 37 (2008) 1783-1791.

[27] I. Ojea-Jimenez*, et al.*, Small Gold Nanoparticles Synthesized with Sodium Citrate and Heavy Water: Insights into the Reaction Mechanism, Journal of Physical Chemistry C 114 (2010) 1800-1804.

[28] S. Kumar*, et al.*, Modeling of formation of gold nanoparticles by citrate method, Industrial & Engineering Chemistry Research 46 (2007) 3128-3136.

[29] J. Polte*, et al.*, Mechanism of Gold Nanoparticle Formation in the Classical Citrate Synthesis Method Derived from Coupled In Situ XANES and SAXS Evaluation, Journal of the American Chemical Society 132 (2010) 1296-1301.

[30] B.K. Pong*, et al.*, New insights on the nanoparticle growth mechanism in the citrate reduction of Gold(III) salt: Formation of the au nanowire intermediate and its nonlinear optical properties, Journal of Physical Chemistry C 111 (2007) 6281-6287.

[31] F. Schulz*, et al.*, Little Adjustments Significantly Improve the Turkevich Synthesis of Gold Nanoparticles, Langmuir 30 (2014) 10779-10784.

[32] X.H. Ji*, et al.*, Size control of gold nanocrystals in citrate reduction: The third role of citrate, Journal of the American Chemical Society 129 (2007) 13939-13948.

[33] W. Patungwasa, J.H. Hodak, pH tunable morphology of the gold nanoparticles produced by citrate reduction, Materials Chemistry and Physics 108 (2008) 45-54.

[34] C.F. Li*, et al.*, Facile synthesis of concentrated gold nanoparticles with low size-distribution in water: temperature and pH controls, Nanoscale Research Letters 6 (2011).

[35] J. Kimling*, et al.*, Turkevich method for gold nanoparticle synthesis revisited, Journal of Physical Chemistry B 110 (2006) 15700-15707.

[36] B. Rodríguez-González*, et al.*, An Electrochemical Model for Gold Colloid Formation via Citrate Reduction, Zeitschrift für Physikalische Chemie, 2007, pp. 415.

[37] I. Ojea-Jiménez*, et al.*, Influence of the Sequence of the Reagents Addition in the Citrate-Mediated Synthesis of Gold Nanoparticles, The Journal of Physical Chemistry C 115 (2011) 15752-15757.

[38] N.G. Bastús*, et al.*, Kinetically Controlled Seeded Growth Synthesis of Citrate-Stabilized Gold Nanoparticles of up to 200 nm: Size Focusing versus Ostwald Ripening, Langmuir 27 (2011) 11098-11105.

[39] C. Ziegler, A. Eychmüller, Seeded Growth Synthesis of Uniform Gold Nanoparticles with Diameters of 15−300 nm, The Journal of Physical Chemistry C 115 (2011) 4502-4506.

[40] D. Wang*, et al.*, How and Why Nanoparticle's Curvature Regulates the Apparent pKa of the Coating Ligands, Journal of the American Chemical Society 133 (2011) 2192-2197.

[41] J. Comenge*, et al.*, Detoxifying Antitumoral Drugs via Nanoconjugation: The Case of Gold Nanoparticles and Cisplatin, Plos One 7 (2012).

[42] H.S. Choi*, et al.*, Renal clearance of quantum dots, Nature Biotechnology 25 (2007) 1165-1170.

[43] S.K. Sivaraman*, et al.*, Monodisperse sub-10 nm gold nanoparticles by reversing the order of addition in Turkevich method – The role of chloroauric acid, Journal of Colloid and Interface Science 361 (2011) 543-547.

[44] J. Piella*, et al.*, Size-Controlled Synthesis of Sub-10-nanometer Citrate-Stabilized Gold Nanoparticles and Related Optical Properties, Chemistry of Materials 28 (2016) 1066-1075.

[45] S.I. Lim*, et al.*, Exploring the Limitations of the Use of Competing Reducers to Control the Morphology and Composition of Pt and PtCo Nanocrystals, Chemistry of Materials 22 (2010) 4495-4504.

[46] T. Ahmad, Reviewing the Tannic Acid Mediated Synthesis of Metal Nanoparticles, Journal of Nanotechnology 2014 (2014) 11.

[47] S.K. Sivaraman*, et al.*, Room-temperature synthesis of gold nanoparticles — Size-control by slow addition, Gold Bulletin 43 (2010) 275-286.

[48] J.W. Slot, H.J. Geuze, A new method of preparing gold probes for multiple-labeling cytochemistry, European Journal of Cell Biology 38 (1985) 87-93.

Publication 1

CHEMISTRY OF MATERIALS

Size-Controlled Synthesis of Sub-10-nanometer Citrate-Stabilized Gold Nanoparticles and Related Optical Properties.

Jordi Piella,[†,‖] Neus G. Bastús,[†] and Victor Puntes[*,†,‡,§]

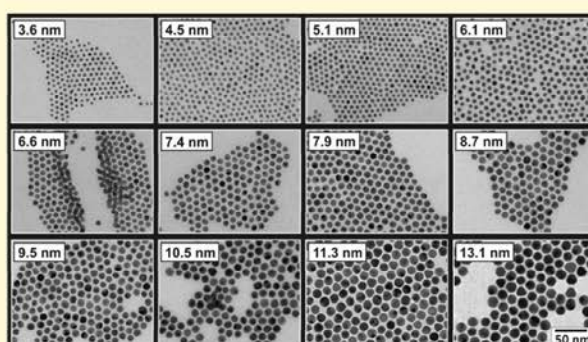[†]Institut Català de Nanociència i Nanotecnologia (ICN2), Campus UAB, 08193 Bellaterra, Barcelona, Spain
[‡]Vall d'Hebron Institut de Recerca (VHIR), 08035, Barcelona, Spain
[§]Institució Catalana de Recerca i Estudis Avançats (ICREA), 08010 Barcelona, Spain
[‖]Universitat Autònoma de Barcelona (UAB), Campus UAB, 08183 Bellaterra, Barcelona, Spain

S *Supporting Information*

ABSTRACT: Highly monodisperse, biocompatible and functionalizable sub-10-nm citrate-stabilized gold nanoparticles (Au NPs) have been synthesized following a kinetically controlled seeded-growth strategy. The use of traces of tannic acid together with an excess of sodium citrate during nucleation is fundamental in the formation of a high number (7×10^{13} NPs/ mL) of small ~3.5 nm Au seeds with a very narrow distribution. A homogeneous nanometric growth of these seeds is then achieved by adjusting the reaction parameters: pH, temperature, sodium citrate concentration and gold precursor to seed ratio. We use this method to produce Au NPs with a precise control over their sizes between 3.5 and 10 nm and a versatile surface chemistry allowing studying the size-dependent optical properties in this transition size regime lying between clusters and nanoparticles. Interestingly, an inflection point is observed for Au NPs smaller than 8 nm in which the sensitivity of the localized surface plasmon resonance (LSPR) peak position as a function of NPs size and surface modifications dramatically increase. These studies are relevant in the design of the final selectivity, activity and compatibility of Au NPs, especially in those (bio)applications where size is a critical parameter (e.g., biodistribution, multiplex labeling, and protein interaction).

■ INTRODUCTION

Gold nanoparticles (Au NPs) are still one of the most interesting nanomaterials because of their exceptional chemical stability, catalytic activity, processability, and metallic nature, which provide them unique size-dependent optical and electronic properties. As a result, Au NPs are used in a wide variety of technologies including catalysis,[1] nanoelectronics,[2] and biomedicine[3] (sensing, diagnosis, imaging, and labeling). To develop nanomaterials to be suitable for the "bottom-up" design of their applicability, their synthesis must lead to monodispersed entities with structure-controlled features that exhibit reproducible properties.[4] Among all sizes, highly monodisperse and functionalizable sub-10 nm Au NPs with tunable surfaces are appealing materials. In this regime, the percentage of surface atoms starts taking over bulk atoms, and their atomic coordination at the surface decreases, increasing their catalytic properties and resulting in large variations in the particles responses and reactivity (i.e., plasmon shifts, corrosion, dissolution, stability, ...).[5–8] Besides, these Au NPs are especially attractive for biomedical applications and nanomedicine since many body barriers falls in the sub-10-nm regime therefore determining NPs' biodistribution, accumulation in tissues, excretion, and interaction with proteins.[9–12]

Most common strategies for the synthesis of sub-10 nm Au NPs are based on the use of strong reducing agents, i.e. sodium borohydride, in the presence of strong capping ligands that quench particle growth, following either a two-phase liquid–liquid method (the so-called Brust method[13]) or single-phase approaches. This is the case of small hydrophobic gold clusters coated by phosphines (1.4–1.5 nm),[14,15] amines (2.5–7 nm),[16] and alkanethiols (1–6 nm).[13,17,18] Similarly, the use of hydrophilic ligands such as poly(ethylene glycol) (PEG) (1.5–18 nm),[19–21] polymeric stabilizers (1.5–4 nm),[22] strong binding cationic surfactants (4–6 nm)[23,24] and other thiol-functionalized molecules (0.7–3.2 nm)[25,26] allow producing Au NPs in this small size regime.[27–29] However, at the end of the synthesis, their surfaces are passivated by a strong binding surfactant layer. In the particular case of aqueous syntheses, it is especially interesting the well-established protocol producing Au NPs in the range 5–40 nm based on the use of cetyltrimethylammonium bromide (CTAB), initially reported by Murphy and co-workers.[30,31] Here, as in the case of the
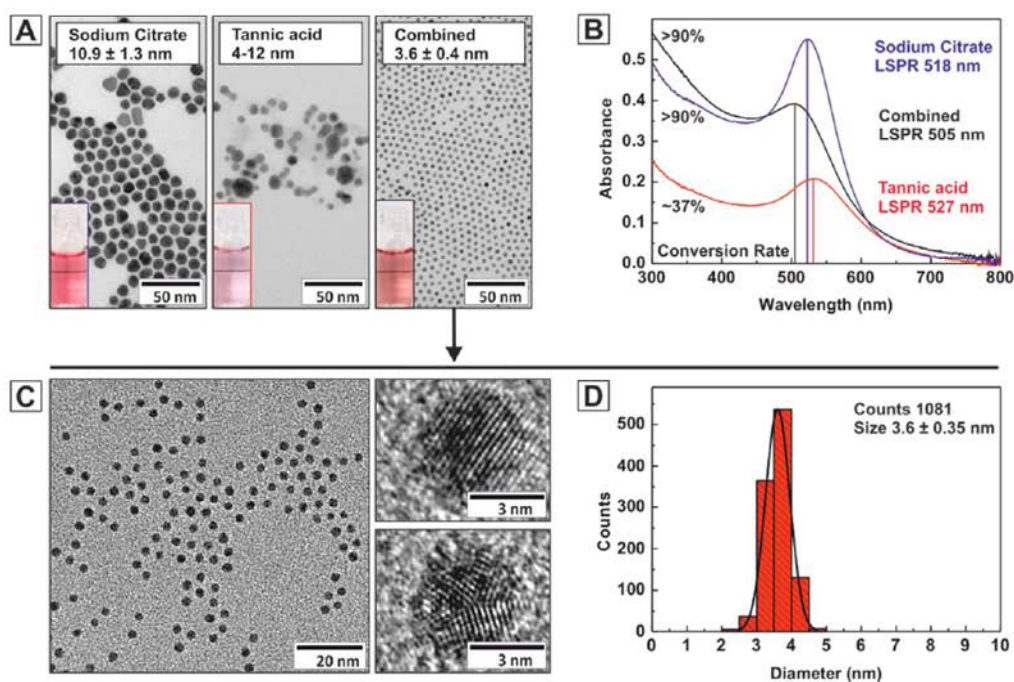
`Article`

Figure 1. (A) Representative TEM images of Au NPs synthesized by injecting 1 mL of HAuCl₄ (25 mM) to a 150 mL solution of: SC, TA or the combination of both SC and TA. Refer to Supporting Information section 2.1 for experimental details. (B) Corresponding UV−vis spectra and estimated precursor conversion rate, by measuring the absorbance at 400 nm[55] of the Au colloids obtained in A. (C) High resolution TEM images of ~3.5 nm Au NPs with individual particle image indicating multiple-twin boundaries. (D) Size distribution profile showing the highly monodispersity of the sample.

syntheses in organic solvents, and despite the excellent size control provided by this method, the use of nonbiocompatible reagents, which entail tedious "detoxification" steps, and/or the use of strong surfactants that blocks NP surface limiting further functionalization, restricts their final use.[32] In this context, the question is still how to produce Au NPs in the small regime, without restricting surface accessibility, while gaining reproducible control over particles' size distribution.

One of the most popular synthetic methods for the production of Au NPs is the aqueous reduction of tetrachloroauric acid (HAuCl₄) by sodium citrate, pioneered by Turkevich[33] and further refined by Frens.[34] The interest of this method relies on the resulting versatile citrate layer on the NP surface which allows an easy (multi)functionalization of the resultant particles with almost any type of molecules[35,36] (including peptides, proteins, and DNA). Many protocols have been developed for the preparation of citrate-stabilized Au NPs, leading to the production of fairly monodisperse quasi-spherical particles from about 10 to 300 nm in diameter by simply varying the reaction parameters (solution pH,[37,38] reducing agents,[39−44] solvent,[38,45] and order of reagents addition[46,47]). Later, seeded-growth based methods resulted in improved size distributions, leading to highly monodisperse samples.[30,38,48,49] However, this strategy has not yet been adapted to produce Au NPs below 10 nm, therefore limiting the availability of high quality samples in this small size regime.

Herein, we take advantage of the recent improvements on the kinetic control of seeded-growth synthesis of citrate-stabilized metal NPs[49,50] to produce Au NPs with controlled morphology and nanometric size resolution between 3.5 and 10 nm. Controlled nucleation of 3.5 nm Au NPs is achieved by the combined use of two competing reducing agents: tannic acid

and sodium citrate. The use of these two reducing agents for the synthesis of Au NPs was initially introduced in the seminal work of Mühpfordt in 1982 and further refined by Slot and Geuze in 1985 as an effective mean to produce Au NPs smaller than those obtained in the standard Turkevich method.[51−53] In this work, we develop a seeded-growth method that allows producing highly monodisperse 3.5 nm Au seeds that can be grown, with nanometric resolution, up to the desired size, and accessible surfaces. While the synthesis of the seed particles involves the combined use of both reducers, the growth process is controlled exclusively by the use of sodium citrate and the fine adjustment of synthetic parameters (temperature, pH, seed particle concentration, and SC to gold precursor ratio). Thus, the initial nucleation promoted by one of the reducers determines the final number of NPs, while the growth of those initial seeds mediated by the other reducer determines their final size. As a result, stable quasi-spherical and functionalizable highly monodisperse smaller than 10 nm Au NPs have been produced.

Furthermore, because of their narrow size distributions and versatile surface chemistry, as-synthesized Au NPs can be used as a model material to study the unique size-dependent optical properties in this small size regime. This regime, lying in the frontier between clusters and large NPs, is especially interesting as size and surface chemistry effects become increasingly important.

■ RESULTS AND DISCUSSION

Synthesis of 3.5 nm Au seeds. The addition of traces of tannic acid (TA) to the Inverse Turkevich method[49] substantially modifies the kinetics of AuNP formation, leading to the fast and systematic production of narrowly dispersed 3.5
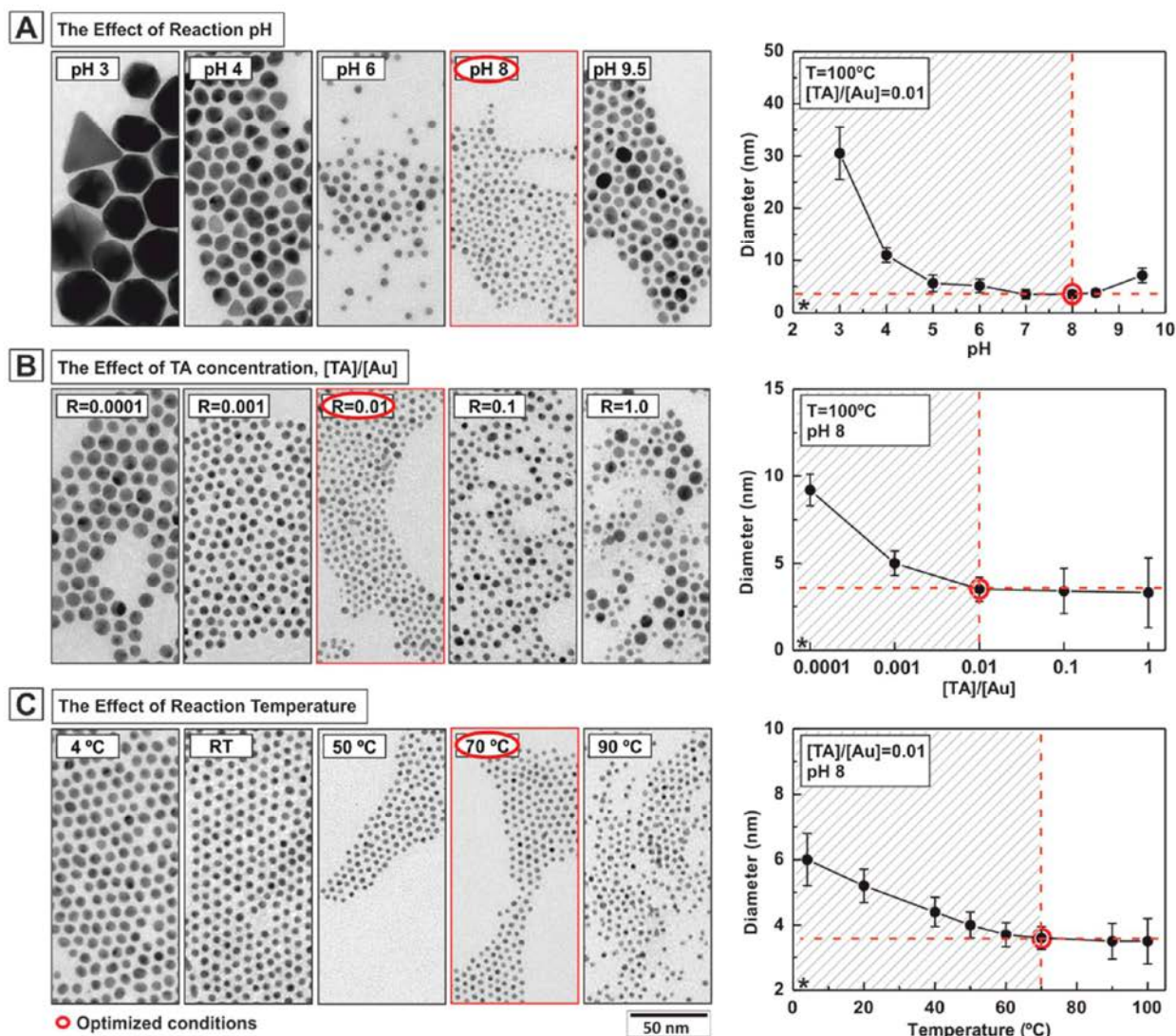
Figure 2. Different tested conditions for the synthesis of Au seeds. In all cases 1 mL of HAuCl$_4$ (25 mM) was injected to a 150 mL solution of SC (2.2 mM) while the concentration of TA was varied. Citric acid and K$_2$CO$_3$ was used to adjust the pH. Refer to section 2.2 of the Supporting Information for detailed conditions. (A) Evaluation of the effect of reaction pH. Reaction pH was systematically varied while all other synthetic parameters were kept constant. (B) Evaluation of the effect of TA. The ratio [TA]/[Au] in the reaction mixture was varied by adjusting the amount of TA added while all other synthetic parameters were kept constant. (C) Evaluation of the effect of reaction temperature. The temperature of the reaction was modified while all other synthetic parameters were kept constant. *Error bars are indicative of the size standard distribution.

nm Au NPs (Figure 1). Briefly, the Au NPs were obtained by injecting 1 mL of tetrachloroauric acid (HAuCl$_4$, 25 mM) into a mixed solution containing 150 mL of sodium citrate (SC, 2.2 mM) and 0.1 mL of tannic acid (TA, 2.5 mM) at 70 °C. Thus, the solution turned from transparent to dark gray instantaneously after gold precursor injection, and then to brownish-orange within a few minutes, indicative of the formation of very small Au NPs. The use of traces of TA, with stronger reducing power than SC, appeared to be crucial for the formation of these small particles. However, both reducing agents were needed, otherwise the resultant particles presented large and rather polydisperse sizes (Figure 1A). The absorption profile obtained when both reducers were combined (Figure 1B) reveals a damped localized surface plasmon resonance (LSPR) band peaking around 504–505 nm, which is in accordance of very small Au NPs.[54] Similarly, absorption profiles centered at

518 and 527 nm obtained when using only SC or TA, respectively, correlate well with the larger sizes seen by TEM. These results further indicate the synergic effect resulting from the combination of the two reducers. HR-TEM morphological characterization shows the faceted (twinned) nature of the synthesized particles along with its high monodispersity (Figure 1C and 1D).

Effect of Reaction Parameters on the Synthesis of Au seeds. To obtain the smallest Au NPs with the narrowest size distributions, three different synthetic parameters play a critical role: pH, TA concentration, and temperature. It is well established that reaction pH defines the reactivity of the gold precursor and the protonation state of the citrate ions, finally determining the reaction mechanism, and therefore the final Au NP morphology.[38] On the other hand, the kinetics of reduction reaction is mainly controlled by the concentration of TA and

Table 1. Summary of Au NP Size and Concentration Obtained after Different Growth Steps

precursor injections	TEM diameter (nm)	SD (%)	DLS diameter (nm)[a]	concentration (NPs/mL)[b]	expected diameter (nm)[b]
seeds	3.6 ± 0.4	11.1	4.4 ± 0.3	7.0×10^{13}	
1	4.5 ± 0.4	8.9	4.8 ± 0.3	4.4×10^{13}	4.4
2	5.1 ± 0.5	9.8	5.7 ± 0.2	4.4×10^{13}	4.9
3	6.1 ± 0.6	9.8	6.5 ± 0.2	2.8×10^{13}	5.6
4	6.6 ± 0.6	9.1	6.7 ± 0.2	2.8×10^{13}	6.2
5	7.4 ± 0.7	9.5	7.7 ± 0.4	1.8×10^{13}	6.9
6	7.9 ± 0.7	8.9	8.2 ± 0.2	1.8×10^{13}	7.9
7	8.7 ± 0.8	9.2	9.1 ± 0.1	1.2×10^{13}	8.3
8	9.5 ± 0.8	8.4	9.6 ± 0.1	1.2×10^{13}	8.9
9	10.5 ± 0.9	8.6	10.1 ± 0.4	7.1×10^{12}	9.8
10	11.3 ± 1.0	8.8	10.5 ± 0.2	7.1×10^{12}	10.5
12	13.1 ± 1.1	8.4	11.8 ± 0.3	4.5×10^{12}	12.6

[a]Number mean and SD from three independent runs. [b]See Supporting Information section 3.2 for theoretical calculations.

the temperature, which governs the degree of monomer supersaturation, ultimately regulating the number and size of nuclei.

The effect of these parameters, that is the pH, concentration of TA and temperature, was studied and are summarized in Figure 2.

Effect of the pH. As seen in Figure 2A, the final morphology of the Au NPs is strongly determined by the pH of the reaction mixture. The optimal size control was achieved at slightly basic pH (pH ~8), by correcting the reaction mixture with K_2CO_3, leading to the production of quasi-spherical Au NPs with small sizes and narrower distributions. On the contrary, the formation of anisotropic shapes and/or larger particles was observed at rather acidic or alkaline conditions, respectively. These results can be explained in terms of both the protonation of citrate ions and the strong pH-dependent reduction potential of Au(III) complexes. Thus, at acidic values the protonation of citrate (pK_1 3.1, pK_2 4.6, and pK_3 6.4) results in the poor stability of the particles while at alkaline values Au ions become less reactive due to the formation of stable hydroxide complexes.[38] As a result, the optimal pH value is found to be that which balances both the reactivity of the gold precursor to promote a fast nucleation while ensuring a good electrostatic stabilization of the particles.

Effect of the TA. Beyond the optimization of the pH, the kinetics of the reaction was highly dependent on the TA concentration (Figure 2B). As a general trend, an initial increase of the concentration of TA increased the reaction kinetics, which was translated into smaller sizes, down to 3.5 nm. However, a further excess of TA (see Supporting Information section 1 for stoichiometry) resulted in polydisperse samples. The reason is still not fully understood but the presence of very small clusters (sub-3-nm) together with a high number of larger particles in these samples indicate some lack of stability of the resultant NPs, presumably due to the saturation of the nucleation process and the consequent rapid nucleation and aggregative growth, together with coalescence, of these small nuclei. Thus, the limiting factor for achieving the smallest Au NPs size is not determined by the reducing power of the TA but by the ability to stabilize the NPs.

Effect of the Temperature. Similarly, formation kinetics of the Au NPs was also dependent on the reaction temperature (Figure 2C). At low temperatures (below 70 °C) the growth process is favored, which was translated into larger Au NPs but preserving highly monodisperse sizes. Oppositely, the sample started to become smaller and more polydisperse when the

temperature was increased (above 70 °C) and the size decreased below 3.5 nm, in a similar trend to that observed in the case of the TA concentration.

Unfortunately, any attempt to decrease the size of the Au NPs below 3.5 nm by further modifying these synthetic parameters resulted in polydisperse samples. Although some hypothesis has been introduced here, this is a subject of ongoing research.

From these results, it can be concluded that the optimal conditions for the production of high quality colloidal solutions of quasi-spherical Au NPs with the smallest possible size involves: (i) the adjustment of the reaction pH at slightly basic values (pH ~ 8) (ii) the use of substoichiometric concentration of TA instead of an excess of that one and (iii) moderately high temperatures (~70 °C). Working at these conditions long-term stable Au colloids of ~3.5 nm and standard deviation less than 10% were routinely produced. Interestingly, under these conditions the synthetic method was easily scaled up to 1 L (Figure S1).

Generally, the observed trend fits well with a mechanism of NPs formation divided in two steps: a nucleation promoted by a strong reducer, TA, and particle growth promoted by a weak reducer, SC. When TA is used under substoichiometric conditions, the rate of nucleation and the final size of NPs are determined by the conversion rates of both processes. Thus, TA leads to the production of initial nuclei that are subsequently grown by the further reduction of the remaining gold precursor by the SC present in the medium. This strategy of competing reducers has been previously exploited in the control of Au NP size[53] and the morphology of Pt NPs in organic solvents.[56,57] When increasing the TA concentration, more gold is reduced during the nucleation and less by SC in the postnucleation process, which leads to a decrease in the Au NPs size while preserving a narrow distribution. Considering that the Au conversion from precursor to NP yield is the same in all cases since an excess of SC is always used (about >90%), the number and size of NPs is then coupled (from many small NPs to fewer larger ones). Interestingly, a similar behavior is observed when modifying the temperature of the reaction.

Seeded-Growth Synthesis of Au NPs from 3.5 to 10 nm. Given the limitations in controlling Au NPs size by modifying the concentration of TA, temperature or pH we studied the possibility of growing successive generations of spherical Au NPs using the smallest ~3.5 nm above synthesized Au NPs as seeds. Taking advantage of the recent improvements on controlled growth of Au[49] and Ag[50] NPs from 10 nm up to
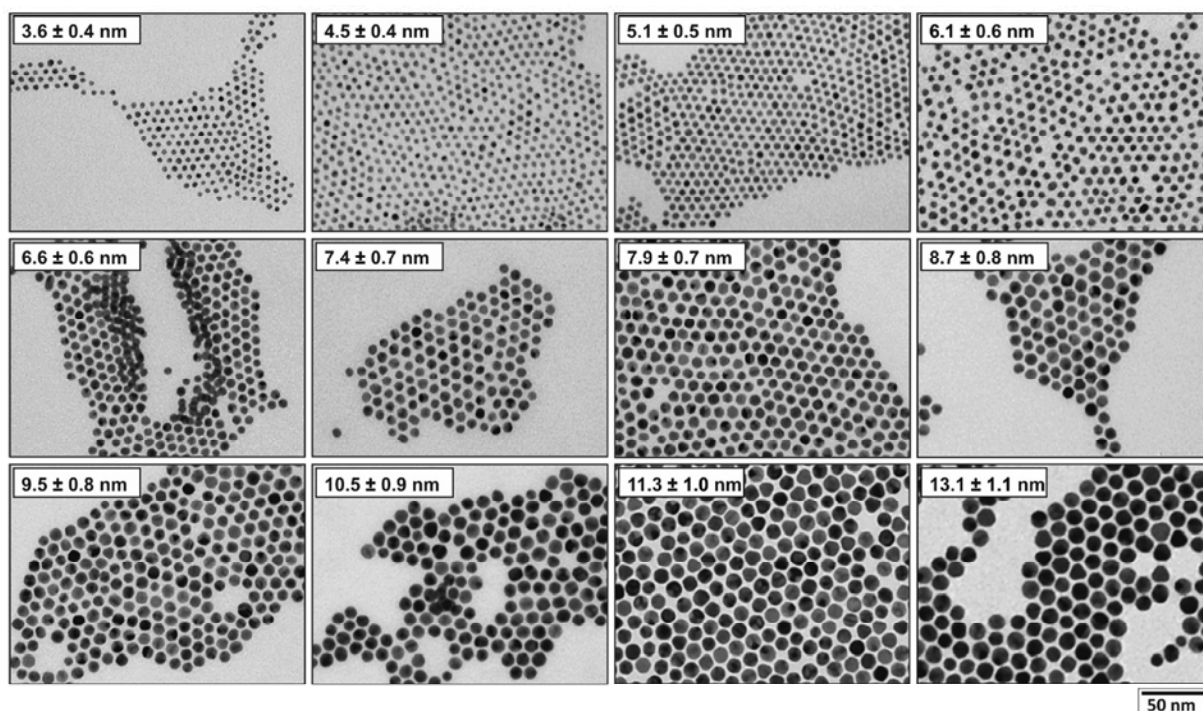
Figure 3. Transmission electron microscopy images of seed particles (3.6 nm) and those obtained after different growth steps. The particle size increases from 3.6 ± 0.4 nm seeds to 13.1 ± 1.1 nm, while its concentration decreases from $\sim 7.0 \times 10^{13}$ to $\sim 4.5 \times 10^{12}$ NPs/mL.

200 nm, we set the conditions by which the kinetic control of the seeded-growth synthesis is achieved, that is, (i) slowing down the reactivity of gold precursor to avoid new nucleation, while (ii) maintaining its concentration high enough to achieve an homogeneous growth (size focusing). These conditions include the control of the reaction temperature, pH and precursor to seed particles ratio.

Thus, to obtain successive generations of highly monodisperse Au NPs up to 10 nm, Au seeds (3.5, 7×10^{13} NPs/mL) were first prepared as previously described. When the reaction was finished the solution was diluted by extracting a sample volume and replacing it with the same volume of 2.2 mM of SC solution (see Scheme S2) to reduce the number of growing seeds, while ensure enough SC for subsequent gold reduction and pH buffering. During the growth process, the temperature was set at 70 °C and no TA was added. At this temperature growth is promoted over nucleation by the weak reducing power of SC. Finally, subsequent aliquots of gold precursor were injected. By repeating this process (dilution plus gold precursor injection) the size of the particles was precisely controlled with an increase of approximately 0.5−1 nm after each injection.

Morphological characterization by TEM of the resultant generations of Au NPs obtained after different growth steps are summarized in Table 1 and shown in Figure 3. Au NPs, progressively larger in size, exhibit high uniformity and very low size dispersity. Size distribution studies performed by the systematic analysis of at least 500 particles for each sample further corroborate the results (Figure S2). Similar size distribution profiles were measured by dynamic light scattering (DLS), obtaining monomodal curves with increasing mean particles diameter (Figure 4A). Besides, particles size can be also estimated considering the diameter of the seeds, its number in solution (concentration) and the amount of gold
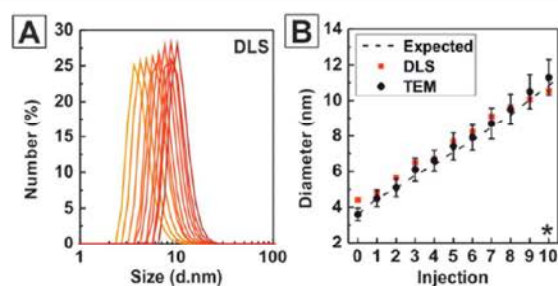
Figure 4. (A) Size distribution profiles measured by dynamic light scattering of Au NPs obtained after different growth steps. Size distribution by number fits well with the size measured by TEM and shows monomodal curves with increasing mean particle diameters as the number of growth steps increase. Size distribution by intensity and volume are shown in Figure S3. (B) Experimental average diameter of Au NPs (TEM and DLS) obtained after several growth steps and comparison with the theoretical calculated values. Obtained results fit with those calculated, which indicates that no nucleation occurred and the Au atoms deposited onto the surfaces of the preformed particles. *Errors bar indicates the size standard distribution.

precursor added (refer to Supporting Information section 3.2). Experimental results (TEM, DLS) fits well with those theoretically calculated (Figure 4B), obtaining a perfect correlation and further confirming both the high reaction yield and the absence of new nucleation.[49] Finally, an extension of the growth process up to 20 nm is shown in section 3.4 of the Supporting Information.

Optical Properties of Au NPs. The unique optical properties of Au NPs are well-known and enabling for many applications. Unfortunately, it is not always easy to produce Au NPs in a wide size range using the same procedure, in particular for the small ones. Taking advantage of the size resolution

herein achieved, we measured the absorbance spectra of the different particles by UV−vis spectroscopy (Figure 5), where it

Figure 5. Optical properties of selected Au colloids obtained after different growth steps (A) normalized at 400 nm and (B) normalized at the LSPR peak maximum. Arrows indicate evolution of the LSPR peak as increasing the size of the Au NPs. In the inset graph, the position of the LSPR peak as a function of particle size is plotted, and extended up to particles of 20 nm for better understanding the tendency, wher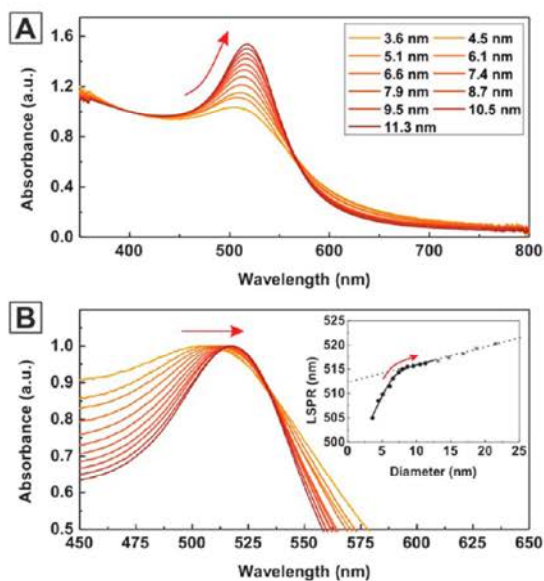e it can be distinguish: (i) the position of the peak always red shift as increasing the size of the particles and (ii) two size-regimes intersecting at 8 nm having different behavior.

can be clearly seen how the localized surface plasmon resonance (LSPR) band narrows and the peak position red-shifts from 505 to 517 nm as increasing particle size from 3.6 to 11.3 nm. Neither broadening of the band nor the appearance of new peaks at longer wavelengths was observed, indicating the absence of any aggregation. Two regions with different behavior are identified. Beyond the damping of the absorption band, for very small Au NPs (<8 nm), slight variations in the size (from 3.6 to 8 nm) are translated into larger shifts in the LSPR peak position (from 505 to 515 nm, respectively). For larger sizes (>8 nm), this size-dependence is smoother, leading to the smaller standard red-shifts observed in Au NPs (from 515 to 517 nm) for similar size variations (from 8 to 13 nm). Oppositely to that recently observed for sub-10-nm Ag NPs,[58] we did not detect a reverse tendency in the size-dependence of the LSPR, that is, for Au NPs, the peak gradually red-shifts as the mean particle size increases.

The higher susceptibility (measured in terms of LSPR shift) observed in this small size regime can be attributed to surface phenomena, that become pronounced in very small particles with a high percentage of surface atoms, and that ultimately account for intrinsic size effect corrections in the standard Mie theory.[7,59] In particular, size-dependent modifications of the dielectric constant with respect to the bulk values because of surface damping.[60] Thus, while red-shifts in large Au NPs are explained in terms of retardations effects (as well as to increasing contributions from multipolar terms), for smaller Au NPs these extrinsic size-effects become negligible and intrinsic size effects prevails, resulting in a the damping of the LSPR

band with decreasing sizes and into additional shifts of the plasmon peak as herein observed. Obtained results are complementary to those experimentally suggested,[21,54,59] but the improved resolution herein accomplished leads to the identification of non-negligible alterations in the LSPR, clarifying the size dependent LSPR peak position for small Au NPs. Although the optical modeling of these systems is out of the scope of this paper, these results could be useful as a reference tool for testing theoretical models in the small size regime, basically based on quantum mechanics calculations, and traditionally difficult to model for being in the limit of Mie theory approximations.

Functionalization of Au NPs. Beyond the possibility to precisely control the size of Au NPs in the sub-10 nm regime, another advantage of this synthetic strategy is that it produces Au NPs with readily accessible and reactive surfaces. The weak interaction between Au surface and the carboxylic terminated groups of the citrate allows easy postsynthetic treatments, and the further functionalization of these Au NPs with a wide variety of (bio)molecules of interest. To proof this point, we carried out conjugation experiments with 11-mercaptoundeca-noic acid (MUA), a model thiol-terminated molecule widely used to build self-assembled monolayers (SAMs) onto Au NPs. Conjugation was performed by adding excess of MUA molecules to Au NPs solutions under vigorous stirring. Molecule adsorption is a spontaneous process because the thiol groups form much stronger bonds with Au surfaces than the carboxylic groups in the original citrate molecules do.[61] Characterization of the Au NPs before and after MUA addition shows that neither aggregation nor observable structural or morphological change took place, confirming that the observed shift in the LSPR peak position is due to modifications on Au NP surface chemistry. This shift could not be observed if the surface of the particles would be passivated by a strongly binding surfactant. Similarly to that previously observed,[54,62] the presence of traces of TA used during the seed nucleation seems not to have a noticeable hindrance on surface accessibility.

Absorption spectra of the Au NPs before and after the conjugation process are summarized in Table 2 and shown in Figure 6 (extended up to 20 nm, see Supporting Information section 4.1), where it can be clearly seen how the corresponding LSPR peak position shifts to the red.

Table 2. Summary of the LSPR Peak Position of Au NPs before and after Conjugation with 11-Mercaptoundecanoic Acid (MUA)

size (TEM)	LSPR (nm)	LSPR after conjugation (nm)[a]	λ_{LSPR}
3.6 ± 0.4	505.5	517.4	11.9
4.5 ± 0.4	508.0	518.5	10.5
5.1 ± 0.5	509.8	519.1	9.3
6.1 ± 0.6	511.8	520.5	8.7
6.6 ± 0.6	513.1	521.1	8.0
7.4 ± 0.7	514.5	522.0	7.5
7.9 ± 0.7	515.3	522.0	6.7
8.7 ± 0.8	516.3	522.8	6.5
9.5 ± 0.8	516.6	522.6	6.0
10.5 ± 0.9	517.2	523.0	5.8
11.3 ± 1.0	517.5	522.7	5.2
13.1 ± 1.1	518.0	522.9	4.9

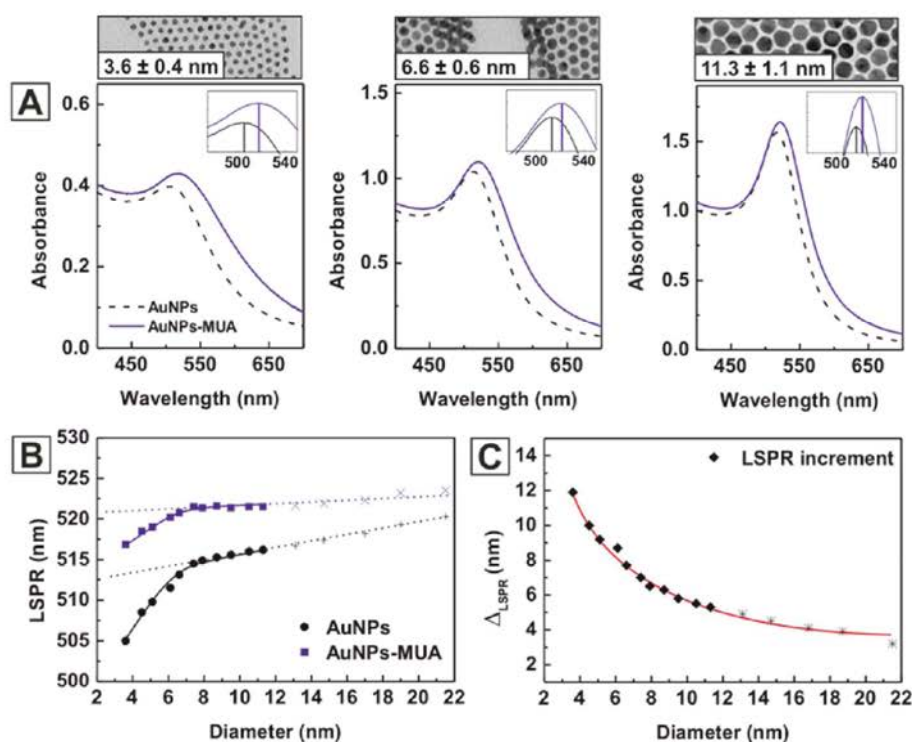[a]Au NPs were conjugated with 11-mercaptoundecanoic acid (MUA).

Figure 6. Conjugation of as-synthesized Au NPs with 11-mercaptoundecanoic acid (MUA).The size has been extended up to 20 nm for better understanding the tendency. (A) UV−vis spectra for different particle size: 3.6 ± 0.4, 6.6 ± 0.58, and 11.3 ± 1.0 nm, recorded before (black dotted line) and after (red line) the addition of MUA. Lines indicate the position of the LSPR peak. (B) Size-dependence evolution of the LSPR peak position as a function of Au NP size before and after conjugation and (C) Δ_{LSPR} shift.

Interestingly, the extent of the red-shift depends on Au NP size, being larger for smaller Au NPs (Figure 6A−C). These results coincide with that observed recently for Ag NPs[58] of similar small sizes and arise from the higher fraction of surface atoms in smaller NPs which it is translated into the fact that similar chemically induced reduction of conduction band electrons (thiols confine more conduction band electrons than native carboxylic acids) produces a sharper effect. Therefore, in addition to the surface to volume ratio effect we clearly see, as in the previous section, higher susceptibility for the smaller particles.

The synthetic strategy herein presented allows to extend the previously citrate-mediated seeded-growth method for the production of Au NPs in the range of 10−200 nm[49] toward smaller 3.5−10 nm sizes, covering the whole nanometric range. As a result we can observe, for the first time, how the susceptibility of the LSPR toward surface modifications (via ligand exchange processes) decreases as the size of the NPs increases reaching a minimum around 50 nm before rising again as the NPs become larger, suggesting that around 50 nm, surface and bulk plasmonic effects intersects (Figure 7).

■ CONCLUSIONS

In the present work, we have shown the possibility to synthesize citrate stabilized Au NPs from 3.5 to 10 nm by a step by step seeded-growth synthetic protocol based on the reduction of a hydrogen tetrachloroaurate with sodium citrate. The use of traces of tannic acid at the first step, nucleation, allows the formation of ∼3.5 nm Au seeds with narrow size distributions which can be then grown with nanometric resolution. As-synthesized Au NPs possess high uniformity in
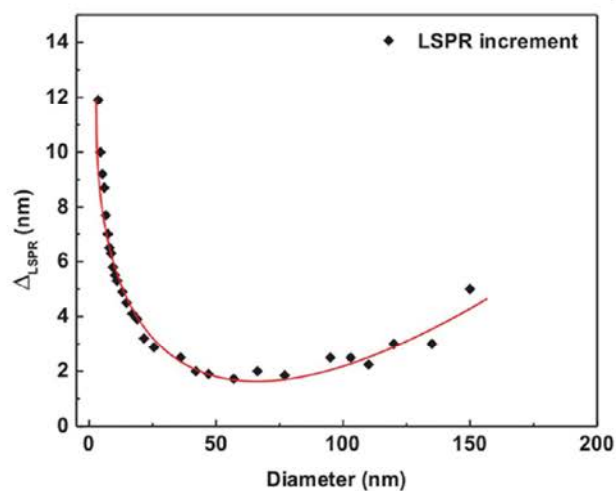
Figure 7. Δ_{LSPR} shift of different Au NPs after conjugation with MUA. The whole size range from 3.5 to 200 nm is covered. Au NPs were synthesized combining the citrate-mediated seeded-growth protocol presented here for the small sizes and the previously published protocol for larger NPs.[49]

size, circularity and readily accessible surface. Of special interest are the optical properties since theoretical predictions usually fail for Au NPs smaller than 20 nm (limit of Mie theory). In this case, additionally to the localized surface plasmon resonance (LSPR) damping, we observed a size dependence on the LSPR peak position in the range between 3.5 to 10 nm but interestingly more pronounced when the particles were

Article

smaller than 8 nm. Moreover, conjugation experiments with 11-mercaptoundecanoic acid, a model thiol-terminated molecule widely used for Au NP self-assembled monolayer functionalization, further showed that these small particles are also more sensitive to surface modifications.

■ MATERIALS AND METHODS

Materials. Tetrachloroauric (III) acid ($\geq$99% trace metal basis), trisodium citrate dihydrate ($\geq$99%), citric acid monohydrate ($\geq$99%), potassium carbonate ($\geq$99%) and tannic acid (MW 1701, ACS reagent) were purchased from Sigma-Aldrich. 11-Mercaptoundecanoic acid (95%) was from Aldrich. Ultrapure water (18.2 MΩ) was used for all procedures.

Synthesis of 3.5 nm Au seeds. A 150 mL of freshly prepared reducing solution of sodium citrate (SC, 2.2 mM) containing 0.1 mL of tannic acid (TA, 2.5 mM) and 1 mL of potassium carbonate (K_2CO_3, 150 mM) was heated with a heating mantle in a 250 mL three-necked round-bottom flask under vigorous stirring. When the temperature reached 70 °C, 1 mL of tetrachloroauric acid ($HAuCl_3$, 25 mM) was injected. The color of the solution changed rapidly to black-gray (less than 10 s) and then to orange-red in the following 1−2 min. The solution was kept at 70 °C for 5 min more to ensure complete reaction of the gold precursor. The resultant particles ($\sim$3.5 nm, 7 × 10^{13} NPs/mL) were narrowly dispersed, negatively charged and stable for weeks. The addition of 1 mM of K_2CO_3 in the reducing solution resulted in a pH $\sim$10, which decreased in the reaction mixture to pH $\sim$8 because of the addition of $HAuCl_4$. This slightly basic value seems to have an advantageous effect resulting in narrower size distributions of the Au NPs. Other tested conditions from the modification of one of the reaction conditions are described in the Supporting Information.

Seeded-Growth of Au NPs. Au NPs used as seeds (7 × 10^{13} NPs/mL) were synthesized following above-described protocol. Immediately after the synthesis and in the reaction same vessel, the sample was diluted by extracting 55 mL and adding 55 mL of SC (2.2 mM). When the temperature reached again 70 °C, two injections of 0.5 mL of $HAuCl_4$ (25 mM) on a time interval of 10 min were done. This growing step comprising sample dilution plus 2 injections of $HAuCl_4$ was repeated until the particles reached the desired size (see Scheme S2).

Conjugation with 11-Mercaptoundecanoic Acid (MUA). To 1 mL of as-synthesized Au NPs, excess of a basic solution of MUA (0.1 mL, 1 mM) was added and stirred gently overnight. Unbounded ligand was removed by further purification of the Au NPs using a regenerated cellulose centrifugal filter (MWCO 10000, Amicon) for particles smaller than 8 nm or by centrifugation (15 000 g, 15 min) for particles bigger than 8 nm.

Characterization. *Transmission Electron Microscopy (TEM).* Au NPs previously conjugated with MUA were visualized using TEM (Jeol 1010) and HRTEM (Tecnai F20 S/TEM). Ten microliters of the solutions were drop-casted onto a carbon-coated grid and left to dry for at least 24h. Average size and size distribution of the samples were measured using ImageJ software by counting at least 500 particles. Conjugation/passivation of the Au NP surface with MUA previous to preparation of the grid was a prerequisite to get good TEM images, otherwise close particles had the tendency to coalesce once deposited onto the film and under the beam irradiation.

UV−vis spectroscopy. UV−visible spectra were acquired with a Shimadzu UV-2100 using 1.5 mL plastic cuvettes in the range from 300 to 800 nm.

Dynamic Light Scattering. Malvern ZetaSizer Nano ZS (Malvern instruments, UK) operating at a light source wavelength of 532 nm and fixed scattering angle of 173° was used to measure Au NPs hydrodynamic size. Measurements were conducted in 1 cm path cell and 25 °C and the samples were previously filtered with 0.2 μm regenerated cellulose filter.

■ ASSOCIATED CONTENT

ⓢ Supporting Information

The Supporting Information is available free of charge on the ACS Publications website at DOI: 10.1021/acs.chemmater.5b04406.

Details of experimental protocols and conditions studied together with extended Au NPs characterization (PDF)

■ AUTHOR INFORMATION

Corresponding Author

*E-mail: victor.puntes@icn.cat.

Notes

The authors declare no competing financial interest.

■ ACKNOWLEDGMENTS

■ REFERENCES

(1) Hvolbaek, B.; Janssens, T. V. W.; Clausen, B. S.; Falsig, H.; Christensen, C. H.; Norskov, J. K. Catalytic activity of Au nanoparticles. *Nano Today* **2007**, *2*, 14−18.

(2) Homberger, M.; Simon, U. On the application potential of gold nanoparticles in nanoelectronics and biomedicine. *Philos. Trans. R. Soc., A* **2010**, *368*, 1405−1453.

(3) Sperling, R. A.; Rivera Gil, P.; Zhang, F.; Zanella, M.; Parak, W. J. Biological applications of gold nanoparticles. *Chem. Soc. Rev.* **2008**, *37*, 1896−1908.

(4) Tomalia, D. A. In quest of a systematic framework for unifying and defining nanoscience. *J. Nanopart. Res.* **2009**, *11*, 1251−1310.

(5) Buffat, P.; Borel, J. P. Size effect on the melting temperature of gold particles. *Phys. Rev. A: At., Mol., Opt. Phys.* **1976**, *13*, 2287−2298.

(6) Wang, D.; Nap, R. J.; Lagzi, I.; Kowalczyk, B.; Han, S.; Grzybowski, B. A.; Szleifer, I. How and Why Nanoparticle's Curvature Regulates the Apparent pK(a) of the Coating Ligands. *J. Am. Chem. Soc.* **2011**, *133*, 2192−2197.

(7) Berciaud, S. p.; Cognet, L.; Tamarat, P.; Lounis, B. Observation of Intrinsic Size Effects in the Optical Response of Individual Gold Nanoparticles. *Nano Lett.* **2005**, *5*, 515−518.

(8) Mei, B. C.; Oh, E.; Susumu, K.; Farrell, D.; Mountziaris, T. J.; Mattoussi, H. Effects of Ligand Coordination Number and Surface Curvature on the Stability of Gold Nanoparticles in Aqueous Solutions. *Langmuir* **2009**, *25*, 10604−10611.

(9) Comenge, J.; Sotelo, C.; Romero, F.; Gallego, O.; Barnadas, A.; Garcia-Caballero Parada, T.; Dominguez, F.; Puntes, V. F. Detoxifying Antitumoral Drugs via Nanoconjugation: The Case of Gold Nanoparticles and Cisplatin. *PLoS One* **2012**, *7*, e47562.

(10) Choi, H. S.; Liu, W.; Misra, P.; Tanaka, E.; Zimmer, J. P.; Ipe, B. I.; Bawendi, M. G.; Frangioni, J. V. Renal clearance of quantum dots. *Nat. Biotechnol.* **2007**, *25*, 1165−1170.

(11) Vasir, J. K.; Reddy, M. K.; Labhasetwar, V. D. Nanosystems in drug targeting: opportunities and challenges. *Curr. Nanosci.* **2005**, *1*, 47−64.

(12) Barua, S.; Mitragotri, S. Challenges associated with penetration of nanoparticles across cell and tissue barriers: A review of current status and future prospects. *Nano Today* **2014**, *9*, 223−243.

(13) Brust, M.; Walker, M.; Bethell, D.; Schiffrin, D. J.; Whyman, R. Synthesis of Thiol-Derivatized Gold Nanoparticles in a 2-Phase Liquid-Liquid System. *J. Chem. Soc., Chem. Commun.* **1994**, 801−802.

(14) Weare, W. W.; Reed, S. M.; Warner, M. G.; Hutchison, J. E. Improved Synthesis of Small (dCORE ≈ 1.5 nm) Phosphine-Stabilized Gold Nanoparticles. *J. Am. Chem. Soc.* **2000**, *122*, 12890−12891.

(15) Schmid, G. The relevance of shape and size of Au$_{55}$ clusters. *Chem. Soc. Rev.* **2008**, *37*, 1909−1930.

(16) Leff, D. V.; Brandt, L.; Heath, J. R. Synthesis and Characterization of Hydrophobic, Organically-Soluble Gold Nanocrystals Functionalized with Primary Amines. *Langmuir* **1996**, *12*, 4723−4730.

(17) Song, J.; Kim, D.; Lee, D. Size Control in the Synthesis of 1−6 nm Gold Nanoparticles via Solvent-Controlled Nucleation. *Langmuir* **2011**, *27*, 13854−13860.

(18) Brust, M.; Fink, J.; Bethell, D.; Schiffrin, D. J.; Kiely, C. Synthesis and reactions of functionalised gold nanoparticles. *J. Chem. Soc., Chem. Commun.* **1995**, 1655−1656.

(19) Wuelfing, W. P.; Gross, S. M.; Miles, D. T.; Murray, R. W. Nanometer Gold Clusters Protected by Surface-Bound Monolayers of Thiolated Poly(ethylene glycol) Polymer Electrolyte. *J. Am. Chem. Soc.* **1998**, *120*, 12696−12697.

(20) Kanaras, A. G.; Kamounah, F. S.; Schaumburg, K.; Kiely, C. J.; Brust, M. Thioalkylated tetraethylene glycol: a new ligand for water soluble monolayer protected gold clusters. *Chem. Commun.* **2002**, 2294−2295.

(21) Oh, E.; Susumu, K.; Goswami, R.; Mattoussi, H. One-Phase Synthesis of Water-Soluble Gold Nanoparticles with Control over Size and Surface Functionalities. *Langmuir* **2010**, *26*, 7604−7613.

(22) Hussain, I.; Graham, S.; Wang, Z.; Tan, B.; Sherrington, D. C.; Rannard, S. P.; Cooper, A. I.; Brust, M. Size-Controlled Synthesis of Near-Monodisperse Gold Nanoparticles in the 1−4 nm Range Using Polymeric Stabilizers. *J. Am. Chem. Soc.* **2005**, *127*, 16398−16399.

(23) Male, K. B.; Li, J.; Bun, C. C.; Ng, S.-C.; Luong, J. H. T. Synthesis and Stability of Fluorescent Gold Nanoparticles by Sodium Borohydride in the Presence of Mono-6-deoxy-6-pyridinium-β-cyclodextrin Chloride. *J. Phys. Chem. C* **2007**, *112*, 443−451.

(24) Liu, Y.; Male, K. B.; Bouvrette, P.; Luong, J. H. T. Control of the Size and Distribution of Gold Nanoparticles by Unmodified Cyclodextrins. *Chem. Mater.* **2003**, *15*, 4172−4180.

(25) Schaaff, T. G.; Whetten, R. L. Giant Gold−Glutathione Cluster Compounds: Intense Optical Activity in Metal-Based Transitions. *J. Phys. Chem. B* **2000**, *104*, 2630−2641.

(26) Yonezawa, T.; Yasui, K.; Kimizuka, N. Controlled Formation of Smaller Gold Nanoparticles by the Use of Four-Chained Disulfide Stabilizer. *Langmuir* **2000**, *17*, 271−273.

(27) Reiss, H. The Growth of Uniform Colloidal Dispersions. *J. Chem. Phys.* **1951**, *19*, 482−487.

(28) LaMer, V. K.; Dinegar, R. H. Theory, Production and Mechanism of Formation of Monodispersed Hydrosols. *J. Am. Chem. Soc.* **1950**, *72*, 4847−4854.

(29) Xia, Y.; Xiong, Y.; Lim, B.; Skrabalak, S. E. Shape-Controlled Synthesis of Metal Nanocrystals: Simple Chemistry Meets Complex Physics? *Angew. Chem., Int. Ed.* **2009**, *48*, 60−103.

(30) Jana, N. R.; Gearheart, L.; Murphy, C. J. Seeding Growth for Size Control of 5−40 nm Diameter Gold Nanoparticles. *Langmuir* **2001**, *17*, 6782−6786.

(31) Zheng, Y. Q.; Zhong, X. L.; Li, Z. Y.; Xia, Y. N. Successive, Seed-Mediated Growth for the Synthesis of Single-Crystal Gold Nanospheres with Uniform Diameters Controlled in the Range of 5−150 nm. *Part. Part. Syst. Charact.* **2014**, *31*, 266−273.

(32) Alkilany, A. M.; Murphy, C. J. Toxicity and cellular uptake of gold nanoparticles: what we have learned so far? *J. Nanopart. Res.* **2010**, *12*, 2313−2333.

(33) Turkevich, J.; Stevenson, P. C.; Hillier, J. A Study of the Nucleation and Growth Processes in the Synthesis of Colloidal Gold. *Discuss. Faraday Soc.* **1951**, *11*, 55.

(34) Frens, G. Controlled Nucleation For Regulation Of Particle-Size In Monodisperse Gold Suspensions. *Nature, Phys. Sci.* **1973**, *241*, 20−22.

(35) Bastús, N. G.; Sanchez-Tillo, E.; Pujals, S.; Farrera, C.; Lopez, C.; Giralt, E.; Celada, A.; Lloberas, J.; Puntes, V. Homogeneous Conjugation of Peptides onto Gold Nanoparticles Enhances Macrophage Response. *ACS Nano* **2009**, *3*, 1335−1344.

(36) Kogan, M. J.; Bastús, N. G.; Amigo, R.; Grillo-Bosch, D.; Araya, E.; Turiel, A.; Labarta, A.; Giralt, E.; Puntes, V. F. Nanoparticle-mediated Local and Remote Manipulation of Protein Aggregation. *Nano Lett.* **2006**, *6*, 110−115.

(37) Ji, X.; Song, X.; Li, J.; Bai, Y.; Yang, W.; Peng, X. Size control of gold nanocrystals in citrate reduction: The third role of citrate. *J. Am. Chem. Soc.* **2007**, *129*, 13939−13948.

(38) Schulz, F.; Homolka, T.; Bastús, N. G.; Puntes, V.; Weller, H.; Vossmeyer, T. Little Adjustments Significantly Improve the Turkevich Synthesis of Gold Nanoparticles. *Langmuir* **2014**, *30*, 10779.

(39) Brown, K. R.; Walter, D. G.; Natan, M. J. Seeding of Colloidal Au Nanoparticle Solutions. 2. Improved Control of Particle Size and Shape. *Chem. Mater.* **1999**, *12*, 306−313.

(40) Brown, K. R.; Lyon, L. A.; Fox, A. P.; Reiss, B. D.; Natan, M. J. Hydroxylamine Seeding of Colloidal Au Nanoparticles. 3. Controlled Formation of Conductive Au Films. *Chem. Mater.* **1999**, *12*, 314−323.

(41) Brown, K. R.; Natan, M. J. Hydroxylamine Seeding of Colloidal Au Nanoparticles in Solution and on Surfaces. *Langmuir* **1998**, *14*, 726−728.

(42) Perrault, S. D.; Chan, W. C. W. Synthesis and Surface Modification of Highly Monodispersed, Spherical Gold Nanoparticles of 50−200 nm. *J. Am. Chem. Soc.* **2009**, *131*, 17042−17043.

(43) Ziegler, C.; Eychmüller, A. Seeded Growth Synthesis of Uniform Gold Nanoparticles with Diameters of 15−300 nm. *J. Phys. Chem. C* **2011**, *115*, 4502−4506.

(44) Niu, J.; Zhu, T.; Liu, Z. One-step seed-mediated growth of 30−150 nm quasispherical gold nanoparticles with 2-mercaptosuccinic acid as a new reducing agent. *Nanotechnology* **2007**, *18*, 325607.

(45) Ojea-Jimenez, I.; Romero, F. M.; Bastus, N. G.; Puntes, V. Small Gold Nanoparticles Synthesized with Sodium Citrate and Heavy Water: Insights into the Reaction Mechanism. *J. Phys. Chem. C* **2010**, *114*, 1800−1804.

(46) Ojea-Jimenez, I.; Bastus, N. G.; Puntes, V. Influence of the Sequence of the Reagents Addition in the Citrate-Mediated Synthesis of Gold Nanoparticles. *J. Phys. Chem. C* **2011**, *115*, 15752−15757.

(47) Sivaraman, S. K.; Kumar, S.; Santhanam, V. Monodisperse sub-10 nm gold nanoparticles by reversing the order of addition in Turkevich method - The role of chloroauric acid. *J. Colloid Interface Sci.* **2011**, *361*, 543−547.

(48) Rodríguez-Fernández, J.; Pérez-Juste, J.; García de Abajo, F. J.; Liz-Marzán, L. M. Seeded Growth of Submicron Au Colloids with Quadrupole Plasmon Resonance Modes. *Langmuir* **2006**, *22*, 7007−7010.

(49) Bastús, N. G.; Comenge, J.; Puntes, V. F. Kinetically Controlled Seeded Growth Synthesis of Citrate-Stabilized Gold Nanoparticles of up to 200 nm: Size Focusing versus Ostwald Ripening. *Langmuir* **2011**, *27*, 11098−11105.

(50) Bastús, N. G.; Merkoçi, F.; Piella, J.; Puntes, V. Synthesis of Highly Monodisperse Citrate-Stabilized Silver Nanoparticles of up to 200 nm: Kinetic Control and Catalytic Properties. *Chem. Mater.* **2014**, *26*, 2836−2846.

(51) Ahmad, T. Reviewing the Tannic Acid Mediated Synthesis of Metal Nanoparticles. *J. Nanotechnol.* **2014**, *2014*, 11.

(52) Mühlpfordt, H. The preparation of colloidal gold particles using tannic acid as an additional reducing agent. *Experientia* **1982**, *38*, 1127−1128.

(53) Slot, J. W.; Geuze, H. J. A new method of preparing gold probes for multiple-labeling cyto-chemistry. *Eur. J. Cell Biol.* **1985**, *38*, 87−93.

(54) Haiss, W.; Thanh, N. T. K.; Aveyard, J.; Fernig, D. G. Determination of Size and Concentration of Gold Nanoparticles from UV−Vis Spectra. *Anal. Chem.* **2007**, *79*, 4215−4221.

(55) Hendel, T.; Wuithschick, M.; Kettemann, F.; Birnbaum, A.; Rademann, K.; Polte, J. In Situ Determination of Colloidal Gold Concentrations with UV-Vis Spectroscopy: Limitations and Perspectives. *Anal. Chem.* **2014**, *86*, 11115−11124.

(56) Lim, S. I.; Ojea-Jiménez, I.; Varon, M.; Casals, E.; Arbiol, J.; Puntes, V. Synthesis of Platinum Cubes, Polypods, Cuboctahedrons, and Raspberries Assisted by Cobalt Nanocrystals. *Nano Lett.* **2010**, *10*, 964−973.

(57) Lim, S. I.; Varon, M.; Ojea-Jimenez, I.; Arbiol, J.; Puntes, V. Exploring the Limitations of the Use of Competing Reducers to Control the Morphology and Composition of Pt and PtCo Nanocrystals. *Chem. Mater.* **2010**, *22*, 4495−4504.

(58) Peng, S.; McMahon, J. M.; Schatz, G. C.; Gray, S. K.; Sun, Y. Reversing the size-dependence of surface plasmon resonances. *Proc. Natl. Acad. Sci. U. S. A.* **2010**, *107*, 14530−14534.

(59) Link, S.; El-Sayed, M. A. Size and Temperature Dependence of the Plasmon Absorption of Colloidal Gold Nanoparticles. *J. Phys. Chem. B* **1999**, *103*, 4212−4217.

(60) Kreibig, U.; Vollmer, M. *Springer Ser. Mater. Sci.* **1995**, DOI: 10.1007/978-3-662-09109-8.

(61) Schulz, F.; Vossmeyer, T.; Bastus, N. G.; Weller, H. Effect of the Spacer Structure on the Stability of Gold Nanoparticles Functionalized with Monodentate Thiolated Poly(ethylene glycol) Ligands. *Langmuir* **2013**, *29*, 9897−9908.

(62) Bastús, N. G.; Piella, J.; Puntes, V. Quantifying the Sensitivity of Multipolar (Dipolar, Quadrupolar, and Octapolar) Surface Plasmon Resonances in Silver Nanoparticles: The Effect of Size, Composition, and Surface Coating. *Langmuir* **2016**, *32*, 290.

Supporting information for:

Size-controlled Synthesis of sub-10 nm Citrate-stabilized Gold Nanoparticles and Related Optical Properties.

Jordi Piella, Neus G. Bastús and Victor Puntes

Table of Contents

1

1. Stoichiometry of the reaction

Tannic acid (TA) structure consists on a central glucose molecule surrounded by 10 polyphenolic groups (see Scheme S1). If each polyphenolic group takes part in the redox reaction of gold and donates 2 electrons to form quinones, then each TA is capable of donating up to 20 electrons. Because an atom of gold needs 3 electrons to be reduced, the stoichiometry of the reaction can be described by Equation (1):

$$3\,[Au] = 20\,[TA] \qquad \text{Equation (1)}$$
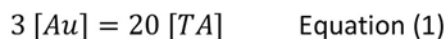
where *[Au]* and *[TA]* are the concentration of gold and TA respectively. In all the tested conditions presented in the main manuscript, 25 mmol of HAuCL$_4$ (1 mL, 25 mM) was added to the reaction mixture, which implies that at least 3.75 mmol of TA is needed to match the stoichiometric requirements. However, highly monodisperse samples were only achieved when using 0.25 mmol of TA (0.1 mL, 2.5 mM), largely below the stoichiometric requirements. From this point it is derived the need of a second reducer, sodium citrate (SC), which ensures a complete consumption of the gold precursor. Additionally, SC is a good stabilizer for the particles and a good pH regulator.
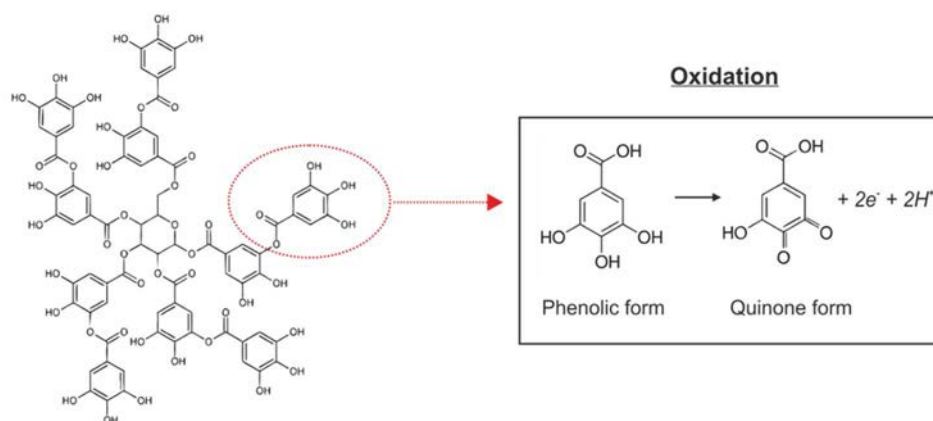
Scheme S1. Structure of tannic acid and oxidation mechanism.

2. Synthesis of seeds Au NPs

2.1 Tested conditions presented in Figure 1 of the main manuscript

Conditions tested for the nucleation of Au NPs presented in **Figure 1** of the main manuscript. In all cases 1 mL of $HAuCl_4$ (25 mM), was injected into a reducing solution containing:

(i) 150 mL of SC (2.2 mM) at 100 ºC.
(ii) 150 mL of water and 0.1 mL of TA (2.5 mM) at 100 ºC.
(iii) 150 mL of SC (2.2 mM) and 0.1 mL of TA (2.5 mM) at 70 ºC.

In the last two cases, the pH of the solution was additionally adjusted with 1 mL of potassium carbonate (K_2CO_3, 150 mM) to ensure the solution remained at slightly alkaline values. The combined use of the two reducers resulted in a largely smaller Au NP' sizes compared to that obtained when they were used separately.

2.2 Tested conditions presented in Figure 2 of the main manuscript

Conditions tested for the nucleation of Au NPs presented in **Figure 2** of the main manuscript. In all cases 1 mL of $HAuCl_4$ (25 mM), was injected into a 150 mL of reducing solution containing sodium citrate (2.2 mM) while varying the TA concentration, pH or temperature. The pH was adjusted with citric acid for acidic solutions or with K_2CO_3 for alkaline solutions. Note that two pH values are presented in the tables below, one corresponding to the pH of the reducing solution previously to the gold precursor addition and another corresponding to the reaction mixture, after addition of the gold precursor. This last value is the one shown in the manuscript.

Table S1. Different pH.

Table S1. Different pH.

TA 2.5 mM (mL)	Temperature	K_2CO_3 150 mM (mL)	pH before gold injection	pH after gold injection	Reaction time (min.)	Size ± SD (nm)
0.1	100 °C	0	3.0	3.0	<1	30.5±5.0**
0.1	100 °C	0	4.1	4.0	<1	11.0±1.4**
0.1	100 °C	0	5.3	5.0	<1	5.6±1.6
0.1	100 °C	0	6.3	5.9	<1	5.1±1.3
0.1	100 °C	0	8.0	7.0	<1	3.8±0.9
<u>0.1</u>	<u>100 °C</u>	<u>1</u>	<u>10.3</u>	<u>8.2</u>	<u>≤1</u>	<u>3.5±0.7*</u>
0.1	100 °C	5	11.0	10.3	5	7.0±1.4
0.1	100 °C	10	11.2	11.0	30	68±20.0

*Chosen as optimal conditions. ** Anisotropic shapes.

Table S2. Different TA concentrations.

TA 2.5 mM (mL)	Temperature	K_2CO_3 150 mM (mL)	pH before gold injection	pH after gold injection	Reaction time (min.)	Size ± SD (nm)
0.001	100 °C	1	10.2	8.3	6	9.1±1.0
0.01	100 °C	1	10.4	8.3	<1	5.0±0.7
<u>0.1</u>	<u>100 °C</u>	<u>1</u>	<u>10.3</u>	<u>8.2</u>	<u>≤1</u>	<u>3.5±0.7*</u>
1	100 °C	1	10.3	7.8	<1	3.4±1.1
10	100 °C	1	10.7	8.0	<1	3.3±2.0

*Chosen as optimal conditions

3

Table S3. Different Temperatures.

TA 2.5 mM (mL)	Temperature	K_2CO_3 150 mM (mL)	pH before gold injection	pH after gold injection	Reaction time (min.)	Size ± SD (nm)
0.1	4 °C	1	10.3	8.1	5 (days)	6.1 ±0.8
0.1	25 °C	1	10.5	8.3	180	5.2±0.5
0.1	40 °C	1	10.4	8.3	30	4.2±0.5
0.1	50 °C	1	10.3	8.2	5	4.1 ±0.4
0.1	60 °C	1	10.3	8.1	2.5	3.7±0.4
0.1	70 °C	1	10.5	8.3	2	3.6±0.4*
0.1	90 °C	1	10.4	8.3	<1	3.5±0.6
0.1	100 °C	1	10.3	8.2	<1	3.5±0.7

*Chosen as optimal conditions

2.3 Tested conditions for 1000 mL scale up.

The reaction volume was increased up to 1000 mL in order to verify the possibility for using this strategy in the production of larger quantities of Au NPs. A 970 mL of freshly prepared reducing solution of sodium citrate (2.2 mM) containing 0.66 mL of TA (2.5 mM) and 6.6 mL of K_2CO_3 (150 mM) was heated with a heating mantle in a 1 L three-necked round-bottom flask under vigorous stirring. When the temperature reached 70 °C, 3.3 mL of $HAuCl_3$ (50 mM) was injected. The solution was kept at 70 °C for 10 minutes to ensure complete reaction of the gold precursor. No relevant differences in the resultant Au NPs were observed (**Figure S1**).
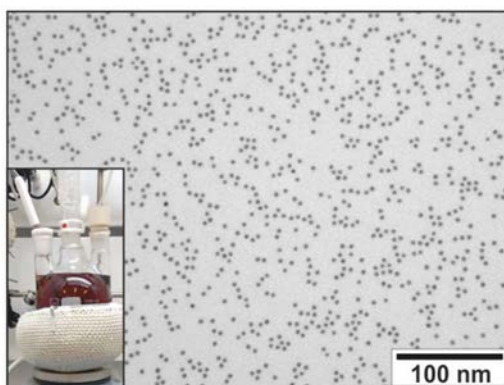
Figure S1. Au NPs synthetized after increasing the volume of the solution from 150 mL to 1000 mL, keeping constant all other parameters of temperature and concentration to that described in the Experimental Methods. Distribution of the particles in the TEM images corresponds to 3.8 ± 0.4 nm.

3. Seeded-growth Synthesis of Au NPs

3.1 Experimental
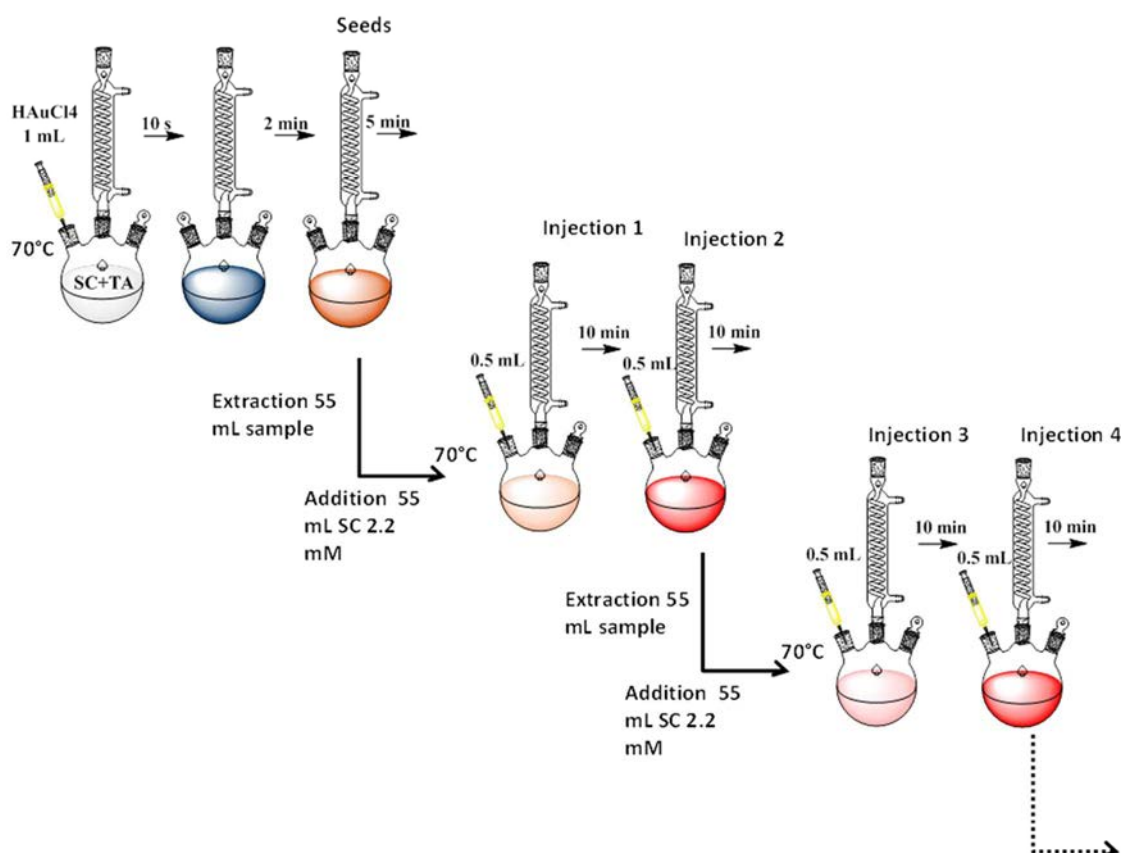
Scheme S2. Gold seeds (~3.5 nm, ~$7 \cdot 10^{13}$ NP/mL) were prepared as follow: 1 mL of $HAuCl_4$ (25 mM) was injected into a 150 mL solution of SC (2.2 mM) containing 0.1 mL of TA (2.5 mM) and 1 mL of K_2CO_3 (150 mM) at 70 °C. After 5 minutes the reaction was finished. To further growth the seeds, the solution was diluted (1:3) by extracting 55 mL of the sample and adding 55 mL of SC 2.2 mM. When the temperature reached again 70 °C, two subsequent injections of 0.5 mL of $HAuCl_4$ (25 mM) were added. By subsequently repeating this process, dilution plus two injections, Au NPs were grown up to the desired size. 1 ml of the solution was taken after each injection and characterized by different techniques.

5

3.2 Theoretical calculations

NP concentration in the initial seed solution was calculated experimentally from the size distribution measured by TEM, assuming that all the gold precursor injected is consumed during the reaction (confirmed by ICP-MS measurements) and the particles are spherical in shape (confirmed by TEM characterization). The procedure is then reduced to Equation 2:

$$[NP]_{seeds} = [Au]_{seeds} \cdot \frac{MW}{\rho \cdot \bar{V}_{NP}} \qquad \text{Equation 2}$$

$$\bar{V}_{NP} = \frac{\sum V_n}{n} \qquad \text{Equation 3}$$

Where *[Au]* is the concentration of gold added to the solution, *MW* and ρ are the molecular weight (197 g/mol) and density (19.32 g/L) of gold, and $\bar{V}_{NP}$ the average NP volume (*n*=1803 NPs counted).

The concentration of each generation of Au NPs was qualitatively predicted from (i) the previous calculated concentration of the initial seed solution and (ii) the dilution factor applied in each growth step, assuming that no new nucleation neither aggregation took place during the growth process (*Table S4*).

On the other hand, expected NP diameter was estimated from the previous NP concentration and gold precursor injected (*Table S4*). Good correlation between the expected and the experimental obtained Au NP diameter validate the previous assumed considerations. This approach was successfully applied for the determination of the concentration of Au and Ag NPs grown by similar seeded-growth strategies.[1,2]

Table S4. Theoretical calculations

Inj.	Particles concentration		Gold concentration		Expected Diameter	
Seeds	$[NP]_{seeds}$= ~$7 \cdot 10^{13}$NPs/mL		$[Au]_{seeds}$=0.167mM		*3.6 $\pm$ 0.4 nm (exp.)*	
1	$[NP]_1$ $= [NP]_{seeds}\left(\frac{95}{150}\right)$	$4.4 \cdot 10^{13}$	$[Au]_1$ $= [Au]_{see}\frac{95}{150}+\frac{12.5}{150}$	0.19	$\frac{4}{3}\pi\left(\frac{d_1}{2}\right)^3 = V_1 = \frac{[Au]_1}{[NP]_1}\frac{MW}{\rho}$	4.4 nm
2	$[NP]_2 = [NP]_1$	$4.4 \cdot 10^{13}$	$[Au]_2 = [Au]_1 + \frac{12.5}{150}$	0.27	$V_2 = \frac{[Au]_2}{[NP]_2}\frac{MW}{\rho}$	4.9 nm
3	$[NP]_3 = [NP]_2\left(\frac{95}{150}\right)$	$2.8 \cdot 10^{13}$	$[Au]_1 = [Au]_2\frac{95}{150}+\frac{12.5}{150}$	0.26	$V_3 = \frac{[Au]_3}{[NP]_3}\frac{MW}{\rho}$	5.6 nm
4	$[NP]_4 = [NP]_3$	$2.8 \cdot 10^{13}$	$[Au]_4 = [Au]_3 + \frac{12.5}{150}$	0.34	$V_4 = \frac{[Au]_4}{[NP]_4}\frac{MW}{\rho}$	6.2 nm
...						

6

3.3 Size distribution profiles.
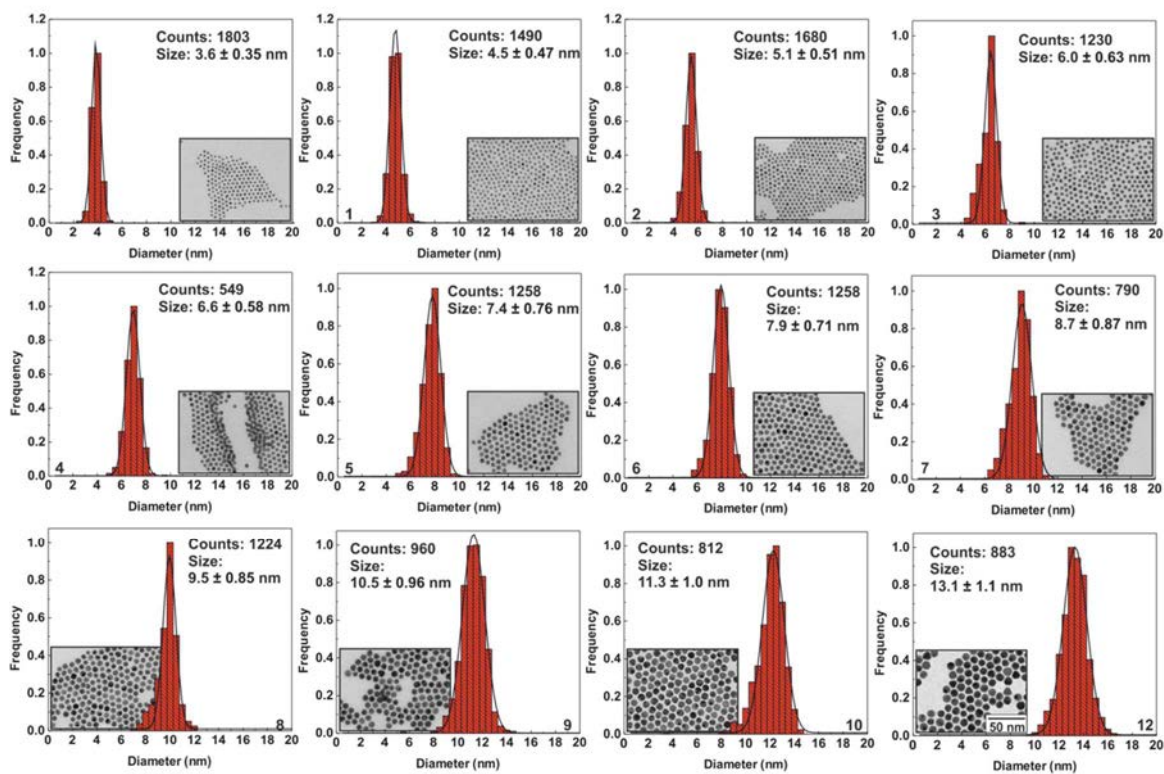
Figure S2. TEM image analysis of Au NPs shown in **Table 1** and **Figure 2** of the main manuscript.

7

3.4 DLS measurements

Table S5. DLS results of Au NPs after different growth steps. Each solution was previously filtered with a 0.2 mm cellulose acetate filter.

Precursor Injections	TEM Diameter (nm)	DLS diameter Intensity mean (nm)[a]	DLS diameter Volume mean (nm)[a]	DLS diameter Number mean (nm)[a]
Seeds	3.6 ± 0.4	7.3 ± 0.4	5.4 ± 0.2	4.4 ± 0.3
1	4.5 ± 0.4	8.9 ± 0.4	6.0 ± 0.2	4.8 ± 0.3
2	5.1 ± 0.5	9.1 ± 0.3	6.9 ± 0.1	5.7 ± 0.2
3	6.1 ± 0.6	9.6 ± 0.1	7.6 ± 0.1	6.5 ± 0.2
4	6.6 ± 0.6	9.7 ± 0.1	7.9 ± 0.1	6.7 ± 0.2
5	7.4 ± 0.7	10.7 ± 0.1	8.3 ± 0.3	7.7 ± 0.4
6	7.9 ± 0.7	11.7 ± 0.1	9.6 ± 0.1	8.2 ± 0.2
7	8.7 ± 0.8	12.4 ± 0.2	10.5 ± 0.1	9.1 ± 0.1
8	9.5 ± 0.8	13.5 ± 0.1	11.1 ± 0.9	9.6 ± 0.1
9	10.5 ± 0.9	15.5 ± 1.0	12.1 ± 0.5	10.1 ± 0.4
10	11.3 ± 1.0	16.7 ± 0.5	12.8 ± 0.5	10.5 ± 0.2
12	13.1 ± 1.1	19.3 ± 0.5	14.5 ± 0.2	11.8 ± 0.3

[a] Number mean and SD from three independent runs.
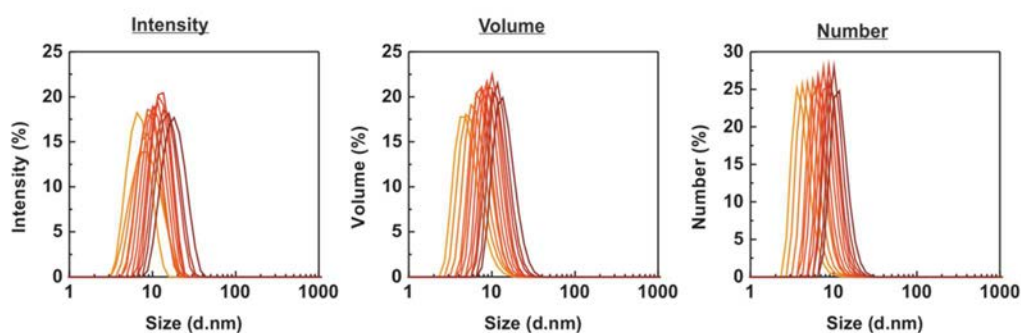
Figure S3. DLS profiles by Intensity (left), Volume (middle) and Number (right) of Au NPs after the different growth steps. Best correlation was observed by Number. For the smallest particles, a secondary larger peak by Intensity was eventually observed when running the measurements. Because we could not correlate this peak with the presence of larger particles, otherwise we would see it by TEM, UV-Vis spectroscopy and in the subsequent samples, we attribute it to work at the limit detection of the DLS instrument and the low scattering of such small particles, being the measurement highly sensitive to any impurity.

8

3.5 Extended growth from 14 nm to 20 nm

Table S6. Extended growth process of Au NPs presented in the main manuscript: injections 14, 16, 18 and 20.

Precursor Injections	TEM Diameter (nm)	SD (%)	DLS Diameter (nm)[a]	Concentration (NPs/mL)	Expected Diameter (nm)
14	14.7 ± 1.2	8.2	13.5	$2.8 \cdot 10^{12}$	14.5
16	16.8 ± 1.3	7.7	16.3	$1.8 \cdot 10^{12}$	16.9
18	18.7 ± 1.5	8.0	18.7	$1.1 \cdot 10^{12}$	19.7
20	21.5 ± 1.7	7.9	20.5	$7.2 \cdot 10^{11}$	23.0

[a] Number mean and SD from three independent runs.
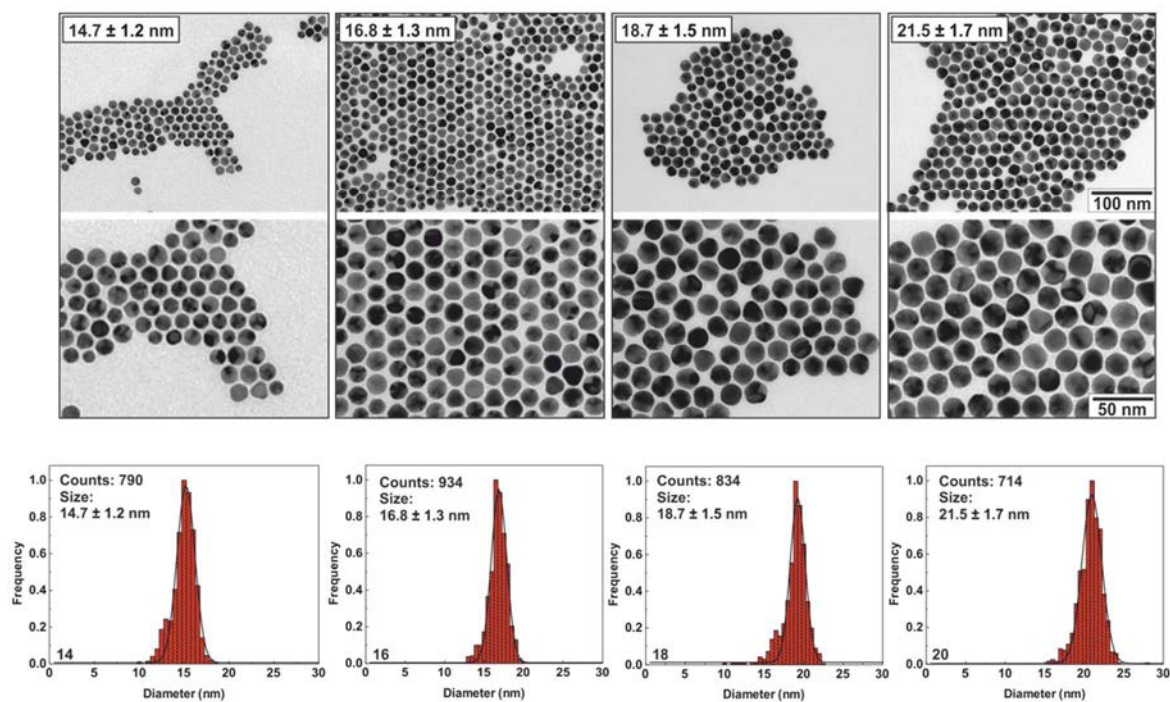
Figure S4. From left to right, representative TEM images and qualitative analysis of Au NPs obtained after injections 14, 16, 18 and 20 of the growing process.

9

4. Functionalization of Au NPs

4.1 Extended conjugation from 14 nm to 20 nm

Table S7. Localised surface Plasmon resonance peak (LSPR) for particles from 14 nm to 20 nm before and after conjugation with 11-mercaptoundecanoic acid (MUA).

Size (TEM)	LSPR (nm)	LSPR after conjugation (nm)*	Δ_{LSPR}
14.7 ± 1.2	517.4	521.9	4.5
17.0 ± 1.3	518.2	522.3	4.1
18.7 ± 1.5	519.3	523.2	3.9
21.5. ± 1.6	520.3	523.5	3.2
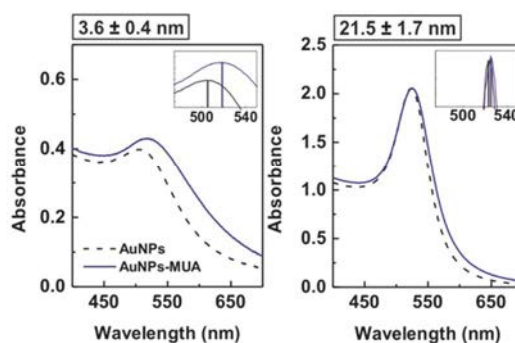
Figure S5. UV-vis spectra before and after conjugation with MUA for particles of 3.6 nm and 21.5 nm respectively.

References:

(1)   Bastús, N. G.; Merkoçi, F.; Piella, J.; Puntes, V., Synthesis of Highly Monodisperse Citrate-Stabilized Silver Nanoparticles of up to 200 nm: Kinetic Control and Catalytic Properties. *Chem. Mater.* **2014,** 26, 2836-2846.

(2)   Bastús, N. G.; Comenge, J.; Puntes, V. F., Kinetically Controlled Seeded Growth Synthesis of Citrate-Stabilized Gold Nanoparticles of up to 200 nm: Size Focusing versus Ostwald Ripening. *Langmuir* **2011,** 27, 11098-11105.

10

Chapter 3:

Synthesis of metal nanoparticles with controllable sizes II: The case of silver

Noble metal nanoparticles are among the most studied class of materials in nanotechnology due to their interesting optical and catalytically properties. However, success in the synthesis of these nanoparticles was restricted to the case of gold, while the synthesis of silver nanoparticles (Ag NPs) lacked reliable and reproducible methods. In this chapter, and related publication, a seeded growth strategy for the synthesis of Ag NPs with various sizes is presented. The method has the additional advantage of being aqueous and results in biocompatible Ag NPs with functionalizable surfaces.

3.1. A general introduction to the synthesis of silver nanoparticles

The importance of obtaining highly monodisperse nanoparticles (NPs) with controllable sizes has been discussed in previous chapters. The extraordinary properties and high performance of these materials originates not only from their small sizes but also from their high degree of monodispersity, which strongly correlates with the physical-chemical characteristics of the particles, and thus it is an essential requirement of any synthesis [1].

Among metals, silver shows the highest electrical and thermal conductivity, making Ag NPs potential candidates for components in electronic devices, as well as being excellent nanocatalysts [2]. Ag nanostructures also present a great plasmonic response, with Ag NPs having the most intense localized surface plasmon resonance among plasmonic NPs (up to 10 times stronger than Au NPs); a characteristic feature that is of interest for many optical applications [3]. Ag NPs have also been found to be an ideal platform for Raman scattering (SERS) detection, which could be significantly improved by advances in their fabrication, providing better sensitivity in chemical analysis and allowing, in some cases, single molecule detection [4, 5]. Furthermore, the antibactericide effect of Ag ions has been known for centuries. The unique ability of Ag NPs to serve as a reservoir of Ag ions and release them *ad libitum* is now an important focus of attention for antibacterial applications [6]. Other fields in which the use of Ag NPs is currently being investigated are those of flexible fibre composites, cryogenic super-conducting materials and cosmetic products [7, 8].

In spite of the fundamental and technological importance of Ag NPs, the success in synthetically controlling the size and surface chemistry of these NPs has achieved limited success [9]. Indeed, it is interesting to note when reviewing the literature that most seminal articles reporting new strategies in the synthesis of metal NPs (i.e. seeded-growth) are related to gold, and attempts to adapt them to the case of Ag have failed. The lack of morphological control of Ag NPs are typically associated with higher reactivity of Ag in comparison with Au, in which oxidation (Ag_2O), precipitation of metal salts (AgCl) and metal ion complexation (Ag-citrate) related processes make their synthesis extremely challenging.

Numerous physical and chemical methods have been exploited for generating and stabilizing Ag NPs including chemical reduction, electrochemical, physical or radiolytic methods [9]. Among them, the most effective and used is the chemical reduction of a metal salt by organic or inorganic reducing agents in an aqueous or non-aqueous solvent where a stabilizing agent is present. For instance, the reduction of silver nitrate ($AgNO_3$) with sodium borohydride (Creighton method) at room temperature has been employed for decades to routinely produce barely disperse colloids of 10 nm Ag NPs [10-12]. Similarly, the combined use of ethylene glycol (a mild reducer) and PVP (a stabilizer) together with variations in the reaction temperature have been demonstrated as effectiveness in the production of Ag NPs in a broad range of both sizes and geometries [13]. Other synthetic strategies involve a two-phase arrested growth process, in which $AgNO_3$/surfactant complexes in organic media are mixed with an aqueous solution containing a strong reducer [14]. Despite the advantages of these methods, their main drawbacks is that they are not yet capable of producing truly reproducible and highly monodisperse Ag NPs with a high yield without the use of organic solvents or strong stabilizers that passivate particle surface, thereby limiting their applicability, especially in biomedicine and catalysis [15]. Additionally, the seeded-growth strategy, which is widely used in the case of Au NPs for size and shape control (see **Chapter 2**), was not successfully applied to the synthesis of Ag NPs in water.

3.2. The classical citrate reduction method

At this point, it is reasonable to consider the citrate reduction method. Indeed, this method still remains the most popular for quickly generating biocompatible noble metal colloids with accessible surfaces and has been proven to be effective in producing highly monodisperse Au NPs in water with different sizes. The first attempts to apply the citrate method to Ag NPs were pioneered by Lee and Meisel in the early 80s [10]. Their studies consisted on the addition of set amounts of aqueous citrate into a boiling solution of $AgNO_3$ and led to the production of well-defined Ag NPs in a single reaction. However, wide size distributions, and a diversity of shapes (spheres, polyhedrons, and plates), were always obtained (**Figure 3.1**). Yang and co-workers [16] recently developed a two-step citrate reduction protocol for the rapid nucleation of silver at high pH followed by a second step of growth at a lower pH. This temporal separation of nucleation and growth
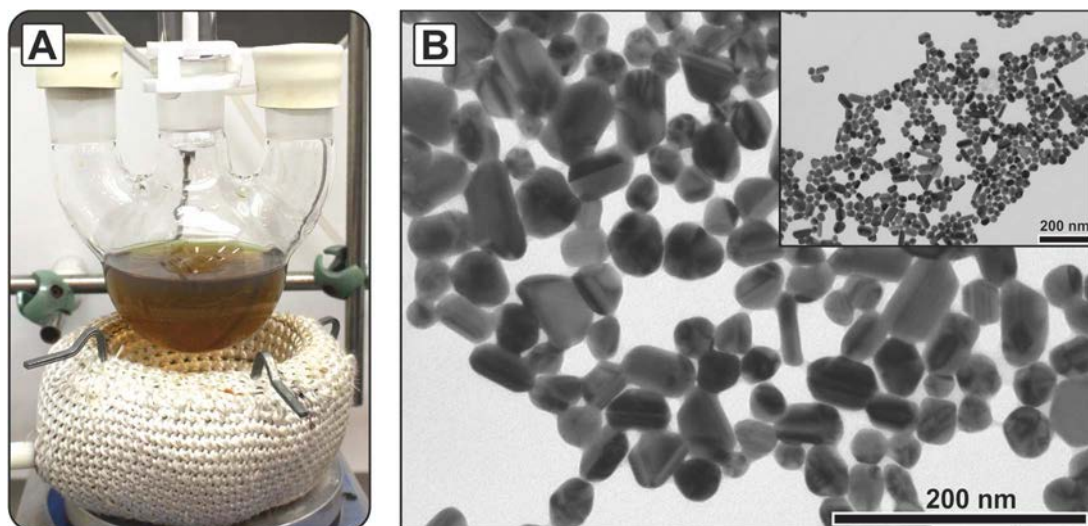
Figure 3.1. Silver nanoparticles obtained using the classical citrate reduction method. In a typical procedure, a solution of Ag NO$_3$ (1 mL, 25 mM) was injected to a boiling solution of sodium citrate (150 mL, 2.2 mM) under vigorous stirring. After 30 min, the solution acquired a greenish colour (A) due to the formation of Ag NPs with sizes from 10 to 150 nm and a variety of shapes (B).

based on the solution pH noticeably improved the size distribution of the Ag NPs, but particle shape was still non uniform. Apart from these two mentioned works, very little progress was made to improve the citrate method [17].

The difficulty of controlling the size of Ag NPs in citrate syntheses derives from the higher reactivity of Ag and multiple roles of citrate, acting the citrate not only as a stabilizer and a weak reducing agent but also as a strong complexing agent [17, 18]. Thus, it is commonly observed that a fast nucleation is hard to achieve during particle formation using only citrate, which arises from the slow and prolonged reduction of Ag-citrate complexes [17]. Moreover, easy hydrolysis and gradual oxidation of Ag atoms prevents a homogeneous growth of the particles. To solve these problems, the use of a secondary reducer to better control the reduction of Ag$^+$ ions to Ag^0 and thus limit the roles of citrate has been recently investigated. For example, in conjunction with citrate, Li *et al* .[19], Schlücker *et al.* [20] and Kelly *et al.* [21] used ascorbic acid; Mukerivhej *et al.* [22] used NaBH$_4$; Perez *et al.* [23] and Gentry *et al.* [24] used hydroquinone; and Dashod *et al.* [25] and Rainville *et al.* [26] effectively employed tannic acid (TA). From these results it can be deduced that the synergic effect of two reducers can significantly improve size control of the obtained Ag NPs.

Encouraged by the limited availability of synthetic protocols for the production of Ag NPs with controlled sizes and narrow distributions, and inspired by the previously

mentioned works, in this chapter we detail a chemical reduction method based on a seeded growth strategy for the production of high quality colloidal dispersions of Ag NPs from 10 to 200 nm in water. The method consists of the reduction of silver nitrate by a combination of two reducing agents: sodium citrate (SC) and tannic acid (TA). The biocompatibility, structure and reducing ability of TA was discussed in **Chapter 2** and was successfully applied in the synthesis of Au NPs. The main difference in this case lies in using the TA not only for the nucleation process (as it is for Au NPs) but also during the subsequent growing steps to complex Ag ions and ensure a homogeneous growth of the particles. This synthetic route leads to the precise control of Ag NP size, offering the advantage of producing long-term stable Ag NPs with a high degree of monodispersity and more accessible surfaces than, for example, PVP coated Ag NPs. All of these results were detailed in the article entitled *Synthesis of Highly Monodisperse Citrate-Stabilized Silver Nanoparticles of up to 200 nm: Kinetic Control and Catalytic Properties*. Attempts to decrease the size of the Ag below 10 nm were also tested.

3.3. Results: Size controlled synthesis of silver nanoparticles from 10 up to 200 nm

The first attempts to synthesize Ag NPs were made via one-pot method by reducing an aqueous solution of $AgNO_3$ with a mixture of sodium citrate (SC) and tannic acid (TA). Typically, an aqueous solution of $AgNO_3$ (1 mL, 25 mM) was injected into a boiling solution of milli-Q water (100 mL) containing a mixture of SC (5 mM) and varying concentrations of TA under vigorous stirring. After the addition of the Ag precursor, the solution changed colour from transparent to yellow within minutes, indicating the presence of Ag NPs. The narrow size distributions of the resultant Ag NPs and the well-defined absorbance peaks shown in **Figure 3.2** highlights the improved degree of particle monodispersity obtained using a mixture of TA and SC compared with that obtained using only SC. This is most likely due to the high level of control over nucleation of the reaction resulting from the stronger reducing ability of the TA.

Interestingly, the size of the Ag NPs increased as the TA concentration increased (**Figure 3.2D**). Similar results were reported by Dadosh *et al.* [25] and Rainville *et al.* [26]. This tendency is completely opposed to our studies of the synthesis of Au NPs
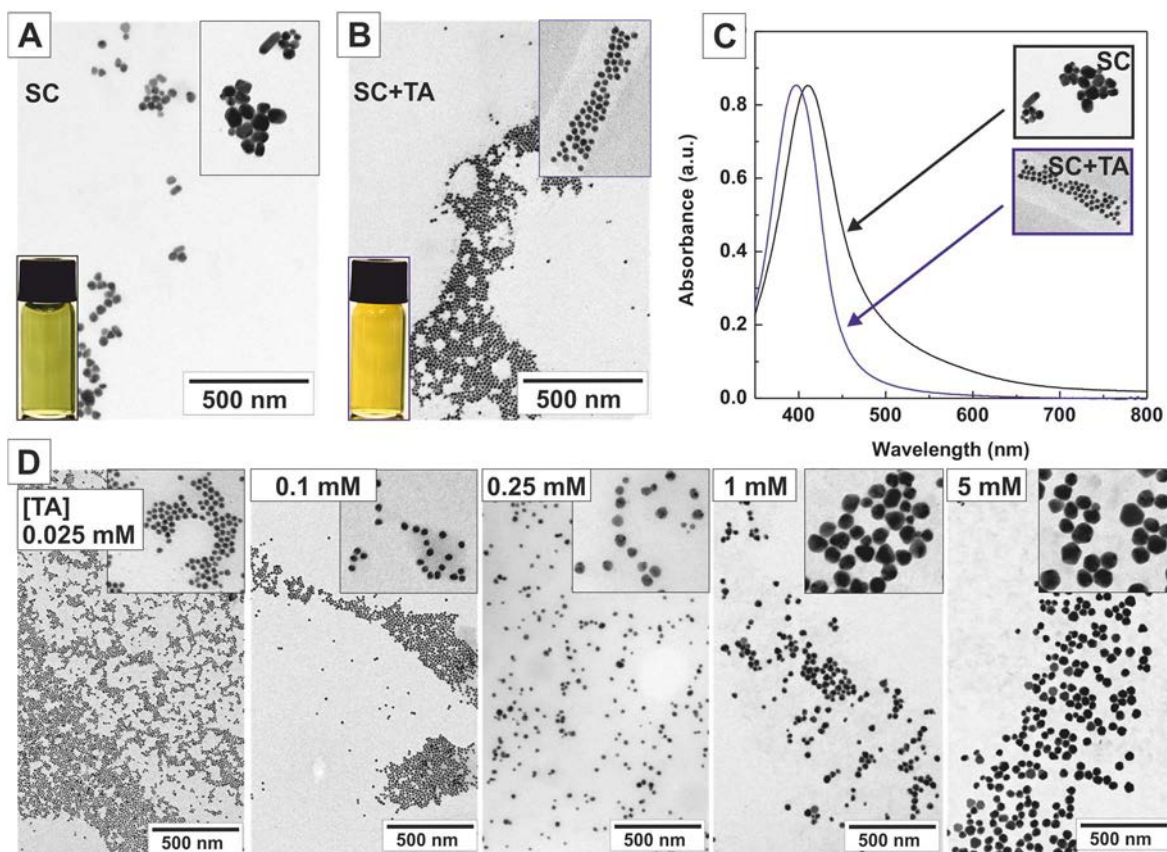
Figure 3.2. Effect of tannic acid in the synthesis of silver nanoparticles. (A-C) TEM images and extinction spectra of Ag NPs synthesized using SC (A, C-black spectrum) or a combination of SC and TA (B, C-blue spectrum). The concentration of Ag NO_3, SC and TA were 0.25 mM, 5 mM and 0.025 mM respectively. (D) Ag NP with mean diameters of 10.1 0.9, to 14.8 1.4, 23.4 5.0, 36.9 + 6.2 and 46.1 8.3 obtained at increasing concentration of TA from 0.025 to 5 mM.

discussed in the previous **Chapter 2**, in which increases in TA concentration promoted the formation of smaller Au NPs due to its stronger reducing power compared with SC (weak reducing). The inversed dependence in the case of Ag NPs evidences an additional role for TA, probably as an organizer, which originates from the ability of TA to form complexes with Ag (**Scheme 3.1**). In contrast to citrate ions, this complexation seems to be beneficial for the synthesis of Ag NPs, which in turn, appears to determine the extent of nucleation and growth processes.

An attempt to explain these observations was first made by Santhanam *et al.* [27]. In his study, TA is conceived as a five-armed chelator able to reduce 20 Ag atoms within a single unit. At low TA concentrations, all TA molecules are completely saturated with 20 Ag atoms acting as nucleation spots and rapid nucleation is favoured. On the other hand, at large TA concentrations, each molecule is on average ligated only to one Ag atom. Under these circumstances the nucleation rate is determined by the interaction
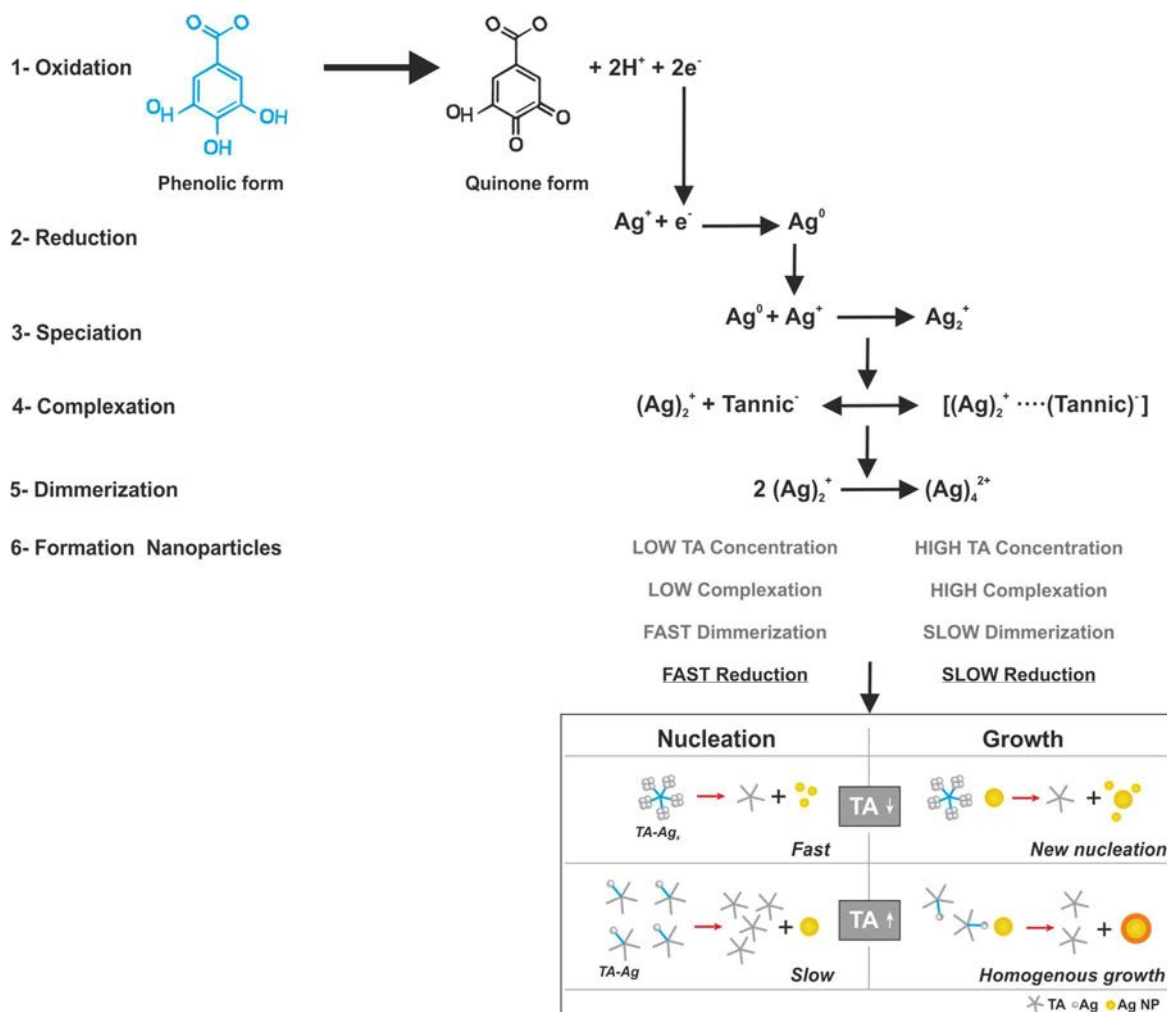
Scheme 3.1. Formation mechanism of silver nanoparticles and effect of the tannic acid. (1, 2) Each of the 10 phenolic hydroxyls of TA undergoes two-electron oxidation to the corresponding quinone and donates two electrons for the reduction of Ag^+. (3) At this moment, a two-step process takes place, the production of Ag^0 and the further formation of a new specie, Ag_2^+. (4) TA interacts with Ag_2^+ mediating its complexation. (5) This TA-Ag complex is the precursor for the dimerization and formation of Ag NPs. (6) Schematic representation of organized-based nucleation and growth processes of Ag NPs. TA is represented as a five armed molecule with each arm capable of reducing and complexing with four Ag atoms. At low concentration of TA, these molecules are saturated by Ag_2^+ promoting the dimerization to $(Ag)_4^{2+}$ and acting as nucleation centres, while at high concentrations only one Ag_2^+ per TA is likely and particle growth is promoted over nucleation [27].

between unsaturated TA-Ag complexes in solution. Because TA is a rather large molecule, it may hinder locally acquiring a sufficient concentration of Ag atoms for self-nucleation and thus growth over nucleation is promoted resulting in larger particle sizes (**Scheme 3.1**, step 6). Consequently, at low concentrations TA acts primarily as a reducing agent while at high concentrations, and due to its strong complexation to Ag, it mainly acts as a growth promoter. This proposed mechanism nicely accounts for the reverse size-tendency observed in the present study, although more research is still needed to fully understand the whole process.

3.3.1. Seeded growth synthesis of silver nanoparticles from 10 to 200 nm

For the production of highly monodisperse Ag NPs of different sizes, a seeded growth protocol similar to that described in **Chapter 2** was developed (**Figure 3.3**). As previously discussed, the seeded growth strategy takes advantage of the catalytic reduction of a metal salt, herein Ag^+, on the surface of pre-synthetized particles used as seeds, thereby promoting their growth. To obtain good kinetic control of the growth process of Ag NPs, the reaction conditions were explored in detail. These conditions included the following: (i) the decrease of temperature from 100 ºC, used for the synthesis of seeds, to 90 ºC; (ii) adjustment of the pH of the solution close to neutral values by adding controlled concentrations of SC; (iii) the precise balance between the
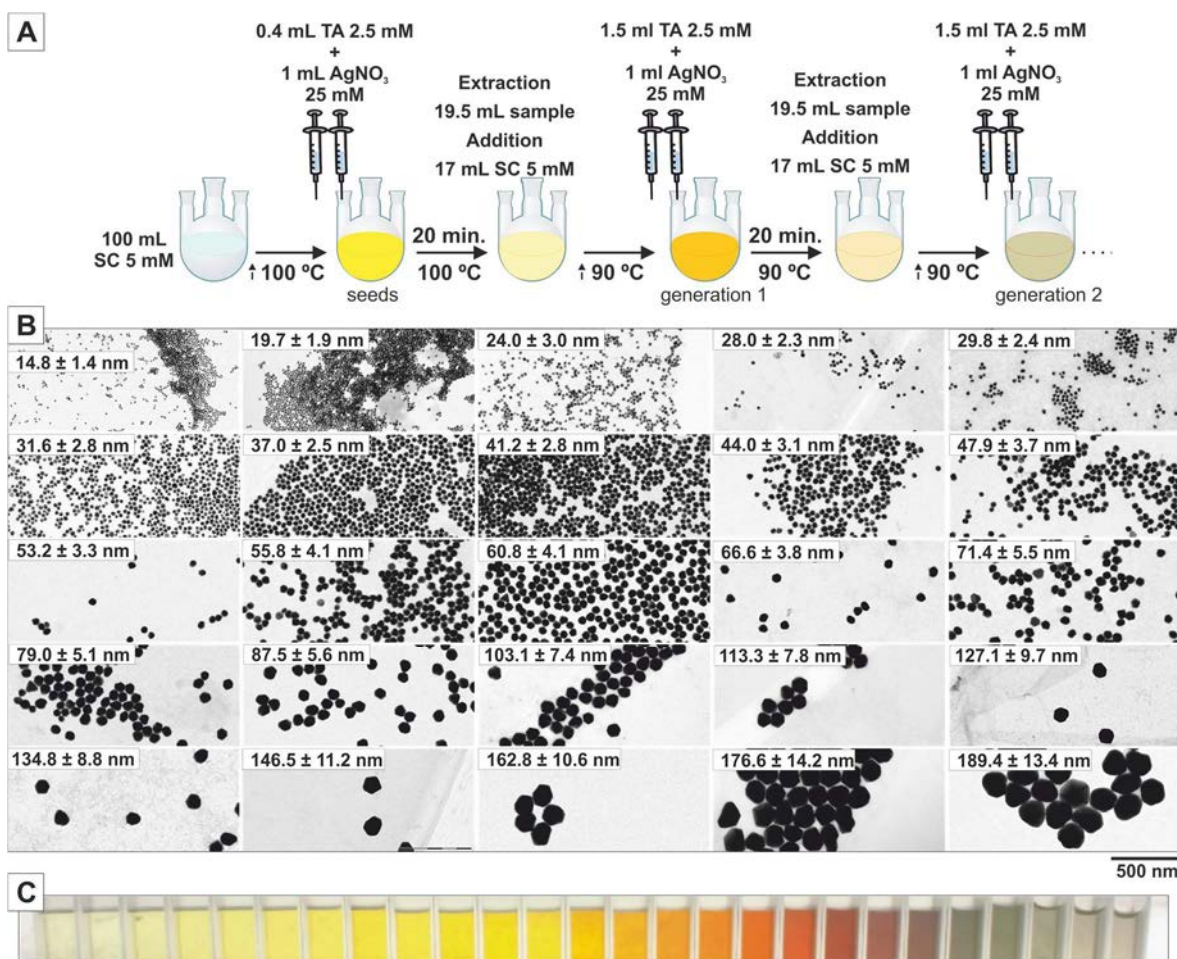
Figure 3.3. Seeded growth synthesis of silver nanoparticles. (A) Synthetic protocol. (B) Representative TEM images of seed particles (14.8 nm) and those obtained after different growth steps. The particle diameter increased from 14.8 ± 1.4 nm to 189.4 ± 13.4 nm, and the concentration decreased from $\sim 2.3 \times 10^{12}$ to $\sim 1.1 \times 10^{10}$ NP/mL. (C) Colloidal solutions of Ag NPs of increasing sizes (from left to right). Solutions composed of small Ag NPs appeared yellow and totally transparent while those of larger Ag NPs appeared grey and opalescent.

Ag precursor injected and the number of Ag seeds in solution; (iv) the successive dilution during growth of the reaction solution to avoid increasing ionic strength; and (v) the addition of an excess of TA previous to every injection of the Ag precursor. Provided that TA was added in excess prior to each growing step, the growth of the Ag NPs was homogeneous and the size standard deviation of the Ag NPs progressively decreased (from 12% to 6%) as particle size increased (from 10 nm to 200 nm), indicating that conditions promoting a size focusing effect were achieved. On the contrary, with only SC the size distribution of the Ag NPs significantly increased during growth. The fact that a small amount of TA was required for a proper nucleation whereas larger amounts were needed during growth highlights the previously discussed role of TA as an Ag complexing agent underlying the reaction.

As a result of the controlled growth of Ag NPs, sample colour changed from bright yellow to dark grey and finally to white. These colours are characteristic of Ag NPs with well-defined localized surface plasmon resonances (LSPR), which were measured by UV-vis spectroscopy (**Figure 3.4**). The symmetry of the LSPR peaks and their high intensity evidences the quality of the resultant colloids with no aggregated particles. Additionally, the emergence of a second LSPR peak for large Ag NPs, corresponding to the quadrupole mode, is indicative of a uniform growth, otherwise this peak is strongly attenuated in polydisperse samples [28]. A more exhaustive analysis of the optical properties of these particles is presented in **Chapter 4** and related **Publication 3**.
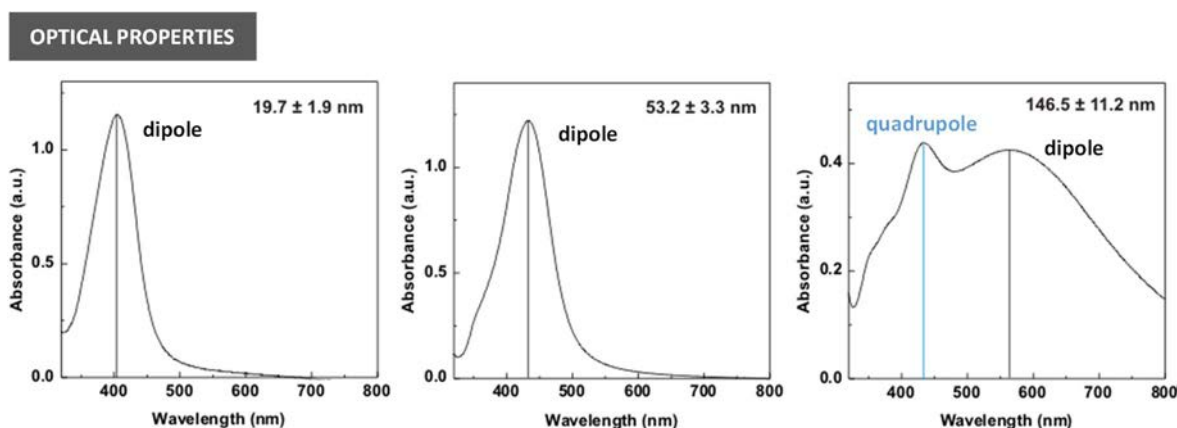

Figure 3.4. Optical properties of silver nanoparticles. Extinction spectra of selected Ag NPs. Black/blue lines indicate the position of the LSPR peaks corresponding to the dipole/quadrupole resonances. Well defined peaks are indicative of highly monodisperse particles, otherwise these peaks would fast attenuate and broadness. Samples have been diluted with water for the measurements.
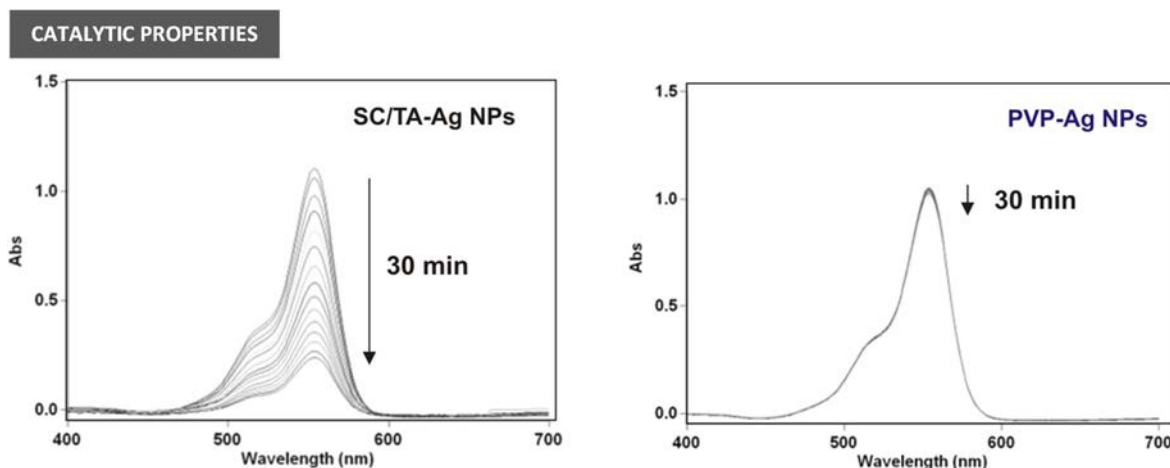
Figure 3.5. Surface activity of silver nanoparticles. Decrease in Rhodamine B absorbance over time using (left) SC/TA-stabilized Ag NPs and (right) PVP-coated Ag NPs of 10 nm as catalysts.

Finally, the surface accessibility of synthesized Ag NPs was compared with Ag NPs obtained using other synthetic methods consisting of the use of strong stabilizers. A catalytic reduction of Rhodamine B (dye) by borohydride ($NaBH_4$) was used as a model reaction [29]. This reaction is known to produces a progressive decolouration of Rhodamine B proportional to its concentration in solution, which is traduced in a decay of a characteristic absorbance peak at 500 nm easily measured by UV-vis spectroscopy. Since it is catalysed on the surface of the particles, the rate of decay of the peak intensity offers an easy way to assess the surface activity of the particle. Two different samples were studied, Ag NPs synthesized using the protocol herein described and another in which PVP was employed as a stabilizer. The intensity of the peak decayed much faster in the SC/TA-Ag NPs than for the PVP coated-Ag NPs (**Figure 3.5**), highlighting the higher accessibility to the surface of the SC/TA-Ag NPs. Different parameters affecting the surface activity of these Ag NPs and thus their potential for catalytic applications are discussed in further detail in **Chapter 5** and related **Publication 4.**

3.4. Additional research

The previously developed seeded growth protocol for the production of highly monodisperse colloids of Ag NPs has two main limitations: first, it is performed under rather diluted conditions and small volumes results in a limited production; second, the size of the Ag NPs is down limited to 10 nm, since the protocol does not lead to the formation of smaller seeds. These two limitations were addressed in subsequent works.
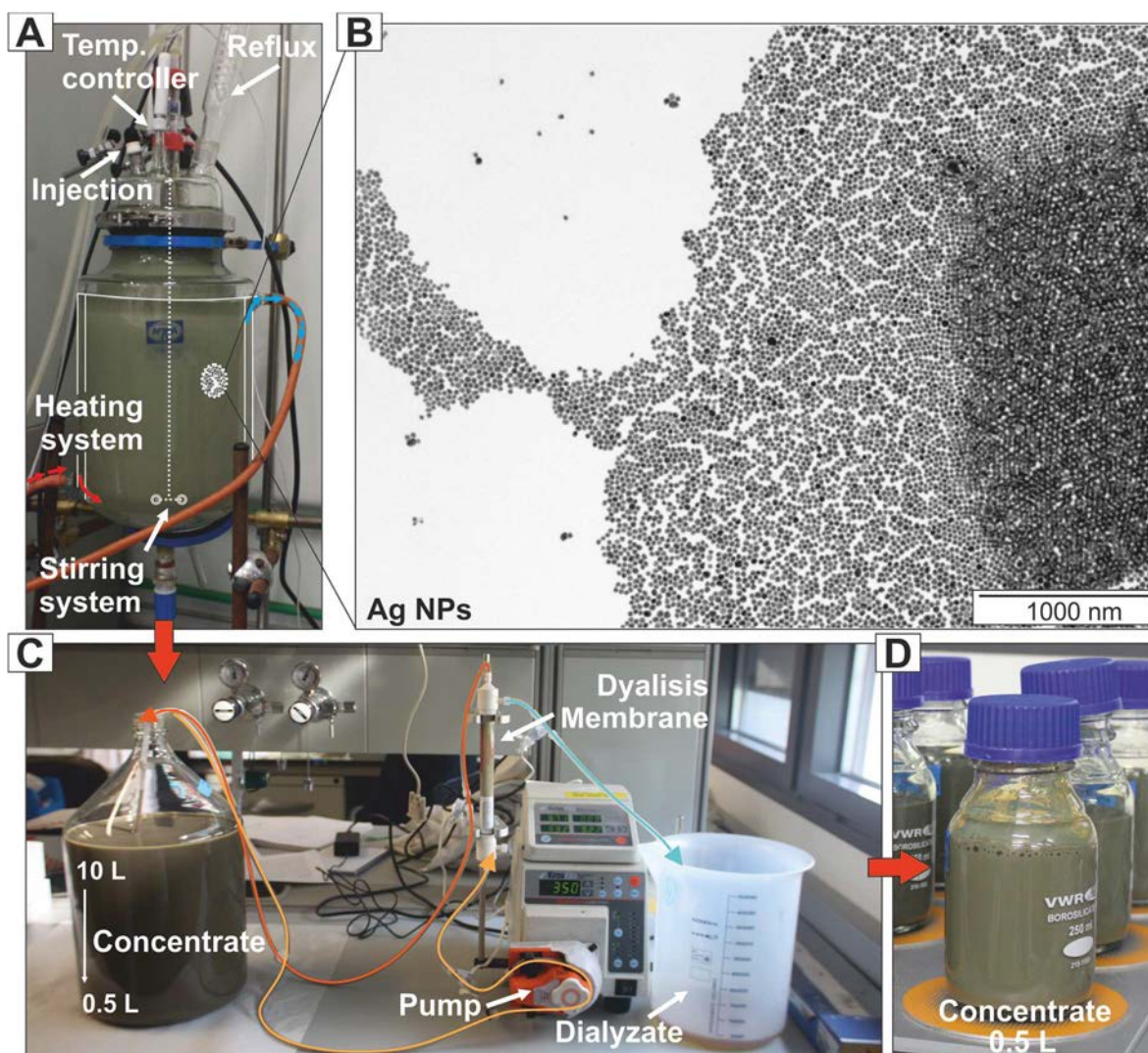
Figure 3.6. Scale-up production of silver nanoparticles. (A) 10 L batch reactor containing Ag NPs of 50 nm. (B) Representative TEM image of the Ag NPs. (C) Tangential flow system used to concentrate the Ag NPs from 10 L (1 g/L) to 0.5 L (20 g/L). (D) Glass bottle containing a concentrated solution of Ag NPs. The synthetic conditions were the same of the standard protocol except that silver precursor solution was 10 times more concentrated. Additionally, the dilution step after each injection was performed additively (without extracting sample).

3.4.1. Scale-up synthesis of Ag NPs

Industrial applications demand synthetic routes that enable at least gram-scale production of NPs [30]. This is where most of the reported synthesis fail, including the one herein presented. Despite the high quality of the resultant Ag NPs, using the developed protocol we were only able to produce an average of 10 mg of particles in a total volume of 100 mL (0.1 g/L of particles). We therefore decided to carry out different studies with the aim of increasing production. To this end, a large-scale batch reactor of 10 L specifically designed to minimize thermal and mass gradients was employed (**Figure 3.6**).

Optimization research was focussed on reducing the dilution steps during growth of the Ag NPs while simultaneously increasing the amount of Ag precursor added at each step. Using this modified protocol we were able to increase the silver concentration in the reaction mixture 10 times with respect to that used in the initial developed protocol without sacrificing particle homogeneity, and to produce 10 g of Ag NPs in 10 L (1 g/L of particles). To date there is no reported aqueous synthesis of Ag NPs in the literature able to produce such quantities of this material, neither in terms of concentration nor volume. Finally, the resultant Ag NPs were concentrated with a tangential flow filtration up to a concentration of 20 g/L of particles, and were stored in a fridge in the same reaction mixture for months with no relevant changes in the particle morphology or stability.

3.4.2. Synthesis of sub-10 nm silver nanoparticles:

Despite the possibility of synthesizing Ag NPs from 10 to 200 nm, another important issue to address was the lack of protocols for producing Ag NPs with sizes smaller than 10 nm. The strong complexation of Ag ions with many reducing and stabilizing agents inevitably slows down the nucleation step during particle formation and consequently large particle sizes are obtained. In this regard, Sivaraman *et al.* [27] recently demonstrated that alkaline conditions are effective in increasing the reactivity of TA. Additionally, it is known that high pH can weakened the coordinative effect of complexing agents as they must compete with the hydroxides in solution for the Ag ions [16, 31, 32]. Thus, we attempted to speed up the nucleation process by increasing the pH of the reaction mixture. This adjustment, together with a reduction in the amounts of TA and citrate to minimize complexation effects, resulted in an overall reduction in the particle diameter from 10-13 nm to 4-5 nm (**Figure 3.7A, B**).

Unexpectedly, we observed that such small Ag NPs were highly reactive and could not be preserved for more than a month, a phenomena that we did not observe for any Ag NPs larger than 10 nm in the same time interval. In particular, the initial yellow coloured solution progressively turned to green and finally blue (**Figure 3.7C**). A more detailed examination of the samples by TEM showed that these colours were due to the fact that the small Ag NPs had converted to larger anisotropic structures, mainly triangles and hexagons (**Figure 3.7D, E**). Because almost no silver precursor was detected in the
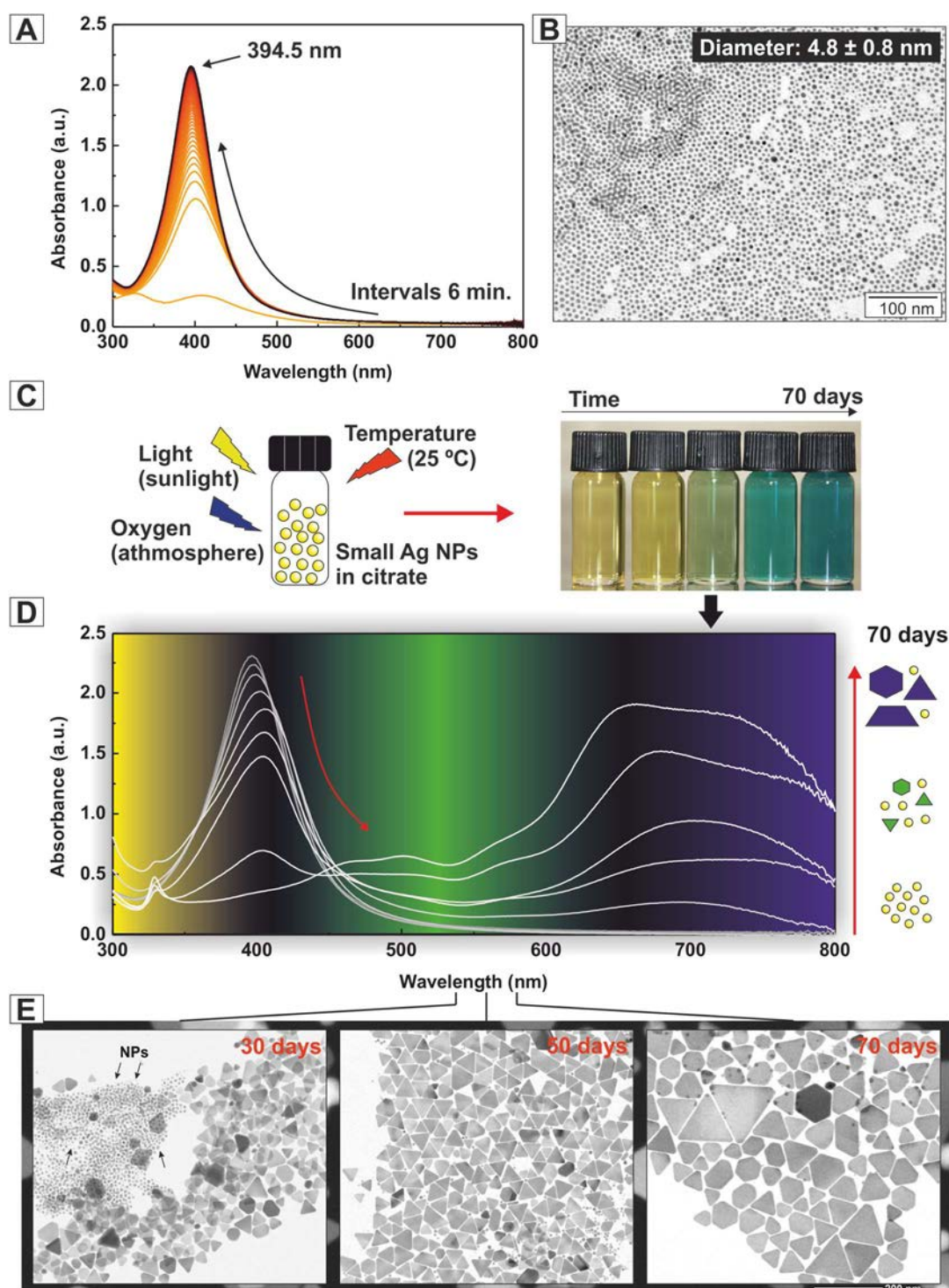
Figure 3.7. Synthesis and time evolution of sub-10 nm silver nanoparticles. A decrease in particle size from 10-15 nm to 4.8 nm was achieved by adjusting the reaction conditions. In a typical procedure, 0.2 mL of AgNO₃ 25 mL ws added into a reaction solution containing 2.2 mM of SC, 1.67 uM of TA and 1 mM of K₂CO₃, and the resultant mixture was left under mild stirring at room temperature for at least 6 h before characterization. (A) Time-evolution extinction spectra during Ag NP formation. (B) Corresponding TEM image showing Ag NPs with a mean diameter of 4.8 ± 0.8 nm. (C) Visual evolution and (D) corresponding extinction spectra of the synthesized Ag NPs after different days from being prepared. Aging conditions were: room temperature, the same medium where Ag NPs were synthesized and no protection from light and oxygen. The appearance of multiple LSPR peaks in the extinction spectra is in agreement with the transformation of the Ag NPs from spheres to 1-D anisotropic structures, as shown by the representative TEM images (E).

reaction mixtures during the formation of these nameplates (conversion yield of the reaction was >90 % measured by ICP-MS), the only possible source of silver was the Ag NPs themselves. To obtain a deeper insight into the related process, a large number of different parameters were evaluated with the observations that (i) light and oxygen, (ii) sodium citrate and (iii) temperatures accelerated the formation of these Ag nanoplates. Light and oxygen are known to be oxidation promoters; SC and TA are reducers; and temperature speeds up the kinetic of both processes. It is feasible that the combination of these three effects results in a dynamic process of dissolution driven oxidation plus recrystallization of the Ag NPs, that is a Ostwald-Ripening like process. This would be in accordance with other works in which similar Ag nanostructures were promoted after adding Ag NPs into a solution containing hydrogen peroxide and a reducing agent [33]. All things considered, these results supports the idea of a strong size dependency in the reactivity of small Ag NPs, whose surface is probably more quickly oxidizable than that of larger Ag NPs.

3.5. Conclusion

In summary, we developed a new synthetic protocol for the production of highly monodisperse, long-term stable and surface active Ag NPs from 10 to 200 nm. These particles possess interesting optical properties with a well-defined surface plasmon resonance bands. Their potential for catalytic applications was also demonstrated. Finally, two additional issues are currently under ongoing research, the scale-up production and the possibility to synthesize Ag NPs with sizes smaller than 10 nm. Preliminary results indicate that both requirements can be achieved with controlled variations of the synthetic conditions.

3.6. References

[1] U. Kreibig, M. Vollmer, Optical properties of metal clusters, Springer, Berlin; New York, 1995.

[2] M. Rycenga, *et al.*, Controlling the Synthesis and Assembly of Silver Nanostructures for Plasmonic Applications, Chemical Reviews 111 (2011) 3669-3712.

[3] P.K. Jain, *et al.*, Review of Some Interesting Surface Plasmon Resonance-enhanced Properties of Noble Metal Nanoparticles and Their Applications to Biosystems, Plasmonics 2 (2007) 107-118.

[4] K. Kneipp, *et al.*, Single Molecule Detection Using Surface-Enhanced Raman Scattering (SERS), Physical Review Letters 78 (1997) 1667-1670.

[5] S. Nie, S.R. Emory, Probing Single Molecules and Single Nanoparticles by Surface-Enhanced Raman Scattering, Science 275 (1997) 1102-1106.

[6] J. Liu, *et al.*, Controlled Release of Biologically Active Silver from Nanosilver Surfaces, ACS Nano 4 (2010) 6903-6913.

[7] K.M.M. Abou El-Nour, *et al.*, Synthesis and applications of silver nanoparticles, Arabian Journal of Chemistry 3 (2010) 135-140.

[8] T. Quang Huy, *et al.*, Silver nanoparticles: synthesis, properties, toxicology, applications and perspectives, Advances in Natural Sciences: Nanoscience and Nanotechnology 4 (2013) 033001.

[9] N.L. Pacioni, *et al.*, Synthetic Routes for the Preparation of Silver Nanoparticles, in: E.I. Alarcon, *et al.* (Eds.) Silver Nanoparticle Applications: In the Fabrication and Design of Medical and Biosensing Devices, Springer International Publishing, Cham, 2015, pp. 13-46.

[10] J.A. Creighton, *et al.*, Plasma resonance enhancement of Raman scattering by pyridine adsorbed on silver or gold sol particles of size comparable to the excitation wavelength, Journal of the Chemical Society, Faraday Transactions 2: Molecular and Chemical Physics 75 (1979) 790-798.

[11] J. Polte, *et al.*, Formation Mechanism of Colloidal Silver Nanoparticles: Analogies and Differences to the Growth of Gold Nanoparticles, ACS Nano 6 (2012) 5791-5802.

[12] D.L. Van Hyning, C.F. Zukoski, Formation Mechanisms and Aggregation Behavior of Borohydride Reduced Silver Particles, Langmuir 14 (1998) 7034-7046.

[13] T. Zhao, *et al.*, Size-controlled preparation of silver nanoparticles by a modified polyol method, Colloids and Surfaces A: Physicochemical and Engineering Aspects 366 (2010) 197-202.

[14] B.A. Korgel, *et al.*, Assembly and Self-Organization of Silver Nanocrystal Superlattices: Ordered "Soft Spheres", The Journal of Physical Chemistry B 102 (1998) 8379-8388.

[15] I. Sondi, *et al.*, Preparation of highly concentrated stable dispersions of uniform silver nanoparticles, Journal of Colloid and Interface Science 260 (2003) 75-81.

[16] X. Dong, *et al.*, Shape Control of Silver Nanoparticles by Stepwise Citrate Reduction, The Journal of Physical Chemistry C 113 (2009) 6573-6576.

[17] Z.S. Pillai, P.V. Kamat, What Factors Control the Size and Shape of Silver Nanoparticles in the Citrate Ion Reduction Method?, The Journal of Physical Chemistry B 108 (2004) 945-951.

[18] A. Henglein, M. Giersig, Formation of Colloidal Silver Nanoparticles: Capping Action of Citrate, The Journal of Physical Chemistry B 103 (1999) 9533-9539.

[19] H. Li, *et al.*, Simple Synthesis of Monodisperse, Quasi-spherical, Citrate-Stabilized Silver Nanocrystals in Water, Langmuir 29 (2013) 5074-5079.

[20] D. Steinigeweg, S. Schlucker, Monodispersity and size control in the synthesis of 20-100 nm quasi-spherical silver nanoparticles by citrate and ascorbic acid reduction in glycerol-water mixtures, Chemical Communications 48 (2012) 8682-8684.

[21] D.M. Ledwith, *et al.*, A rapid, straight-forward method for controlling the morphology of stable silver nanoparticles, Journal of Materials Chemistry 17 (2007) 2459-2464.

[22] S. Agnihotri, *et al.*, Size-controlled silver nanoparticles synthesized over the range 5-100 nm using the same protocol and their antibacterial efficacy, RSC Advances 4 (2014) 3974-3983.

[23] M.A. Pérez, *et al.*, Hydroquinone Synthesis of Silver Nanoparticles: A Simple Model Reaction To Understand the Factors That Determine Their Nucleation and Growth, Crystal Growth & Design 8 (2008) 1377-1383.

[24] S.T. Gentry, *et al.*, Controlled Particle Growth of Silver Sols through the Use of Hydroquinone as a Selective Reducing Agent, Langmuir 25 (2009) 2613-2621.

[25] T. Dadosh, Synthesis of uniform silver nanoparticles with a controllable size, Materials Letters 63 (2009) 2236-2238.

[26] L. Rainville*, et al.*, Controlled synthesis of low polydispersity Ag@SiO2 core-shell nanoparticles for use in plasmonic applications, RSC Advances 3 (2013) 13953-13960.

[27] S.K. Sivaraman*, et al.*, A green protocol for room temperature synthesis of silver nanoparticles in seconds, Current Science 97 (2009) 1055-1059.

[28] A.S. Kumbhar*, et al.*, Multipole Plasmon Resonances of Submicron Silver Particles, Journal of the American Chemical Society 127 (2005) 12444-12445.

[29] P. Zhao*, et al.*, Basic concepts and recent advances in nitrophenol reduction by gold- and other transition metal nanoparticles, Coordination Chemistry Reviews 287 (2015) 114-136.

[30] L. Zhang, Y.N. Xia, Scaling up the Production of Colloidal Nanocrystals: Should We Increase or Decrease the Reaction Volume, Advanced Materials 26 (2014) 2600-2606.

[31] K.K. Caswell*, et al.*, Seedless, Surfactantless Wet Chemical Synthesis of Silver Nanowires, Nano Letters 3 (2003) 667-669.

[32] M. Singh*, et al.*, Role of pH in the green synthesis of silver nanoparticles, Materials Letters 63 (2009) 425-427.

[33] H. Yu*, et al.*, Thermal Synthesis of Silver Nanoplates Revisited: A Modified Photochemical Process, ACS Nano 8 (2014) 10252-10261.

Publication 2

Synthesis of Highly Monodisperse Citrate-Stabilized Silver Nanoparticles of up to 200 nm: Kinetic Control and Catalytic Properties

Neus G. Bastús,*,[†] Florind Merkoçi,[†] Jordi Piella,[†] and Victor Puntes*,[†,‡]

[†]Institut Català de Nanociència i Nanotecnologia (ICN2), Campus UAB, 08193 Bellaterra, Barcelona, Spain
[‡]Institut Català de Recerca i Estudis Avançats (ICREA), 08010 Barcelona, Spain

⑤ *Supporting Information*

ABSTRACT: Highly monodisperse sodium citrate-coated spherical silver nanoparticles (Ag NPs) with controlled sizes ranging from 10 to 200 nm have been synthesized by following a kinetically controlled seeded-growth approach via the reduction of silver nitrate by the combination of two chemical reducing agents: sodium citrate and tannic acid. The use of traces of tannic acid is fundamental in the synthesis of silver seeds, with an unprecedented (nanometric resolution) narrow size distribution that becomes even narrower, by size focusing, during the growth process. The homogeneous growth of Ag seeds is kinetically controlled by adjusting reaction parameters: concentrations of reducing agents, temperature, silver precursor to seed ratio, and pH. This method produces long-term stable aqueous colloidal dispersions of Ag NPs with narrow size distributions, relatively high concentrations (up to 6×10^{12} NPs/mL), and, more important, readily accessible surfaces. This was proved by studying the catalytic properties of as-synthesized Ag NPs using the reduction of Rhodamine B (RhB) by sodium borohydride as a model reaction system. As a result, we show the ability of citrate-stabilized Ag NPs to act as very efficient catalysts for the degradation of RhB while the coating with a polyvinylpyrrolidone (PVP) layer dramatically decreased the reaction rate.
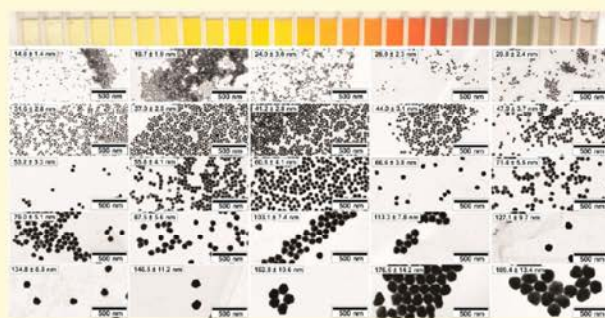
■ INTRODUCTION

The ability to produce silver nanoparticles (Ag NPs) with fine control of their physical, chemical, and structural properties is crucial for expanding their applicability in many areas, including optoelectronics, energy harvesting, catalysis, chemical and biological sensing, imaging, and biomedicine.[1,2] Ag has also been found to be the best platform for surface-enhanced Raman scattering (SERS) detection, providing important improvements for sensitive chemical analysis and allowing, in some cases, single molecule detection.[3,4] Moreover, Ag has the highest electrical and thermal conductivity among all metals, making it an ideal component for electrical interconnections, as well as an excellent catalyst. Ag is also an important focus of attention in nanotoxicology, since Ag⁺ ions released from Ag NPs have been proved to be antibiotic.[5] In this context, the design of generic and reproducible methods for the preparation of Ag NPs with a broad range of defined morphologies is a cornerstone to fully exploit the unique properties and promising applicability of Ag NPs.

In spite of its fundamental and technological importance, the challenge of synthetically controlling the size and surface chemistry of Ag NPs has achieved limited success.[6] In current methods, the choice of both the reducing agent and the stabilizer allows control over the growth process, providing

effective means to tune the size, and often also the shape of Ag NPs. For instance, the reduction of AgNO₃ with sodium borohydride (Creighton method) at room temperature routinely yields ~10 nm particles of quite narrow size distribution.[7] Similarly, the combined use of ethylene glycol—as reducer—and polyvinylpyrrolidone (PVP)—as stabilizer—produces Ag NPs over a broad range of sizes and geometries, as it allows control of the nucleation and growth processes through careful regulation of the temperature.[8] Other synthetic strategies involve the reduction of a supersaturated Ag₂O solution pressurized by hydrogen gas, producing Ag NPs in the range 10 to 140 nm[9] and the combined use of ascorbic acid and potassium iodide to tailor the growth of the Ag NPs from 10 to 40 nm.[10]

Despite the individual advantages of these methods, their central drawback is that they are not yet capable of producing truly reproducible highly monodisperse Ag NPs with a high yield and versatile surface chemistry, restricting the possibility of further Ag NP's functionalization, and therefore limiting their applicability, especially in biomedicine and catalysis. The

lack of morphological control over Ag particle's geometry and the use of strong surfactants that block the surface's accessibility are typically associated with the highest reactivity of Ag atoms in comparison to other metals, such as Au, where size and shape control has been extensively achieved by using surfactants and other complexing molecules.[11−13]

Among all synthetic strategies, citrate reduction of noble metal salts remains the most popular approach to quickly generate noble metal colloids with accessible surfaces due to the weak interaction of sodium citrate molecules with metal surfaces. Although it has been recently proved effective to produce highly monodisperse spherical Au NPs in water and control its monodisperse size from 10 to 200 nm with nanometric resolution,[14] the challenge of synthetically controlling the morphology of Ag NPs using sodium citrate as reducing agent has not been solved yet. First attempts were pioneered by Lee and Meisel[15] in the early 80s. Their studies, based on the addition of set amounts of aqueous citrate into a boiling solution of AgNO₃, led to the production of well-defined Ag NPs in a single reaction but with a large variety of sizes (30−150 nm) and a diversity of shapes (spheres, polyhedrons, and plates). Since then, very little progress has been made in order to make this method more efficient and alternative seeded-growth routes based on the use of Au spheres as templates and sodium citrate[16] or PVP[17,18] as stabilizers have been recently proposed.

The main drawback of the citrate-mediated synthesis of Ag NPs is the multiple roles of citrate ions, acting as a weak reducing agent and strong complexing stabilizer, which affects Ag reduction kinetics and ultimately hinders the control of Ag NP's nucleation and growth, and, therefore, their morphology. Thus, in the process of oxidation of sodium citrate into dicarboxyacetone and its further decomposition into acetoacetate,[19] sodium citrate forms relatively stable complexes with positively charged Ag^+ and Ag^{2+} ions, stabilizing them and slowing their conversion into Ag_4^{2+}. The uncontrolled formation of Ag_4^{2+}, which acts as a monomer for the formation of Ag NPs,[20,21] leads initially to the slow and heterogeneous nucleation of Ag NPs and finally to the formation of large and polydisperse products. In front of this, several studies have been focused on the possibility to control the complexation of Ag^+ ions by sodium citrate by adjusting the synthetic parameters involved in the reaction. Thus, the role of the pH was systematically investigated by Dong et al.,[22] aiming to control Ag reduction rate via the modification of the different protonation states of citrate ions.[23] As a result, they reported a two-step seeded-growth method in which nucleation and growth processes were controlled by adjusting the pH of the solution, obtaining Ag NPs with improved quality and uniformity but with a significant second population of nonspherical shapes.

Beyond the control of protonation states of the citrate ions, other strategies aiming to control the reduction kinetics of metal NPs have been widely explored, among them, the addition of chemical species limiting the availability (or reactivity) of precursor molecules,[24,25] the coupling of reduction with oxidative etching,[26] the use of extremely mild reducing agents and/or the control of the temperature of the solution,[14] among others.[27,28]

In this context, we herein report a method for the kinetic control of the synthesis of highly monodisperse Ag NPs based on the reduction of silver nitrate by a combination of two reducing agents: sodium citrate and tannic acid. Sodium citrate

is a common reducing agent while tannic acid is a highly biocompatible mixed gallotannin composed of gallic esters of glucose, which has been previously used for the synthesis of metal NPs.[29,30] Rainville and co-workers[31] reported very recently the synthesis of Ag NPs using the combination of sodium citrate and tannic acid acting as a reducing agent and PVP as a stabilizer. As a result, they produced PVP-coated Ag NPs with controllable sizes from 26 to 118 nm by modifying the ratio between both reducing agents. Although this method produces Ag NPs fairly monodisperse in the low size regime (26 to 59 nm), Ag nanoplates appear more abundant, as the reagent concentration were adjusted to yield bigger Ag NPs. Besides, the presence of PVP at the surface restricts the further functionalization of as-synthesized NPs. The synthetic route herein presented leads to the precise control of Ag NP size from 10 to 200 nm, offering the advantage of being able to produce long-term stable Ag NPs with narrow size distributions, high concentrations, and readily accessible surfaces by, for example, thiol- and amine-terminated molecules, and proteins.[32] Besides, this control over seed-mediated growth not only allows for the manipulation of the size of a nanostructure but also provides a robust route that can be extended to other metals.

■ EXPERIMENTAL SECTION

Chemicals. Silver nitrate ($AgNO_3$), trisodium citrate ($Na_3C_6H_5O_7$), and tannic acid ($C_{76}H_{52}O_{46}$) were purchased from Sigma-Aldrich. All chemicals were used as received without further purification. Distilled water passed through a Millipore system ($\rho = 18.2$ MΩ) was used in all experiments. All glassware was first rinsed with acetone and then with Millipore water before use.

Methods. The typical procedure for the production of Ag NPs is given below.

Synthesis of Silver Seeds. A 100 mL volume of aqueous solution containing sodium citrate (SC) (5 mM) and tannic acid (TA) was prepared and heated with a heating mantle in a three-neck round-bottomed flask for 15 min under vigorous stirring. A condenser was used to prevent the evaporation of the solvent. After boiling had commenced, 1 mL of AgNO₃ (25 mM) was injected into this solution. The solution became bright yellow immediately. The size of the Ag seeds was controlled by adjusting the concentration of tannic acid. Thus, by increasing the TA concentration from 0.025 mM to 0.1 mM, 0.25 mM, 1 mM, and 5 mM, the size of Ag NPs increased from 10.1 ± 0.9 nm, to 14.8 ± 1.4 nm, 23.4 ± 5.0 nm, 36.9 ± 6.2 nm, and 46.1 ± 8.3 nm, respectively. Resultant Ag NPs were purified by centrifugation (10000g to 18000g, depending on its size) in order to remove the excess of TA and further redispersed in Milli-Q-water or SC 2.2 mM before sample characterization.

Growth of Silver Nanoparticles. *Growth of Ag NPs from 10 to 20 nm.* Ag seeds of ~10 nm (~6 × 10¹² NPs/mL) in diameter were synthesized following the above-described protocol. Immediately after the synthesis of the Ag seeds and in the same vessel, the reaction was cooled until the temperature of the solution reached 90 °C. Then, 100 μL of SC (25 mM), 250 μL of TA (2.5 mM), and 250 μL of AgNO₃ were sequentially injected (time delay ~ 1 min). After 15 min, aliquots of 0.5 mL were extracted for further characterization. By repeating this process and adjusting the amount of Ag precursor injected, different generations of Ag NPs of progressively larger sizes were grown. The concentration of each generation of NPs is the same as that of the original seed solution (~6 × 10¹² NPs/mL). Aliquots were purified by centrifugation (18000g) in order to remove the excess of TA and further redispersed in Milli-Q-water or SC 2.2 mM before sample characterization.

Growth of Ag NPs from 15 to 200 nm. Ag seeds of ~15 nm (~2.3 × 10¹² NPs/mL) in diameter were synthesized following the above-described protocol. An aliquot of 0.5 mL was extracted for further characterization. Immediately after the synthesis of Ag seeds and in the
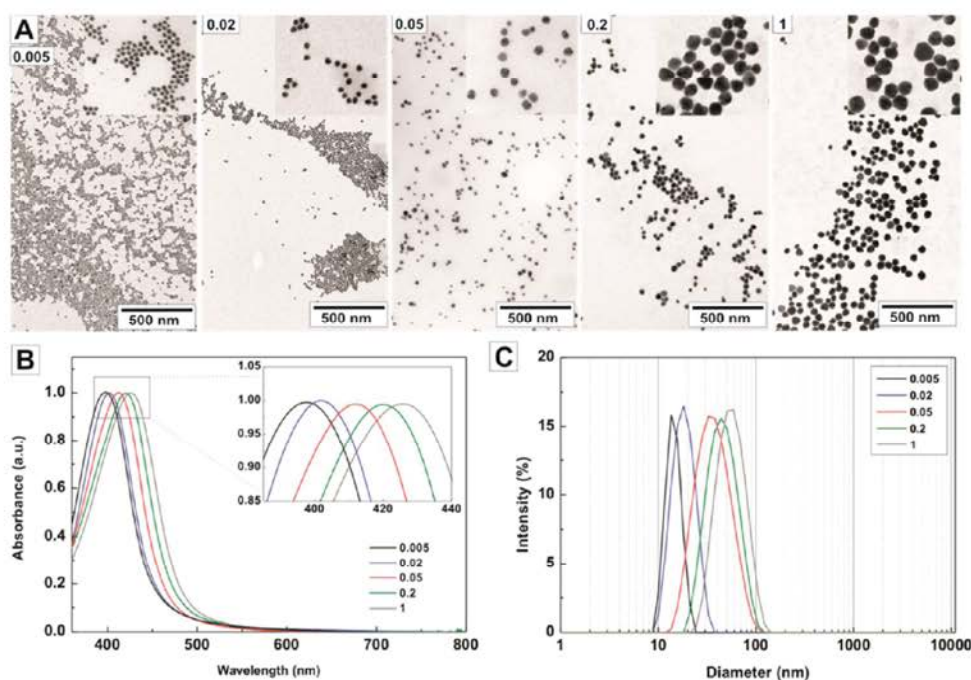
Figure 1. (A) Transmission electron microscopy images of silver nanoparticles obtained by using different TA to SC ratios. Mean Ag NP's diameter increased from 10.1 ± 0.9 nm, to 14.8 ± 1.4 nm, 23.4 ± 5.0 nm, 36.9 ± 6.2 nm, and 46.1 ± 8.3 nm as the concentration of TA increased from 0.025 mM to 5 mM (TA to SC ratios from 0.005/1 to 1/1). (B) UV−vis spectra of Ag NPs obtained using different TA to SC ratios from 0.005/1 to 1/1. The position of the surface plasmon resonance band red-shifts from ∼397 nm to ∼401.5 nm, ∼411.5 nm, ∼420 nm, and ∼427 nm as the TA/SC ratio increased from 0.005/1 to 1/1. (C) Size distribution measured by DLS of Ag NPs obtained using different TA to SC ratios. Mean particle diameter increases from 13.8 to 18.2 nm, 34.5 nm, 43.6 nm, and 58.0 nm as the concentration of TA increased from 0.025 mM (0.005/1) to 5 mM (1/1) ([SC] = 5 mM).

same vessel, seed solution was diluted by extracting 19.5 mL of sample and adding 16.5 mL of Milli-Q-water. Then, the temperature of the solution was set to 90 °C and 500 μL of SC (25 mM), 1.5 mL of TA (2.5 mM), and 1 mL of AgNO₃ were sequentially injected (time delay ∼ 1 min). After 20−30 min, an aliquot of 0.5 mL was extracted for further characterization. This solution was then used as a seed solution, and the process was repeated again. By repeating and adjusting the amount of Ag precursor injected, different generations of Ag NPs of progressively larger sizes were grown. By adjusting the volume extracted in each growth step, it is possible to tune the seed particle concentration and therefore the growth rate. Aliquots were purified by centrifugation (from 6000g to 18000g, depending on its size) in order to remove the excess of TA and further redispersed Milli-Q-water or SC 2.2 mM before sample characterization.

Conjugation of Silver Nanoparticles with NH₂-PEG. Ag NPs (19.7 nm, 53.2 nm, and 103.1 nm) were synthesized as described above. Then, aliquots of 2 mL were purified by centrifugation (18000, 10000, and 6000 g during 20 min) and further redispersed in 2.2 mM SC. For ligand exchange, an aqueous solution of amino-modified poly(ethylene glycol) (NH₂-PEG-COOH) (MW = 3400 kDa) was added to the Ag NP solution at 5 mM final concentration and stirred for 12 h at room temperature. Then, Ag NPs were washed again and further redispersed in the same volume of SC 2.2 mM.

Conjugation of Silver Nanoparticles with Polyvinylpyrrolidone. Ag NPs (∼31 nm, 7.5×10^{11} NPs/mL) were synthesized with the method described previously. Then, two aliquots of 1 mL each were purified by centrifugation at 8000 rpm during 20 min. One of the aliquots was redispersed in sodium citrate (SC) 2.2 mM while the other was redispersed in a fresh solution of 5 mM polyvinylpyrrolidone (PVP, MW = 55,000 kDa) and left during 72 h under vigorous stirring. Then, the Ag NPs were washed again in order to eliminate the excess of PVP for a further redispersion in SC 2.2 mM. Thus, we obtained two different conjugated Ag NPs: sodium citrate/tannic acid Ag NPs (SC/TA-Ag NPs) and PVP-Ag NPs.

Catalytic Reaction. The standard catalytic test reaction was carried out with 4.5 mL PS-disposable cuvettes. The NaBH₄ solution (100 mM) was freshly prepared before each set of kinetic trials. Experimentally, 2 mL of Milli-Q-water, 50 μL of a Rhodamine B solution (0.5 mM), and 50 μL of an aqueous solution containing Ag NPs (SC/TA-Ag NPs or PVP-Ag NPs) (∼31 nm, 7.5×10^{11} NPs/ mL) were sequentially added into a PS-disposable. Then, the NaBH₄ was injected into the cuvette to start the reaction, and the intensity of the absorption peak at 554 nm was monitored by UV−vis spectroscopy as a function of time (15 runs, 120 s each). The experiments were carried out by triplicate in order to evaluate the reproducibility.

Calculation of Kinetic Rate Constants. The data were analyzed according to the first-order rate law. The negative natural logarithm of the absorbance at 554 nm was plotted against time, and the steepest part of the curve was fit with a line, the slope of which was considered the rate constant k.

Techniques. *UV−Vis Spectroscopy.* UV−visible spectra were acquired with a Shimadzu UV-2400 spectrophotometer. An Ag NP solution was placed in a cell, and spectral analysis was performed in the 300−800 nm range at room temperature. In the case of time-dependent measures, aliquots of the solution were taken out and samples were cooled in ice water to quench the reaction.

Transmission Electron Microscopy. Ag NPs were visualized using 80 keV TEM (Jeol 1010, Japan). Ten microliter droplets of the sample were drop cast onto a piece of ultrathin Formvar-coated 200-mesh copper grid (Ted-pella, Inc.) and left to dry in air. TEM images of the prepared colloidal Ag NPs were used for the size distribution measurements. For each sample, the size of at least 500 particles was measured and the average size and standard deviation obtained.

Dynamic Light Scattering. A Malvern ZetaSizer Nano ZS instrument (Malvern Instruments, U.K.) operating at a light source wavelength of 532 nm and a fixed scattering angle of 173° was used to measure Ag NP size. One milliliter of the Ag NPs was placed in a cell,

Table 1. Summary of Sizes and Optical Properties of the Ag NPs Obtained after Different Growth Steps[a]

sample	TEM size	SD (%)	SPR peak	DLS size (intensity)[b]	expected diameter
seeds	10.3 ± 1.0 nm	9.7	~397 nm	12.7 ± 1.4 nm	------
g-01	12.1 ± 1.2 nm	10	~397.5 nm	13.2 ± 1.4 nm	12.0 nm
g-02	13.0 ± 1.1 nm	8.4	~399 nm	14.6 ± 1.8 nm	13.5 nm
g-03	14.2 ± 1.3 nm	9.1	~399.5 nm	15.4 ± 1.4 nm	14.6 nm
g-04	15.1 ± 1.4 nm	9.8	~400 nm	19.2 ± 1.6 nm	15.6 nm
g-06	17.3 ± 1.7 nm	9.8	~401 nm	23.7 ± 1.5 nm	17.4 nm
g-07	18.1 ± 1.7 nm	9.4	~401.5 nm	24.8 ± 1.9 nm	18.2 nm
g-08	19.0 ± 1.9 nm	10	~402 nm	25.9 + 1.8 nm	18.9 nm
g-09	19.9 ± 1.9 nm	9.5	~402.5 nm	27.3 ± 2.1 nm	19.6 nm

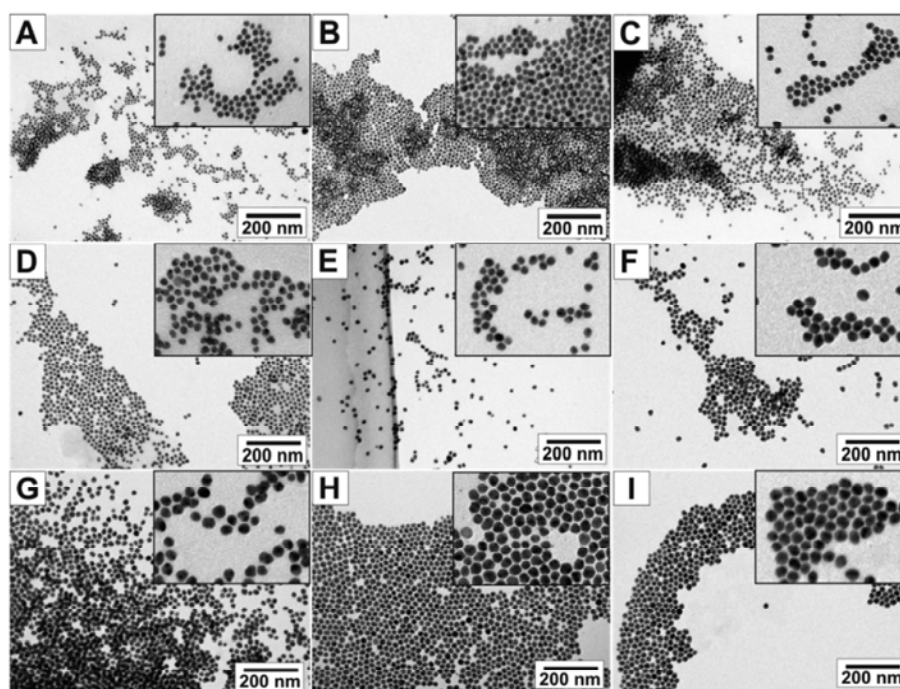[a]g stands for generation. [b]Mean and SD from three independent runs.

Figure 2. Seeded-growth synthesis of silver nanoparticles from 10 to 20 nm. Transmission electron microscopy images of seed particles and those obtained after 1, 2, 3, 4, 6, 7, 8, and 9 growth steps. (A) 10.3 ± 1.0 nm, (B) 12.1 ± 1.2 nm, (C) 13.0 ± 1.1 nm, (D) 14.2 ± 1.3 nm, (E) 15.1 ± 1.4 nm, (F) 17.3 ± 1.7 nm, (G) 18.1 ± 1.7 nm, (H) 19.0 ± 1.9 nm, (I) 19.9 ± 1.9 nm.

and DLS analyses were performed. Measurements were conducted in a 1 cm optical path cell with precise control of temperature (25 °C).

■ RESULTS AND DISCUSSION

Effect of Tannic Acid in the Final Morphology of Ag NPs. Colloidal solutions of Ag NPs were prepared by reducing an aqueous solution of $AgNO_3$ with a mixture of two reducing agents, sodium citrate (SC) and tannic acid (TA). In a typical synthesis, an aqueous solution of $Ag NO_3$ (1 mL, 25 mM) was injected into a boiling solution of Milli-Q-water (100 mL) containing the mixture of SC and TA. After the addition of Ag precursor, the solution changed its color from transparent to dark yellow within minutes, indicating the presence of Ag NPs. Resultant NPs were purified by centrifugation and further redispersed in 2.2 mM sodium citrate (SC). Samples were systematically characterized by transmission electron microscopy (TEM), UV−vis spectroscopy, and dynamic light scattering (DLS).

Figure 1A shows representative TEM images of roughly spherical Ag NPs prepared by using increasing amounts of TA.

Final Ag NP's size depends on the concentration of TA, obtaining larger sizes (from 10.1 ± 0.9 nm to 46.1 ± 8.3 nm) for increasing concentrations of TA (from 0.025 mM to 5 mM), corresponding to TA/SC ratios from 0.005/1 to 1/1. Interestingly, the addition of small amounts of TA narrows the size distribution of Ag NPs (Figure S1 of the Supporting Information). The degree of monodispersity also depends on the amount of TA used, observing that smaller NPs present a narrower size distribution (8.9%) than larger ones (18%) (Figure S2). Optical characterization of samples by means of UV−vis spectroscopy confirms these results (Figure 1B), showing red-shifts from ~397 nm to ~427 nm. Size distribution profiles measured by DLS (Figure 1C and Figure S3) confirm the increase of the mean particle diameter from 13.8 to 58.0 nm (note that size distribution by intensity is given). Similar results were reported by Dadosh[33] for the production of Ag NPs with restricted size ranges between 10 and 30 nm that were, for kinetics reasons, more polydisperse. Additionally, such a strategy cannot be extended to the production of larger Ag NPs (from 40 to 200 nm) due to
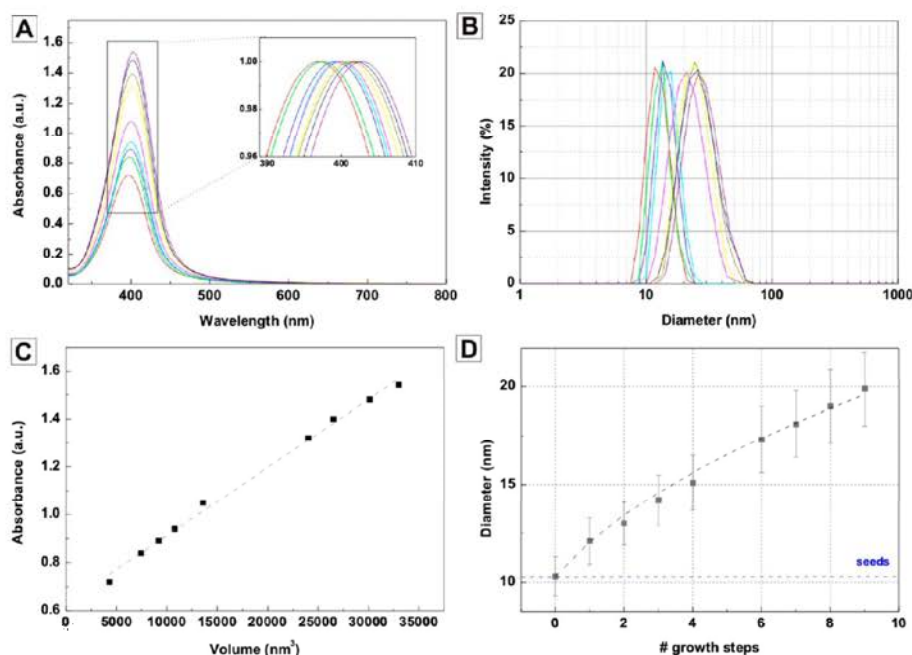
Figure 3. Absorption spectra of Ag colloids obtained after different growth steps (A). From left to right, spectra correspond to colloidal solutions of Ag NPs with increasing diameters shown in Figure 2. The dependence of the SPR peak with Ag NP's size is shown in the inset plot, where spectra are normalized in order to facilitate comparison. Size distribution determined by dynamic light scattering (B). Size distribution by intensity shows monomodal curves with increasing mean particle diameter from 12.7 ± 1.4 nm to 27.3 ± 2.1 nm, as the number of growth steps increased. Maximum absorbance intensity as a function of Ag NP's volume for different generations of Ag NPs (C). The linear dependence is in agreement with results predicted by Mie theory and a further indication that number of Au NPs was constant during the entire growth process and no new nucleation occurred. Average diameter of Ag NPs obtained after several growth steps and comparison with the expected results (D). The blue-dashed line corresponds to the size of the initial Ag seed particles used (10.3 ± 1.0 nm). Obtained results fit with those calculated, and indicate not only that injected Ag atoms deposited onto the surfaces of the preformed particles but also that the use of TA leads to very high reaction yields.

multiple nucleation events, growth limitations, and compromised colloidal stability. Details about the effect of TA in the final morphology of Ag NPs, the reduction mechanism of Ag ions by TA, and the formation mechanisms of Ag NPs, including time-evolution of UV−vis spectra, DLS analysis, and TEM characterization, can be found in the Supporting Information (Figure S1−4 and Scheme 1).

Seeded-Growth Synthesis of Ag NPs from 10 to 20 nm with Nanometric Growth Resolution. Given the limitations in controlling Ag NP's morphology by modifying the concentration of TA, we studied the possibility of tuning Ag NP's size by growing successive generations of spherical Ag NPs using the above synthesized 10 nm Ag NPs as seeds. The presence of Ag seeds favors the catalytic reduction of Ag precursor, promoting their growth and therefore the precise (nanometric) control of Ag NP's size. The study of reaction conditions allowing kinetic control of the seeded-growth process, that is providing enough precursor for homogeneous and significant growth while avoiding new nucleation,[14] includes the following: (i) the decrease of the temperature to 90 °C, (ii) the adjustment of the pH of the solution close to neutral values by adding controlled concentrations of sodium citrate, and (iii) the precise control of the ratio between the silver precursor injected and the number of seed particles in solution. Moreover, another aspect of crucial importance in controlling Ag NP's morphology is the concentration of TA added in each growth step. Thus, it has to be adjusted to be high enough to induce the fast reduction of the Ag ions for homogeneous growth while suppressing new nucleation of Ag

NPs, and low enough to avoid the formation of intermediate complexes which are responsible for inhomogeneous particle growth. Thus, the concentration of TA used in each growth step was experimentally determined to promote the homogeneous growth of Ag NP's.

Therefore, in order to obtain successive generations of highly monodisperse Ag NPs larger in size, silver seeds (10.3 ± 1.0 nm, $\sim 6 \times 10^{12}$ NPs/mL) were prepared as previously described. When the reaction was finished, the solution was cooled down to 90 °C. Then, 100 μL of SC (25 mM), 250 μL of TA (2.5 mM), and 250 μL of $AgNO_3$ were sequentially injected (time delay ~ 1 min) and the reaction was run for 15 min. By repeating this process and adjusting the amount of silver precursor injected, the size of the final Ag NPs was precisely controlled (Table 1). Aliquots were purified by centrifugation in order to remove the excess of TA and further redispersed in 2.2 mM SC before sample characterization.

Figure 2 displays TEM images of Ag NPs obtained after different growth steps with 1 nm growth resolution. The Ag NPs synthesized in the above manner exhibit high uniformity in size, shape, and crystallinity. By systematically measuring at least 500 Ag NPs for each sample, we statistically obtained the size distribution of the products showing that Ag NPs are highly uniform with standard deviation less than 10% (Figure S5). Optical properties and size distribution profiles measured by DLS confirmed the above obtained results (Figure 3A and B). Absorption spectra show a rather symmetric surface plasmon absorption band, which red-shifts from ~ 397 nm to ~ 402.5 nm (inset of Figure 3A) and increases in intensity as a

2840

dx.doi.org/10.1021/cm500316k | Chem. Mater. 2014, 26, 2836−2846

- 97 -

Table 2. Summary of Sizes and Optical Properties of the Ag NPs Obtained after Different Growth Steps[a]

	TEM	SD (%)	conc (NPs/mL)	SPR dipolar	SPR quadrupolar	intensity[b]	expected diameter
G00	14.8 ± 1.4 nm	9.5	~2.3 × 10¹²	~401 nm	--------	20.9 ± 3.2 nm	
G01	19.7 ± 1.9 nm	9.6	~1.8 × 10¹²	~404 nm	--------	27.7 ± 2.2 nm	19.5 nm
G02	24.0 ± 3.0 nm	12.5	~1.5 × 10¹²	~408 nm	--------	32.8 ± 0.9 nm	23.3 nm
G03	28.0 ± 2.3 nm	8.2	~1.2 × l0¹²	~411.5 nm	--------	36.0 ± 0.9 nm	26.8 nm
G04	29.8 ± 2.4 nm	8.0	~9.4 × 10¹¹	~416 nm	--------	39.6 ± 1.1 nm	30.2 nm
G05	31.6 ± 2.8 nm	8.8	~7.5 × 10¹¹	~418.5 nm	--------	44.1 ± 3.9 nm	33.6 nm
G06	37.0 ± 2.5 nm	6.8	~6.0 × 10¹¹	~421 nm	--------	48.6 ± 1.1 nm	36.9 nm
G07	41.2 ± 2.8 nm	6.8	~4.8 × 10¹¹	~425 nm	--------	52.3 ± 1.8 nm	40.5 nm
G08	44.0 ± 3.1 nm	7.0	~3.9 × 10¹¹	~427.5 nm	--------	56.2 ± 0.9 nm	44.2 nm
G09	47.9 ± 3.7 nm	7.7	~3.1 × 10¹¹	~430 nm	--------	62.6 +1.1 nm	48.1 nm
G10	53.2 ± 3.3 nm	6.2	~2.5 × 10¹¹	~432 nm	--------	68.3 ± 0.7 nm	52.3 nm
G11	55.8 ± 4.1 nm	7.3	~2.0 × 10¹¹	~438 nm	--------	73.7 ± 0.4 nm	56.7 nm
G12	60.8 ± 4.1 nm	6.7	~1.6 × 10¹¹	~442 nm	--------	79.2 ± 0.5 nm	61.4 nm
G13	66.6 ± 3.8 nm	5.7	~1.3 × 10¹¹	~446 nm	--------	84.9 ± 1.0 nm	68.2 nm
G14	71.4 ± 5.5 nm	7.7	~1.0 × 10¹¹	~452 nm	--------	91.4 ± 2.1 nm	75.1 nm
G15	79.0 ± 5.1 nm	6.5	~8.1 × 10¹⁰	~460 nm	--------	98.3 ± 1.0 nm	82.3 nm
G16	87.5 ± 5.6 nm	6.4	~6.5 × 10¹⁰	~ 471 nm	~ 405 nm	102.6 ± 1.0 nm	89.8 nm
G17	103.1 ± 7.4 nm	7.2	~5.2 × 10¹⁰	~482.5 nm	~408 nm	116.5 ± 0.5 nm	102.2 nm
G18	113.3 ± 7.8 nm	6.9	~4.1 × 10¹⁰	~496 nm	~413 nm	128.8 ± 0.9 nm	112.5 nm
G19	127.1 ± 9.7 nm	7.6	~3.3 × 10¹⁰	~508 nm	~420 nm	152.9 ± 1.1 nm	123.2 nm
G20	134.8 ± 8.8 nm	6.5	~2.6 × 10¹⁰	~527 nm	~423.5 nm	176.2 ± 1.4 nm	134.3 nm
G21	146.5 ± 11.2 nm	7.7	~2.1 × 10¹⁰	~565 nm	~434.5 nm	196.0 ± 4.2 nm	146.0 nm
G22	162.8 ± 10.6 nm	6.5	~1.7 × 10¹⁰	~603 nm	~445 nm	208.1 ± 2.7 nm	167.6 nm
G23	176.6 ± 14.2 nm	8.0	~1.3 × 10¹⁰	~644 nm	~457.5 nm	245.1 ± 4.7 nm	188.5 nm
G24	189.4 ± 13.4 nm	7.0	~1.1 × 10¹⁰	~715 nm	~467.5 nm	266.7 ± 2.9 nm	198.1 nm

[a]G stands for generation. [b]Mean and SD from three independent runs.

consequence of particle growth. The high uniformity of the resultant NPs is translated into narrow absorption peaks (full width at half-maximum (FWMH) ~58 nm) which did not broaden as the particle's size increased. Moreover, the maximum absorbance intensity linearly depends on Ag NP's volume (Figure 3C), in agreement with results predicted by Mie theory and with those previously reported by other groups,[33] which indicates uniform growth and the absence of new nucleation. These results are further evidence that the number of particles stays constant during the entire growth process, and the Ag atoms injected in the solution were deposited onto the surface of the seed particles, leading to large and highly monodisperse Ag NPs while avoiding new nucleation. Similarly, the size distribution of NPs synthesized after different growth steps shows increasing hydrodynamic sizes, from ~12.7 nm to ~27.3 nm (Figure 3B, Figure S6) with distributions that are monomodal, confirming that neither secondary nucleation nor aggregation of Ag NPs occurred. Consequently, Ag NP's size can be predicted by (i) knowing the seed particle diameter and concentration, (ii) knowing the amount of silver precursor added in each growth step, and assuming a complete consumption of precursor with no formation of new particles. Figure 3D shows the calculated curve of Ag NP's diameter for the conditions used in the experiment, where it can be observed how expected results fit perfectly with those obtained experimentally, confirming the previous assumptions.

Besides, as the growth of Ag NPs is determined by the ratio between silver atoms added in each growth step and seeds present in the reaction solution, the growth rate drastically decreases as the particles become larger. This problem cannot be solved by injecting higher amounts of silver precursor, since it broadens the size distribution of particles and/or induces the

nucleation of new Ag NPs.[14] Therefore, the concentration of Ag seeds has to be reduced.

Seeded-Growth Synthesis of Ag NPs from 15 to 200 nm. Thus, to obtain larger and highly monodisperse Ag NPs, we studied the possibility to grow successive generations of spherical particles by adjusting both the seed particle concentration and the total number of silver atoms injected into the solution in each growth step. Morphological and optical properties of different generations of Ag NPs of progressively larger sizes are summarized in Table 2.

The morphology of the resultant Ag NPs was assessed by TEM (Figure 4), obtaining sizes ranging from 19.7 ± 1.9 nm (G1) to 189.4 ± 13.4 nm (G24). Independently from their size, Ag NPs exhibit high uniformity with standard deviations below 10% (Figure S7).

Similar size distribution profiles were measured by DLS, obtaining monomodal curves with increasing mean particle diameters from 20.9 ± 3.2 nm to 266.7 ± 2.9 nm (Figure 5A). Here again, the calculated curve of the Ag NP's diameter for the conditions used in the experiment perfectly fits with those obtained experimentally (Figure 5B), confirming the growth model, that is, the absence of new nucleation and the high reaction yields.

As shown in Figure 5C, the growth of Ag NPs led to color changes from yellow to dark gray. Colloidal solutions of small particles appear yellow and totally transparent while, in larger particles, increased opalescence can be observed, as the resonant scattering contribution of the multipole resonance becomes a dominating spectral component. The optical properties of selected generations of Ag NP solutions, measured by UV−Vis spectroscopy, are depicted in Figure 5D, where it can be seen how obtained values agree well with the expected changes in optical behavior for increasing Ag NP's
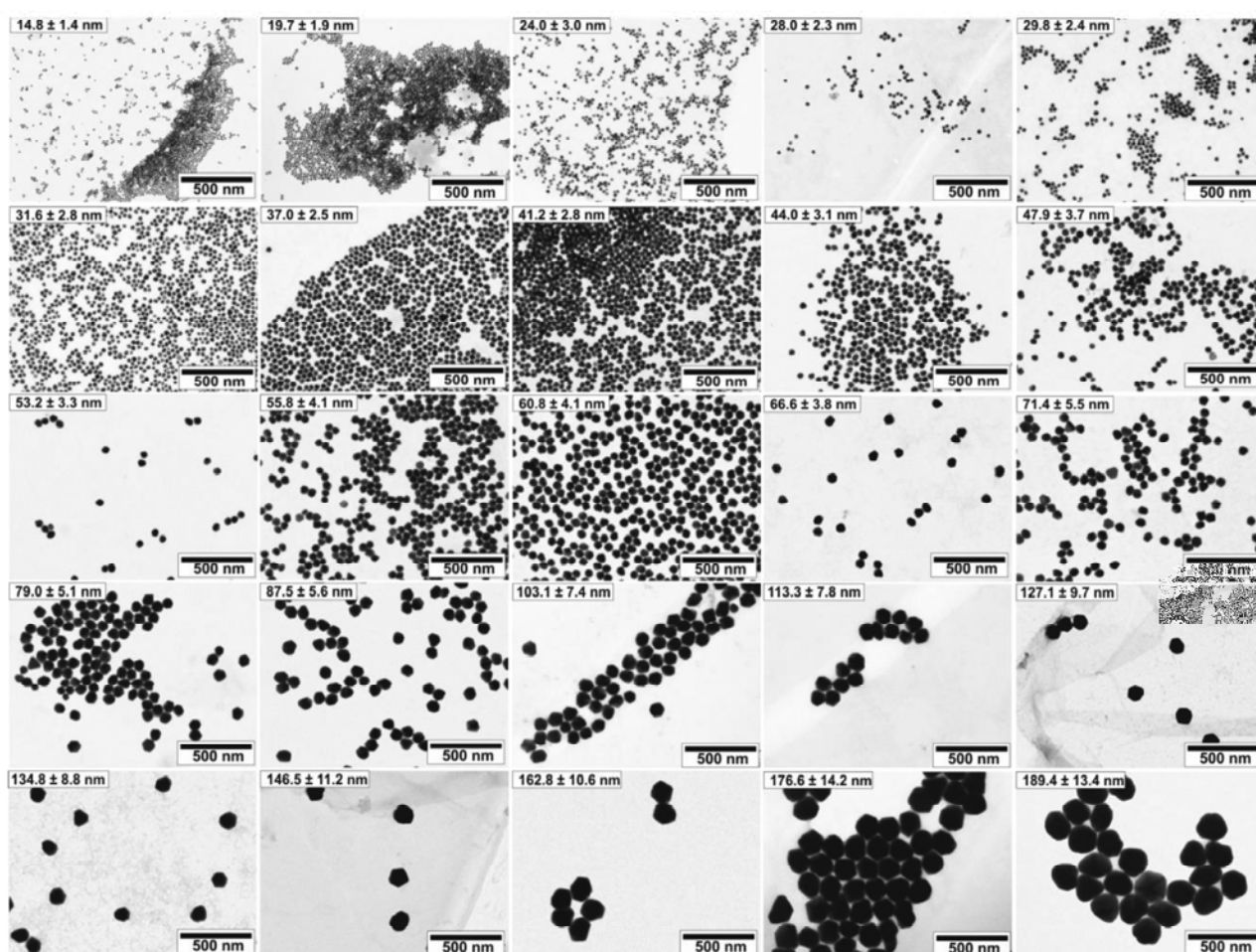
2841

dx.doi.org/10.1021/cm500316k | Chem. Mater. 2014, 26, 2836−2846

Figure 4. Seeded-growth synthesis of silver nanoparticles. Transmission electron microscopy images of seed particles and those obtained after different growth steps. The particle size increases from 14.8 ± 1.4 nm to 189.4 ± 13.4 nm, and its concentration decreases from ~ 2.3 × 10^{12} to ~ 1.1 × 10^{10} NPs/mL.

sizes, i.e., the red-shift of the SPR peak as particle size increases. Thus, starting from the peak position around 400 nm, typical of the plasmon resonance of ~15 nm Ag NPs, it red-shifts to longer wavelengths, peaking at ~416 nm for Ag NPs with an average diameter of ~30 nm. When Ag NP's size further increases, the main dipolar resonance band red-shifts and broadens, peaking at ~432 nm for Ag NPs with an average diameter of ~53 nm. Above this size, a new peak started to develop at shorter wavelengths, at ~410 nm, characteristic of the quadrupole component of the plasmon resonance for Ag NPs of 103.1 nm in diameter, which broadens and red-shifts to ~434.5 nm as the size of the Ag NPs increases up to 146.5 nm. Experimental absorbance was compared to calculations based on the standard Mie theory of spherical particles using MiePlot software. Figure S8 plots the extinction spectra (containing both absorption and scattering contributions) calculated for Ag spheres. Three different sizes of 53.2 nm, 103.1 nm, and 146.5 nm have been selected. Calculations include the monodisperse case (SD = 0%) and the standard distribution experimentally measured from TEM (SD < 10%). Although obtained results are in quite good agreement with those experimentally measured, significant differences were found in the case of small Ag NPs, where Mie theory fails to explain the dependence

of the surface plasmon absorption band on Ag NP's size due to the size-dependent Ag NP dielectric function.[34,35]

Long-Term Stability and Functionalization of Ag NPs. One of the most important advantages of the synthetic strategy herein described is the possibility to produce aqueous solutions of long-term stable Ag NPs with readily accessible and reactive surfaces that allow an easy further functionalization. In comparison with other synthetic strategies widely reported in the literature, which use long water-soluble polymeric surfactants such as PVP, SC is a labile capping agent which can be easily displaced by other molecules. This is of relevant importance in diffusion processes, such as catalysis, where the precise control of the Ag NPs surface chemistry is of fundamental importance in the development of improved catalysts.[36]

Long-term stability against aggregation has been proved by recording UV−vis spectra of Ag NPs of different selected sizes (19.7 nm, 53.2 nm, and 103.1 nm) at different times: immediately after synthesis and 7 weeks later. Samples were stored at room temperature and dark conditions. Results in Figure 6A−C show how UV−vis spectra perfectly overlap, which is indicative of a strong stability against aggregation and/ or chemical dissolution. It is important to note that, despite the excellent dispersibility and stability of the colloids, they slowly
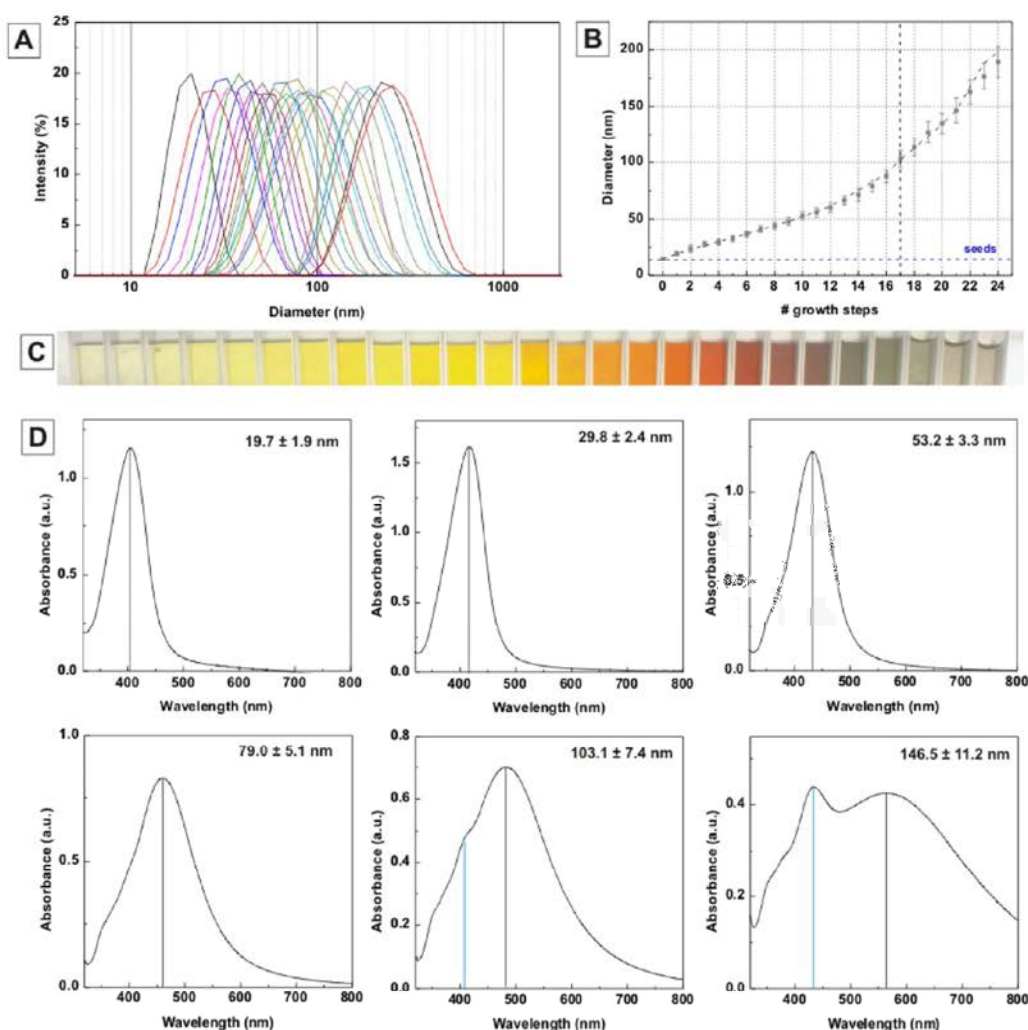
Figure 5. (A) Size distribution profiles measured by dynamic light scattering of Ag colloids obtained after different growth steps. Size distribution by intensity shows monomodal curves with increasing mean particle diameters from 20.9 ± 3.2 nm to 266.7 ± 2.9 nm with increase of the number of growth steps, from 1st to 24th (from left to right). (B) Average diameter of Ag NPs obtained after several growth steps and comparison with the expected results. The blue-dashed line corresponds to the size of the initial Ag seed particles used (14.8 ± 1.4 nm). The black-dashed vertical line indicates a change in the total Ag mass added in the growth process. In detail, 1 mL of Ag NO_3 was injected from the 1st to 17th growth steps while this amount was increased to 1.5 mL from the 17th to 24th growth steps. Obtained results fit with those calculated, which indicates that no nucleation occurred and the Ag atoms deposited onto the surfaces of the preformed particles. (C) Colloidal solutions of Ag NPs of increasing sizes (from left to right). Colloidal solutions of small Ag NPs particles appear yellow and totally transparent, as the absorption contribution of the dipole resonance dominates the extinction spectrum. For larger particles, increased opalescence can be observed, as the resonant scattering contribution of the multipole resonance becomes a dominating spectral component. (D) Optical properties of Ag NPs synthesized. UV−vis spectra of selected Ag colloids obtained after different growth steps. Black/blue lines indicate the position of the dipolar/quadrupolar band.

sediment due to gravitational forces, with a settling time and sedimentation rate that depend on particle size and that can be calculated by using Stokes' law.[37,38] Thus, we observed how very large Ag NPs (150−200 nm) completely sediment in few days while Ag NPs in the range of 60 to 80 nm needed weeks to sediment. Importantly, this sedimentation is reversible, i.e., a hand shake of Ag colloids restores the initial as-synthesized conditions, which indicates that particles did not aggregate, but rather sediment as single particles. The possibility of functionalization has been proved by studying the ligand exchange of as-synthesized Ag NPs with an amino-terminated PEG molecule (NH$_2$-PEG), which has a well-known affinity for Ag.[39] Ligand exchange was performed by adding known amounts of NH$_2$-PEG molecules to as-synthesized (purified)

Ag NPs solutions under vigorous stirring. The mixture was allowed to react for 12 h, and PEG-modified Ag NPs were then centrifuged to remove the excess of NH$_2$-PEG molecules. The ligand exchange is a spontaneous process because the amino groups form stronger bonds with Ag surfaces than the COOH/OH groups in the original citrate/tannic molecules.[39] Figure 6D−F presents the absorption spectra of Ag NPs with different sizes before and after the ligand exchange process. Once the native molecules are replaced by NH$_2$-PEG molecules, the corresponding absorption peak shifts to the red. Functionalization has also been extended to well-known surfactants, such as PVP, and proteins, such as bovine serum albumin (BSA), obtaining similar conjugation profiles (Figure S9).
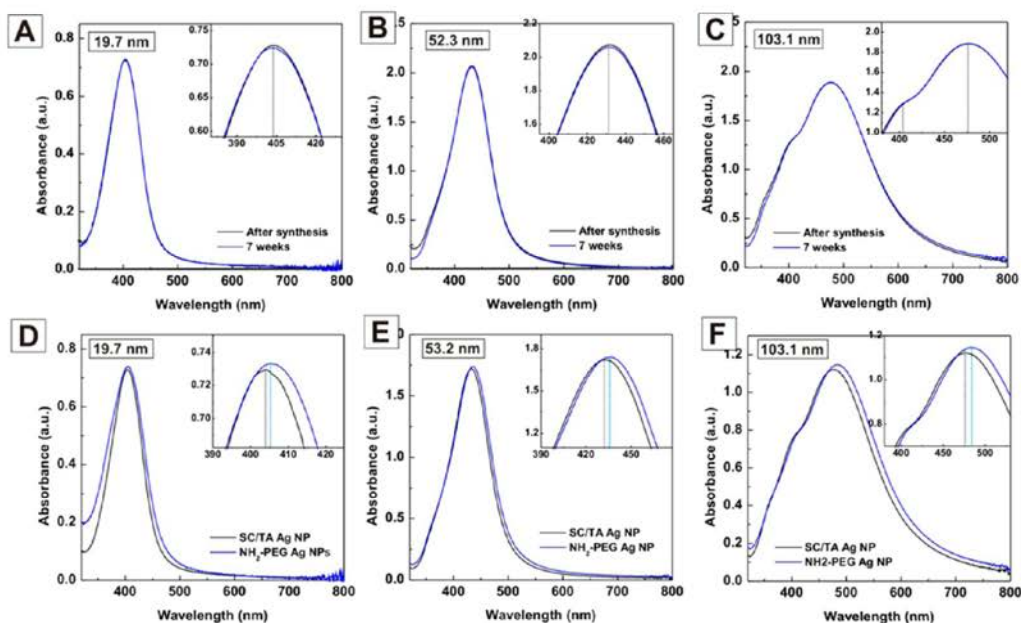
Figure 6. Long-term stability of Ag NPs. UV−vis spectra of Ag NPs of different sizes, 19.7 nm (A), 53.2 nm (B), and 103.1 nm (C), recorded at different times: immediately after synthesis (black line) and (ii) 7 weeks after (blue line). The perfect overlapping is indicative of an improved stability against long-term aggregation and/or chemical dissolution. Functionalization of as-synthesized Ag NPs with amino-terminated PEG. UV−vis spectra of Ag NPs of different sizes, 19.7 nm (D), 53.2 nm (E), and 103.1 nm (F), recorded after (blue line) and before (black line) the ligand exchange process. Once the native molecules are replaced by NH_2-PEG molecules, the corresponding absorption peak shifts to the red, which is indicative of the successful Ag NP's functionalization.
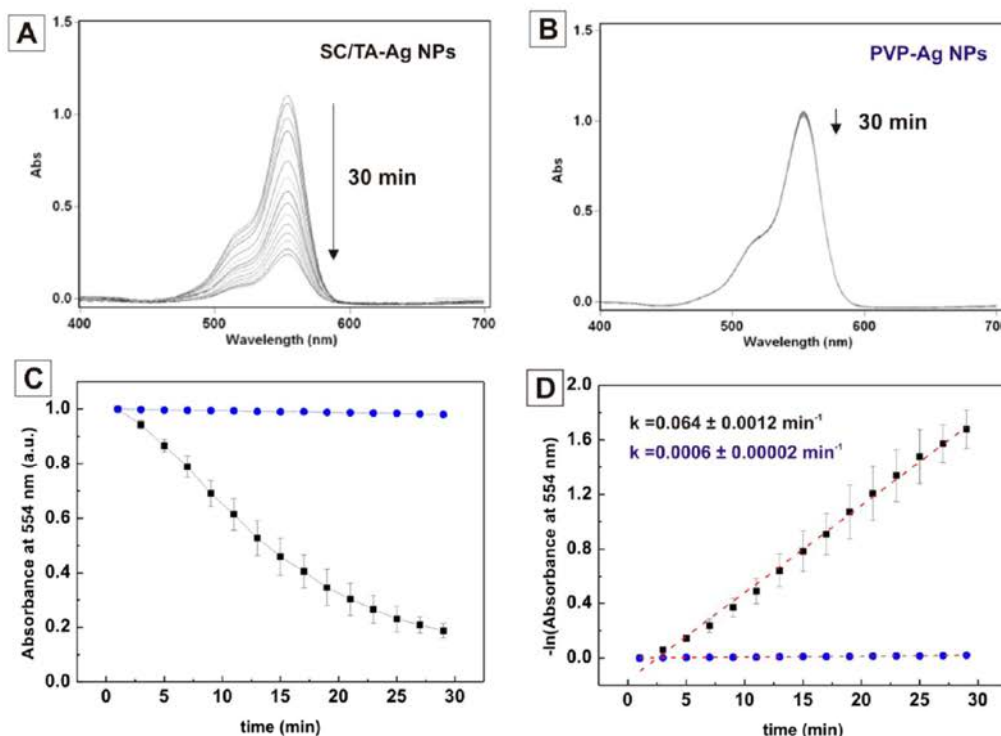
Figure 7. Catalytic properties of as-synthesized SC/TA-stabilized Ag NPs and PVP-coated Ag NPs. Decrease in Rhodamine B concentration over time using SC/TA- stabilized Ag NPs (A) and PVP-coated Ag NPs (B) catalysts. (C) Normalized kinetic trace of the absorbance at 554 nm during the reduction of Rhodamine B. (D) Kinetic rate constants. The negative natural log of the absorbance at 554 nm was plotted against time, and the steepest part of the curve was fit with a linear fit, the slope of which was considered the rate constant k. The reproducibility of the experiment was repeated by triplicate.

Catalytic Properties of Ag NPs: Influence of Ag NP's Coating Molecule. In order to prove the influence of the coating molecules in the reactivity of metal NPs, Ag NPs were used as catalysts in the electron-transfer reaction between Rhodamine B (RhB) and borohydride ions. In the presence of Ag NPs, the reaction proceeds through a two-step process. First, borohydride injects electrons on the particles, which act as a reservoir, whereas in the second and slow step, RhB diffuses toward the Ag NP's surface and is reduced by the excess surface electrons. Two different samples were studied: as-synthesized SC/TA-stabilized Ag NPs and PVP-coated Ag NPs. In both cases the metallic Ag NPs were identical and only the Ag NP's surface was modified. After studying the parameters affecting the reaction, we selected the conditions (in terms of Ag NPs/RhB ratios, reaction time, and type of catalyzed molecule) to evaluate the effect of the surface coating on the catalytic activity of Ag NPs, especially due to mass transport through the surfactant layer. Obviously, as recently reported,[40] a higher NP's concentration (or NPs/RhB ratios) leads to the rapid degradation of RhB molecules. Besides, surface oxidation effects could be discarded, since no variation was observed by UV–vis spectroscopy, very sensitive to Ag NP's surface state, DLS, or ξ-potential.

The progress of the reduction was monitored through changes in the UV–vis spectrum of RhB using as-synthesized SC/TA-stabilized Ag NPs (Figure 7A) and PVP-coated Ag NPs (Figure 7B) as catalyst. As can be seen, under the experimental conditions used, SC/TA-stabilized Ag NPs are able to catalyze RhB degradation in 30 min. Thus, the characteristic absorption band at 554 nm was observed to decrease with time as reduction proceeded, offering a good correlation with first-order kinetics (Figure 7C). Oppositely, PVP-coated Ag NPs are not able to efficiently catalyze the reduction reaction, which is translated into a very low reaction rate constant, 2 orders of magnitude lower than that obtained for SC/TA-stabilized Ag NPs (Figure 7D). This dramatic decrease of the catalytic efficiency of PVP-stabilized Ag NPs can be explained in terms of the density and robustness of the coating layer, since PVP is a long bulky polymer that impedes the diffusion of reactant molecules toward the catalytic Ag core.

CONCLUSION

In summary, we show the possibility to synthesize highly monodisperse and long-term stable and functionalizable Ag NPs from 10 to 200 nm by the precise kinetic control of the reaction, in particular the use of two reducing agents, the temperature of the solution, and the Ag seeds to Ag precursor ratio. The slow complexation of Ag^+ ions by tannic acid allows the control of reduction kinetics, in particular, the fast nucleation of a controlled number of Ag seeds, whose size is determined by the substoichiometric amounts of TA, and its further homogeneous growth. Besides, obtained results also evidence the very high yield of the reaction in the presence of TA, close to 100%; otherwise, the model would not fit with the experimental results found.

We also show how the catalytic activity of the Ag NPs is affected by the composition of the organic shell and therefore by the surfactant used in the synthetic process. This is explained in terms of the density and robustness of the coating layer, since the use of long polymers impedes the diffusion of reactant molecules toward the catalytic Ag core.

ASSOCIATED CONTENT

S **Supporting Information**

Effect of tannic acid on the final morphology of Ag NPs, kinetics of the reduction reaction, formation mechanism of Ag nanoparticles, calculated Mie spectra, and ligand exchange of Ag nanoparticles. This material is available free of charge via the Internet at http://pubs.acs.org.

AUTHOR INFORMATION

Corresponding Author
*E-mail: neus.bastus@icn.cat, victor.puntes@icn.cat.

Notes
The authors declare no competing financial interest.

ACKNOWLEDGMENTS

REFERENCES

(1) Rycenga, M.; Cobley, C. M.; Zeng, J.; Li, W.; Moran, C. H.; Zhang, Q.; Qin, D.; Xia, Y. *Chem. Rev.* **2011**, *111*, 3669.
(2) Jain, P.; Huang, X.; El-Sayed, I.; El-Sayed, M. *Plasmonics* **2007**, *2*, 107.
(3) Kneipp, K.; Wang, Y.; Kneipp, H.; Perelman, L. T.; Itzkan, I.; Dasari, R. R.; Feld, M. S. *Phys. Rev. Lett.* **1997**, *78*, 1667.
(4) Nie, S.; Emory, S. R. *Science* **1997**, *275*, 1102.
(5) Liu, J.; Sonshine, D. A.; Shervani, S.; Hurt, R. H. *ACS Nano* **2010**, *4*, 6903.
(6) Sondi, I.; Goia, D. V.; Matijević, E. *J. Colloid Interface Sci.* **2003**, *260*, 75.
(7) Creighton, J. A.; Blatchford, C. G.; Albrecht, M. G. *J. Chem. Soc., Faraday Trans. 2* **1979**, *75*, 790.
(8) Zeng, J.; Zheng, Y.; Rycenga, M.; Tao, J.; Li, Z.-Y.; Zhang, Q.; Zhu, Y.; Xia, Y. *J. Am. Chem. Soc.* **2010**, *132*, 8552.
(9) Evanoff, D. D.; Chumanov, G. *J. Phys. Chem. B* **2004**, *108*, 13948.
(10) Li, H.; Xia, H.; Wang, D.; Tao, X. *Langmuir* **2013**, *29*, 5074.
(11) Grzelczak, M.; Perez-Juste, J.; Mulvaney, P.; Liz-Marzan, L. M. *Chem. Soc. Rev.* **2008**, *37*, 1783.
(12) Jana, N. R.; Gearheart, L.; Murphy, C. J. *Langmuir* **2001**, *17*, 6782.
(13) Rodríguez-Fernández, J.; Pérez-Juste, J.; García de Abajo, F. J.; Liz-Marzán, L. M. *Langmuir* **2006**, *22*, 7007.
(14) Bastús, N. G.; Comenge, J.; Puntes, V. F. *Langmuir* **2011**, *27*, 11098.
(15) Lee, P. C.; Meisel, D. *J. Phys. Chem.* **1982**, *86*, 3391.
(16) Samal, A. K.; Polavarapu, L.; Rodal-Cedeira, S.; Liz-Marzán, L. M.; Pérez-Juste, J.; Pastoriza-Santos, I. *Langmuir* **2013**, *29*, 15076.
(17) Liu, X.; Yin, Y.; Gao, C. *Langmuir* **2013**, *29*, 10559.
(18) Zong, R.; Wang, X.; Shi, S.; Zhu, Y. *Phys. Chem. Chem. Phys.* **2014**, *16*, 4236−4241.
(19) Ojea-Jimenez, I.; Bastús, N. G.; Puntes, V. *J. Phys. Chem. C* **2011**, *115*, 15752.
(20) Janata, E.; Henglein, A.; Ershov, B. G. *J. Phys. Chem.* **1994**, *98*, 10888.
(21) Pillai, Z. S.; Kamat, P. V. *J. Phys. Chem. B* **2003**, *108*, 945.
(22) Dong, X.; Ji, X.; Wu, H.; Zhao, L.; Li, J.; Yang, W. *J. Phys. Chem. C* **2009**, *113*, 6573.
(23) Henglein, A.; Giersig, M. *J. Phys. Chem. B* **1999**, *103*, 9533.
(24) Xiong, Y.; Siekkinen, A. R.; Wang, J.; Yin, Y.; Kim, M. J.; Xia, Y. *J. Mater. Chem.* **2007**, *17*, 2600.
(25) González, E.; Arbiol, J.; Puntes, V. F. *Science* **2011**, *334*, 1377.
(26) Wiley, B.; Herricks, T.; Sun, Y.; Xia, Y. *Nano Lett.* **2004**, *4*, 1733.

(27) Wiley, B.; Sun, Y.; Mayers, B.; Xia, Y. *Chem.—Eur. J.* **2005**, *11*, 454.

(28) Xiong, Y.; Xia, Y. *Adv. Mater.* **2007**, *19*, 3385.

(29) Yi, Z.; Li, X.; Xu, X.; Luo, B.; Luo, J.; Wu, W.; Yi, Y.; Tang, Y. *Colloids Surf., A* **2011**, *392*, 131.

(30) Huang, X.; Wu, H.; Pu, S.; Zhang, W.; Liao, X.; Shi, B. *Green Chem.* **2011**, *13*, 950.

(31) Rainville, L.; Dorais, M.-C.; Boudreau, D. *RSC Adv.* **2013**, *3*, 13953.

(32) Casals, E.; Pfaller, T.; Duschl, A.; Oostingh, G. J.; Puntes, V. F. *Small* **2011**, *7*, 3479.

(33) Dadosh, T. *Mater. Lett.* **2009**, *63*, 2236.

(34) Kelly, K. L.; Coronado, E.; Zhao, L. L.; Schatz, G. C. *J. Phys. Chem. B* **2002**, *107*, 668.

(35) Zhao, J.; Pinchuk, A. O.; McMahon, J. M.; Li, S.; Ausman, L. K.; Atkinson, A. L.; Schatz, G. C. *Acc. Chem. Res.* **2008**, *41*, 1710.

(36) Li, Y.; El-Sayed, M. A. *J. Phys. Chem. B* **2001**, *105*, 8938.

(37) Pusey, P. N.; van Megen, W.; Bartlett, P.; Ackerson, B. J.; Rarity, J. G.; Underwood, S. M. *Phys. Rev. Lett.* **1989**, *63*, 2753.

(38) van Blaaderen, A.; Wiltzius, P. *Science* **1995**, *270*, 1177.

(39) Sun, Y.; Gray, S. K.; Peng, S. *Phys. Chem. Chem. Phys.* **2011**, *13*, 11814.

(40) Panáček, A.; Prucek, R.; Hrbáč, J.; Nevečná, T. j.; Steffková, J.; Zbořil, R.; Kvítek, L. *Chem. Mater.* **2014**, *26*, 1332.

■ NOTE ADDED AFTER ASAP PUBLICATION

This paper was published ASAP on April 28, 2014, with an error to Table 1's footnotes. The corrected version was reposted on April 30, 2014.

Supporting Information for:

Synthesis of Highly Monodisperse Citrate-Stabilized Silver Nanoparticles of up to 200 nm: Kinetic Control and Catalytic Properties

Neus G. Bastús, Florind Merkoçi, Jordi Piella and Victor Puntes

1. **The Effect of Tannic Acid in the Final Morphology of Ag NPs**
2. **Kinetics of Reduction Reaction**
3. **Formation Mechanism of Ag Nanoparticles**
4. **Calculated Mie Spectra**
5. **Ligand Exchange of Ag Nanoparticles**

1

1.   The Effect of Tannic Acid (TA) in the Final Morphology of Ag NPs

The addition of small amounts of Tannic Acid (TA) narrows the size distribution, producing highly monodisperse Ag NPs of 10.1 ± 0.9 nm in diameter **(Fig. S1)**. These results correlate with the absorption profile observed by UV-Vis spectroscopy, displaying a sharp and rather symmetric plasmon band placed at ~397 nm. When running the reaction in the absence of TA, a broad band peaking at ~420 nm was obtained together with an increase of the full width at half maximum (FWHM) of the spectra from 58 to 83 nm. This broadening and the notable band asymmetry of the spectrum is representative of the wide dispersity of Ag NP's, particularly the presence of elongated oval-shaped, polyhedrons and plate-like Ag NPs, with a low nanosphere yield, as previously reported by Lee and Meisel[1]. Interestingly, this improve in size dispersity is also associated to very high reaction yields, obtaining that Ag precursor conversion to metallic Ag is much higher when using TA as a co-reducer.
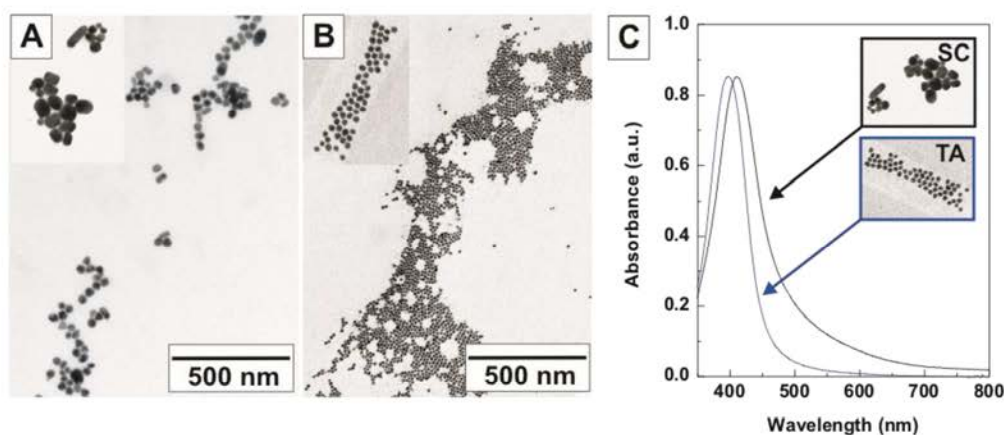
Figure S1- Effect of TA in the synthesis of citrate-stabilized Ag NPs. Transmission electron microscopy images and UV–Vis spectra of Ag NPs synthesized using sodium citrate (A, C-black spectrum) or a combination of SC and TA (B, C-blue spectrum).

Concentration of TA dictates the rate and extent of nucleation, with lower concentrations favoring fast nucleation and small particles, and larger (and less abundant) particles with higher size dispersity are produced as TA concentration increases. Similar results were reported by Dadosh in the synthesis of Ag NPs with diameters ranging from 18 to 30 nm[2] and by Rainville et al. in the synthesis of PVP-coated Ag NPs from 26 to 118 nm[3]. However, comparing these results with those obtained by Slot and Geuze for the synthesis of Au NPs[4] the concentration of TA has the opposite effect, i.e., in the case of Au, increased concentrations of TA resulted in

2

smaller particles. This inversed dependence of Ag NP's size on TA concentration is related to its stronger ability to form complexes with Ag^+ ions as SC does. On the contrary, Au^{3+}, with a stronger oxidizer potential, do not form stable complexes with TA, therefore leading to the synthesis of smaller NPs (faster burst nucleation and higher number of Au NPs) when increasing TA concentration.

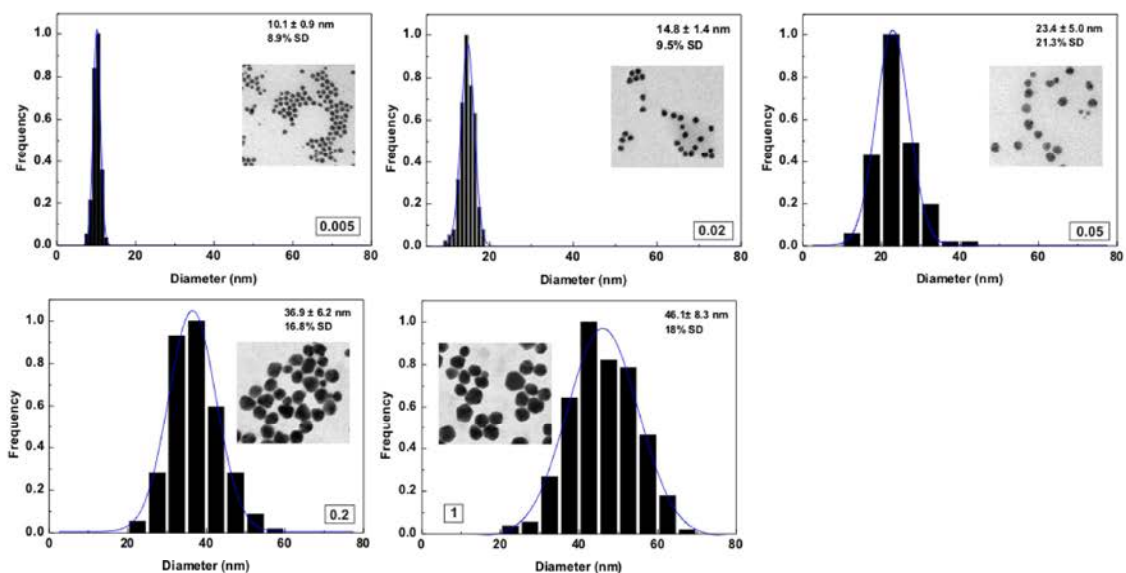**Figure S2- TEM image Analysis of Ag NPs shown in Figure 2A**. Ag seed diameter increases from 10.1 ± 0.9 nm to 46.1 ± 8.3 nm by using different TA/SC ratios, from 0.005/1 to 1/1. At least, 500 NPs were counted in each case.
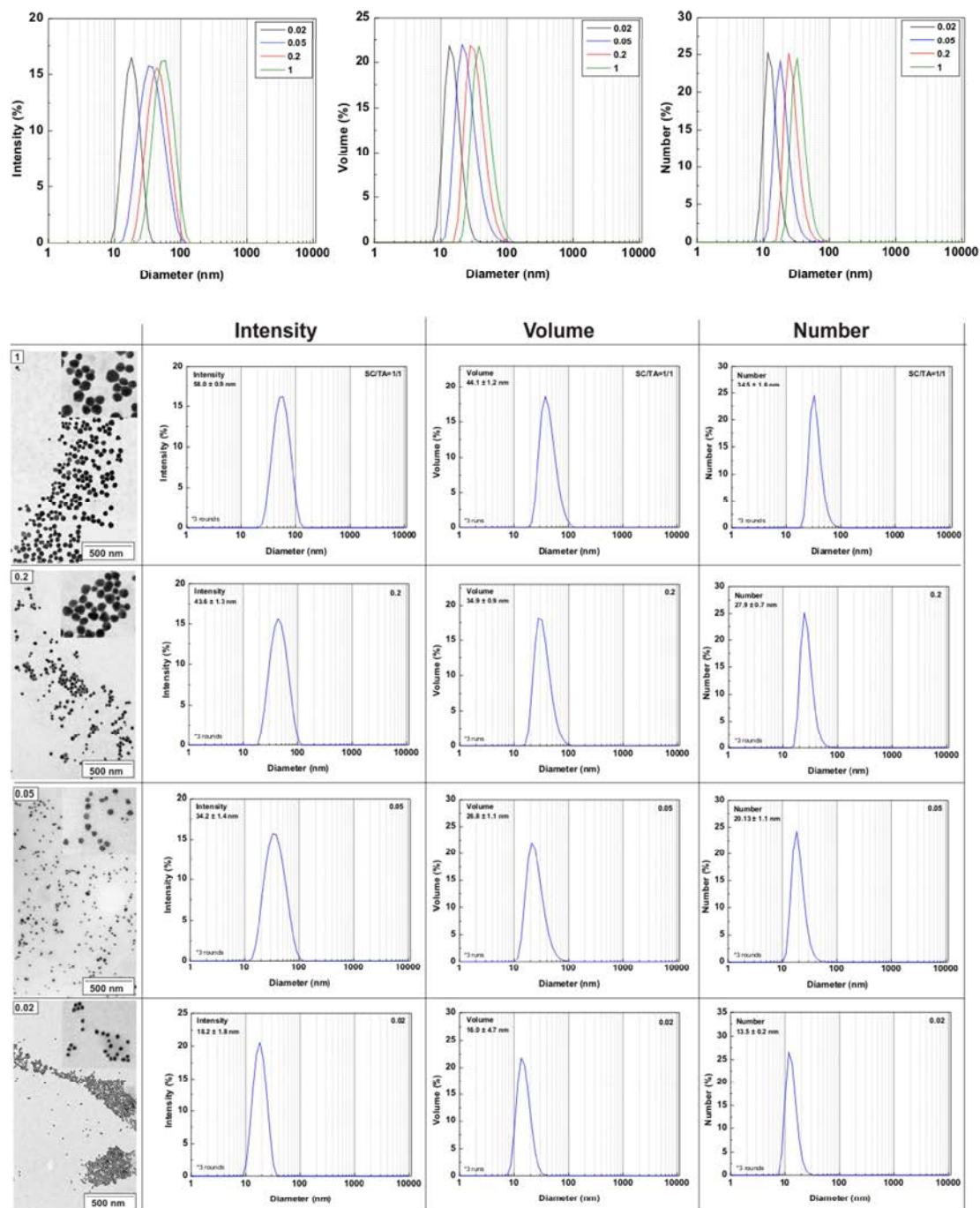
3

Figure S3- Size distribution measured by Dynamic Light Scattering. Size Distribution by Intensity, Volume and Number of Ag NPs synthesized by using different concentrations of TA.

4

2. Kinetics of Reduction Reaction

In order to understand the role of TA in the formation mechanism of Ag NPs, we studied the reduction reaction by monitoring the temporal evolution of UV-Vis spectra. Changes in the absorption spectra using a fixed concentration of TA (1 mM) are shown in **Figure S4-A,B**. As can be seen, at the initial stages of the reaction the solution presented a slightly yellow color which correlates with the appearance of a weak absorption band, initially peaking at ~418 nm. Then, as the reaction proceeded (1-10 min), the solution turned bright yellow and the absorption peak gradually blue-shifted from ~418 nm to ~410 nm. This continuous increase in the absorbance intensity was followed by a plateau state, where the absorbance remained almost unchanged.

Interestingly, time needed to reach the stationary state depends on the concentration of TA, being substantially faster in the low TA concentration regime (**Figure S4-C**). Thus, when the concentration of TA used was 0.1 mM the reaction took less than 10 min to reach the maximum absorbance value while it needed more than 30 min when TA concentration increased up to 1 mM. Similarly, the evolution of the SPR band and its final value also depend on the concentration of TA used, evolving slower and peaking at longer wavelengths (indicative of larger particles) for increasing concentration of TA (**Figure S4-D**). These results indicate that Ag NP's formation rate and final particle size is strongly determined by the concentration of TA used. Moreover, when comparing these results with those obtained in the direct citrate reduction (**Figure S4-C grey curve**) it can be seen how SC brings about slow growth of Ag NPs, needing more than 45 min to achieve a stationary growth stage. These results suggest the possibility to kinetically control the reduction of Ag ions by adding controlled amounts of TA to the reaction, which act as a primary reducer of the reaction, while SC plays the role of secondary reducer and stabilizer. Even more, a partial amount of TA can be used for nucleation while SC can drive the growth process once the catalytic nuclei are formed.

The dependence of Ag NP's morphology with the formation rate can be understood in terms of the commonly known La Mer model. Thus, a fast reduction leads to a burst nucleation, producing small nuclei which further grow to form, in homogeneous conditions, narrowly distributed NPs. On the contrary, if the reduction is slow, the nucleation overlaps with growth processes, easily leading to the inhomogeneous formation of particles, and consequently, in the difficulty of controlling their size

5

distribution. Although a fast reduction is typically associated with a strong reducing environment, we found herein the opposite behavior, i.e., the faster Ag NP's formation takes place at lower concentrations of TA, due to the strong complexing ability of TA stabilizing intermediate forms of Ag^+ ions[5].
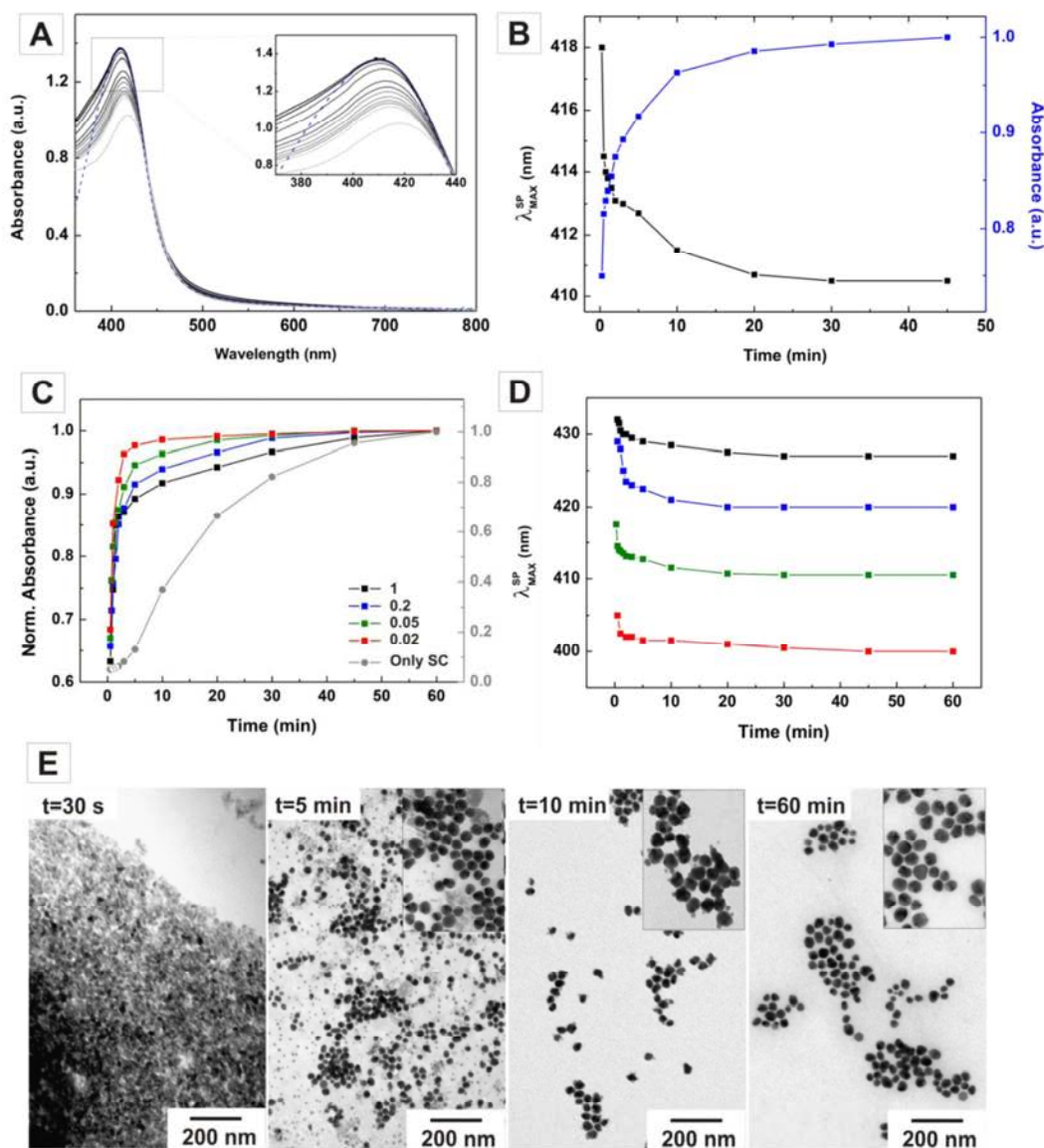
Figure S4- Kinetics of the Ag Reduction Reaction and Ag NP's Formation. (A) Time evolution UV-Vis spectra of Ag NPs obtained using 1mM of TA (TA/SC=0.02/1). Dotted-line corresponds to Ag NPs after the washing process. **(B)** Time evolution of the SPR band and the intensity maximum as a function of time for Ag NPs obtained using 1mM of TA (TA/SC=1/1). **(C)** Time evolution of the intensity maximum of Ag NP obtained using different concentrations TA, from 0.1mM (TA/SC=0.02/1) to 5mM (TA/SC=1/1). Results obtained using only SC were plot for comparison. **(D)** Time evolution of the SPR of Ag NP obtained using different concentrations TA, from 0.1mM to 5mM. **(E)** Representative TEM images of Ag NP grown at different times for TA/SC=0.2/1. The formation of inhomogeneous Ag

6

intermediates was observed at early stages (30 s) in which small particles formed (5 min) and then dissolved, acting as a source of atoms for the growth of large particles (10 min and 60 min).

The study of the morphology at selected reaction times (and at a fixed concentration of TA, 1mM) provides further information. As can be seen in **Figure S4-D**, at short reactions times (30s), large and inhomogeneous fluffy intermediates were observed. As the reaction proceeded (5 min), the size of these intermediate products decreased while spherical, rather monodisperse Ag NPs appeared. These particles were accompanied by small-sized Ag NPs of 3-5 nm in diameter which progressively disappeared (10 min), acting as a temporal Ag reservoir and leading finally to well-defined Ag crystals. These results, together with the time-dependent evolution of the SPR band (**Figure S4-D**), suggest that nucleation of Ag NPs is mediated by the presence of small Ag aggregates, probably due to the complexation of Ag ions by TA formed at the early stages of the reaction. These intermediates species further dissolve acting as a source of atoms for the nucleation and growth of Ag NPs. Similar proto-particles in form of fluffy aggregates have also been observed at very short times in the citrate-mediated synthesis of Au NPs[6,7].

3.   Formation Mechanism of Ag Nanoparticles

This formation process can be understood taking into account the interaction of silver precursor with TA, in particular the fact that a single reagent plays multiple roles, as reducing agent, stabilizer and complexation agent (**Scheme 1**). The representative structure of TA consists of a central core of glucose linked by ester bonds to polygalloyl ester chains, where phenolic hydroxyls undergo two-electron oxidation to the corresponding quinone form (**Scheme 1-1**) and donate two electrons for the reduction of Ag^+ precursor (**Scheme 1-2**). At this moment, a two-step process takes place, the production of Ag^0 and the further formation of a new spice, Ag_2^+ [8,9] (**Scheme 1-3**). Later, the dimmerization of Ag_2^+ leads to the formation of Ag_4^{2+} which acts as a monomer for the formation of Ag NPs. This reaction is influenced by the presence of TA, which readily interacts with Ag_2^+, mediating its complexation with positively charged silver dimers at high concentrations (**Scheme 1-4**). This $[Ag_2^+-TA]$ complex undergoes slower transformations compared to the un-complexed Ag_2^+, which leads to the formation of Ag NPs with irregular sizes. Obviously, this complexation depends on

7

the concentration of TA used, achieving higher complexation rates as the concentration of TA increases **(Scheme 1-5)**. Thus, the increase of TA concentration promotes the formation of the $[Ag_2^+-TA]$ complex which slows down the conversion of Ag_2^+ into Ag_4^{2+} and leads to the slow particle formation, which in turn, favor the formation of large and polidisperse Ag NPs. On the contrary, at low concentrations, TA acts primary as a reducer leading the fast nucleation of monodisperse Ag NPs, following a conventional La Mer bust nucleation process **(Scheme 1-6)**.

Based on this fact; we promote this initial fast reduction of Ag^+ ions by using low concentrations of TA leading to the formation of small, highly monodisperse Ag NPs.
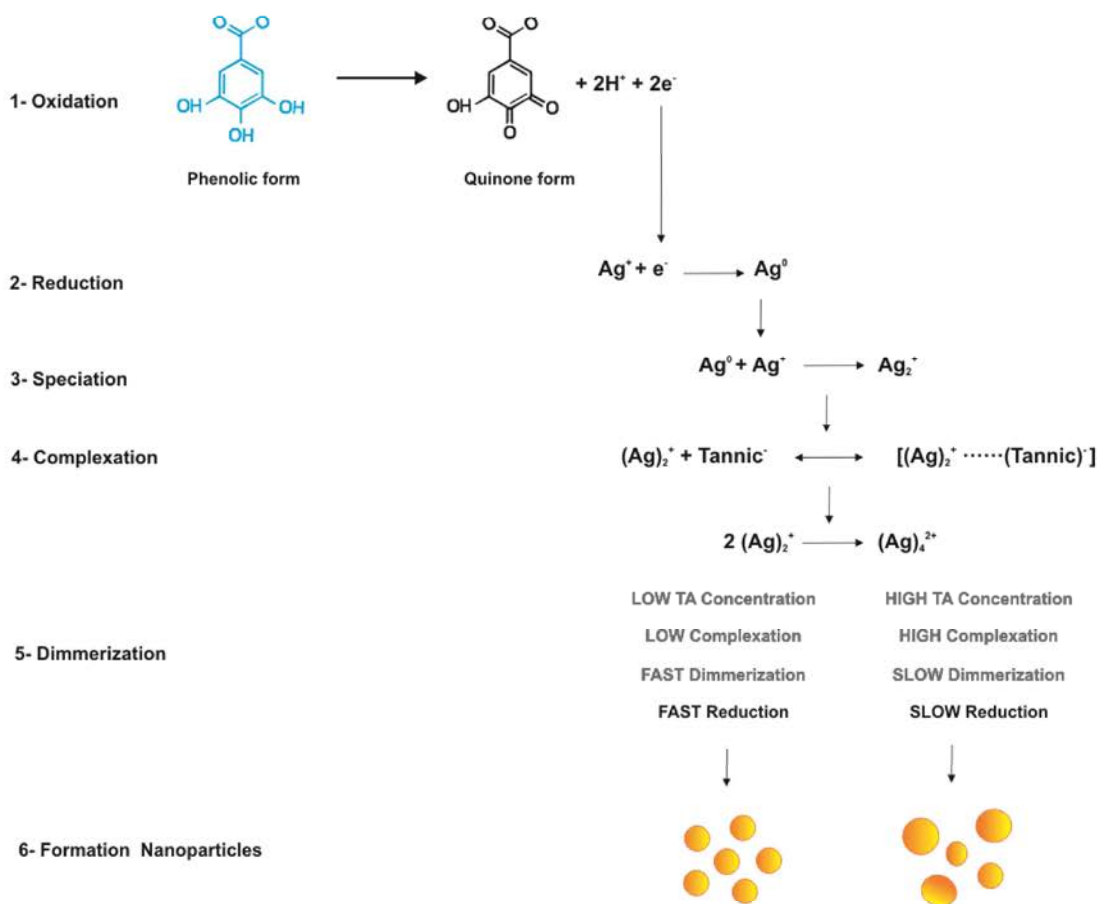
Scheme 1- Reduction Mechanism of Silver Ions by TA. (1) Phenolic hydroxyls of TA undergo two-electron oxidation to the corresponding quinone form and donate two electrons for the reduction of Ag^+ precursor **(2)**. At this moment, a two-step process takes place, the production of Ag^0 and the further formation of a new spice, Ag_2^+ **(3)**. TA interacts with Ag^{2+} mediating its complexation **(4)**. This $[Ag_2^+-TA]$ complex undergoes slower transformations compared to the uncomplexed Ag_2^+, which leads to the formation of larger Ag NPs with irregular sizes **(5, 6)**.

8
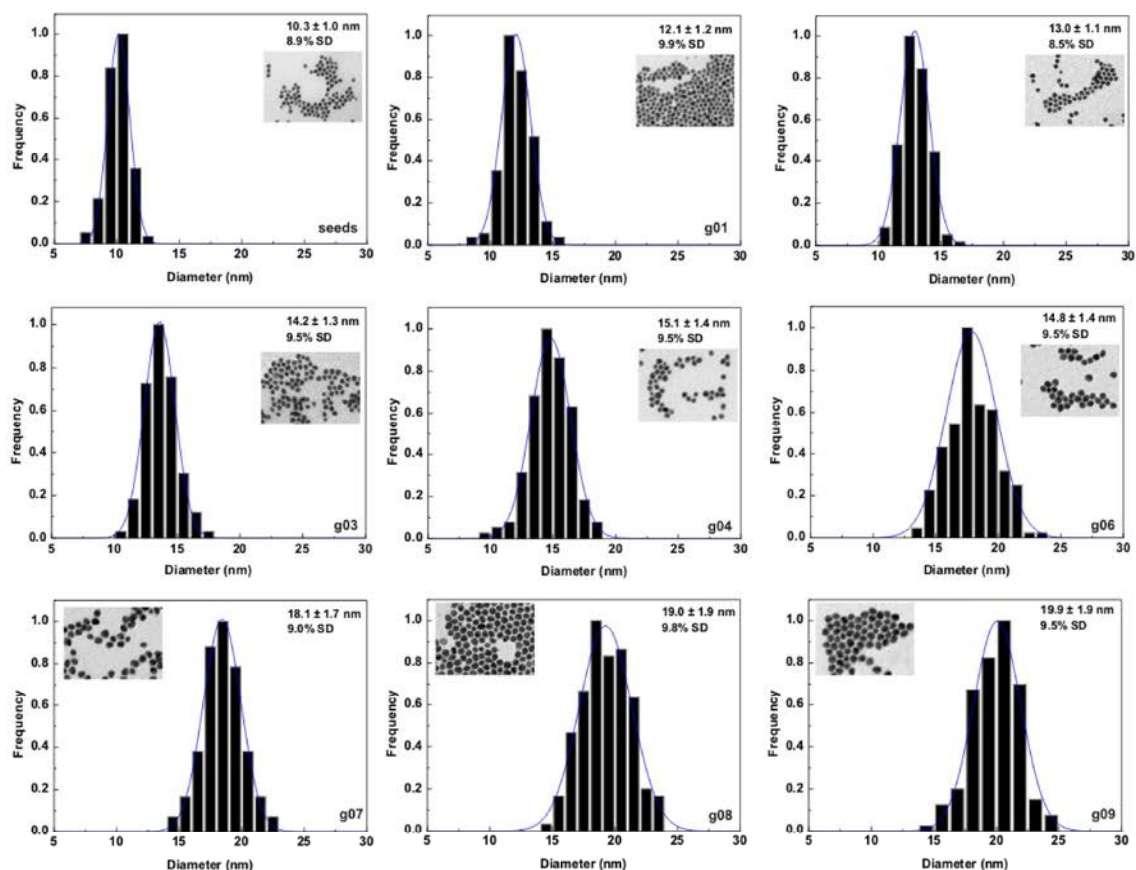
Figure S5- TEM image Analysis of Ag NPs shown in Figure 2. Ag seed diameter increases from 10.3 ± 10.9 nm to 19.9 ± 1.9 nm after different growing steps. In all cases, the concentration of the Au NP solution is the same ($\sim 6 \ 10^{12}$ NPs/mL). At least, 500 NPs were counted in each case.
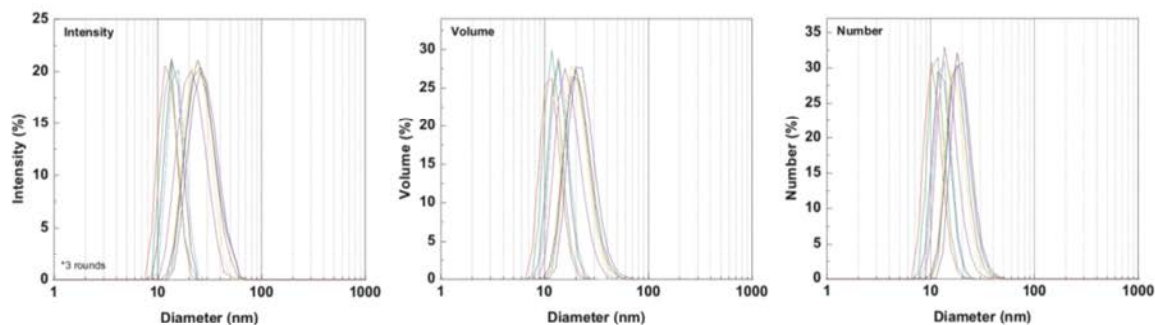
Figure S6- Size Distribution by Intensity (Left), Volume (Middle) and Number (Right) of silver colloids obtained after different growth steps.

9
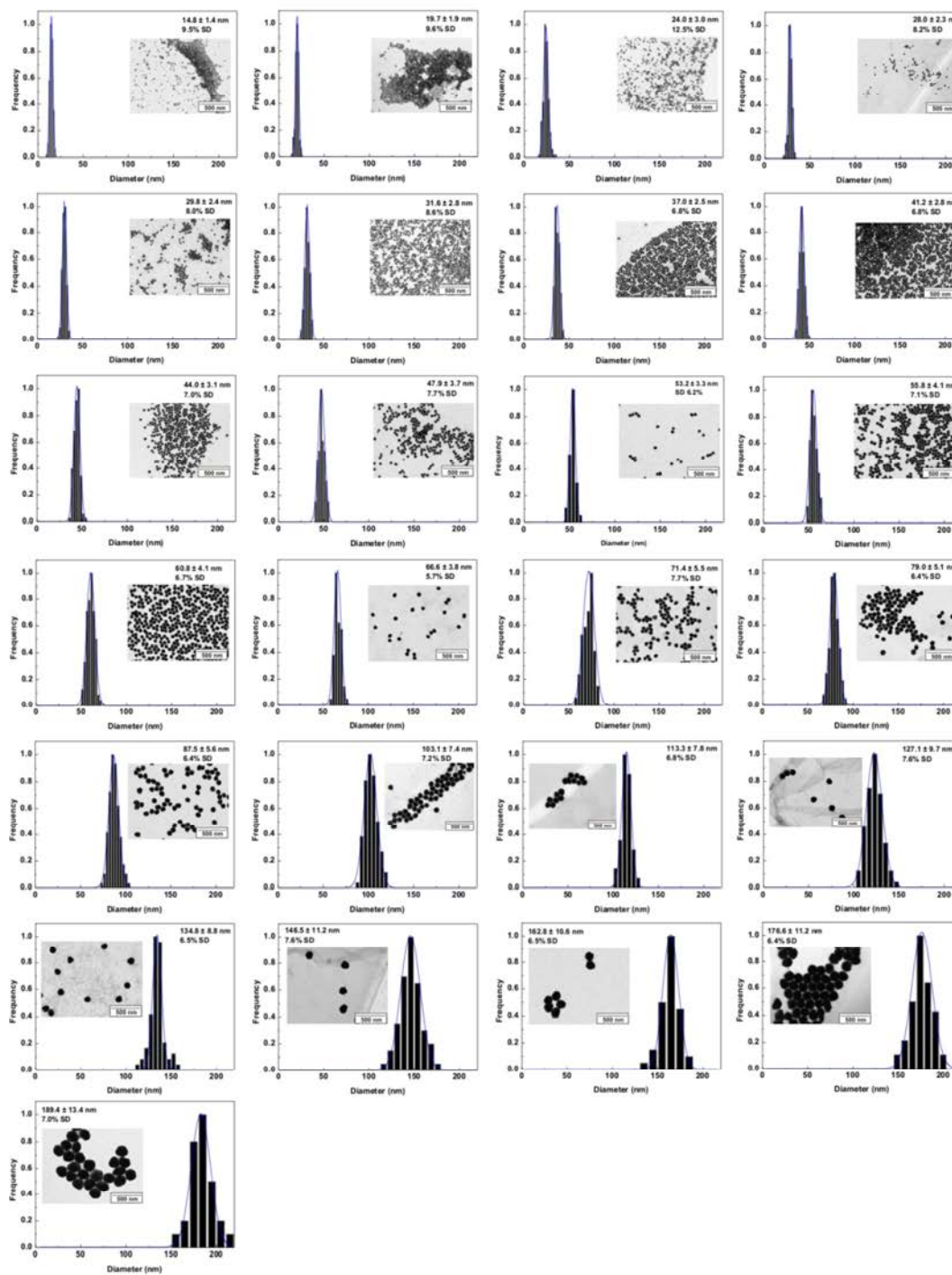
Figure S7- TEM image Analysis of Ag NPs shown in Figure 7. Ag seed diameter increases from $14.8 \pm$ 1.4 nm to 189.4 ± 13.4 nm after different growing steps. At least, 500 NPs were counted in each case.

10

4. Calculated Spectra

Experimental absorbance was compared to calculations based on the standard Mie theory of spherical particles. Calculations of the scattering coefficient of colloidal Ag NPs of different diameters were obtained using Mie plot software considering Ag spheres embedded in water at 25 °C. Mean size and standard distribution measured by TEM were used for the calculations.
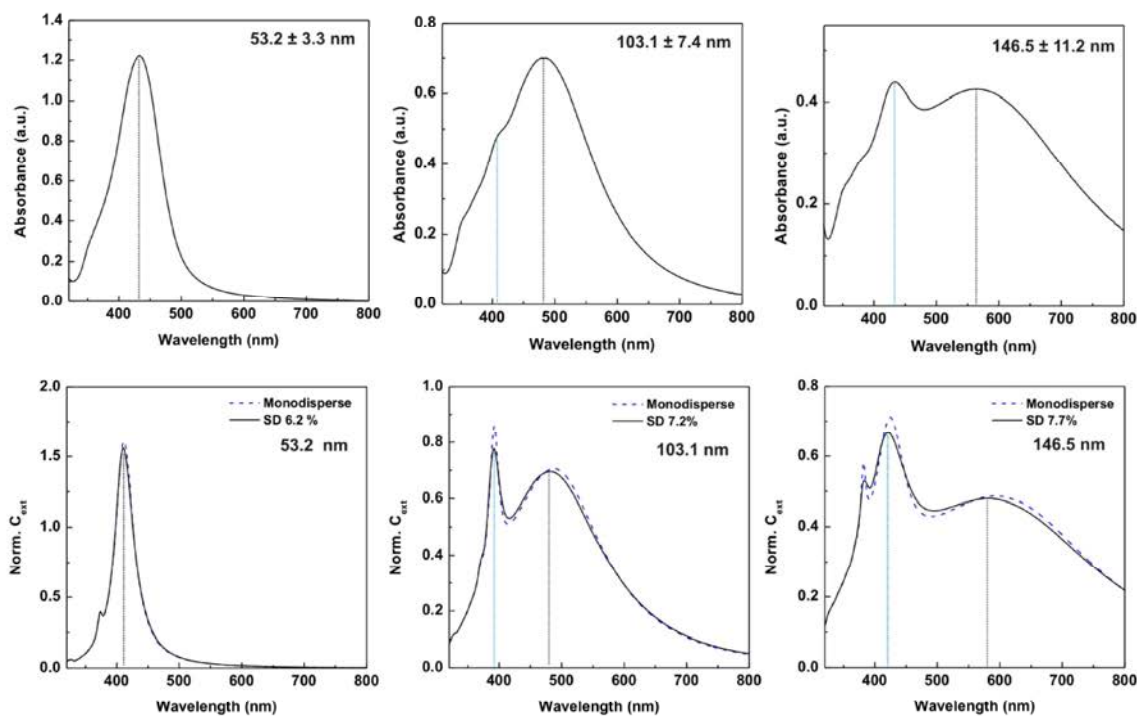
Figure S8. Top) Experimental absorption spectra of Ag NPs of different sizes 53.2 nm, 103.1 nm, and 146.5 nm. **Bottom)** Calculated extinction spectra of monodisperse Ag spheres (dashed line) and with the same mean size and size deviation as obtained experimentally (solid line).

11

5. Ligand Exchange of Ag Nanoparticles

Ligand exchange was performed by adding aqueous solution of known amounts of ligands (PVP or BSA) to as-synthesized Ag NPs solutions (final concentration 5 mM (PVP), 1mM BSA) under vigorous stirring. Functionalized Ag NPs were purified and further characterized by UV-Vis and DLS.
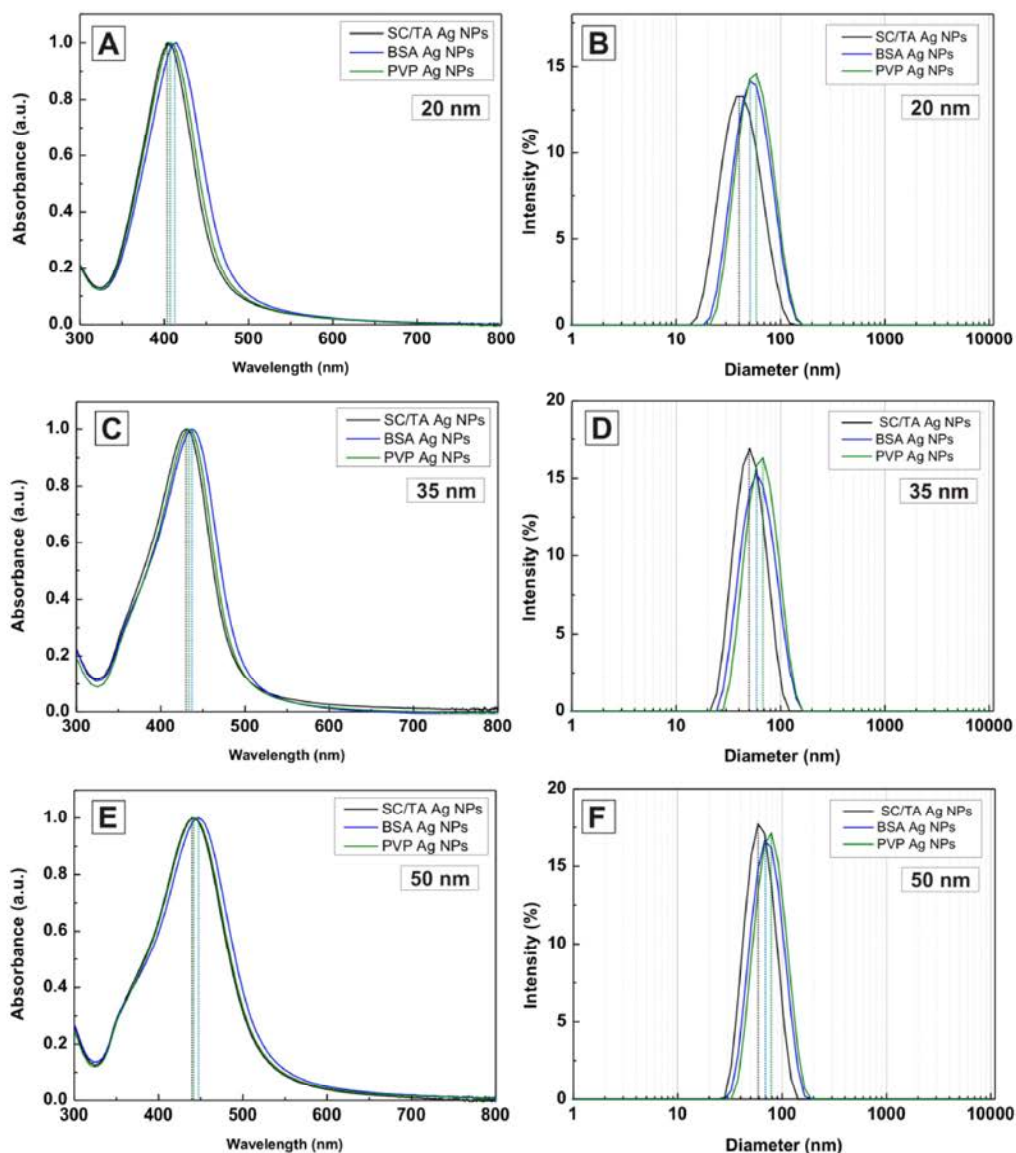
Figure S9. Functionalization of Ag NPs with PVP and BSA. UV-Vis spectra and DLS of Ag NPs of different sizes 20 nm (A, B), 35 nm (C, D) and 50 nm (E, F) recorded before (black line) and after the ligand exchange process with BSA (blue line) and PVP (green line). Once the native molecules are replaced by PVP or BSA the corresponding absorption peak shifts to the red and the hydrodynamic diameter increases.

12

References

(1)   Lee, P. C.; Meisel, D. *The Journal of Physical Chemistry* **1982**, *86*, 3391-3395.

(2)   Dadosh, T. *Materials Letters* **2009**, *63*, 2236-2238.

(3)   Rainville, L.; Dorais, M.-C.; Boudreau, D. *RSC Advances* **2013**, *3*, 13953-13960.

(4)   Slot, J. W.; Geuze, H. J. *European journal of cell biology* **1985**, *38*, 87-93.

(5)   Tao, A. R.; Habas, S.; Yang, P. *Small* **2008**, *4*, 310-325.

(6)   Bastús, N. G.; Comenge, J.; Puntes, V. c. *Langmuir* **2011**, *27*, 11098-11105.

(7)   Ji, X.; Song, X.; Li, J.; Bai, Y.; Yang, W.; Peng, X. *Journal of the American Chemical Society* **2007**, *129*, 13939-13948.

(8)   Janata, E.; Henglein, A.; Ershov, B. G. *The Journal of Physical Chemistry* **1994**, *98*, 10888-10890.

(9)   Pillai, Z. S.; Kamat, P. V. *The Journal of Physical Chemistry B* **2003**, *108*, 945-951.

13

Chapter 4:

Localized surface plasmon resonances in metal NPs: the effect of size, composition and surface coating

Gold and silver nanoparticles (Au and Ag NPs) are a particularly interesting class of nanomaterials due to their optical signatures. The extinction spectra of these NPs in the visible range is characterized by a series of extinction bands called localized surface plasmon resonances (LSPRs) that has been proved to be very promising for many applications, e.g. biomolecular sensing and imaging. Additionally, because these bands are sensitive to the particle structure and surrounding environment, they can be tuned at will. Recent developments in the synthesis of highly monodisperse colloids of spherical Au and Ag NPs opens the possibility for detailed and systematic studies of the LSPRs of these NPs and thus the selection of appropriate NPs for particular applications. In this chapter, the LSPRs of previously synthetized Au and Ag NPs are discussed in detail.

4.1. Introduction to optical properties of metal nanoparticles

One of the most fascinating aspects of metal nanoparticles (NPs) is their optical properties. It is widely known that at the nanoscale Au and Ag colloids exhibit rich colours, e.g., yellowish for Ag and burgundy for Au NPs. The origin of these colours were first predicted by Faraday in the 19th century and stems from an optical phenomenon termed localized surface plasmon resonance (LSPR). When an incident electromagnetic radiation of an appropriate wavelength interacts with a metallic NP, the conduction electrons near the metal-dielectric interface are excited and undergo collective oscillations in resonance with the electric field generated by the incident light (**Figure 4.1**). As a consequence of these electron oscillations, the electric field is strongly enhanced, resulting in novel properties of the NPs. Indeed, LSPRs are one of the clearest example that things are different at the nanoscale [1-4]; they are absent in individual atoms as well as in bulk and, despite the terminology, are definitely not a quantum effect.

From time immemorial, three metals, namely gold, silver, and copper, have been used extensively by mankind since they can be found in nature in their native state. Coincidence or not, NPs made of these metals are the ones in which the resonance conditions are fulfilled at visible frequencies, thus constituting the group of plasmonic NPs and making them the first choice for optical applications. Due to LSPRs, the light absorption and scattering of these NPs (in particular Au and Ag NPs) can be several orders of magnitude stronger than that of the most absorbing organic dyes and the most emitting fluorescent molecules [5][6]. Furthermore, the large polarization associated with LSPRs also results in a huge electric fields near the NP surface (the near field enhancement), with relevant implications, e.g., for molecule detection [7].

The spectral characteristics of LSPRs are dominated by four factors: the density of the electrons, the effective electron mass, the shape and the size of the charge distribution. Consequently, LSPRs depend not only on the composition of the material, but also on the particle size and shape, the dielectric surrounding environment and the inter-particle coupling interactions [8-10], thus imparting a unique tunability of the NP optical properties. Thanks to the development of our ability to fabricate and manipulate nanomaterials, success in the application of LSPRs is rapidly increasing. In the last few years, many exciting research lines have emerged in this directions, including surface
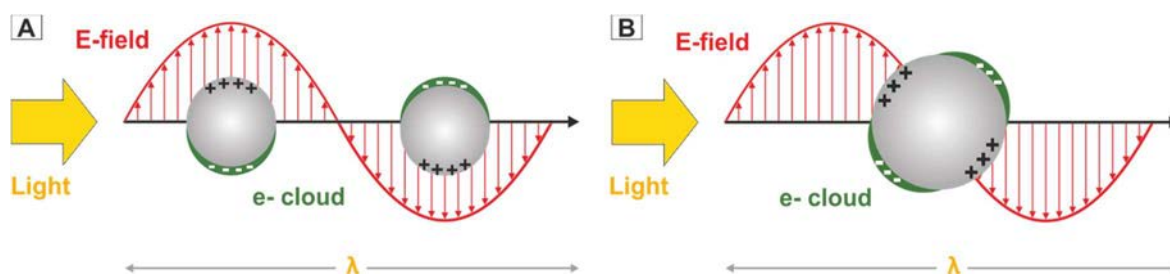
Figure 4.1. Scheme of electron oscillations in a metal sphere under the influence of an electric field induced by an incident light radiation. (A) The sphere responds to a spatially constant electric field when its size is much smaller than the light wavelength, resulting in a coherent dipolar oscillation of the conduction electrons. (B) The electric field is no longer homogeneous along the sphere when its size is comparable to the light wavelength, leading to multipole oscillations.

enhanced Raman spectroscopy (SERS) [11, 12], plasmonic tags and NP-based therapies [12, 13], biomolecular sensing and imaging [12, 13], and photocatalysis [14].

In addition to technological implications, the optical signature of NPs is also useful as a characterization tool. This is interesting because optical techniques are nondestructive, and with proper implementation, they enable measurements *in situ* and in real time, providing statistical information of the state of the NPs in different conditions. These attributes are important because NPs are usually synthetized in very controlled environments, and when added to a more realistic situations they are susceptible to experiment significant changes, such as aggregation, dissolution and corrosion [15] (see **Chapter 1**). Thus, optical spectroscopies are a valuable characterization tool complementary to techniques like transmission electron microscopy (TEM) that can only provide an image of a small piece of the sample, giving local information and only characterizing a few NPs at a time.

The synthesis of highly monodisperse colloids of NPs is a prerequisite for detailed and systematic studies of their optical signatures. Following the synthetic protocols previously described (see **Chapters 2** and **3**), Ag and Au NPs with different sizes were prepared and their optical properties were studied in detail by UV-vis spectroscopy. Attention was focused on the effect that NP size and composition have on the position, bandwidth and intensity of the LSPRs. Correlation between the LSPRs and NP surroundings was also examined in relation to molecule adsorption. The results were collected in the article entitled *Quantifying the Sensitivity of Multipolar (Dipolar, Quadrupolar, and Octapolar) Surface Plasmon Resonances in Silver Nanoparticles: The Effect of Size, Composition, and Surface Coating*, which is presented here.

4.2. Light interaction with spherical metal nanoparticles

In order to interpret the results, some theoretical considerations now follow, in particular the Mie theory.

When a NP is under the action of an electromagnetic field, its electrons start to oscillate, transforming energy from the incident electromagnetic wave into, for example, thermal energy in an adsorption process. Alternatively, the electrons can be accelerated, and radiate energy in all directions in a scattering process, either at the same frequency as the incident light (e.g. Rayleigh scattering) or at a shifted frequency (e.g. Raman scattering). Both processes can be quantified by the absorption and scattering cross sections, σ_{abs} and σ_{sca}, which are defined as the effective area over which a NP absorbs or scatters light [1, 2]. The sum of σ_{abs} and σ_{sca} is termed light extinction, σ_{ext}, and quantifies the capability of a NP to extinguish (absorb and scatter) incident light (**4.1**). It can be understood as the virtual area of a completely opaque object that blocks the same amount of radiation as the NP. Dividing the interaction cross-sections $\sigma_{ext}, \sigma_{abs}$ and σ_{sca} by the geometrical cross-section A_{cs}, one obtain the interaction efficiencies Q shown in equation (**4.2**). At the resonance frequency, a plasmonic NP can absorb and scatter light from a much larger area than its physical cross section because of the LSPRs, and thus show efficiencies much larger than the unit.

$$\sigma_{ext} = \sigma_{sca} + \sigma_{abs} \qquad\qquad (\textbf{4.1})$$

$$Q_{ext} = \frac{\sigma_{ext}}{A_{cs}}; \; Q_{sca} = \frac{\sigma_{sca}}{A_{cs}}; \; Q_{abs} = \frac{\sigma_{abs}}{A_{cs}} \qquad\qquad (\textbf{4.2})$$

In 1908, Gustav Mie found the exact solutions to $\sigma_{abs}, \sigma_{sca}$ and σ_{ext} after solving Maxwell equations for the optical response of a sphere. He used a series expansion of spherical harmonic wave equations, known as Mie theory [16]. The solutions requires the particle volume V, the frequency dependent dielectric function of the metal $\varepsilon(\omega)$ and the dielectric constant of the embedded medium ε_m as input parameters [17]. Remember that the dielectric function is a measure of how a material responds to an external electric field, particularly how much separation of charge occurs, and depends on the electronic structure of the material. Because commonly used dispersing media, such as water, have slowly varying dielectric functions with the frequency, they are considered constant and

referred to as dielectric constant. The derivation of Maxwell's equations is tedious and lengthy and a full explanation can be found in the original work of Mie [16] and other related books [1, 2], thus we will focus on its discussion qualitatively.

4.2.1. The dipole approximation

For sizes much smaller than the wavelength of the incident light ($d \leq 25$ nm), the NP is under the effect of a field that can be considered as spatially constant but with a time-dependent phase, which is known as the *quasistatic limit*. In this limit, the displacement of electrons in the NP is homogeneous, yielding a dipolar charge distribution (**Figure 4.1A**). The Mie theory then simplifies and σ_{abs} and σ_{sca} respond to the following expressions (dipole approximation):

$$\sigma_{sca} = \frac{24\pi^3 V^2 \varepsilon_m^2}{\lambda^4} \frac{(\varepsilon_1 - \varepsilon_m)^2 + \varepsilon_2^2}{(\varepsilon_1 + 2\varepsilon_m)^2 + \varepsilon_2^2}, \tag{4.3}$$

$$\sigma_{abs} = \frac{18\pi V \varepsilon_m^{\frac{3}{2}}}{\lambda} \frac{\varepsilon_2}{(\varepsilon_1 + 2\varepsilon_m)^2 + \varepsilon_2^2}, \tag{4.4}$$

where λ is the wavelength of the incident light, $\varepsilon_1(\omega)$ and $\varepsilon_2(\omega)$ denote the real and imaginary part of the metal dielectric funtion $\varepsilon(\omega)$ and ε_m is the dielectric constant of the medium [18]. Equations (**4.3**) and (**4.4**) show that absorption scales with V while scattering with V^2. Consequently, for large NPs, scattering is stronger than absorption ($\sigma_{ext} \approx \sigma_{sca}$) while for small NPs, where the dipole approximation basically applies, extinction is dominated by absorption ($\sigma_{ext} \approx \sigma_{abs}$). This fact can guide the choice of NP size for different applications. For imaging, lager NPs are preferred because of higher scattering efficiencies, whereas for photothermal therapy, smaller NP are preferred as light is mainly adsorbed by the NPs and thus efficiently converted to heat for selective cell and tissue destruction.

The oscillating electrons of the NP enter in resonance with the incident light (maximum of equations x and) when $\varepsilon_1(\omega) = -2\varepsilon_m$ [1]. This resonance of dipolar character dominates the extinction spectra of small NPs, and results in a characteristic extinction peak around 400 nm for Ag NPs and around 520 nm for Au NPs dispersed in water (**Figure 4.2**).
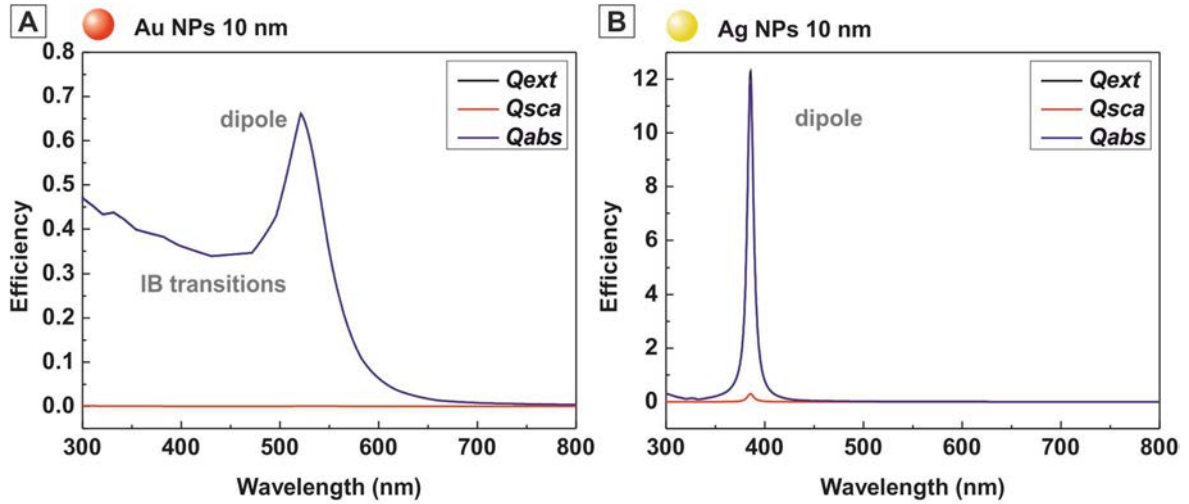
Figure 4.2. Calculated absorption, scattering, and extinction efficiencies in water of spherical metal nanoparticles of 10 nm in diameter. Au (red) and Ag (yellow) NPs. MiePlot software was used for the calculation [19]. Frequency dependent dielectric function for bulk gold and silver were taken from [17].

The fact that the dipole peak, as well as other LSPR peaks, depends on the dielectric constant of the medium ε_m is particularly important for sensing applications since it underpins the sensing mechanism for refractive index measurements using NPs.

Overall, one can consider the system as similar to a harmonic oscillator, where a gas of free electrons moves against a fixed background of positive ions that acts as a restoring force. This kind of harmonic oscillators are characterized by resonances with a Lorentzian form similar to the dipole peak of Ag NPs. However, the Au NPs shown an asymmetric peak, with a significant intensity below 500 nm, which differs from what would be expected (**Figure 4.2**). There are two main mechanisms for a NP to absorb energy: through collective oscillation of the conduction electrons, the LSPRs, or by electronic transitions of valence electrons from occupied to empty bands, so called interband transitions (IB) [3]. The IB are usually produced at higher energies than the LSPRs (UV region), but for noble metals, and in particular for gold, the energy thresholds extend to the visible. For example, *5d-to Fermi* IB transition in Au is set at around ~2.4 eV (λ=516.6 nm) [3, 20]. This is, for instance, the reason for the 'golden' colour of bulk gold, since it strongly absorbs the blue and violet while reflecting the yellow and red. Both, the IB transitions and the plasmon oscillations, contribute to the extinction of light:

$$\varepsilon(\omega) = \varepsilon_{IB}(\omega) + \varepsilon_{LSPR}(\omega) \tag{4.5}$$

where $\varepsilon_{IB}(\omega)$ represents the intreband contributions and $\varepsilon_{LSPR}(\omega)$ the free electron contributions of the metal dielectric function, also denoted as Lorentz (ε_{IB}) and Drude (ε_{LSPR}) terms respectively [10, 20-22]. Overlapping of the two terms gives the asymmetric extinction (absorption) peak of the Au NPs.

4.2.2. The case of small nanoparticles

The dipole approximation in the quasistatic limit predicts that, except for a volume depending scaling factor, the dipole peak (position and bandwidth) is size-independent (see (**4.3**), where $\varepsilon(\omega)$ only depends on the frequency). However, different experiments have revealed that electron oscillations are strongly damped for Au and Ag NPs smaller than 10 nm. This damping is caused by a surface dispersion phenomena, since the size of the NPs becomes significantly smaller compared with the electron mean free path, typically in the range of tens of nanometres for noble metals at room temperature. As a result, the electrons colloid with the particle surface during oscillation, making the resonance less efficient and thus resulting in wider and less intense dipole peaks, as experimentally reported by different authors [22, 23]. In addition, different quantum mechanical effects [3] may further contribute to the resonance conditions and change the position of the peak. Because these effects are usually accounted into equation (**4.3**) by assuming a size dependent metal dielectric function, the related changes in the extinction spectra are referred to as *intrinsic size effects* [1, 22]:

$$\varepsilon_{LSPR}(\omega) \rightarrow \varepsilon_{LSPR}(\omega, r) \qquad (4.6)$$

4.2.3. The case of large nanoparticles

For large NPs ($d > 25$ nm), one enters in the full Mie regime [10, 24]. The displacement of the electron cloud in the particle is no longer homogeneous, such that, high-multipole charge distributions are induced (**Figure 4.1B**). As a consequence, the spectral band splits into several peaks: one peak for the dipole, two peaks for the quadrupole, three peaks for the octapole, etc (**Figure 4.3**). These high multipole peaks are always located at smaller wavelengths with respect to the dipolar peak, which, additionally, is always red-shifted (move to larger wavelengths) by the presence of the electric field generated by the other multipolar charge distributions [14, 24, 25]. Scattering also becomes
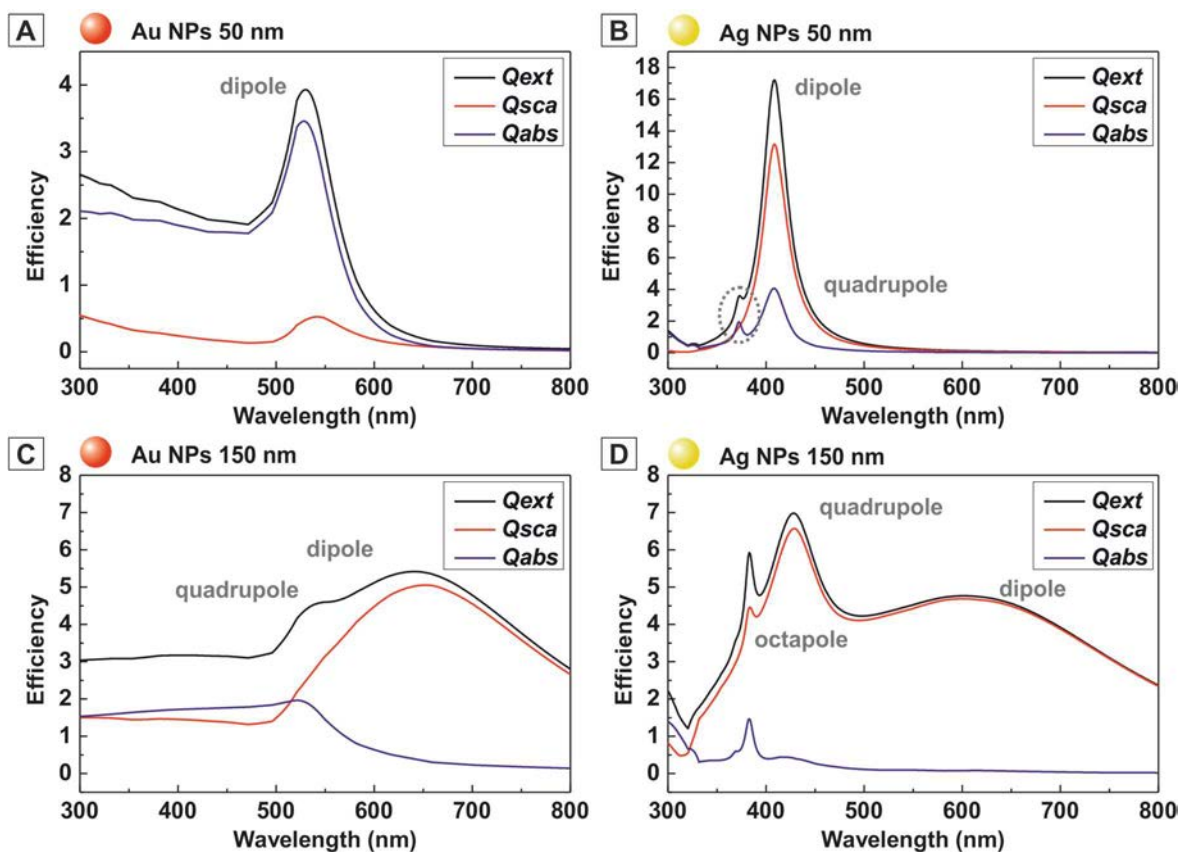
Figure 4.3. Calculated absorption, scattering, and extinction efficiencies in water of spherical metal nanoparticles with different diameters. Au (red) and Ag (yellow) NPs. MiePlot software was used for the calculations [19]. Dielectric function for bulk gold and silver were taken from [17].

important at these sizes. Electrons accelerated by the incident light radiate energy in all directions. Due to this secondary radiation, they lose energy and experience a damping on their motion, resulting in wider peaks [10, 11]. The secondary radiation also generates a polarization field that acts against that generated by the incident light and further moves the position of these peaks to lower energies [10, 25]. This size-dependent behaviour of LSPRs for large NPs is associated purely with electrodynamics. Consequently, the related changes in the extinction spectra are referred to as *extrinsic size effects* [1, 22].

In summary, the optical signature of small NPs is given by the dipolar resonance, which is influenced by the particle size, such that for particles of a few nanometers the dipole peak broadens and attenuates because of surface dispersion and quantum mechanical effects (*intrinsic size effects*). When the size increases, multiple oscillations result in multiple peaks that become wider and move their position to lower frequencies (*extrinsic size effects*). Thus, to describe the optical response of plasmonic NPs, it is crucial to understand the number, position, and width of the resonance peaks.

4.3. Relation between extinction cross section and attenuation

As the light extinction of NPs is measured experimentally by UV-vis spectroscopy, it is worth introducing the relation between the measured value and the previously mentioned extinction cross section σ_{ext}.

In the presence of a diluted dispersion containing N particles per unit volume (NP m^{-3}), the measured attenuation A of incoming light of intensity I_0 over a pathlength d (m) is given by the empirical relationship of Beer-Lambert:

$$A = log_{10} \frac{I_0}{I_d} = \frac{\sigma_{ext}}{2.303} \, d \, N = \frac{Q_{ext} A_{cs}}{2.303} \, d \, N. \tag{4.7}$$

The Beer-Lambert law correlates the experimentally measured A of a colloidal solution, usually called indistinctly absorbance or extinction in spectroscopic measurements, with the previously discussed extinction cross section σ_{ext} of a NP. Because quantum physicists are accustomed to cross sections for various parameters and nuclear processes, they are probably most comfortable with σ_{ext} (m^2 NP^{-1}), but there is obviously other ways of representation. The dimensionless parameter of Q_{ext} has a widespread use among the nanotechnology community. As previously mentioned, Q_{ext} is defined as the extinction cross section σ_{ext} divided by the geometric cross-section A_{cs}(m^2 NP^{-1}) and represents the efficiency of a material to extinguish light compared to its perfect opaque counterpart (**4.2**). Intuitively, if geometrical optics were a completely trustworthy guide in the world of NPs, Q_{ext} would never exceed 1: all rays incident on a particle are extinguished, either by adsorption or scattering ($\sigma_{ext} = A_{cs}$). Nevertheless, there are many NPs that have extinction efficiencies greater than 1, which means that they can scatter and absorb light beyond that geometrically incident to them, like a nanoscopic "antenna". The large polarization associated with the LSPRs results in enhanced local electric fields at the particle surface whose effects extend beyond their physical size. Because Q_{ext} does not scale with size, it is a commonly used parameter when comparing spectra of NPs with different diameters.

On the other hand, the molar extinction coefficient ε (m^{2}M$_{atom}^{-1}$) is a parameter more commonly used in biology than the σ_{ext}. The reason is that it directly correlates the extinction properties A with the atom concentration c (M$_{atom}$). As a consequence, it

is more commonly used to compare the dose response of NPs of different sizes since it accounts for the fact that the larger NPs contain more atoms than the smaller ones [2]. The Beer-Lambert law then acquires the following expression:

$$A = \varepsilon \, d \, c; \quad \varepsilon = \frac{\sigma_{ext} \, MW}{2.303 \, V \, \rho} = \frac{Q_{ext} A_{cs} \, MW}{2.303 \, V \, \rho}, \tag{4.8}$$

where V (m^3 NP^{-1}) is the particle volume; ρ (g L^{-1}) and MW are the density and molecular weight of the metal. Except for a scale factor, all mentioned parameters (σ_{ext}, Q_{ext}, ε) plotted as a function of wavelength have identical form, and thus can be seen as different ways of normalization, i.e. NP number, cross-section area or atom concentration.

4.4. Results I: Localized surface plasmon resonances in silver nanoparticles: the effect of size, composition and surface coating

Ag NPs with diameters from 10 to 200 nm were prepared following the method described in **Chapters 3**. With other synthetic procedures, the by-products remaining after the chemical reduction of the metal and/or initially added capping molecules limit the growth of NPs to large dimensions and affect their chemical and optical properties. In this case, not only were large Ag NPs easily produced, but also the degree of monodispersity was preserved below 10%, thus allowing the experimental observation of high order multipoles, such as the quadrupole and the octapole peaks, with unpreceded precision. Au NPs in the same size range were also prepared following a previously mentioned protocol [26] and the LSPRs compared with that of the Ag NPs (**Figures 4.4** and **4.5**).

The experimental spectra for the different NP clearly reflect the previously discussed fact that the resonance wavelength as well as the extent of the extinction enhancement is highly dependent on the size and composition of the NPs, thus allowing easy optical tunability, which is lacking in the case of, e.g., dyes. A detailed description of the observed shape, position and intensity of the LSPR peaks can be found in the corresponding **Publication 3**. However, to aid the selection of an appropriate NP for a suitable application, a brief quantitative discussion of the trends in the LSPR peaks of these NPs now follow.
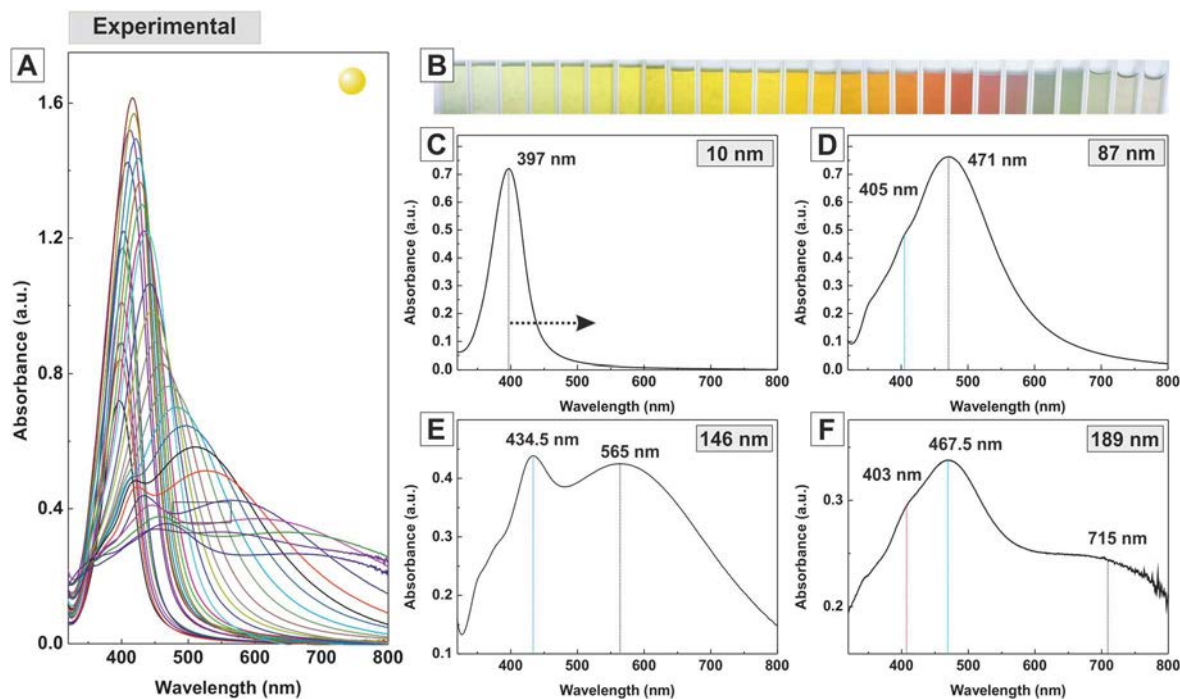
Figure 4.4. Size-dependent extinction spectra of Ag NPs. (A) Extinction spectra of synthetized Ag NPs with diameter from 10 to 218 nm and size deviation from 10% to 7%. Ag concentration in solution was 0.05 mM for the 10 nm and 0.15 mM for the 218 nm Ag NPs (B) Sample vials at increasing NP size. (C-F) Extinction spectra of selected sizes: 10 nm (0.05 mM), 87 nm (0.15 mM), 146 nm (0.15 mM) and 189 nm (0.15 mM). Black/blue/red lines correspond to the dipole/quadrupole/octapole.
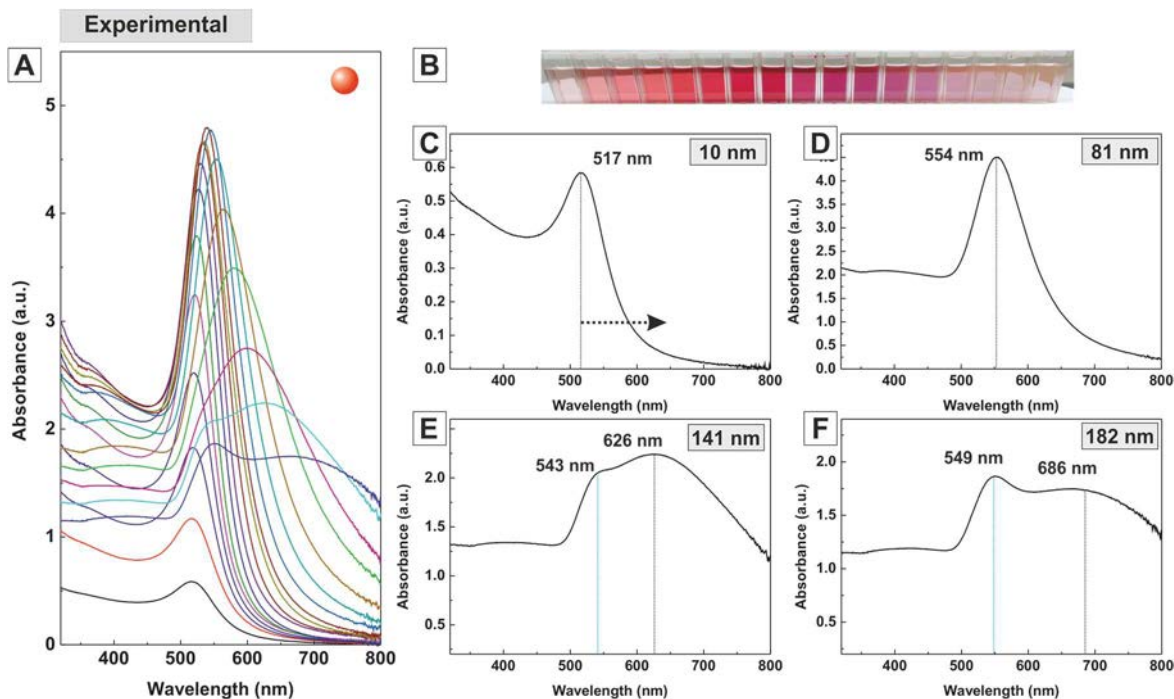
Figure 4.5. Size-dependent extinction spectra of Au NPs. (A) Extinction spectra of synthetized Au NPs with diameters ranging from 10 to 182 nm and size deviation from 11% to 7%. Au concentration in solution was 0.17 mM for the 10 nm and 1 mM for the 182 nm Au NPs. (B) Sample vials at increasing NP size. (C-F) Extinction spectra of selected sizes: 10 nm (0.17 mM), 81 nm (1 mM), 141 nm (1 mM) and 181 nm (0.91 mM). Black/blue lines correspond to the dipole/quadrupole.

4.4.1. Dependence of LSPRs on nanoparticle size

A close look at the spectra of Ag and Au NPs (**Figures 4.4** and **4.5**) shows distinctive LSPR characteristics. In both cases, the initial dipole peak corresponding to 10 nm particles moves to longer wavelengths, or correspondingly to lower energies, as the NPs grow and enters the so called extrinsic size region (the electron cloud is less confined, there is more room for radiation dissipations and high order multipoles increasingly dominate). However, the dipole of Ag NPs covers a wider spectrum in the visible range, starting from a strong and narrow peak around 397 nm for Ag NPs of 10 nm in diameter and ending with a broad and attenuated peak at the near-infrared (>700 nm) for very large Ag NPs of 200 nm. Conversely, the dipole peak of the Au NPs is restricted to a much narrower window for starting at a larger wavelength of 518 nm and ending at the same near-infrared region.

Significant differences in the high multipole peaks can also be observed. The quadrupole appears at smaller sizes and with stronger intensity in the case of Ag NPs than for Au NPs, and the octapole, which can be perfectly observed for Ag NPs of 189 nm (**Figure 4.4 F**), is absent in the Au NPs of the same size (**Figure 4.5 F**). For diameters above 200 nm, these peaks strongly attenuated and became difficult to distinguish, with broad overlapping bands.

Mie plot software was used to compare the experimental spectra with that predicted by the Mie theory (**Figure 4.6**). Overall, experimental results were in general agreement with that theoretically obtained and major differences could be attributed to sample size distribution, which despite being very narrow for the synthetized particles, with size deviations below 10%, still had a significant effect in the final spectra of the NPs. For example, quadrupole and octapole peaks shown in the calculations were experimentally difficult to observe in the large NPs even when these had a relatively low disparity, because high multipole resonances are spectrally very close and quickly overlap to form a broad spectrum (**Figure 4.6F**). From these results, it is highlighted the importance of synthetic protocols for the production of monodisperse NPs for optical applications. Additional differences in the peak position and bandwidth were attributed to slight deviations from a spherical shape, different degree of faceting of each specific NP, the effect of citrate on the surface and/or surface roughness.
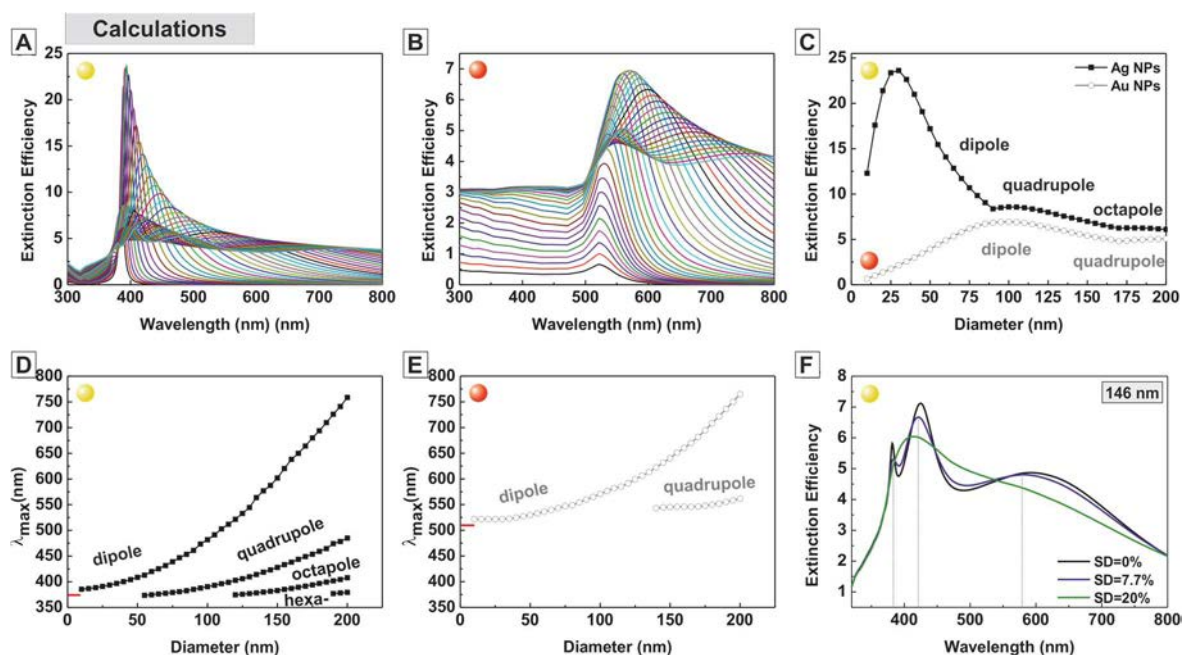
Figure 4.6. Calculated extinction efficiencies of spherical Au and Ag NPs in water. Extinction spectra of (A) Ag and (B) Au NPs with monodisperse size distributions from 10 to 200 nm in diameter. (C) Maximum extinction efficiency and (D-E) position of the dipole peak as a function of particle size. (F) Extinction spectra of 146 nm Ag NPs with varying degree of polydispersity expressed in standard deviation from mean diameter. Calculations obtained from MiePlot software [19] using tabulated frequency dependent dielectric function for bulk gold and silver [17].

This detailed description of the LSPRs for Ag and Au NPs confirm the larger tunability of the Ag NPs, with stronger size dependencies and a larger number of multipoles, more advantageous for optical applications. Additionally, one has to account for the fact that Ag NPs can extinguish light 10-15 times higher than that of Au NPs (in absence of surface oxidation), as deduced from the calculated extinction efficiencies. The lower extinction efficiency of Au NPs arise from their electron IB transitions. As previously mentioned (see **Section 4.2.1.**), these IB transitions overlap with the LSPRs and, consequently, the oscillating electrons may relax via the creation of electron-hole pairs in the upper limit of the IB transitions. This fact however does not deprive Au NPs from still having absorption and scattering coefficients much higher than those of conventionally used dyes, and being of particular interest in many optical applications due to their higher biocompatibility and chemical stability, in particular, against surface oxidation and dissolution [6]. Here, the point is how to achieve a NP with the plasmonic properties of Ag NPs and the chemical stability of Au NPs.

4.4.2. Dependence of LSPRs on surface coating

Besides the influence of NP morphology, it is well established that LSPRs are strongly dependent on the local surrounding medium of the NPs, including substrate, solvent and coating molecules such that those used for stabilising the NPs. This dependence can be seen in equations (**4.3**) and (**4.4**) where the extinction cross-section of the NPs σ_{ext}, is a function of the dielectric constant of the medium, ε_m. In fact, the resonance conditions in the dipole approximation is fulfilled when the real part of the NP dielectric function coincides with the dielectric constant of the medium $\varepsilon_1 = -2\varepsilon_m$, the point at which (**4.3**) and (**4.4**) are maximum. As a result, a change in the dielectric constant of the medium is reflected as shift in the position of the dipole peak. Thus, by monitoring the LSPRs by adsorption or scattering-based techniques in response to surfactant-induced changes in the local environment of the NP, a nanoscale chemical or biosensor can be developed. However, little was known about how the LSPRs respond to the presence of different molecules, particularly, if these molecules chemically interact with the NP surface. Observed LSPR peaks were reported to blue-shift or red-shift depending on a variety of features [1, 27] and reliable theoretical predictions were very difficult (or even impossible) to obtain because of the complexity of the chemical bonding and coating formation on the NP surface. For this reason, a systematic study on the extinction spectra of Au and Ag NPs before and after the addition of different capping molecules was performed in order to quantify the resultant shift in the position of the different peaks (**Figure 4.7**).

Polyethylene glycol (PEG) chains were chosen as model molecules for their widespread use and special interest in biomedicine [28]. The most noticeable effect was a shift in the dipole peak, always to the red, after replacing the initial citrate/tannic coating of the NPs for a PEG coating. This shift depended on both parameters, the chain length and anchoring terminal group of the PEG (**Figure 4.7B, C**). In this regards, larger molecules resulted in larger shifts in the position of the peak than the shorter ones, mostly because they modify to a larger extent the dielectric environment in the surroundings of the NP. In the case of noble metals, the real part of the NP dielectric function ε_1 decreases with increasing wavelength in the visible range (300-800 nm) [3]. An increase in the medium dielectric constant ε_m, on the surface of the NP due to the PEG coating is therefore reflected as a red, and not as a blue, shift in the resonance conditions ($\varepsilon_1 = -2\varepsilon_m$).
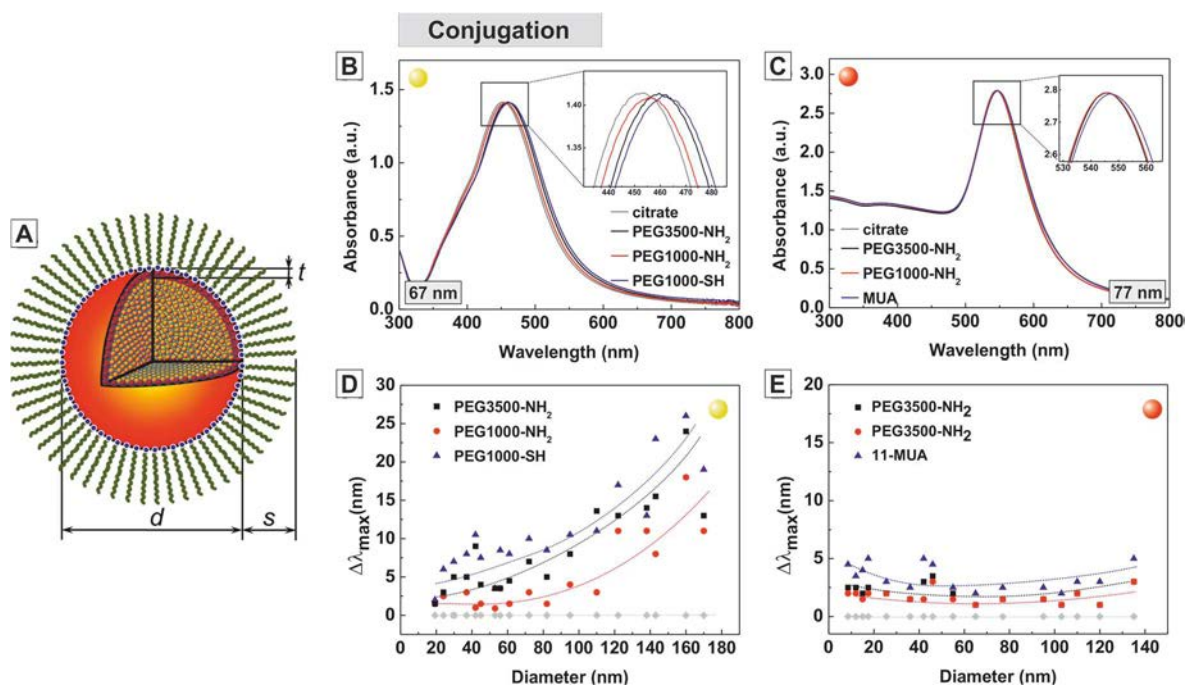
Figure 4.7. Influence of coating molecules on the surface plasmon resonances. (A) Three layer model proposed by Sun *et al.* [27] where *d* is the diameter of the NP, *t* is the thickness of surface atoms behaving as non-metallic due to the chemical bonding and *s* is the thickness of the coating layer. (B, D) Ag and (C, E) Au NPs extinction spectra and shift in the peak position before and after the addition of different PEG molecules.

PEG molecules with different anchor groups were also tested (SH-, NH_3-, COOH). The anchor group additionally contributed to the red-shift of the dipole peak, being the sequences: SH->NH_3->COOH-. In this case, the formation of an outer shell of Au atoms with a non-metallic character has been recently suggested as one possible reason, which would also agree with the observed sequence [27, 29, 30]. Thus, the stronger interactions of PEG molecules with thiol terminated groups confine more electrons at the NP surface than those with amine and carboxylic groups, creating a greater charge localization that interact electrostatically against the oscillating conduction electrons of the LSPRs and changes the position of the peaks to lower energies. The interdependence of both effects, the anchor group and the molecule length, and whether they are perfectly additive or not, is, however, a question that was not solved and needs further research.

Finally, the molecule coating induced shift on the position of the LSPR peaks was also compared between NPs of different sizes, composition and among different resonance modes (**Figure 4.7D, E**). First, in line with previous observations, the resonance peaks of Ag NPs were systematically more sensitive towards surface changes than of Au NPs. Second, the most effective peak for detecting changes on the surface of

NPs was the dipole over the other multipoles. Finally, it was not so evident which was the best NP size. Overall, shifts in the peak position were slightly larger for large NPs but at the same time with lower resolution due to broadening of the bandwidth. This is rather a surprising result in that large NPs experienced larger shifts in the LSPR peaks when coated by the molecules than the small NPs. Because the effect of the anchor group should be larger for the smaller NPs (percentage of electrons involved in the chemical bonding decreases), the reasons underlying this size dependence is probably related to an increasing susceptibility of large NPs to changes in the surface dielectric constant caused by coating molecules [31, 32].

4.5. Results II: Dependences of LSPRs in sub-10 nm gold nanoparticles

In **Chapter 3** and related **Publication 1,** a synthetic protocol for the production of sub-10 nm Au NPs was developed and their extinction spectra were measured experimentally. Because the theory of the LSPR has been introduced in the present chapter, we found interesting to briefly discuss these results here.

Obtained spectra (see **Chapter 3**, spectra of **Figure 2.6**) showed a strong size dependency of the dipole peak of such small Au NPs not counted in the dipole approximation of Mie theory (according to it the LSPR is the same for all NPs smaller than 25 nm). This size dependency is explained as the diameter of the NPs becomes smaller than the mean free path of the conduction electrons and thus they are susceptible to suffer surface scattering during electron oscillation. As a modification of the Mie theory, the metal dielectric function of such small NPs is then assumed to become size-dependent, therefore rendering a size-dependent NP extinction cross section even within the dipole approximation (see **Section 4.2.2.**). This classical picture was suggested by Kreibig [1] and nicely accounts for the tendency of the dipole peak to damp and become wider as the diameter of the NPs decreases below 10 nm.

However, larger discrepancies arise in the literature regarding whether the position of the dipole peak should move to the blue or red as decreasing particle size below 25 nm. The number of quantum effects that predicts a blue shift are comparable to those

predicting a red shift [4]. Moreover, experimental results were often hard to interpret due to the difficulty in separating the effect of size from other contributions, e.g., changes in the particle structure or surface state due to the use of different synthetic pathways for size control. In this context, the experiments described in Chapter 3 acquire special relevance. Because the formation of the Au NPs was achieved following the same protocol and with the same surfactants, the shift to the blue in the dipolar peak from 517 nm down to 505 nm when the diameter of the Au NPs was reduced from 10 to 3.5 nm reflects exclusively the effect of size in the LSPR position of such small NPs..

From these results, it was also observed that small Au NPs were increasing more sensitivity to surface modifications (see **Chapter 3,** table of **Figure 2.6**). As previously discussed, this is probably because the electrons involved in the chemical bond with the coating molecules accounts for a larger percentage in the small NPs than in the large NPs. Interestingly, combining the results of Chapter 3 (Au NPs from 3.5 nm to 10 nm) with the results described previously in this chapter (Au NPs from 10 nm to 200 nm) one can detect a minimum of sensitivity of the dipole peak towards surface modifications for Au NPs with diameters around 50 nm (Figure 4.8). Probably, this is because the LSPR peaks of small NPs are more susceptible to surface modifications because of the chemical bonding with coating molecules counts for a larger percentage of NP conducting electrons while LSPR peaks of large NPs are more susceptible to changes in the local dielectric constant caused by these molecules.
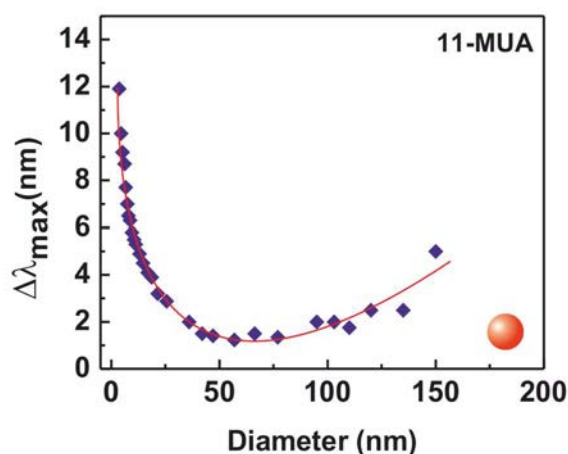
Figure 4.8. Influence of coating molecules on the surface plasmon resonances. Shift in the LSPR position after conjugating citrate-stabilized Au NPs from 3.5 to 200 nm wit 11-mercaptoundecanoic acid.

4.6. Conclusions

In this chapter, a detailed and systematic study of the optical signatures of Ag and Au NPs, including the particular effects that size and surface coating exert on the bandwidth and position of the different LSPR peaks, have been presented. Ag and Au NPs were synthesized following the protocols developed in previous, thus all NPs had the same surface chemistry. Apart from emphasizing the large optical tunability of Ag NPs over Au NPs, with relevant implications for many optical applications, these studies can guide the evaluation of plasmonic NPs subjected to different physicochemical transformations since it is known that the LSPRs are sensitive to changes in the structure of the NPs. An extended discussion related to this point can be found in one of our recent publication [15].

4.7. References

[1] U. Kreibig, M. Vollmer, Optical properties of metal clusters, Springer-Verlag1995.

[2] C.F. Bohren, D.R. Huffman, Absorption and scattering of light by small particles, Wiley1983.

[3] V. Amendola*, et al.*, Surface plasmon resonance in gold nanoparticles: a review, Journal of Physics-Condensed Matter 29 (2017).

[4] X.F. Fan*, et al.*, Light scattering and surface plasmons on small spherical particles, Light-Science & Applications 3 (2014).

[5] Although copper nanoparticles show LSPRs in the visible reagion, these are weaker compared to gold and silver nanoparticles.

[6] P.K. Jain*, et al.*, Calculated Absorption and Scattering Properties of Gold Nanoparticles of Different Size, Shape, and Composition: Applications in Biological Imaging and Biomedicine, The Journal of Physical Chemistry B 110 (2006) 7238-7248.

[7] A. Shiohara*, et al.*, Recent approaches toward creation of hot spots for SERS detection, Journal of Photochemistry and Photobiology C: Photochemistry Reviews 21 (2014) 2-25.

[8] P. Mulvaney, Surface Plasmon Spectroscopy of Nanosized Metal Particles, Langmuir 12 (1996) 788-800.

[9] K.L. Kelly*, et al.*, The Optical Properties of Metal Nanoparticles: The Influence of Size, Shape, and Dielectric Environment, The Journal of Physical Chemistry B 107 (2003) 668-677.

[10] C. Noguez, Surface Plasmons on Metal Nanoparticles: The Influence of Shape and Physical Environment, The Journal of Physical Chemistry C 111 (2007) 3806-3819.

[11] J.Z. Zhang, C. Noguez, Plasmonic Optical Properties and Applications of Metal Nanostructures, Plasmonics 3 (2008) 127-150.

[12] P.K. Jain*, et al.*, Review of Some Interesting Surface Plasmon Resonance-enhanced Properties of Noble Metal Nanoparticles and Their Applications to Biosystems, Plasmonics 2 (2007) 107-118.

[13] X. Huang, M.A. El-Sayed, Gold nanoparticles: Optical properties and implementations in cancer diagnosis and photothermal therapy, Journal of Advanced Research 1 (2010) 13-28.

[14] M.A. Garcia, Surface plasmons in metallic nanoparticles: fundamentals and applications, Journal of Physics D: Applied Physics 44 (2011) 283001.

[15] J. Piella*, et al.*, Modeling the Optical Responses of Noble Metal Nanoparticles Subjected to Physicochemical Transformations in Physiological Environments: Aggregation, Dissolution and Oxidation, Zeitschrift für Physikalische Chemie, 2017, pp. 33.

[16] G. Mie, Contributions to the Optics of Turbid Media: Particularly of Colloidal Metal Solutions, H.M. Stationery Office1976.

[17] P.B. Johnson, R.W. Christy, Optical Constants of the Noble Metals, Physical Review B 6 (1972) 4370-4379.

[18] J. Olson*, et al.*, Optical Characterization of Single Plasmonic Nanoparticles, Chemical Society reviews 44 (2015) 40-57.

[19] P. Laven, http://philiplaven.com/mieplot.htm.

[20] A. Derkachova*, et al.*, Dielectric Function for Gold in Plasmonics Applications: Size Dependence of Plasmon Resonance Frequencies and Damping Rates for Nanospheres, Plasmonics (Norwell, Mass.) 11 (2016) 941-951.

[21] G.V. Hartland, Optical Studies of Dynamics in Noble Metal Nanostructures, Chemical Reviews 111 (2011) 3858-3887.

[22] S. Link, M.A. El-Sayed, Spectral Properties and Relaxation Dynamics of Surface Plasmon Electronic Oscillations in Gold and Silver Nanodots and Nanorods, The Journal of Physical Chemistry B 103 (1999) 8410-8426.

[23] J. Piella*, et al.*, Size-Controlled Synthesis of Sub-10-nanometer Citrate-Stabilized Gold Nanoparticles and Related Optical Properties, Chemistry of Materials 28 (2016) 1066-1075.

[24] V. Myroshnychenko*, et al.*, Modelling the optical response of gold nanoparticles, Chemical Society Reviews 37 (2008) 1792-1805.

[25] S.A. Maier, S.A. Maier, Plasmonics: Fundamentals and applications, Springer2007.

[26] N.G. Bastús*, et al.*, Kinetically Controlled Seeded Growth Synthesis of Citrate-Stabilized Gold Nanoparticles of up to 200 nm: Size Focusing versus Ostwald Ripening, Langmuir 27 (2011) 11098-11105.

[27] S. Peng*, et al.*, Reversing the size-dependence of surface plasmon resonances, Proceedings of the National Academy of Sciences of the United States of America 107 (2010) 14530-14534.

[28] H. Otsuka*, et al.*, PEGylated nanoparticles for biological and pharmaceutical applications, Advanced Drug Delivery Reviews 55 (2003) 403-419.

[29] M.A. Garcia*, et al.*, Surface plasmon resonance of capped Au nanoparticles, Physical Review B 72 (2005) 241403.

[30] B. Foerster*, et al.*, Chemical Interface Damping Depends on Electrons Reaching the Surface, ACS Nano 11 (2017) 2886-2893.

[31] J. Singh Sekhon, S. S Verma, Refractive Index Sensitivity Analysis of Ag, Au, and Cu Nanoparticles, Plasmonics 6 (2011) 311-317.

[32] H. Chen*, et al.*, Shape- and Size-Dependent Refractive Index Sensitivity of Gold Nanoparticles, Langmuir 24 (2008) 5233-5237.

Publication 3

LANGMUIR

Quantifying the Sensitivity of Multipolar (Dipolar, Quadrupolar, and Octapolar) Surface Plasmon Resonances in Silver Nanoparticles: The Effect of Size, Composition, and Surface Coating

Neus G. Bastús,[*,†] Jordi Piella,[†,‡] and Víctor Puntes[*,†,§]

[†]Institut Català de Nanociència i Nanotecnologia (ICN2), Campus UAB, 08193 Bellaterra, Barcelona, Spain
[‡]Universitat Autònoma de Barcelona (UAB), Campus UAB, 08193 Bellaterra, Barcelona, Spain
[§]Institut Català de Recerca i Estudis Avançats (ICREA), 08010 Barcelona, Spain

Ⓢ Supporting Information

ABSTRACT: The effect of composition, size, and surface coating on the sensitivity of localized multipolar surface plasmon resonances has been spectroscopically investigated in high-quality silver colloidal solutions with precisely controlled sizes from 10 to 220 nm and well-defined surface chemistry. Surface plasmon resonance modes have been intensively characterized, identifying the size-dependence of dipolar, quadrupolar, and octapolar modes. Modifications of the NP's surface chemistry revealed the higher sensitivity of large sizes, long molecules, thiol groups, and low-order resonance modes. We also extend this study to gold nanoparticles, aiming to compare the sensitivity of both materials, quantifying the higher sensitivity of silver.
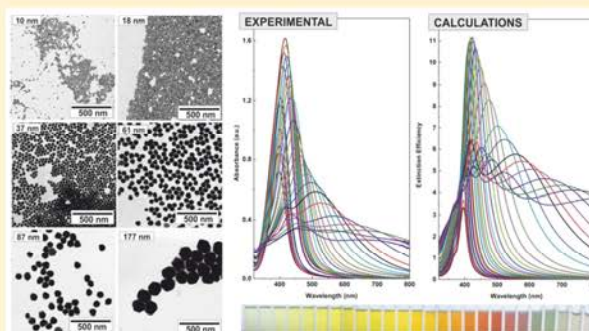
INTRODUCTION

Metal nanoparticles (NPs), particularly those of the noble metals, exhibit strong surface plasmon resonances (SPRs) with intense and broad optical absorption bands that arise from the coherent oscillations of conduction electrons near the NP surfaces and that result in strong localized electric fields at its vicinity. The ability to control those SPRs is critical for achieving advances in many areas, including chemical and biological sensing, imaging, optoelectronics, energy harvesting and conversion, and medicine.[1,2]

Interestingly, the intrinsic properties of NPs can be tailored by controlling their morphology[3] (e.g., size and shape), composition[4] (e.g., monocomponent vs alloys), structure[5] (e.g., solid vs hollow), surface chemistry[6] and structure,[7] and the refractive index of the local environment.[8] Among the three metals that display plasmon resonances in the visible spectrum (Ag, Au, Cu), Ag exhibits the highest efficiency of plasmon excitation, and it is the only material whose plasmon resonance can be tuned to any wavelength in the visible and near-infrared (NIR) range by modifying Ag NP's morphology.[9] Owing to these unique optical properties, Ag is probably the most important material for the next-generation plasmonic technologies.[2] A well-known example is the plasmonic enhancement of Raman scattering, known as surface-enhanced Raman scattering (SERS), where the strong near-fields near the NP's surface allow enhancing spectroscopic signals from molecules, providing ultrasensitive and ultraselective information about its structure and offering molecular-specific signatures for chemical

imaging.[10] Other examples are the plasmonic field-enhanced emission from fluorophores,[11] the relatively unexplored near-field enhancing processes such as natural and magnetic circular dichroism,[12] the local photolithography,[13] the photochemistry and photocatalysis,[14] and the fast dissipation of energy upon plasmon excitation for localized heating.[15]

In this context, one of the key priorities for expanding the applicability of plasmonic NPs is to produce advanced NPs with engineered SPR modes (frequency and intensity) and fields (near-field enhancements, far-field signatures, and spatial profiles). Up to date, most investigations have been focused on the dipolar and quadrupolar resonances in the small particle size regime (2−100 nm),[16,17] while high-order multipole modes in larger or anisotropic NPs have only recently begun to attract attention.[18] The identification of multipolar resonances has been traditionally difficult to achieve due to the relatively wide distributions of Ag NP's sizes and morphologies involved or the restricted size ranges studied, which is translated into the overlapping of the resonance frequencies of the various multipolar plasmons in a broad spectrum.[19] (For instance, the calculated separation between the two peaks of dipolar and quadrupolar absorption in Ag NPs is <75 nm.[20]) In this regard, previous attempts have been restricted to the detection of multipolar modes in nonspherical geometries[21,22] and
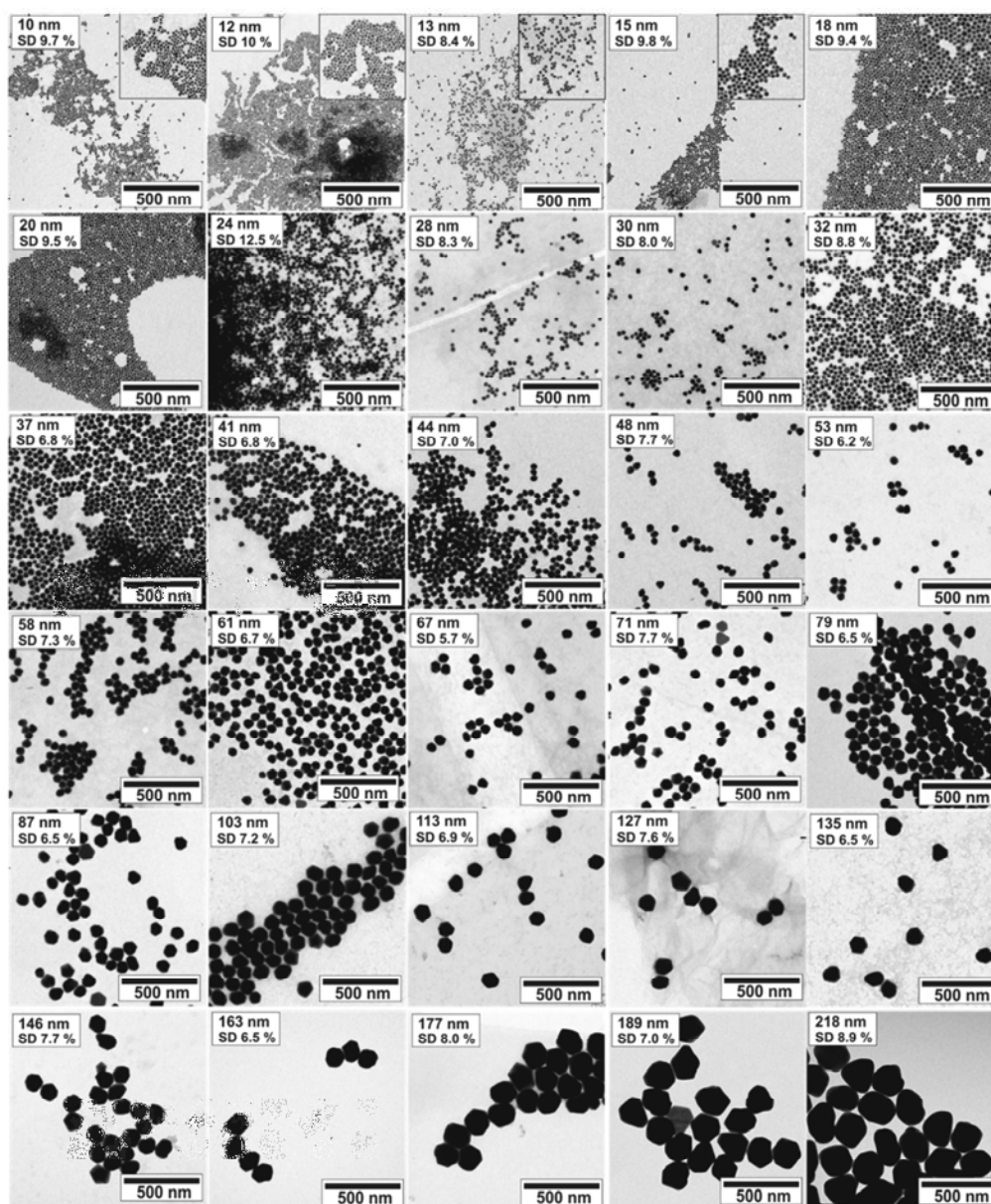
Figure 1. Seeded-growth synthesis of silver nanoparticles. Transmission electron microscopy images of seed particles and those obtained after different growth steps. These Ag NPs represent an ideal class of materials for the study of the precise size and surface-coating dependences of surface plasmon resonances. The particle size increases from ~10 to ~218 nm.

shells.[23,24] Several studies also report the size-dependent optical properties of spherical Au[25,26] and Ag[27−32] NPs observing, in addition to the dipolar resonances, the quadrupolar mode. High-order modes, in particular, the octapolar and hexadeca-polar modes, were theoretically predicted[33] and recently observed for spherical Ag NPs[18] and metallic nanoshells.[23,34]

Beyond the size control, an important requisite is the control of the interaction between the NPs and the surrounding environment, which is usually achieved by its functionalization with the appropriate molecules. In the case of plasmonic NPs, these molecules act as transducers that, after binding to the NPs, convert small increases in the local refractive index (most of these molecules have a higher refractive index than the hosting solution) into spectral red shifts. The magnitude of this red shift usually depends on the size, morphology, and

composition of the metal particle,[35] the nature of the molecule, in detail, its length (the thickness of the dielectric media surrounding the metal core)[36] and chemical bonds formed with surface atoms (the degree of confinement of surface electrons),[16] and its degree of packaging at the surface of the NPs.[37] This molecular binding, which is routinely observed after NP's functionalization,[38−41] has been monitored in real time with high sensitivity[42−44] but not systematically studied, due in part to the complexity of physical and chemical processes involved (oxidation and dissolution) and uncertainties in experimental samples (lack of size control and aggregation). Pioneering studies were reported by Mulvaney and Henglein in Ag NPs;[45,46] however, since then, only a few reports address the study of how optical properties are affected by modifications of the nature of the NP−molecule chemical
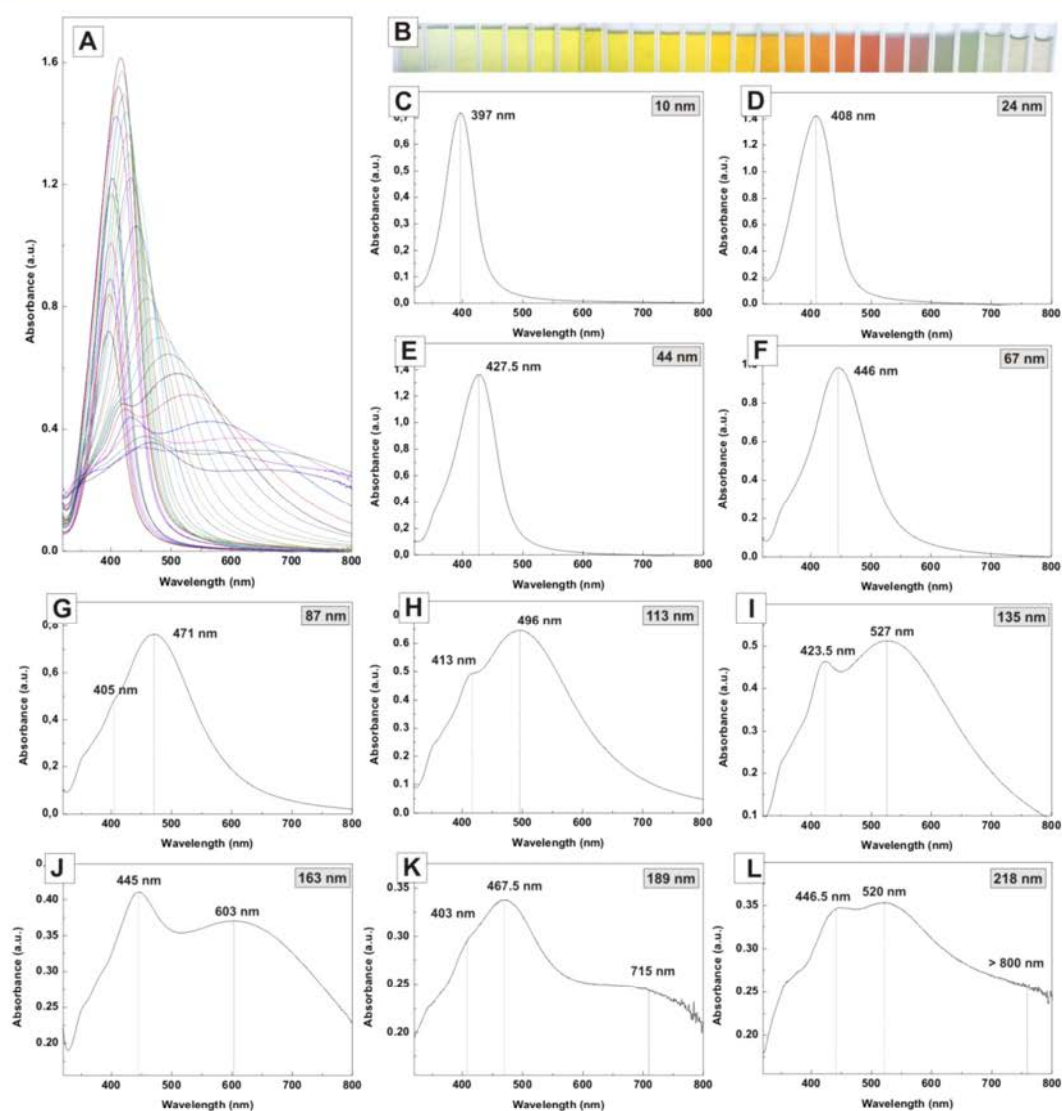
Figure 2. Size-dependent optical properties of silver nanoparticles. (A) Experimental absorption spectra of as-synthesized Ag NPs with diameters ranging from 10 to 218 nm. (B) Photograph of cuvettes showing color tunability with increasing size of Ag NPs (from left to right). Colloidal solutions of small Ag NPs particles appear yellow and totally transparent, while an increased opalescence can be observed in larger particles. (C−L) Individual UV−vis spectra of selected Ag colloids obtained after different growth steps. Black/blue/red lines indicate the position of the dipolar/quadrupolar/octapolar band.

bonding[16] or the thickness of the inorganic[47] or organic coating.[48]

In this work, we present a comprehensible study on how the optical properties of noble metal NPs are affected by systematic variations of NP's size, composition, and surface coating. First of all, we exhaustively analyze the size-dependent optical properties of colloidal solutions of Ag NPs from 10 to 220 nm, with very narrow size distributions (<10%), uniform morphology, and excellent stability, identifying and characterizing the dipolar, quadrupolar, and octapolar modes as the NP size increases. Second, we study how these properties are affected by modifications of NP's surface chemistry, in particular, the nature of the chemical bonding and the length of coating molecule. Finally, we extend this study to Au NPs, aiming to study how different materials present different optical responses after similar variations of its surface. As a result, we found a higher sensitivity (defined as the relative shift in the resonance

wavelength of the SPR mode) of silver than gold, larger than small particles, more dipolar than higher-order modes, more thiol than amine groups, and longer than short molecules. We believe that this study provides not only a better basic understanding of NP's physical properties but also a quantification of the sensitivity of the plasmonic response to the environment, which can be used to select the optimum NP size and composition for a desired application and provide a framework through which the effects of potential system improvements can be assessed. This information is of crucial importance in the engineering of advanced materials with applicability in plasmonic technologies, enhanced spectroscopies and biosensing, integrating for instance, the multiple chemical quantification, molecule identification, and detection of their biological states.
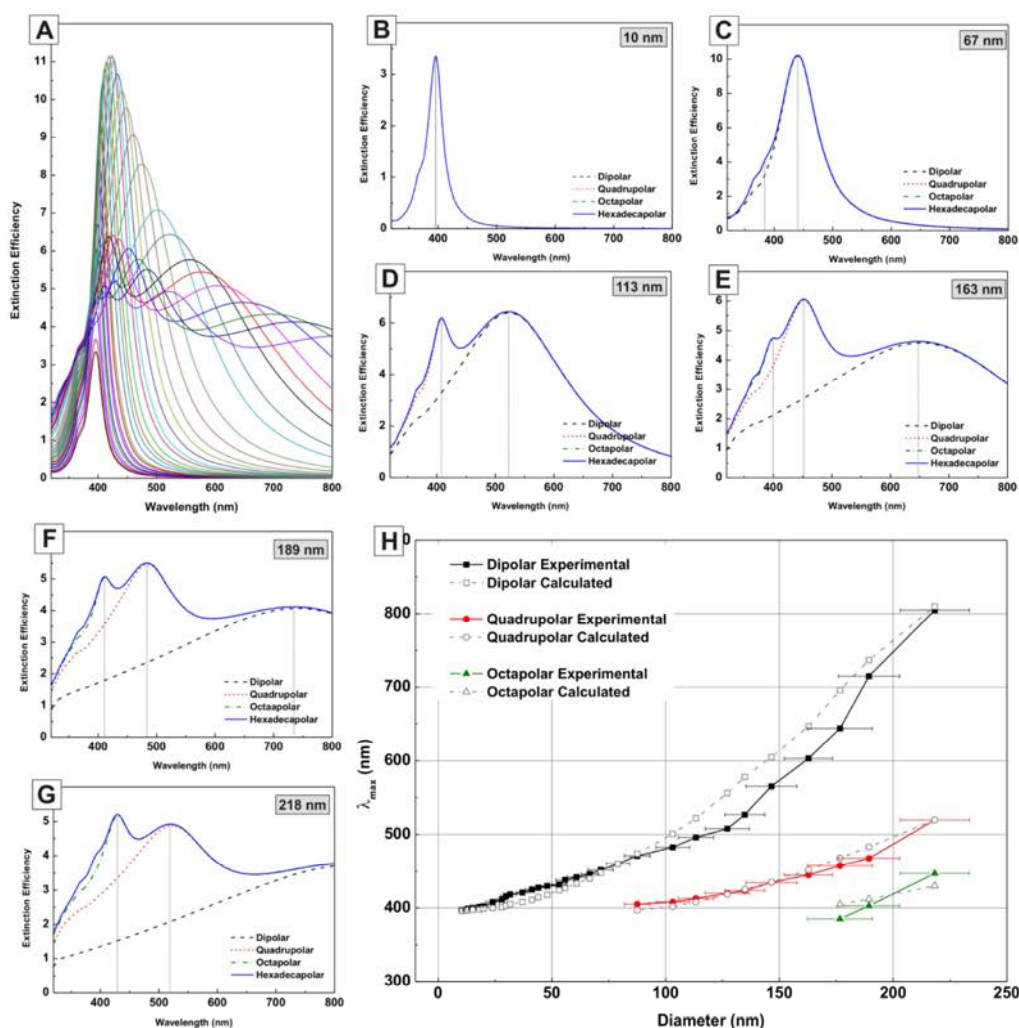
Figure 3. Size-dependent optical properties of silver nanoparticles. (A) Calculated extinction spectra of Ag spheres with diameters ranging from 10 to 218 nm with the average size and standard distribution measured from TEM images of each experimental sample. (B−G) Individual extinction spectra of selected Ag NP's with varying diameters (as-labeled). Full lines were calculated with multipoles up to $l = 4$, whereas dashed-dotted green lines correspond to $l = 3$ (octapoles, quadrupoles, and dipoles), red short dashed lines $l = 2$ (quadrupoles and dipoles), and black dashed lines $l = 1$ (only dipoles). (H) Comparison of size-dependent experimental and calculated dipolar, quadrupolar, and octapolar plasmon resonance positions of Ag NPs. Dipolar modes are plotted in black curves, quadrupolar modes in red curve, and octapolar modes in green curves. Obtained results allow us to reasonably infer a relationship between NP's size measured by TEM and optical absorption peaks that could be useful in determining Ag NP's size from optical data. The contribution of higher order modes (beyond the hexadecapole) can be neglected for the particle sizes under consideration. Similar calculations were performed to confirm the presence of the quadrupolar mode in larger Au NPs.[26]

■ RESULTS AND DISCUSSION

Synthesis of Silver Nanoparticles. The aqueous synthesis of Ag NPs is based on a recently reported improved seeded-growth strategy.[41] $AgNO_3$ is used as a silver precursor, and the reduction was achieved by the combined use of two competing reducing agents: sodium citrate (SC) and tannic acid (TA). The growth of seed particles was kinetically controlled by adjusting the temperature of the reaction, the pH, the seed to Ag precursor ratio, and the balance between both reducing agents. By the control of these synthetic parameters, successive generations of Ag NPs with precisely controlled sizes and nanometer resolution can be produced. Resultant Ag NPs were purified by centrifugation and further redispersed in SC 2.2 mM. Ag NPs are coated with SC/TA molecules, which allow an easy functionalization and excellent dispersibility in aqueous media. The SC/TA capping layer confers stability against

oxidation, corrosion, dissolution, and aggregation in solution.[41] Obtained particles exhibit high uniformity in size, shape, and crystallinity. Representative transmission electron microscopy (TEM) images of Ag NPs used to study the different plasmonic modes and various sizes ranging from 10 to 218 nm can be found in Figure 1, clearly showing their homogeneity, highly monodispersity, and narrow size distribution, with standard deviations below 10% (Figure S1).

Size Dependence of Localized Multipolar Plasmon Resonances in Silver Nanoparticles. Because of their high monodispersity, controlled morphology, long-term stability, and identical surface chemistry, these Ag NPs represent ideal candidates for the study of the precise size-dependent SPRs. Experimental absorbance spectra of the different generations of Ag NPs measured by UV−vis spectroscopy are depicted in Figure 2A (for individual plots see Figure S2). The observed

trend agrees well with the expected changes for increasing Ag NP's sizes, that is, the red shift of the SPR peak and the appearance of higher order modes as the size of the NP increases, and retardation effects gain relevance. Thus, starting from a single and strong peak around 397 nm, corresponding to the dipolar plasmon resonance of ∼10 nm Ag NPs (Figure 2C), it red shifts to longer wavelengths and broadens, peaking at ∼446 nm for Ag NPs with an average diameter of ∼67 nm but still depicting a single band (Figure 2D−F). Above this size, phase retardation effects become more and more important and a new peak starts to develop at shorter wavelengths (∼400 nm) characteristics of quadrupole component of the plasmon resonance (Figure 2G). Even broader dipolar bands located from ∼496 to ∼715 nm and well-defined quadrupolar resonances peaking from ∼413 to ∼467.5 nm can be seen as the size of the Ag NP's increases from ∼87 to ∼189 nm (Figure 2H−K). In this size regime, another feature in the low-wavelength range (∼400 nm) of the spectra also appears as a result of higher-order multipole of the resonance, the octapole, that is no longer hidden under the contribution of the dipole resonance.

The position of the octapolar mode also depends on size, shifting from ∼403 nm to ∼446.5 nm as Ag NP's increases from ∼189 nm to ∼218 nm (Figure 2K,L). In this size regime the dipole is in the near IR spectral range, outside of the spectral window shown in Figure 2. The broadening of resonant bands as particle's size increases can be explained in terms of radiative losses.[26] Thus, when the dimensions of the particle is much smaller than the wavelength of the incident light, such as Ag NPs in the range of 10−65 nm, all electrons in the entire particle experiences a roughly uniform electric field leading to the excitation of the dipolar plasmon resonance. As Ag NP's size increases, light cannot polarize homogeneously and the field is no longer uniform throughout the NP, which result in phase retardation effects. As a consequence, a red-shift and broadening of the dipolar resonance is observed in larger particles along with the appearance of higher-order modes. Similar results were reported by Chumanov and coworkers[18] that identifies spectroscopically the multipolar plasmon resonances (up to the hexadecapolar mode) of spherical Ag NPs produced at low concentration by hydrogen reduction method. The analysis was carried out during Ag NP's growth process, without directly correlating the optical and morpho-logical (size-shape) characterization of the samples. Herein we extent this study, providing the size dependence of Ag multipolar modes.

As a result of these unique optical properties, Ag NPs of different sizes exhibit different colors (Figure 2B) and different degrees of absorption and scattering of light. Thus, suspensions of small particles appear yellow and totally transparent as the absorption contribution of the dipole resonance dominates the extinction spectrum. For larger particles, increased scattering (iridescence) can be observed, as the resonant scattering of the multipole resonance becomes a dominating spectral compo-nent. In this size regime, the scattering cross section exceeds their geometric cross section (for instance, the scattering cross section of 60 nm Ag NPs is more than 6 times greater than their geometric cross section[17]), which makes Ag NPs unique optical labels that can easily be seen by optical microscopy.

Experimental absorbance data can be easily compared with calculations based on the standard Mie theory of spherical particles. Figure 3A plots the extinction spectra, containing both absorption and scattering contributions, calculated for Ag spheres of different sizes using MiePlot software (for individual plots see Figure S3), where it can be seen how the above assignments in the modes as Ag NP size increases are consistent with theoretical calculations. This is further confirmed by calculating the deconvoluted spectra restricted to just one mode (Figure 3B−G) using Nanosphere Optics Lab Field Simulator.[49] The calculations restricted to dipoles (black dashed curves) exhibit just the dipolar band and work extremely well for small particles, while high-order modes corrections are needed for larger particles. Thus, the inclusion of quadrupolar modes (red short-dashed lines) results in an additional band that increases in intensity as the particle size increases. For even larger particles, the contribution of high-order modes, in particular, the octapolar moment (green dashed-dotted lines), explains additional features (band/shoulder) seen in the UV−vis spectra.

The general experimental trend is really predictable, as revealed in Figure 3H, where dipolar, quadrupolar, and octapolar plasmon resonance positions are plotted as a function of Ag NP's diameter for both experimental and calculated spectra. Despite the impressive correlation between exper-imental results and Mie calculations, full agreement is not observed in band position and intensity. These differences, previously observed in other systems,[50] may be related to slight deviations from the spherical shape, different degree of faceting of each specific particle, or surface roughness;[7] however, major differences can be attributed to sample dispersity because the degree of monodispersity dramatically affects the overall UV−vis spectra. In this regard, we compared the calculated results for the same Ag NP size but with varying standard deviations, that is, the monodisperse case (SD = 0%), the standard distribution measured from TEM images of each sample (SD < 10%), and the polydisperse case with SD = 20% (the standard dispersity of Ag NPs obtained following other reported synthetic strategies) (Figure S3). As expected, while no substantial differences are observed for small particles, quadrupolar and octapolar bands cannot be observed in larger particles if the degree of dispersity is >10% because these resonances are spectrally very close and overlap to form a broad spectrum.

The assignment of the resonance modes is also illustrated by calculating the near-field enhancement (NFE) when Ag NPs are illuminated with light of the respective maximum absorption wavelengths. Results obtained for spheres of selected sizes (Figures S4 and S5) clearly demonstrate that the excitation of plasmon resonances results in an enhanced field that is several orders of magnitude larger than the incident field. This field and the corresponding hot spots generated by the higher order resonances can be potentially exploited for the enhancement of many optical processes such SERS, enhanced fluorescence, and enhanced IR absorption. Apart from these size considerations, this near-field Ag NP is also influenced by the variations of the density of conduction band electrons in the particles that take place when the dielectric constant around NPs is modified. As a result, applications related to the near field phenomena (e.g., SERS) may be improved by controlling Ag NP's surface chemistry (vide infra).

Effect of the Surface Coating on the SPR Shifts Induced by Modifications in NP's Surface Chemistry. Beyond the size-dependent optical properties previously presented, highly monodisperse Ag NPs herein synthesized are model materials to study the effect of the surface interactions on the SPRs, in particular, how the nature of the
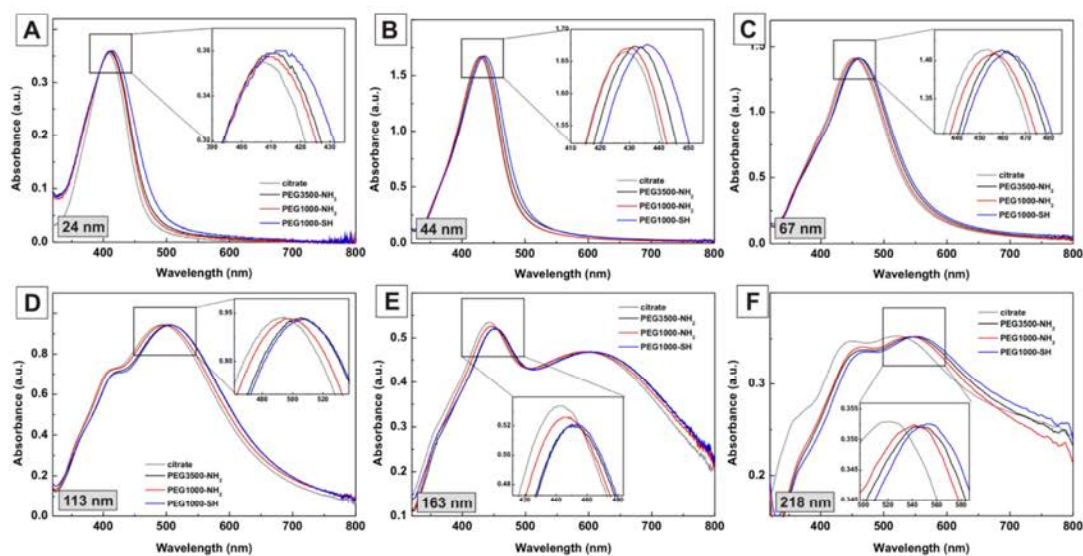
Figure 4. Functionalization of Ag NPs with different PEG molecules. UV−vis spectra of Ag NPs of different sizes 24 (A), 44 (B), 67 (C), 113 (D), 163 (E), and 218 nm (F) recorded before (gray line) and after the ligand exchange process with PEG3500-NH$_2$ (black line), PEG1000-NH$_2$ (red line), and PEG1000-SH (blue line). Once the native molecules are replaced by PEG molecules the corresponding absorption peak shifts to the red a certain value that depends on Ag NP's size, molecule's length, and nature of the chemical bonding. Spectra reveal the higher sensitivity (measured in terms of larger red shifts) of larger Ag NPs for a determined coating and of long and thiol-terminated molecules for a determined size.
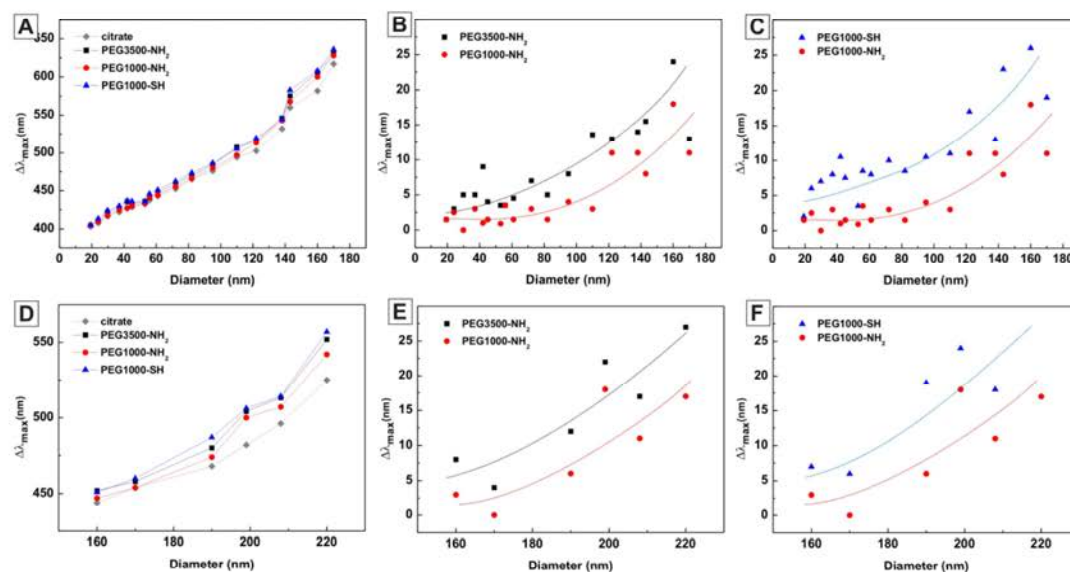

Figure 5. Influence of functionalization on the SPR absorption peak of Ag NPs of different sizes. Dependence of the dipolar (A) and quadrupolar (D) absorption peak position for Ag NPs of varying sizes before (gray symbol) and after ligand exchange with PEG3500-NH$_2$ (black symbol), PEG1000-NH$_2$ (red symbol), and PEG1000-SH (blue symbol). Dependence of absorption peak shift on molecule's length and nature of the chemical bonding (anchor group) for different Ag NP sizes. Dipolar (B) and quadrupolar (E) absorption peak shift after ligand exchange with PEG3500-NH$_2$ (black symbol) and PEG1000-NH$_2$ (red symbol). Both molecules present the same anchor group (NH$_2$) but different lengths (MW1000 vs MW3500). Dipolar (C) and quadrupolar (F) absorption peak shift after ligand exchange with PEG1000-NH$_2$ (red symbol) and PEG1000-SH (blue symbol). Both molecules present the length (MW1000) but differ in the anchor group. Results reveal the higher sensitivity of the dipolar mode in comparison with the quadrupolar and octapolar mode for a determined size.

anchor group and the length of the molecule attached to Ag NP's surface affect plasmon resonances. We chose polyethylene glycol (PEG) ligands as model molecules for their wide use and special interest in biomedicine;[51,52] however, obtained results extend this particular use because the quantification of the sensitivity of the plasmonic response to the environment is of

crucial importance for the general engineering of plasmonic nanostructures.

To investigate the effect of surface interactions we carried out ligand exchange experiments to replace the native SC/TA molecules on the Ag NP's surface with three different molecules: (i) thiol-modified poly(ethylene glycol) (SH-PEG1000-COOH, $M_W \approx 1000$ g/mol), (ii) amino-modified
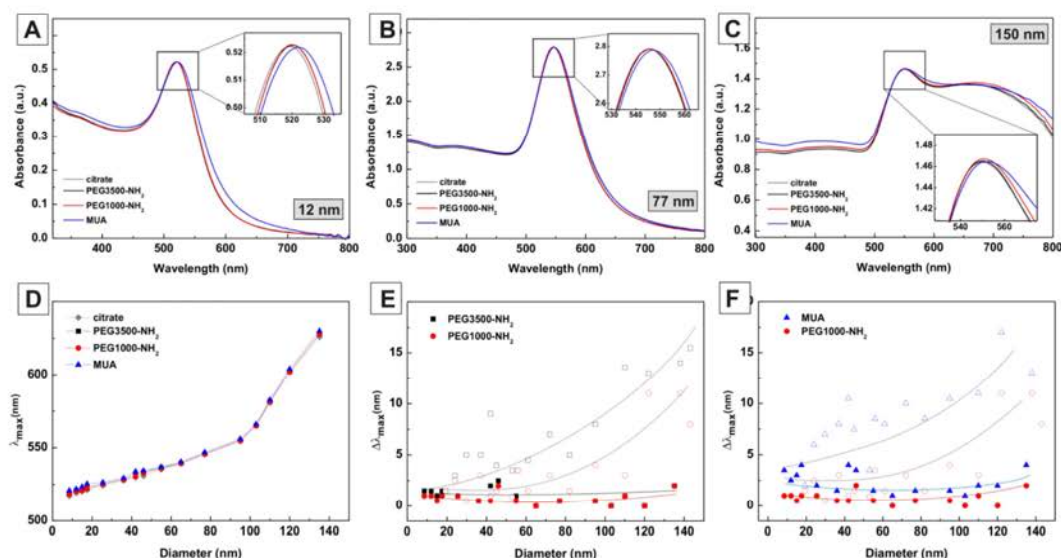
- 144 -

Figure 6. Functionalization of Au NPs with different PEG molecules. UV−vis spectra of Au NPs of different sizes 12 (A), 77 (B), and 150 nm (C) recorded before (gray line) and after the ligand exchange process with PEG3500-NH$_2$ (black line), PEG1000-NH$_2$ (red line), and MUA (blue line). Once the native molecules are replaced the corresponding absorption peak shifts to the red a certain value that depends on Au NP's size, molecule's length, and nature of the chemical bonding. Influence of ligand exchange on the SPR absorption peak of Au NPs of different sizes. (D) Dependence of the dipolar absorption peak positions for Au NPs of varying sizes before (gray symbol) and after ligand exchange with PEG3500-NH$_2$ (black symbol), PEG1000-NH$_2$ (red symbol), and MUA (blue symbol). Dependence of absorption peak shift on molecule's length and nature of the chemical bonding (anchor group) for different Au NP sizes. (E) Dipolar absorption peak shift after ligand exchange with PEG3500-NH$_2$ (black symbol) and PEG1000-NH$_2$ (red symbol). Both molecules present the same anchor group (NH$_2$) but different lengths (MW1000 vs MW3500). For comparison, the values obtained for Ag NPs were also plotted (gray line, hollow symbol). (F) Dipolar absorption peak shift after ligand exchange with PEG1000-NH$_2$ (red symbol) and MUA (blue symbol). Both molecules present similar length but differ in the anchor group. For comparison, values obtained for Ag NPs were also plotted (gray line, hollow symbol). For Ag NPs, PEG1000-SH was used instead of MUA.

poly(ethylene glycol) (NH$_2$-PEG1000-COOH, $M_W \approx$ 1000 g/mol), and (iii) amino-modified poly(ethylene glycol) (NH$_2$-PEG3500-COOH, $M_W \approx$ 3500 g/mol). SH-PEG1000 and NH$_2$-PEG1000 differ in the anchor group (i.e., the nature of the chemical bonding), while their length is the same ($M_W \approx$ 1000 g/mol, ~4.3 nm[53]). On the contrary, NH$_2$-PEG1000 and NH$_2$-PEG3500 present the same anchor group (NH$_2$) but different lengths ($M_W \approx$ 1000 g/mol, ~4.3 nm vs $M_W \approx$ 3500 g/mol, ~7.9 nm[53]). In all cases, the PEG chain length was calculated according to Hill,[54] and a full coating layer of PEG in a mushroom conformation at Ag NP's surface in water was considered. Ligand exchange was performed by adding known amounts of PEG molecules to Ag NPs solutions under vigorous stirring. The mixture was allowed to react for 2 (SH-PEG) or 12 h (NH$_2$−PEG), when no further peak evolution was detected by UV−vis spectroscopy. PEG-modified particles were then centrifuged to remove excess PEG and finally redispersed in the same volume of milli-Q water. The ligand exchange is a spontaneous process because the thiol and amino groups form stronger bonds with Ag surfaces than the carboxylic groups in the original citrate/tannic molecules. Intensive characterization of Ag NPs before and after ligand exchange shows that neither aggregation nor observable structural or morphological change took place, indicating that the observed results are due to modifications on NP's surface chemistry.

The absorption spectra of Ag NPs of selected sizes before and after the ligand exchange process with the different PEG molecules are shown in Figure 4. Once SC/TA molecules are replaced the corresponding absorption resonance peaks shift to the red. Results are summarized in Figure 5. In a simplified manner we attribute that the extent of the red shift depends on

molecule length and nature of the chemical bonding, assuming a full surface coverage of the NP, as previously considered in the study of the affinity of different functional groups onto Au thin films and electrodes.[40] In this scenario, spectra reveal a higher sensitivity (measured in terms of higher red shifts) of (i) large sizes, (ii) long PEG molecules, (iii) SH anchor groups, and (iv) low-order resonance modes. Thus, higher sensitivity of larger sizes and the different sensitivity of dipolar and quadrupolar modes can be correlated with the size-dependent near-field profiles of the different resonance modes shown in Figure S4.[55] Besides, its dependence on the length of the molecule is directly related to the increase in the thickness of the dielectric layer in the vicinity of the Ag NP surface.[35] Thus, SPRs peaks shift toward the red as the coating layer thickness increases, reaching a maximum value (Figure S7). This limiting thickness of the organic layer that has an effect on the SPRs depends on the maximum distance to which the local field extends from NP's surface.[35] This phenomenon has been widely reported for the dipolar mode in silica-coated Ag NPs[47] and in multilayers of long-chain thiols,[48] and it is expected to have a similar effect for the higher order multipoles.[18]

It is important to clarify that we assume that NPs are surrounded by a dense coating layer (full surface coverage) with a thickness determined by the length of the molecule and a refractive index determined by its nature. In this regard, observed effects could be affected by the different degree of packaging of the molecules in NPs of different sizes (Figure S8). Thus, the radius of curvature of spherical NPs of varying sizes determines the respective molecule loading density, being lower in small NPs due to its higher curvature radii.[56] This factor, along with the length and particular hydrophobicity/
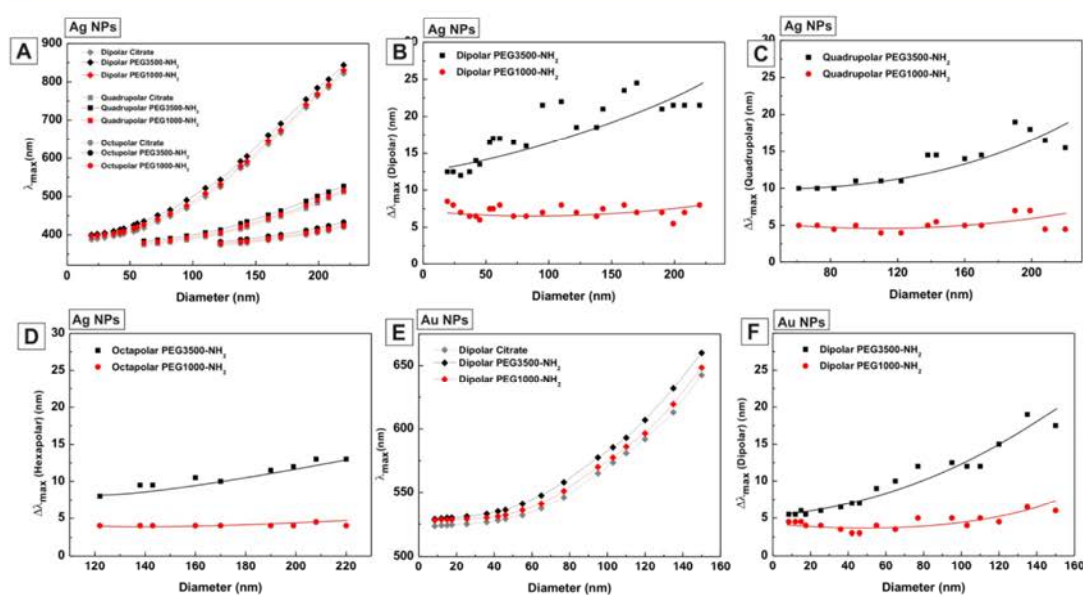
Figure 7. Influence of functionalization on the SPR absorption peak of silver and gold NPs of different sizes. (A) Dependence of the surface plasmon resonance absorption peaks positions for Ag NPs of varying sizes before (gray symbol) and after ligand exchange with PEG3500-NH₂ (black symbol) and PEG1000-NH₂ (red symbol). Dependence of the dipolar, quadrupolar, and octapolar absorption peak shifts on molecule's length for Ag and Au NPs of different sizes. Dipolar (B), quadrupolar (C), and octapolar (D) absorption peak shift for Ag NPs after ligand exchange with PEG3500-NH₂ (black symbol) and PEG1000-NH₂ (red symbol). Dipolar (E) and quadrupolar (F) absorption peak shift of Au NPs after ligand exchange with PEG3500-NH₂ (black symbol) and PEG1000-NH₂ (red symbol). Calculations were performed considering a PEG shell of 4.3 nm (PEG1000) or 7.9 nm (PEG3500) and refractive index 1.46. For citrate-stabilized Au or Ag NPs, a shell thickness of 0.7 nm and refractive index 1.3735 was used.

hydrophilicity of the molecule,[36,40] and the effectivity of the ligand exchange determine the effective dielectric constant, which ultimately affects the red shift of SPRs.[57]

Finally, the chemically induced reduction of the conduction band electrons is a major reason behind the red shift seen in the spectral changes when the anchor group of the molecule was modified. Thus, thiol groups can confine more conduction-band electrons of the Ag surface atoms, reducing the overall electronic density and thus leading to greater red shift of the SPR peak position. In this regard, a multilayer model based on the modification of the density of conduction band electrons of the outer core material has been recently suggested,[16] reporting that the formation of chemical bonds with amines or thiols reduces the density of conduction band electrons in the surface by 36.8 and 45.2%, respectively, in comparison with that of bulk Ag. We believe that this study can provide valuable information about the use of metal NPs in sensing applications, surface-enhanced spectroscopies, fluorescence, and even catalysis because it can be used to select the optimum NP size and composition for a desired application while providing a framework through which potential improvements can be assessed.

Effect of the Composition on the SPR Shifts Induced by Modifications in NP's Surface Chemistry. To study the effect of composition on the plasmonic response, highly monodisperse citrate-stabilized Au NPs with diameters ranging from ~10 to ~150 nm, uniform quasi-spherical shape, and narrow size distribution (<10%) were synthesized following an improved kinetically controlled seeded growth strategy[25,41] and ligand exchange experiments were performed with mercaptoundecanoic acid (MUA), PEG1000-NH₂ and PEG3500-NH₂ following a similar procedure than that described for Ag NPs. Herein, MUA was chose as a model thiol-terminated molecule

for its widely and extensively use, as the other molecules, in the functionalization of Au NPs and chosen for the study of the affinity of different functional groups for Au.[58] Results summarized in Figure 6 after and before ligand exchange with the different molecules show a higher sensitivity of (i) larger Au NPs, (ii) longer molecules, (iii) SH anchor groups, and (iv) dipolar modes, in agreement with that observed for Ag NPs. It can be clearly seen how the sensitivity of Au NPs is systematically lower than that Ag NPs obtaining, for the dipolar moment and PEG3500-NH₂ ligand, $\Delta\lambda \approx 5$ nm (Au NPs, 150 nm) and $\Delta\lambda \approx 20$ nm (Ag NPs, 150 nm) (Figure 6D−F). This difference was attributed to lower electromagnetic field strength at the surface of the Au NPs and was proved by calculating the near-field enhancement maps of spherical Au NPs of different sizes and shapes induced by optical excitation of their plasmon resonances (Figure S6).[55]

Simulations Surface Coating. With the aim of gaining further insight into the surface chemistry effect, extinction efficiencies of Ag and Au spheres of varying diameters and surface coatings have been calculated following the standard Mie theory. We chose Mie approach due to the simplicity of the modeling, the availability of the calculation software,[59] and the many previous works that have shown it to be powerful method for modeling SPRs.[60] Calculations were carried out considering a total spherical core with the average size determined from TEM analysis coated by an organic shell with a thickness of 4.3 (MW1000) or 7.9 nm (MW3500). The refractive index (RI) of the organic PEG layer used was 1.465 (20 °C), and NPs were considered dispersed in water (RI = 1.333, 20 °C). Figure 7 shows a series of calculations for PEG-coated Ag and Au systems confirming experimentally obtained results. Thus, it can be seen how independently of the thickness of the organic coating the optical sensitivity depends on the

composition of the core and the size of the NPs, being systematically higher for Ag than Au, and for larger than small NPs (Figure 7A–D). The dependence on the surface coating is further illustrated by plotting the position of the different modes versus the size of the Ag (Figure 7B,C,E) and Au (Figure 7F) NPs for different thicknesses of the organic coating. Calculated spectra confirm the higher sensitivity of the dipolar mode than higher-order modes reaching maximum red shifts of ~20 (dipolar), ~5 (quadrupolar), and ~5 nm (octopolar) for ~200 nm Ag NPs coated with PEG-3500. Unfortunately, the dependences of the anchor group could not be modeled with the multilayer Mie theory platform used. In this regard, the incorporation of the contribution of the chemical bonds between capping molecules and surface atoms through variations of the dielectric constant of the NP's core could lead to results that better match the experimental observations.[16] All in all, the excellent correlation between experimental results and Mie calculations confirms the working hypothesis, that is, the possibility of precisely controlling SPR modes by adjusting NP size, composition, and surface chemistry.

CONCLUSIONS

In summary, we studied the effect of composition, size, and surface coating on the sensitivity of localized multipolar surface plasmon resonances in colloidal solutions of silver and gold nanoparticles with precisely controlled sizes from 10 to 220 nm and well-defined surface chemistry. We spectroscopically characterize the size dependence of higher order resonances, in particular, the quadrupolar and octopolar modes. Besides, obtained nanoparticles were also used as model materials to study the dependence of surface chemistry on the optical properties and infer the impact of anchor group and length of the surface molecules on the sensitivity of surface plasmon resonance modes. As a result, we reveal how surface plasmon resonances are very sensitive toward chemical bonds formed between the surface Ag atoms and capping molecules, which can be used, in turn, to fine control the light-induced particle interactions. This general idea could allow reaching the advanced use of noble-metal NPs as analytical tools for plasmonics and chemical-sensing quantification, detention, and molecular identification.

MATERIALS AND METHODS

Chemicals. Silver nitrate ($AgNO_3$), hydrogen tetrachloroaurate-(III) ($HAuCl_4 \cdot 3H_2O$), trisodium citrate ($Na_3C_6H_5O_7$), tannic acid ($C_{76}H_{52}O_{46}$), poly(ethylene glycol) 2-aminoethyl ether acetic acid ($M_W \approx 1000$ g/mol, $n = 22$) (NH_2-PEG1000-COOH), poly(ethylene glycol) 2-aminoethyl ether acetic acid ($M_W \approx 3500$ g/mol, $n = 77$) (NH_2-PEG3500-COOH), poly(ethylene glycol) 2-mercaptoethyl ether acetic acid ($M_W \approx 1000$ g/mol, $n = 22$) (SH-PEG1000-COOH), and 11-mercaptoundecanoic acid (MUA) were purchased from Sigma-Aldrich. All chemicals were used as received without further purification. Distilled water passed through a Millipore system ($\rho = 18.2$ MΩ) was used in all experiments. All glassware was first rinsed with acetone and then with Millipore water before use.

Methods. *Synthesis of Noble-Metal Nanoparticles.* Highly monodisperse sodium-citrate-coated spherical silver nanoparticles with controlled sizes ranging from 10 to 220 nm have been synthesized by following a kinetically controlled seeded-growth approach via the reduction of silver nitrate by the combination of two chemical reducing agents: sodium citrate and tannic acid.[41] A similar seeded-growth strategy has been followed to produce citrate-stabilized Au NPs from 10 to 150 nm.[25] Resultant NPs were purified by centrifugation (10 000g to 18 000g, depending on its size) to

remove the excess of tannic acid and further redispersed in Milli-Q-water or sodium citrate 2.2 mM before sample characterization and ligand exchange experiments.

Ligand Exchange of Noble-Metal Nanoparticles with Poly-(ethylene glycol). For ligand exchange experiments, aqueous solutions of (i) thiol-modified poly(ethylene glycol) (SH-PEG1000-COOH, $M_W \approx 1000$ g/mol), (ii) amino-modified poly(ethylene glycol) (NH_2-PEG1000-COOH, $M_W \approx 1000$ g/mol), (iii) amino-modified poly-(ethylene glycol) (NH_2-PEG3500-COOH, $M_W \approx 3500$ g/mol), and (iv) mercaptoundecanoic acid (MUA) were prepared and added to as-synthesized NPs solutions under vigorous stirring (final concentration 0.5 mM). The mixture was allowed to react for 2 h (SH-PEG1000-COOH) or 12 h (NH_2-PEG1000-COOH, NH_2-PEG3500-COOH), and resultant NPs were then centrifuged to remove excess of unreacted molecules and finally redispersed in the same volume of milli-Q water.

Techniques. *UV–vis Spectroscopy.* UV–visible spectra were acquired with a Shimadzu UV-2400 spectrophotometer. NP solutions were placed in a cell, and spectral analysis was performed in the 300–800 nm range at room temperature.

Transmission Electron Microscopy. NPs were visualized using 80 keV TEM (Jeol 1010, Japan). Ten microliter droplets of the sample were drop cast onto a piece of ultrathin Formvar-coated 200-mesh copper grid (Ted-pella) and left to dry in air. TEM images of the prepared colloidal NPs were used for the size distribution measurements. For each sample, the size of at least 500 particles was measured and the average size and standard deviation were obtained.

Calculations. Calculations of extinction, absorption, and scattering spectra of colloidal Au and Ag NPs of different diameters were obtained using Mie plot software considering Au or Ag spheres embedded in water at 25 °C. In all cases, mean size and standard distribution of SD = 0%, SD < 10% (that measured by TEM), and SD = 20% were used for the calculations. Deconvoluted extinction, absorption and scattering spectra and near-field intensity and distribution profiles of Ag and Au NPs were calculated using the "Nanosphere Optics Lab Field Simulator" platform. Effects of surface coating were modeled using the "Extinction, Scattering and Absorption efficiencies of single and multilayer nanoparticles" platform. Calculations were carried out considering a total Au/Ag spherical core with the average size determined from TEM analysis coated by an organic shell with a thickness of 4.3 nm (M_W 1000) or 7.9 nm (M_W 3500). The refractive index (RI) of the organic PEG layer used was 1.465 (20 °C), and NPs were considered dispersed in water (RI = 1.333, 20 °C).

ASSOCIATED CONTENT

Ⓢ Supporting Information

The Supporting Information is available free of charge on the ACS Publications website at DOI: 10.1021/acs.lang-muir.5b03859.

Details of characterization and analysis of Ag samples together with calculated extinction spectra and near-field enhancement maps. (PDF)

AUTHOR INFORMATION

Corresponding Authors
*E-mail: neus.bastus@icn.cat (N.B.).
*E-mail: victor.puntes@icn.cat (V.P.).

Notes
The authors declare no competing financial interest.

■ REFERENCES

(1) Jain, P.; Huang, X.; El-Sayed, I.; El-Sayed, M. Review of Some Interesting Surface Plasmon Resonance-enhanced Properties of Noble Metal Nanoparticles and Their Applications to Biosystems. *Plasmonics* **2007**, *2* (3), 107−118.

(2) Rycenga, M.; Cobley, C. M.; Zeng, J.; Li, W.; Moran, C. H.; Zhang, Q.; Qin, D.; Xia, Y. Controlling the Synthesis and Assembly of Silver Nanostructures for Plasmonic Applications. *Chem. Rev.* **2011**, *111* (6), 3669−3712.

(3) Lu, X.; Rycenga, M.; Skrabalak, S. E.; Wiley, B.; Xia, Y. Chemical Synthesis of Novel Plasmonic Nanoparticles. *Annu. Rev. Phys. Chem.* **2009**, *60* (1), 167−192.

(4) Jain, P. K.; Huang, X.; El-Sayed, I. H.; El-Sayed, M. A. Noble Metals on the Nanoscale: Optical and Photothermal Properties and Some Applications in Imaging, Sensing, Biology, and Medicine. *Acc. Chem. Res.* **2008**, *41* (12), 1578−1586.

(5) Wiley, B.; Sun, Y.; Mayers, B.; Xia, Y. Shape-Controlled Synthesis of Metal Nanostructures: The Case of Silver. *Chem. - Eur. J.* **2005**, *11* (2), 454−463.

(6) Chanana, M.; Liz-Marzán, L. M. Coating matters: the influence of coating materials on the optical properties of gold nanoparticles. *Nanophotonics* **2012**, *1* (3), 199−220.

(7) Rodriguez-Fernandez, J.; Funston, A. M.; Perez-Juste, J.; Alvarez-Puebla, R. A.; Liz-Marzan, L. M.; Mulvaney, P. The effect of surface roughness on the plasmonic response of individual sub-micron gold spheres. *Phys. Chem. Chem. Phys.* **2009**, *11* (28), 5909−5914.

(8) Kreibig, U.; Vollmer, M. Optical Properties of Metal Clusters. *Springer Ser. Mater. Sci.* **1995**, *25*, 1−535.

(9) Evanoff, D. D.; Chumanov, G. Synthesis and Optical Properties of Silver Nanoparticles and Arrays. *ChemPhysChem* **2005**, *6* (7), 1221−1231.

(10) Camden, J. P.; Dieringer, J. A.; Zhao, J.; Van Duyne, R. P. Controlled Plasmonic Nanostructures for Surface-Enhanced Spectroscopy and Sensing. *Acc. Chem. Res.* **2008**, *41* (12), 1653−1661.

(11) Tam, F.; Goodrich, G. P.; Johnson, B. R.; Halas, N. J. Plasmonic Enhancement of Molecular Fluorescence. *Nano Lett.* **2007**, *7* (2), 496−501.

(12) Lieberman, I.; Shemer, G.; Fried, T.; Kosower, E. M.; Markovich, G. Plasmon-Resonance-Enhanced Absorption and Circular Dichroism. *Angew. Chem., Int. Ed.* **2008**, *47* (26), 4855−4857.

(13) Sundaramurthy, A.; Schuck, P. J.; Conley, N. R.; Fromm, D. P.; Kino, G. S.; Moerner, W. E. Toward Nanometer-Scale Optical Photolithography: Utilizing the Near-Field of Bowtie Optical Nano-antennas. *Nano Lett.* **2006**, *6* (3), 355−360.

(14) Seh, Z. W.; Liu, S.; Low, M.; Zhang, S.-Y.; Liu, Z.; Mlayah, A.; Han, M.-Y. Janus Au-TiO2 Photocatalysts with Strong Localization of Plasmonic Near-Fields for Efficient Visible-Light Hydrogen Generation. *Adv. Mater.* **2012**, *24* (17), 2310−2314.

(15) Di Corato, R.; Palumberi, D.; Marotta, R.; Scotto, M.; Carregal-Romero, S.; RiveraGil, P.; Parak, W. J.; Pellegrino, T. Magnetic Nanobeads Decorated with Silver Nanoparticles as Cytotoxic Agents and Photothermal Probes. *Small* **2012**, *8* (17), 2731−2742.

(16) Peng, S.; McMahon, J. M.; Schatz, G. C.; Gray, S. K.; Sun, Y. Reversing the size-dependence of surface plasmon resonances. *Proc. Natl. Acad. Sci. U. S. A.* **2010**, *107* (33), 14530−14534.

(17) Evanoff, D. D.; Chumanov, G. Size-Controlled Synthesis of Nanoparticles. 2. Measurement of Extinction, Scattering, and Absorption Cross Sections. *J. Phys. Chem. B* **2004**, *108* (37), 13957−13962.

(18) Kumbhar, A. S.; Kinnan, M. K.; Chumanov, G. Multipole Plasmon Resonances of Submicron Silver Particles. *J. Am. Chem. Soc.* **2005**, *127* (36), 12444−12445.

(19) Krenn, J. R.; Schider, G.; Rechberger, W.; Lamprecht, B.; Leitner, A.; Aussenegg, F. R.; Weeber, J. C. Design of multipolar plasmon excitations in silver nanoparticles. *Appl. Phys. Lett.* **2000**, *77* (21), 3379−3381.

(20) Kreibig, U.; Schmitz, B.; Breuer, H. D. Separation of plasmon-polariton modes of small metal particles. *Phys. Rev. B: Condens. Matter Mater. Phys.* **1987**, *36* (9), 5027−5030.

(21) Payne, E. K.; Shuford, K. L.; Park, S.; Schatz, G. C.; Mirkin, C. A. Multipole Plasmon Resonances in Gold Nanorods. *J. Phys. Chem. B* **2006**, *110* (5), 2150−2154.

(22) Millstone, J. E.; Park, S.; Shuford, K. L.; Qin, L.; Schatz, G. C.; Mirkin, C. A. Observation of a Quadrupole Plasmon Mode for a Colloidal Solution of Gold Nanoprisms. *J. Am. Chem. Soc.* **2005**, *127* (15), 5312−5313.

(23) Oldenburg, S. J.; Jackson, J. B.; Westcott, S. L.; Halas, N. J. Infrared extinction properties of gold nanoshells. *Appl. Phys. Lett.* **1999**, *75* (19), 2897−2899.

(24) Sun, Y.; Mayers, B.; Xia, Y. Metal Nanostructures with Hollow Interiors. *Adv. Mater.* **2003**, *15* (7−8), 641−646.

(25) Bastús, N. G.; Comenge, J.; Puntes, V. F. Kinetically Controlled Seeded Growth Synthesis of Citrate-Stabilized Gold Nanoparticles of up to 200 nm: Size Focusing versus Ostwald Ripening. *Langmuir* **2011**, *27* (17), 11098−11105.

(26) Rodríguez-Fernández, J.; Pérez-Juste, J.; García de Abajo, F. J.; Liz-Marzán, L. M. Seeded Growth of Submicron Au Colloids with Quadrupole Plasmon Resonance Modes. *Langmuir* **2006**, *22* (16), 7007−7010.

(27) Evanoff, D. D.; Chumanov, G. Size-Controlled Synthesis of Nanoparticles. 1. "Silver-Only" Aqueous Suspensions via Hydrogen Reduction. *J. Phys. Chem. B* **2004**, *108* (37), 13948−13956.

(28) Cao, Y.; Zheng, R.; Ji, X.; Liu, H.; Xie, R.; Yang, W. Syntheses and Characterization of Nearly Monodispersed, Size-Tunable Silver Nanoparticles over a Wide Size Range of 7−200 nm by Tannic Acid Reduction. *Langmuir* **2014**, *30* (13), 3876−3882.

(29) Rainville, L.; Dorais, M.-C.; Boudreau, D. Controlled synthesis of low polydispersity Ag@SiO2 core-shell nanoparticles for use in plasmonic applications. *RSC Adv.* **2013**, *3* (33), 13953−13960.

(30) Dadosh, T. Synthesis of uniform silver nanoparticles with a controllable size. *Mater. Lett.* **2009**, *63* (26), 2236−2238.

(31) Zong, R.; Wang, X.; Shi, S.; Zhu, Y. Kinetically Controlled Seed-mediated Growth of Narrow Dispersed Silver Nanoparticles up to 120 nm: Secondary Nucleation, Size Focusing, and Oswald Ripening. *Phys. Chem. Chem. Phys.* **2014**, *16*, 4236.

(32) Samal, A. K.; Polavarapu, L.; Rodal-Cedeira, S.; Liz-Marzán, L. M.; Pérez-Juste, J.; Pastoriza-Santos, I. Size Tunable Au@Ag Core−Shell Nanoparticles: Synthesis and Surface-Enhanced Raman Scattering Properties. *Langmuir* **2013**, *29* (48), 15076−15082.

(33) Noguez, C. Surface Plasmons on Metal Nanoparticles: The Influence of Shape and Physical Environment. *J. Phys. Chem. C* **2007**, *111* (10), 3806−3819.

(34) Yin, J.; Zang, Y.; Xu, B.; Li, S.; Kang, J.; Fang, Y.; Wu, Z.; Li, J. Multipole plasmon resonances in self-assembled metal hollow-nanospheres. *Nanoscale* **2014**, *6* (8), 3934−3940.

(35) Shen, H.; Lu, G.; Zhang, T.; Liu, J.; Gu, Y.; Perriat, P.; Martini, M.; Tillement, O.; Gong, Q. Shape effect on a single-nanoparticle-based plasmonic nanosensor. *Nanotechnology* **2013**, *24* (28), 285502.

(36) Hinterwirth, H.; Kappel, S.; Waitz, T.; Prohaska, T.; Lindner, W.; Lämmerhofer, M. Quantifying Thiol Ligand Density of Self-Assembled Monolayers on Gold Nanoparticles by Inductively Coupled Plasma-Mass Spectrometry. *ACS Nano* **2013**, *7* (2), 1129−1136.

(37) Kedem, O.; Tesler, A. B.; Vaskevich, A.; Rubinstein, I. Sensitivity and Optimization of Localized Surface Plasmon Resonance Transducers. *ACS Nano* **2011**, *5* (2), 748−760.

(38) Bastús, N. G.; Sanchez-Tillo, E.; Pujals, S.; Farrera, C.; Kogan, M. J.; Giralt, E.; Celada, A.; Lloberas, J.; Puntes, V. Peptides

Conjugated to Gold Nanoparticles Induce Macrophage Activation. *Mol. Immunol.* **2009**, *46* (4), 743–748.

(39) Bastús, N. G.; Sanchez-Tillo, E.; Pujals, S.; Farrera, C.; Lopez, C.; Giralt, E.; Celada, A.; Lloberas, J.; Puntes, V. Homogeneous Conjugation of Peptides onto Gold Nanoparticles Enhances Macrophage Response. *ACS Nano* **2009**, *3* (6), 1335–1344.

(40) Schulz, F.; Vossmeyer, T.; Bastus, N. G.; Weller, H. Effect of the Spacer Structure on the Stability of Gold Nanoparticles Functionalized with Monodentate Thiolated Poly(ethylene glycol) Ligands. *Langmuir* **2013**, *29* (31), 9897–9908.

(41) Bastús, N. G.; Merkoçi, F.; Piella, J.; Puntes, V. Synthesis of Highly Monodisperse Citrate-Stabilized Silver Nanoparticles of up to 200 nm: Kinetic Control and Catalytic Properties. *Chem. Mater.* **2014**, *26* (9), 2836–2846.

(42) Yonzon, C. R.; Stuart, D. A.; Zhang, X.; McFarland, A. D.; Haynes, C. L.; Van Duyne, R. P. Towards advanced chemical and biological nanosensors—An overview. *Talanta* **2005**, *67* (3), 438–448.

(43) Dahlin, A. B.; Tegenfeldt, J. O.; Höök, F. Improving the Instrumental Resolution of Sensors Based on Localized Surface Plasmon Resonance. *Anal. Chem.* **2006**, *78* (13), 4416–4423.

(44) Anker, J. N.; Hall, W. P.; Lyandres, O.; Shah, N. C.; Zhao, J.; Van Duyne, R. P. Biosensing with plasmonic nanosensors. *Nat. Mater.* **2008**, *7* (6), 442–453.

(45) Linnert, T.; Mulvaney, P.; Henglein, A. Surface chemistry of colloidal silver: surface plasmon damping by chemisorbed iodide, hydrosulfide (SH-), and phenylthiolate. *J. Phys. Chem.* **1993**, *97* (3), 679–682.

(46) Mulvaney, P. Surface Plasmon Spectroscopy of Nanosized Metal Particles. *Langmuir* **1996**, *12* (3), 788–800.

(47) Evanoff, D. D.; White, R. L.; Chumanov, G. Measuring the Distance Dependence of the Local Electromagnetic Field from Silver Nanoparticles. *J. Phys. Chem. B* **2004**, *108* (5), 1522–1524.

(48) Haes, A. J.; Zou, S.; Schatz, G. C.; Van Duyne, R. P. A Nanoscale Optical Biosensor: The Long Range Distance Dependence of the Localized Surface Plasmon Resonance of Noble Metal Nanoparticles. *J. Phys. Chem. B* **2004**, *108* (1), 109–116.

(49) Ausman, L.; Schatz, G. C. *J. Chem. Phys.* **2008**, *129*, 054704.

(50) Rodríguez-Fernández, J.; Pastoriza-Santos, I.; Pérez-Juste, J.; García de Abajo, F. J.; Liz-Marzán, L. M. The Effect of Silica Coating on the Optical Response of Sub-micrometer Gold Spheres. *J. Phys. Chem. C* **2007**, *111* (36), 13361–13366.

(51) Sperling, R. A.; Rivera Gil, P.; Zhang, F.; Zanella, M.; Parak, W. J. Biological applications of gold nanoparticles. *Chem. Soc. Rev.* **2008**, *37* (9), 1896–1908.

(52) Sperling, R. A.; Casals, E.; Comenge, J.; Bastus, N. G.; Puntes, V. F. Inorganic Engineered Nanoparticles and Their Impact on the Immune Response. *Curr. Drug Metab.* **2009**, *10* (8), 895–904.

(53) Warren, P. B. *The Physics of Floppy Polymers*; CRC Press-Taylor & Francis Group: Boca Raton, FL, 2006; pp 49–62.

(54) Hill, R. J. Hydrodynamics and electrokinetics of spherical liposomes with coatings of terminally anchored poly(ethylene glycol): Numerically exact electrokinetics with self-consistent mean-field polymer. *Phys. Rev. E* **2004**, *70* (5), 051406.

(55) Lee, Y. H.; Chen, H.; Xu, Q.-H.; Wang, J. Refractive Index Sensitivities of Noble Metal Nanocrystals: The Effects of Multipolar Plasmon Resonances and the Metal Type. *J. Phys. Chem. C* **2011**, *115* (16), 7997–8004.

(56) Hill, H. D.; Millstone, J. E.; Banholzer, M. J.; Mirkin, C. A. The Role Radius of Curvature Plays in Thiolated Oligonucleotide Loading on Gold Nanoparticles. *ACS Nano* **2009**, *3* (2), 418–424.

(57) Nusz, G. J.; Curry, A. C.; Marinakos, S. M.; Wax, A.; Chilkoti, A. Rational Selection of Gold Nanorod Geometry for Label-Free Plasmonic Biosensors. *ACS Nano* **2009**, *3* (4), 795–806.

(58) Chen, F.; Li, X.; Hihath, J.; Huang, Z.; Tao, N. Effect of Anchoring Groups on Single-Molecule Conductance:Comparative Study of Thiol-, Amine-, and Carboxylic-Acid-Terminated Molecules. *J. Am. Chem. Soc.* **2006**, *128* (49), 15874–15881.

(59) Juluri, B. K.; Huang, J.; Jensen, L., Extinction, Scattering and Absorption efficiencies of single and multilayer nanoparticles, 2010. https://nanohub.org/resources/8228.

(60) Myroshnychenko, V.; Rodriguez-Fernandez, J.; Pastoriza-Santos, I.; Funston, A. M.; Novo, C.; Mulvaney, P.; Liz-Marzan, L. M.; Garcia de Abajo, F. J. Modelling the optical response of gold nanoparticles. *Chem. Soc. Rev.* **2008**, *37* (9), 1792–1805.

Supplementary Information for

Quantifying the Sensitivity of Multipolar (Dipolar, Quadrupolar and Octapolar) Surface Plasmon Resonances in Silver Nanoparticles: The Effect of Size, Composition and Surface Coating.

Neus G. Bastús, Jordi Piella and Víctor Puntes

1
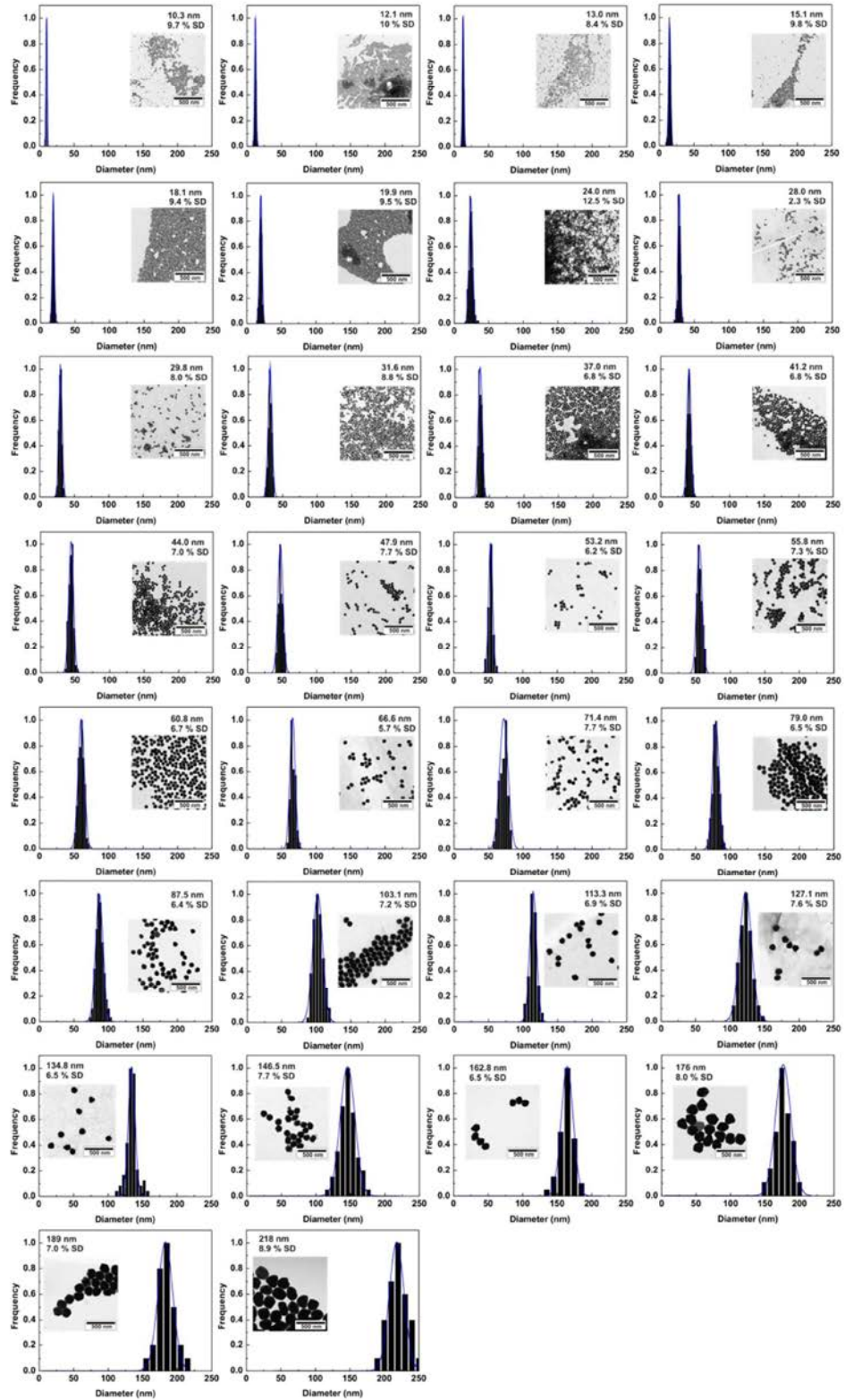
Figure S1: TEM image analysis of Ag NPs shown in Figure 1
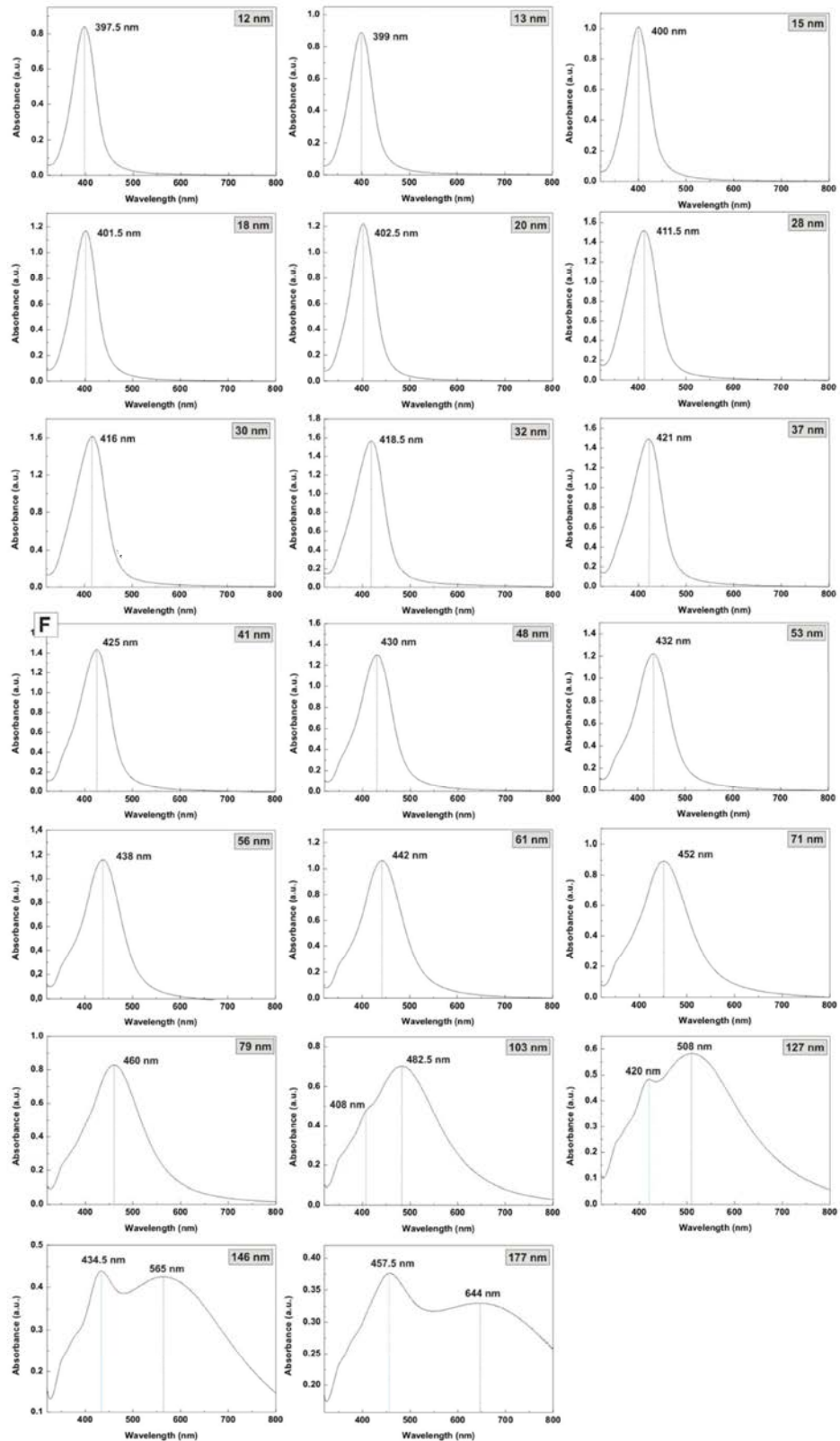
Figure S2: Individual UV-Vis spectra of Ag colloids obtained after different growth steps. Black/blue lines indicate the position of the dipolar/quadrupolar band.
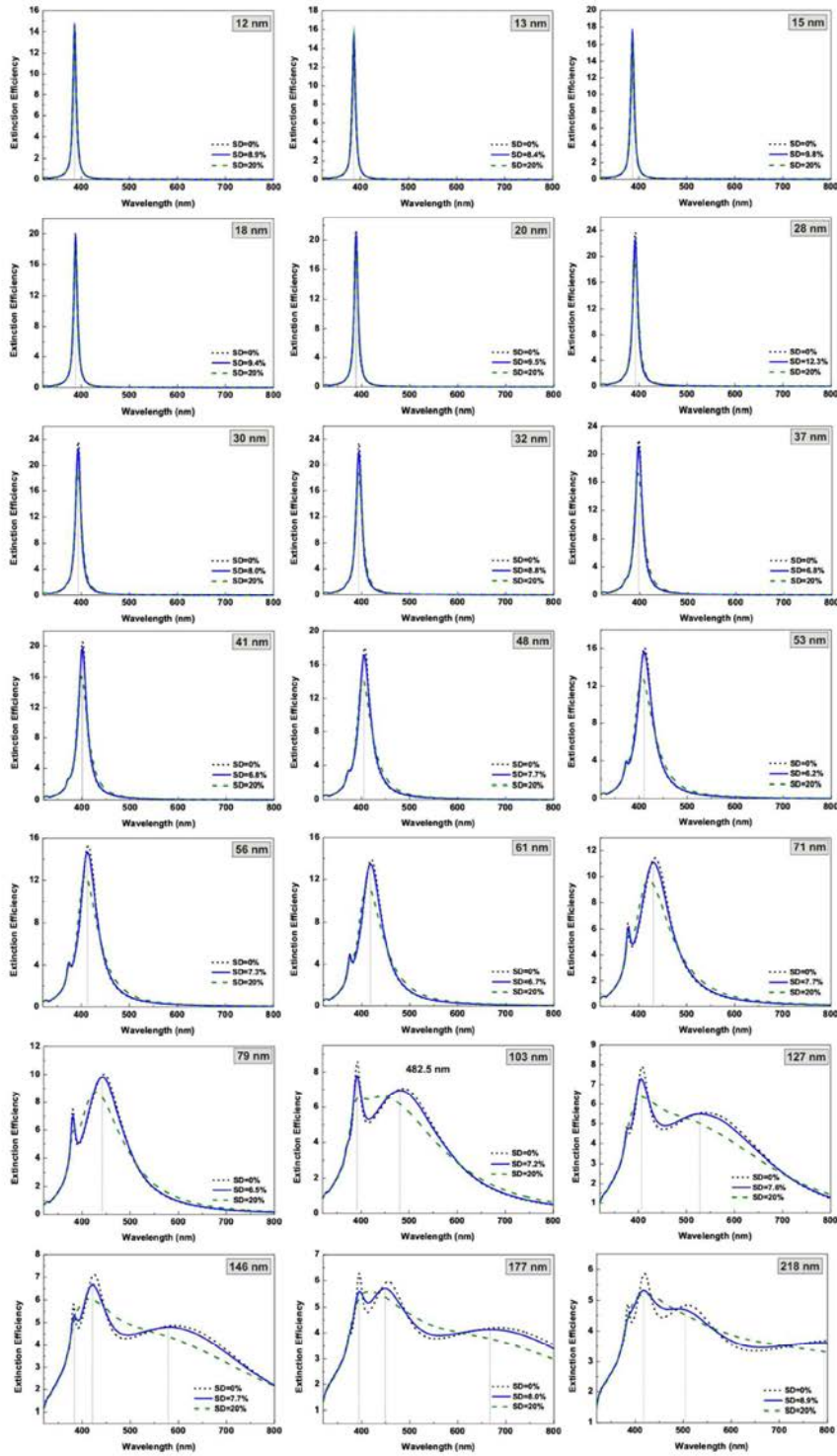
Figure S3: Calculated extinction spectra of selected Ag NP's sizes (as labeled) and different standard deviations: black-dotted line is the monodisperse case (SD=0%), blue-solid line the standard deviation measured from TEM images of each sample and green-dashed curve the polidisperse case with SD=20% .
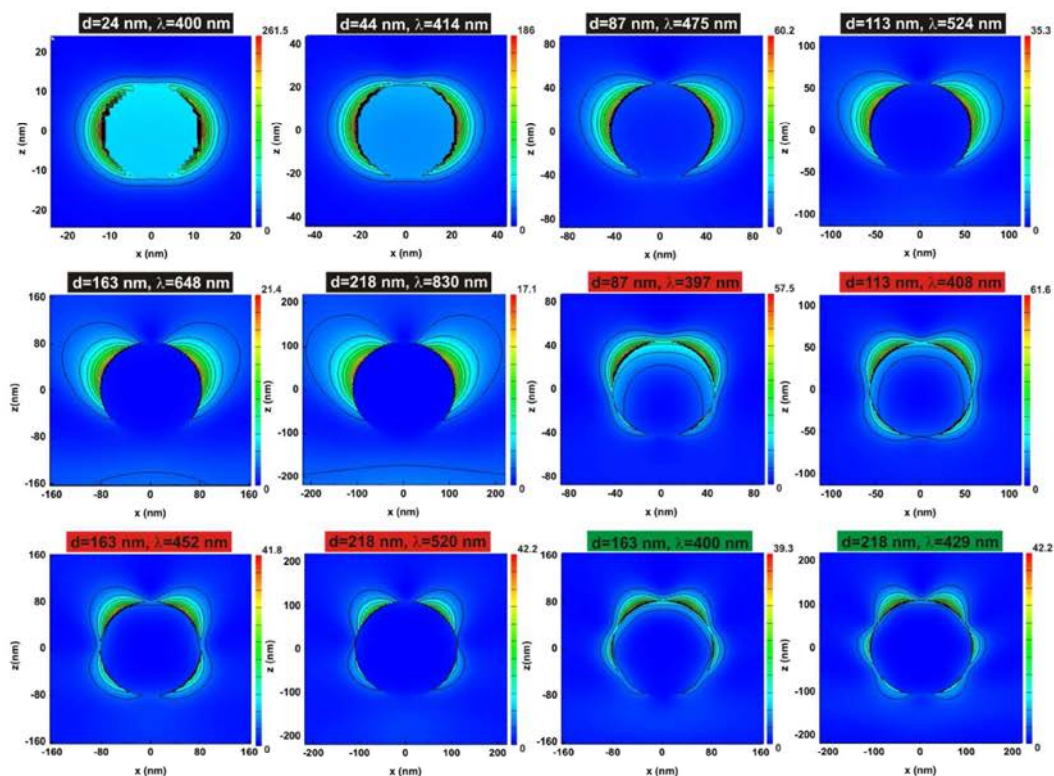
Figure S4- Calculated Near-field enhancement maps (2D field distributions diagrams in planar cross sections XZ**) of spherical Ag NPs of various sizes in water when illuminated at their corresponding calculated dipole (black box), quadrupole (red box) and octupole (green box) maximum wavelengths.** Calculations were performed with radiation polarized along the x axis. The field amplitude inside and outside the particle varies from blue (equal to zero) to red, corresponding to a maximum field amplitude (as-labeled). The symmetry in the field distribution outside the particles is broken and the regions of significant near field enhancement are shifted toward the direction of the incident radiation.

5
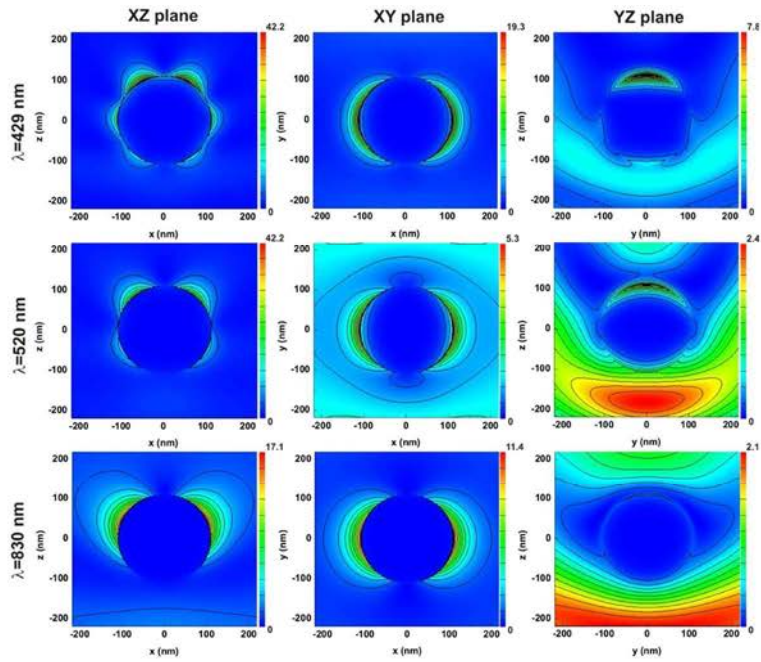
Figure S5 : 2D field distributions diagrams in planar cross sections XZ, XY and YZ of Ag spheres of radius 218 nm and illuminated with wavelengths 429 nm (octapolar resonance), 520 nm (quadrupolar resonance) and 830 nm (dipolar resonance). Calculations were performed with radiation polarized along the x axis. The field amplitude inside and outside the particle varies from blue (equal to zero) to red, corresponding to a maximum field amplitude (as labeled). The symmetry in the field distribution outside the particles is broken and the regions of significant near field enhancement are shifted toward the direction of the incident radiation.
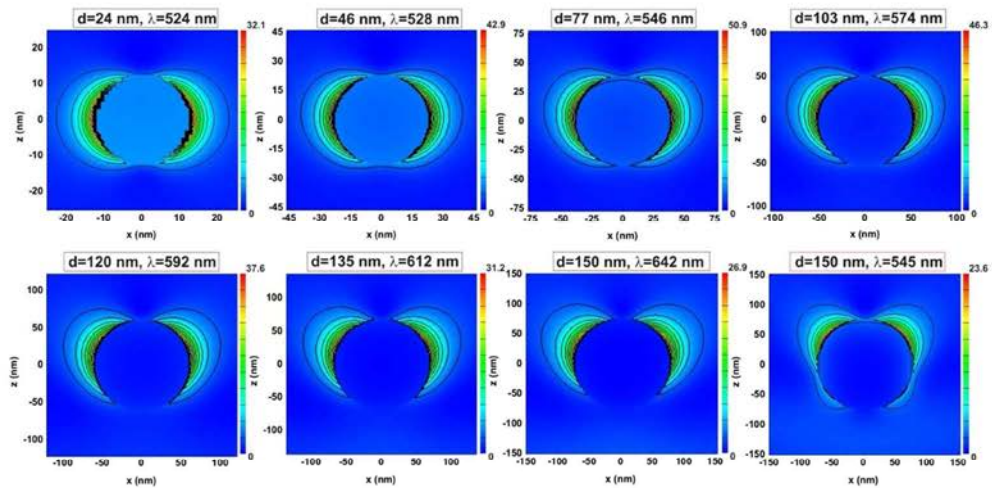
Figure S6- 2D field distributions diagrams in planar cross sections XZ **of spherical Au NPs of various sizes in water when illuminated at their corresponding calculated dipole (black box) and quadrupole (red box) maximum wavelengths.** Calculations were performed with radiation polarized along the x axis. The field amplitude inside and outside the particle varies from blue (equal to zero) to red, corresponding to a maximum field amplitude (as labeled). The symmetry in the field distribution outside the particles is broken and the regions of significant near field enhancement are shifted toward the direction of the incident radiation.
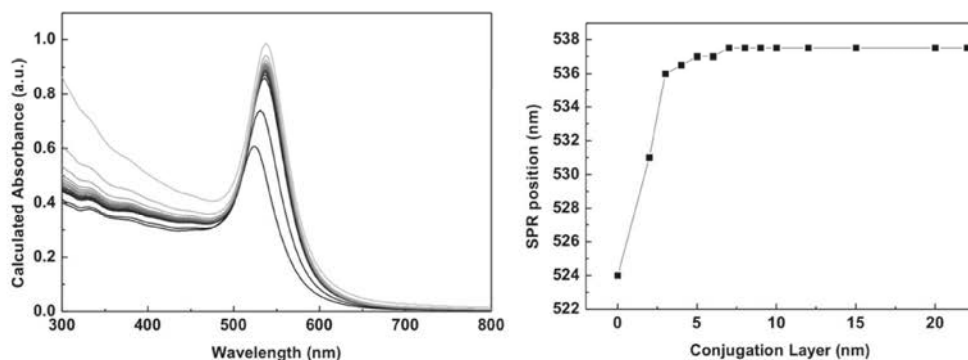
Figure S7-Dependence of the peak position on the length of the molecule is directly related to the increase of the thickness of the dielectric layer in the vicinity of Ag NP's surface. Thus, SPRs peaks shift towards the red as the coating layer thickness increases until it reaches a constant value. The limiting thickness of the organic layer that has an effect on the SPRs depends on the maximum distance to which the local field extends from NP's surface.
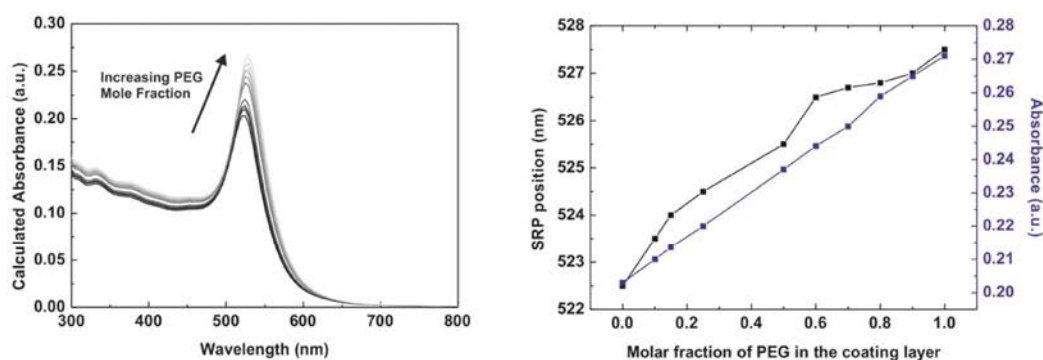
Figure S8- Effect of the degree of molecule packaging of the position of SPR peak. An increase in the degree of packaging (higher molar fraction of PEG in the coating layer) is translated into a shift in the position of the SPR resonance. Thus, in small particles, where the curvature radii is very high, the molar fraction of PEG that occupies the coating layer is lower than in larger NPs, which is translated into different red-shifts. In this regard, the higher sensibility of larger NPs could be associated (among other factors) to higher allocation capabilities. Calculations were modeled for 10 nm Au NPs coated by an organic PEG shell of 4 nm thickness for increasing PEG contents in the Shell. Mole Fraction=0 represents No PEG. Mole Fraction=1 represents a dense PEG layer (full coating).

Chapter 5:

Probing the surface reactivity of metal nanoparticles by the catalytic degradation of organic dyes

In the previous chapter, the size- and surface-dependent optical properties of Au and Ag NPs were studied in detail. Here, a similar analysis is presented in relation to the surface activity of these NPs, in particular, the effect of particle size, surface coating and composition on the catalytic reduction of 4-nitrophenol. All data was collected in the article entitled *Probing the surface reactivity of nanocrystals by the catalytic degradation of organic dyes: the effect of size, surface chemistry and composition.*

5.1. Introduction to catalysis by nanoparticles

Nanoparticles (NPs) are undoubtedly among the most widely studied systems in modern nanoscience. This is due to the fact that materials often show totally different properties when dispersed down to nanometer dimensions. These novel properties are nonexclusively related to optics and plasmonics. Due to their exceedingly high surface-to-volume ratios, abundance of edges and corners and electronic confinement, NPs often present catalytic properties that are not revealed in their bulk forms. For example, Haruta *et al.* [1] found some twenty years ago that Au NPs are active catalysts for oxidation reactions, while bulk gold is inactive. This study and subsequent discoveries have proven that the catalytic properties of a material are not exclusively determined by the material composition, as traditionally believed, since they can also be influenced by changes in size and shape, giving rise to the concept of nanocatalyst as one of the most promising areas in nanoscience. [2]

Nowadays, a number of comprehensive reviews are available, focusing on specific reactions catalysed by NPs, including atmospheric N_2 fixation, water splitting, hydrogenation and cross-coupling reactions [2]. Among NPs, those made of metals of Pt, Pd and Rh remain the most commonly used in catalysis. For example, Pd NPs have attracted great interest due to their high efficiency for the Suzuki reaction in organic syntheses [3] while Pt NPs are particularly attractive in hydrogen fuel cells due to their extremely high hydrogenation ability [4]. More recently, the use of Au and Ag NPs of different sizes in important electron transfer and oxidation processes, such as CO oxidation, has generated great interest [5].

In colloidal form, NPs combine the advantages of heterogeneous and homogeneous catalysis while circumventing many of their individual drawbacks [6]. The drawbacks of homogeneous catalysis include poor recycling potential and contamination of products by the catalyst. Heterogeneous catalysis in solution alleviates these drawbacks because the contamination of the products is low and the catalysts can be phase separated from the reaction media and reused. However, heterogeneous catalysts often shows poor performance because the percentage of surface atoms, which are the ones that directly participate in the reaction, is low. The use of colloidal NPs alleviate these dimensional

limitations because they expose a great number of surface atoms per unit volume and are highly mobile through the solution.

Nevertheless, the surface activity of the NPs may be affected by their large tendency to reduce the excess of surface energy either via passivation through chemical reactions with capping molecules, crystalline changes or via particle aggregation, which are other associated processes with relevant consequences on their final catalytic performances. Current advances in the science of synthetizing NPs has opened the way for detailed studies on the surface activity of NPs. These include the possibility of synthetizing NPs with different sizes, crystallinity, atomic composition and surface chemistry. Furthermore, high resolution transmission electron microscopy (HRTEM) and the development of optical and spectroscopic techniques specific for the characterization of NPs (see **Chapter 4**) now allows for full characterization of these systems, which can be used in detailed studies with the same rigor as earlier investigations carried out on macroscopic surfaces.

5.2. Model reactions

Well-characterized model reactions are a prerequisite for the study of the fundamental aspects of surface activity of NPs. These should satisfy the following conditions:

- Well-controlled chemical reaction with minimum formation of by-products that can potentially interact with the surface of the NPs.

- The reaction should only take place in the presence of NPs in solution.

- The rate of reaction must be measurable with high precision, leading to a detailed understanding of the reaction kinetics.

- The reaction should proceed under mild conditions, in which NPs are stable and no degradation or transformation occurs. It excludes all reactions in which the NPs serve as a source for ions in solution.

Some of the most common model reactions consist of the reduction of different organic dyes (e.g. 4-nitrophenol and Rodhamine B) and inorganic dyes (e.g. hexacyanoferrate) by borohydride (**Scheme 5.1**).
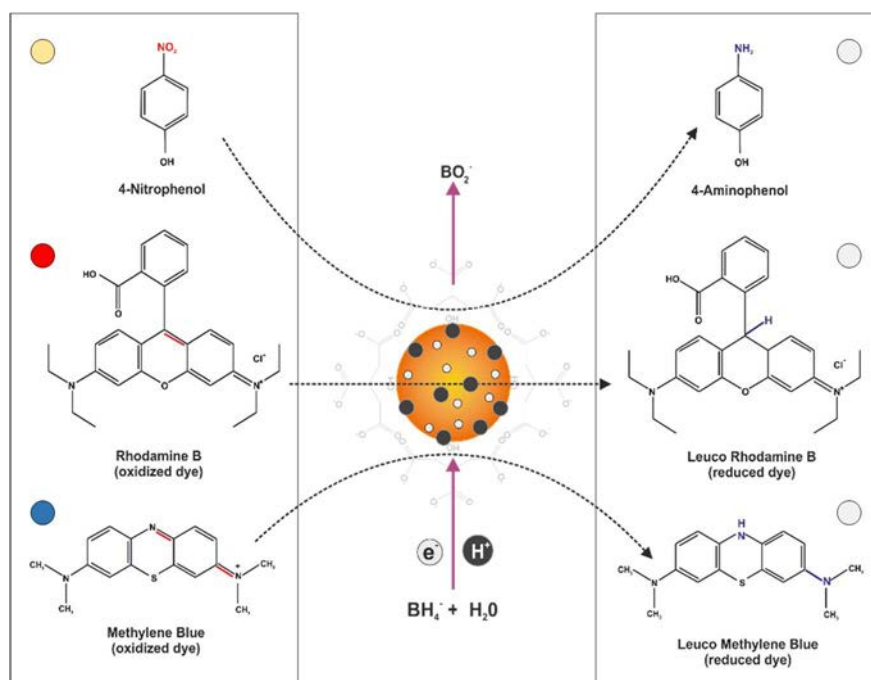
Scheme 5.1. Catalytic degradation of organic dyes by metal nanoparticles. The reduction reaction takes place at the metal surface between the dye (4-nitrophenol, Rhodamine B, Methylene blue, etc) and the NaBH$_4$, resulting in dye's decoloration [18].

These reactions take place in water under ambient conditions and can be analysed with high accuracy using relatively easy techniques such as spectroscopies. The choice of these reactions has also been prompted by the fact that there is a huge bulk of kinetic data available [7-9].

5.3. Reduction of 4-nitrophenol in aqueous solutions

The reduction of 4-nitrophenol (4-NP) by borohydride on catalytic surfaces is probably the most used model reaction for assessing the surface activity of metal nanostructured materials [10, 11]. It also has enormous industrial significance as nitro compounds are reduced to their less toxic nitrate or amine counterparts. Pal *et al.*[12] and Esumi *et al.*[13] first identified this reaction as a suitable reaction for testing the surface activity of free or immobilized metal NPs. Its designation as a model reaction stems from both its simplicity and the ease by which the reaction can be monitored using spectroscopic techniques; the reaction is conducted in aqueous media under ambient conditions, has no known side reactions, and only proceeds if a catalyst is present. The successive reduction in the characteristic absorbance of 4-NP at 400 nm directly correlates with its concentration in solution and can therefore be used for high-precision real-time

monitoring of the reaction kinetics by UV-vis spectroscopy. Additionally, the product 4-aminophenol (Amp) imparts no colour to the aqueous solution and hence does not hamper the spectroscopic determination (**Figure 5.1**).
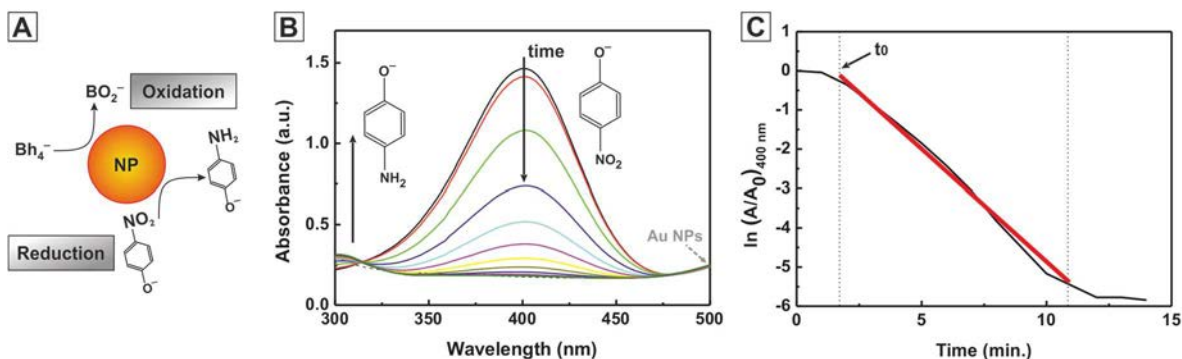
Figure 5.1. Catalytic reduction of 4-nitrpohenol by borohydride. (A) Schematic representation of the reaction. (B) Representative time-evolution absorption spectra during the reduction of 4-NP and (C) corresponding plot of ln (A/A$_0$) vs reaction time at 400 nm. Red line displays the linear section from which k_{app} can be calculated.

After an induction time t_0 in which no reduction takes place, the reaction starts and reaches a stationary state that is well described by a pseudo first-order rate law for conditions satisfying [dye]<<[BH$_4^-$] [8]:

$$-\frac{dc_t}{t} = k_{app}c_t ,\qquad(5.1)$$

where c_t is the concentration of 4-NP at time t and k_{app} is the apparent rate constant (s^{-1}). Integration of equation (**5.1**) gives:

$$ln\frac{c_t}{c_0} = -k_{app}t,\qquad(5.2)$$

Because the absorbance A is proportional to the 4-NP concentration, k_{app} can be easily obtained from the slope of the linear dependence of $ln[(A-A_\infty)/(A_0-A_\infty)]$ with t [8] (**Figure 5.1C**, red line). Many studies, including that of Mahmoud *et al.* [14], has further pointed out that the k_{app} is proportional to the total surface area of the metal NPs, demonstrating that the metal surface of the NPs is acting as the true catalyst for the reaction [14-17]. Hence, a kinetic constant, k'_{app} (s^{-1}m^{-2}L), can be defined through normalization to the total surface area S (m^{2}L^{-1}) of the system:

$$k'_{app} = k_{app}S^{-1}\qquad(5.3)$$

In addition to this, different authors have reported the presence of an induction period t_0 needed to have an active catalyst [18] (**Figure 5.1C**, arrow). The origin of this lag phase remains somewhat of an enigma and has been ascribed to different causes. Some of which are the presence of an oxide layer on the metal surface[12] the diffusion of reactants to the catalyst surface [19, 20], a surface reconstructing process [8, 9, 21], the time for NaBH$_4$ to inject electrons to the NPs [14, 22]or the time required to remove the surfactant from the surface of the NPs [23]. Discussion is certainly complicated by the varied nature of catalysts, catalyst supports and surface ligands. Very recently, two independent works from Neretina *et al.* [10] and Blanco *et al.* [24] reported that the induction period is highly affected by the sequence of reactants addition which can give further insights of its origin. The induction period, however, is inconsequential with the calculation of the k_{app} at the stationary stage of the reaction and thus it does not prevent a full kinetic analysis.

Mechanistically, the catalytic reduction of 4-NP by NPs is commonly understood in terms of the Langmuir-Hinshelwood model (LH) [7, 25, 26]. First, borohydride ions and 4-NP molecules adsorb on the surface of the NPs. Then, both reactants diffuse to active sites, where the reaction take places to form the product that finally desorbs from the surface. This is certainly a complicated process that consists of several steps and it is not yet fully understood. For example, there is no consensus in the literature regarding whether the reduction reaction proceeds via transfer of hydrogen atoms on the surface of the NP (surface-mediated hydrogen transfer), or, on the contrary, BH$_4^-$ charges the particle by injecting electrons that are later used to reduce the 4-NP (surface-mediated electron transfer) [26]. The common ground for the two proposed mechanisms is that the reactants are absorbed on to the surface of the NPs prior to reacting. Wunder *et al.* [8, 9] dealt with the kinetic aspects of the reaction by evaluating Pt and Au NPs supported in polyelectrolyte brushes for the reduction of 4-NP. The authors investigated both the effects of variations in 4-NP and BH$_4^-$ concentrations on the rate of the reaction and concluded that the rate-limiting step is the reduction of adsorbed 4-NP. These results were further corroborated by the same authors for dispersed bare Au NPs [27] and the reaction model was finally improved by accounting for the intermediate specie of 4-hydroxylaminophenol (4-Hx) [7]. Published works by other authors come to similar conclusions as regards to the rate-determining step and the kinetic model [24, 26, 28].

Additionally, other important factors known to affect the reaction mechanism have also been evaluated, including the presence of dissolved oxygen and pH of the solution [10]. Thus, the mechanism of catalytic reduction of 4-NP seems to be sufficiently studied to serve as a model reaction (**Scheme 5.2**).

Following these considerations, and the progress achieved previously in the synthesis of metal NPs (see **Chapters 2** and **3**), a full analysis of the catalytic performance of these NPs for the reduction of 4-NP by borohydride was accomplished. Au NPs were chosen over other metal NPs for their great stability and the possibility of ruling out other side effects that can alter the integrity of the NPs during evaluation, e.g. oxidation and dissolution. Attention was focused on the effect of particle size and surface chemistry on the final catalytic performance. All data were collected in the article entitled: *Probing the surface reactivity of nanocrystals by the catalytic degradation of organic dyes: the effect of size, surface chemistry and composition.*
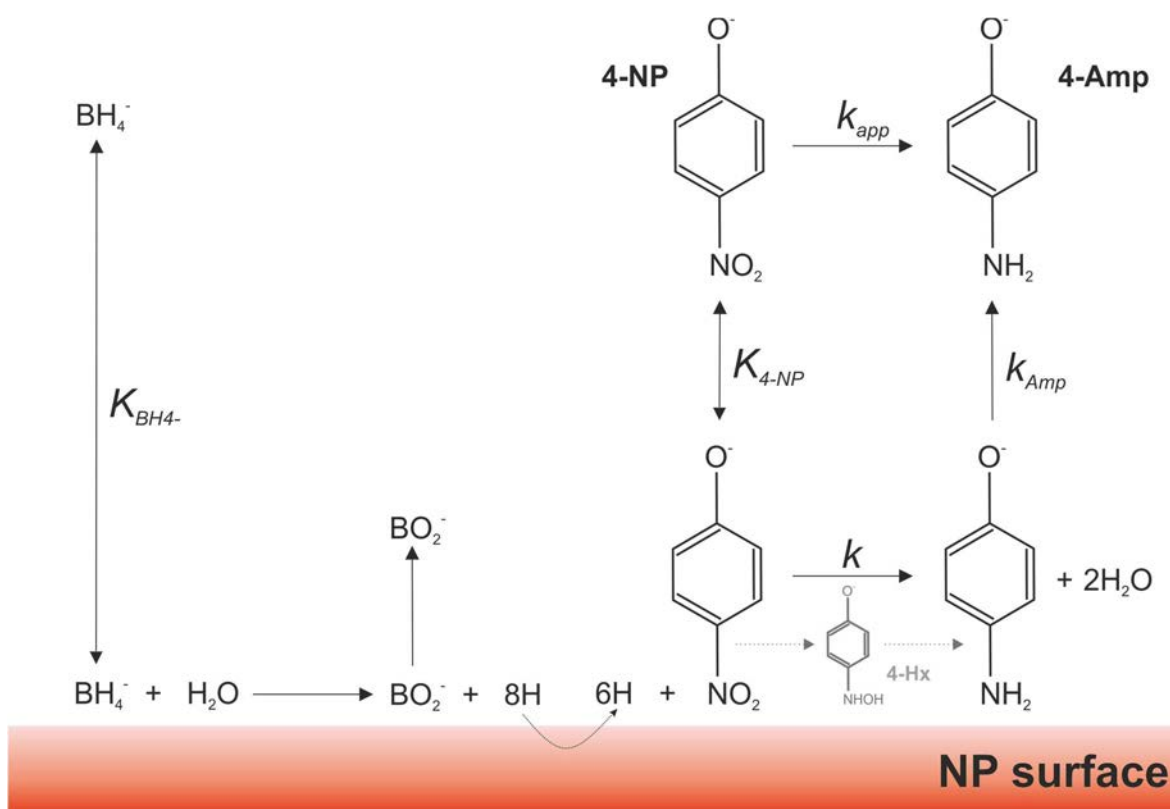
Scheme 5.2. Model of Langmuir-Hinshelwood mechanism for the reduction of 4-nitrophenol to aminophenol via surface-mediated hydrogen transfer. In the first step, the NaBH4 is decomposed by hydrolysis on the metal surface and BO2- and active hydrogen are formed; then the 4-NP is adsorbed at the surface and reacts with the active hydrogen to form Amp (rate-limiting step); finally, BO2- and Amp fast desorbs from the surface. The reduction of 4-NP to Amp passes through the formation of 4-Hx [26].

5.4. Results: The effect of size and surface chemistry on the reduction of 4-nitrophenol by metal nanoparticles.

5.4.1. Effect of particle size

In the first part of the work, the catalytic reduction of 4-NP by $NaBH_4$ was evaluated using citrate-stabilized Au NPs with diameters ranging from 3.5 to 200 nm (**Figure 5.2**). The effect of particle size was highlighted by the improved catalytic performance shown by the smaller Au NPs compared to the larger ones. This can be accounted for the fact that, at equal concentration of Au atoms, the number of surface atoms for the catalysis decreases with increasing particle size, i.e. the higher reaction rate of smaller Au NPs is due to the larger surface area. However, when compared by surface area, differences in the observed rate constants further revealed a size dependence surface activity (**Figure 5.2J**). Overall, the tendency was that surface activity increased as particle size decreased. Additionally, for Au NPs of relatively small sizes (less than 20 nm) there was some discrete sizes that were significantly more efficient for the reaction than others. For example, Au NPs of 10 nm in diameter showed a higher k_{app} than that of 5 and 15 nm.

The size-dependent crystalline structure of NPs is a well-known nanoscale effect. This may result in the exposition of different crystalline faces, rendering different surface activities. To address this possibility, Au NPs with selected diameters were fully characterized by HR-TEM and HAADS-STEM. In most of the samples, synthetized Au NPs presented five-fold symmetry twined structures, with decahedron geometry being the most commonly observed (**Figure 5.3**). Indeed, computational simulations performed by different researchers have demonstrated that, together with the cuboctahedra and icosahedron, these are the most stable structures for novel metals [29, 30]. Interestingly, small Au NPs presented a spheroidal decahedral shape while the morphology of Au NPs with intermediate sizes was close to the ideal decahedron, with sharper external facets. Finally, Au NPs of even large sizes (>100 nm) shown an increasing number of external facets that progressively distorted the decahedron structure to an icosahedron. Despite these differences, all the Au NPs were characterized by the exposure of {111} facets, leading to a ruling out of crystal plane effects in the observed size-dependent surface activity. As a result, this was attributed to a higher reactivity of
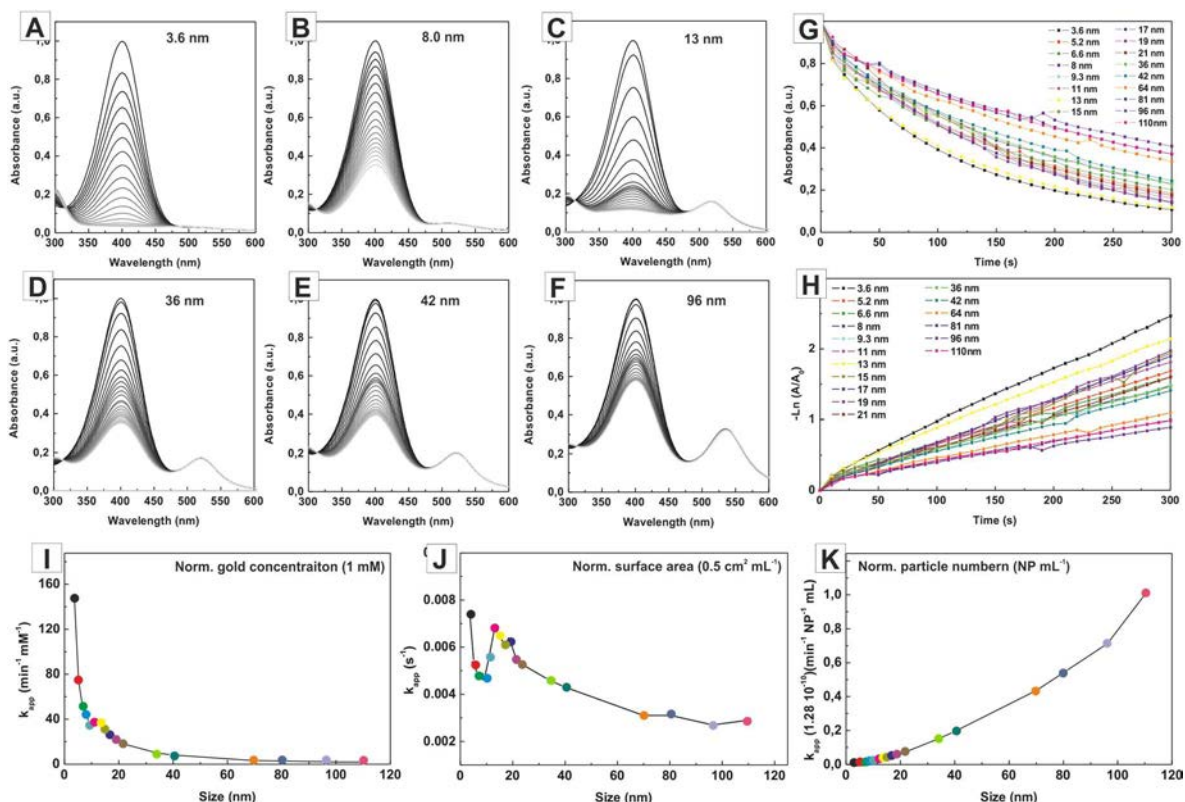
Figure 5.2. Effect of particle size on the catalytic reduction of 4-NP by NaBH₄. (A-F) Time-evolution absorption spectra during the reduction of 4-NP, (G) plot of time-dependent absorbance at 400 nm and (G) plot of ln (A/A$_0$) vs reaction time for Au NPs of different diameters. Calculated k_{app} normalized by total Au atoms (I), total surface area (J) and particle number (K). Conditions: [4-NP]=0.16 mM; [NaBH₄]/[4-NP]=37.5:1; pH=10; V$_{total}$=3 mL; V$_{NP}$=0.05-0.25 mL.
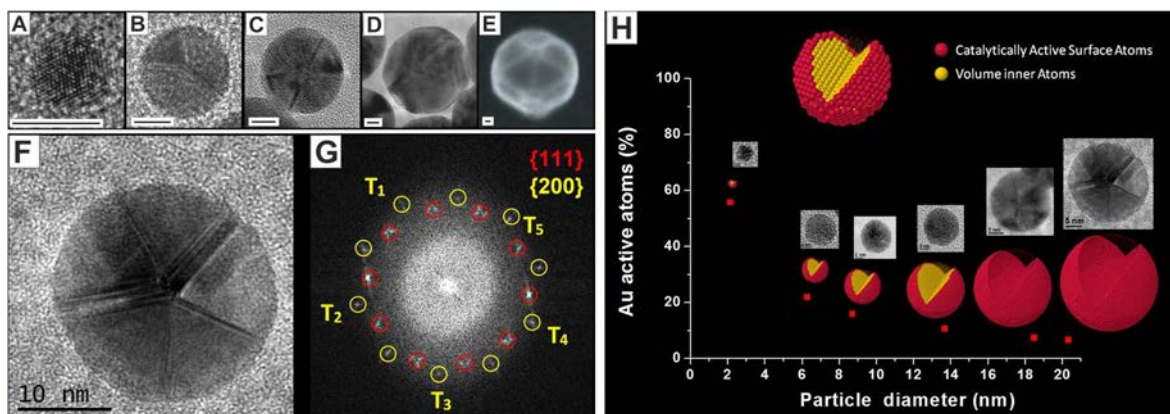
Figure 5.3. Structural characterization of gold nanoparticles with different sizes. (A-E) Representative micrographs showing the typical structure of Au NPs of 5.2 nm (A), 9.3 nm (B), 19 nm (C), 42 nm (D) and 96 nm (E). Au NPs from (A) to (D) show spheroidal decahedron morphology while (E) shows an icosahedral morphology. (F) HRTEM image and (G) corresponding power spectrum (FTT) of a 24.4 nm Au NP. Diffraction spots of {111} and {200} family planes form a perfect symmetry, which is typical of a decahedral geometry [30]. (H) Ratio of catalytically active Au atoms to total Au atoms. A spheroidal decahedron model (inset) was used for the calculations [34].

the coordinative unsaturated surface atoms in small Au NPs due their higher surface curvature.

However, a higher surface reactivity entails other consequences, particularly when NPs are in colloidal form. These can be advantageous or disadvantageous for the catalytic performance. For example, Hutchison *et al.* [31] showed that molecules tend to form stronger chemical bonds with lower coordinated surface atoms of small NPs which may slow down the adorption/desorption of reactants from NP surface. For the same reason, the displacement of capping molecules by substrates, which is needed to access the catalytic sites on the surface of the NPs, may be harder in this case. In this regards, we observed that small NPs could be reused fewer times compared to the larger ones. On the other hand, the curvature radi may also influence the interaction of NP with planar dyes, a fact that according to Fenger et *al.* [32] becomes particularly relevant for NPs smaller than 5 nm. All these effects may contribute to the existence of optimum sizes where the catalytic rate is unexpectedly great. For the catalytic reduction of 4-NP by Au NPs, this size was found to be around 10 nm (**Figure 5.2I**).

5.4.2. Effect of capping molecules

Colloidal NPs are frequently employed due to their large surface-to-volume ration and great mobility in solution. Besides the element that make these nanosystems highly attractive in catalysis, concomitantly with the low diameter, the protection against aggregation is imperative. The dilemma is that the capping molecules needed to preserve the stability of the NPs also acts to block the reactive surface and eliminate catalytic activity. To circumvent this dilemma, the NPs can be deposited onto a support and treated to remove the bound ligand, but this results in potential changes in the surface properties, a significant decrease in the available surface area, and influence of the support material on the catalyst activity. Therefore, there is a trade-off between the stability of colloidal NPs in solution and their catalytic activity due to passivation of active surface sites [33]. While understood phenomenologically, an in-depth study of the impact of stabilizing molecules on NP's catalytic activity is an area that requires further exploration. For this reason, we decided to study some of the most commonly used stabilizing molecules in Au NP synthesis and evaluate their influence on the final catalytic activity.
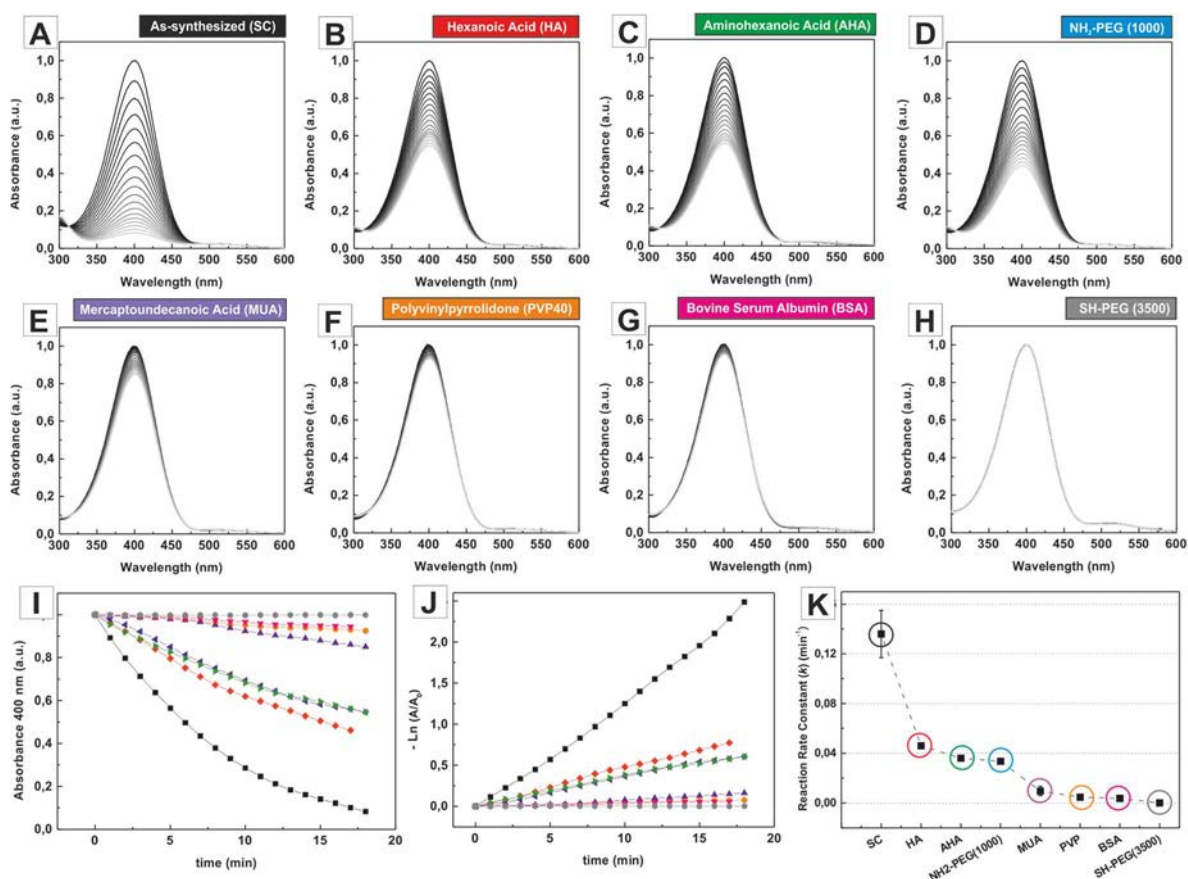
Figure 5.4. Influence of surface coating on the catalytic performance of Au NPs. (A-F) Time-evolution absorption spectra during the reduction of 4-NP by $NaBH_4$ in the presence of 3.6 nm Au NPs stabilized with: sodium citrate (A), hexanoic acid (B), aminohexanoic acid (C), NH_2-PEG (1000 kDa) (D), mercaptoundecanoic acid (E), polyvinylpyrrolidone (F), bovine serum albumin (G), and SH-PEG (3500 kDa) (H). (I) Plot of time-dependent absorbance at 400 nm. (J) Plot of $\ln(A_t/A_0)$ vs. time. (K) Calculated k_{app}. Conditions: [4-NP]=0.16 mM; [$NaBH_4$]/[4-NP]=37.5:1; pH=10; V_{total}=3 mL; V_{NP}=0.02 mL.

Overall, the effects of capping molecules were found to greatly exceed the previously described size effects, including the total inhibition of the catalytic activity of the NPs in some cases (**Figure 5.4**). For example, simple citrate-protected Au NPs gave higher apparent kinetic constant (k_{app}) for the 4-NP reaction than hexanoic, aminohexanoic and mercaptoundecanoic acids, while large molecules, especially polymers (PVP and PEG), gave very low kinetic constants (k_{app}). As regards the anchor terminal groups, higher reaction rates were obtained with Au NPs stabilized by molecules of carboxylic motifs when compared with capping molecules with thiol and amine anchor groups; a trend that agrees with the different affinity of these groups by gold surfaces, being this: thiol>amine>carboxylic.

5.5. Conclusions

In this chapter, the surface activity of Au NPs has been discussed on the basis of their ability to catalyse the reduction of 4-NP by BH_4^-. Obtained results highlight that, beyond the total surface area, particle size and capping molecules strongly influence the catalytic efficiency of Au NPs. Thus, a decrease of particle size tends to contribute positively to the reaction kinetics due to the higher reactivity of their surfaces. However, for very small Au NPs, this higher surface reactivity also entails some negative side effects (i.e. surface degradation, blockage and poison), resulting in the presence of a relative maximum of catalytic efficiency for Au NPs with intermediate sizes. For the system herein studied this size is around 10 nm. As regard to the capping molecules, the general trend is: the more protected the particle, the less catalytically active. This compromise between colloidal stability and catalytic activity due to the passivation of active surface sites still constitutes the main drawback in the use of these NPs for catalytic applications. These results, including additional catalytic studies with NPs of different compositions (Ag and Pt NPs) and dyes other than 4-NP (Rhodamine B and Methylene Blue) can be found in the following **Publication 4**.

5.6. References

[1] M. Haruta, Size- and support-dependency in the catalysis of gold, Catalysis Today 36 (1997) 153-166.

[2] Nanoparticles and Catalysis, 2008.

[3] M. Pérez-Lorenzo, Palladium Nanoparticles as Efficient Catalysts for Suzuki Cross-Coupling Reactions, The Journal of Physical Chemistry Letters 3 (2012) 167-174.

[4] Z. Peng, H. Yang, Designer platinum nanoparticles: Control of shape, composition in alloy, nanostructure and electrocatalytic property, Nano Today 4 (2009) 143-164.

[5] B. Hvolbæk, T.V.W. Janssens, B.S. Clausen, *et al.*, Catalytic activity of Au nanoparticles, Nano Today 2 (2007) 14-18.

[6] C. Tabor, R. Narayanan, M.A. El-Sayed, Catalysis with Transition Metal Nanoparticles in Colloidal Solution: Heterogeneous or Homogeneous?, 2010.

[7] S. Gu, S. Wunder, Y. Lu, *et al.*, Kinetic Analysis of the Catalytic Reduction of 4-Nitrophenol by Metallic Nanoparticles, The Journal of Physical Chemistry C 118 (2014) 18618-18625.

[8] S. Wunder, F. Polzer, Y. Lu, *et al.*, Kinetic Analysis of Catalytic Reduction of 4-Nitrophenol by Metallic Nanoparticles Immobilized in Spherical Polyelectrolyte Brushes, The Journal of Physical Chemistry C 114 (2010) 8814-8820.

[9] S. Wunder, Y. Lu, M. Albrecht, *et al.*, Catalytic Activity of Faceted Gold Nanoparticles Studied by a Model Reaction: Evidence for Substrate-Induced Surface Restructuring, ACS Catalysis 1 (2011) 908-916.

[10] E. Menumerov, R.A. Hughes, S. Neretina, Catalytic Reduction of 4-Nitrophenol: A Quantitative Assessment of the Role of Dissolved Oxygen in Determining the Induction Time, Nano Letters 16 (2016) 7791-7797.

[11] P. Zhao, X. Feng, D. Huang, *et al.*, Basic concepts and recent advances in nitrophenol reduction by gold- and other transition metal nanoparticles, Coordination Chemistry Reviews 287 (2015) 114-136.

[12] N. Pradhan, A. Pal, T. Pal, Silver nanoparticle catalyzed reduction of aromatic nitro compounds, Colloids and Surfaces A: Physicochemical and Engineering Aspects 196 (2002) 247-257.

[13] K. Esumi, K. Miyamoto, T. Yoshimura, Comparison of PAMAM–Au and PPI–Au Nanocomposites and Their Catalytic Activity for Reduction of 4-Nitrophenol, Journal of Colloid and Interface Science 254 (2002) 402-405.

[14] M.A. Mahmoud, B. Garlyyev, M.A. El-Sayed, Determining the Mechanism of Solution Metallic Nanocatalysis with Solid and Hollow Nanoparticles: Homogeneous or Heterogeneous, The Journal of Physical Chemistry C 117 (2013) 21886-21893.

[15] Y. Mei, G. Sharma, Y. Lu, *et al.*, High Catalytic Activity of Platinum Nanoparticles Immobilized on Spherical Polyelectrolyte Brushes, Langmuir 21 (2005) 12229-12234.

[16] S. Panigrahi, S. Basu, S. Praharaj, *et al.*, Synthesis and Size-Selective Catalysis by Supported Gold Nanoparticles: Study on Heterogeneous and Homogeneous Catalytic Process, The Journal of Physical Chemistry C 111 (2007) 4596-4605.

[17] S. Saha, A. Pal, S. Kundu, *et al.*, Photochemical Green Synthesis of Calcium-Alginate-Stabilized Ag and Au Nanoparticles and Their Catalytic Application to 4-Nitrophenol Reduction, Langmuir 26 (2010) 2885-2893.

[18] P. Hervés, M. Pérez-Lorenzo, L.M. Liz-Marzán, *et al.*, Catalysis by metallic nanoparticles in aqueous solution: model reactions, Chemical Society Reviews 41 (2012) 5577-5587.

[19] K. Esumi, R. Isono, T. Yoshimura, Preparation of PAMAM− and PPI−Metal (Silver, Platinum, and Palladium) Nanocomposites and Their Catalytic Activities for Reduction of 4-Nitrophenol, Langmuir 20 (2004) 237-243.

[20] J. Zeng, Q. Zhang, J. Chen, *et al.*, A Comparison Study of the Catalytic Properties of Au-Based Nanocages, Nanoboxes, and Nanoparticles, Nano Letters 10 (2010) 30-35.

[21] X. Zhou, W. Xu, G. Liu, *et al.*, Size-Dependent Catalytic Activity and Dynamics of Gold Nanoparticles at the Single-Molecule Level, Journal of the American Chemical Society 132 (2010) 138-146.

[22] G. Weng, M.A. Mahmoud, M.A. El-Sayed, Nanocatalysts Can Change the Number of Electrons Involved in Oxidation–Reduction Reaction with the Nanocages Being the Most Efficient, The Journal of Physical Chemistry C 116 (2012) 24171-24176.

[23] R. Ciganda, N. Li, C. Deraedt, *et al.*, Gold nanoparticles as electron reservoir redox catalysts for 4-nitrophenol reduction: a strong stereoelectronic ligand influence, Chemical Communications 50 (2014) 10126-10129.

[24] E. Blanco, P. Atienzar, P. Hernández, *et al.*, The Langmuir–Hinshelwood approach for kinetic evaluation of cucurbit[7]uril-capped gold nanoparticles in the reduction of the antimicrobial nitrofurantoin, Physical Chemistry Chemical Physics 19 (2017) 18913-18923.

[25] N.C. Antonels, R. Meijboom, Preparation of Well-Defined Dendrimer Encapsulated Ruthenium Nanoparticles and Their Evaluation in the Reduction of 4-Nitrophenol According to the Langmuir–Hinshelwood Approach, Langmuir 29 (2013) 13433-13442.

[26] J.-H. Noh, R. Meijboom, Catalytic evaluation of dendrimer-templated Pd nanoparticles in the reduction of 4-nitrophenol using Langmuir–Hinshelwood kinetics, Applied Surface Science 320 (2014) 400-413.

[27] S. Gu, J. Kaiser, G. Marzun, *et al.*, Ligand-free Gold Nanoparticles as a Reference Material for Kinetic Modelling of Catalytic Reduction of 4-Nitrophenol, Catalysis Letters 145 (2015) 1105-1112.

[28] T. Aditya, A. Pal, T. Pal, Nitroarene reduction: a trusted model reaction to test nanoparticle catalysts, Chemical Communications 51 (2015) 9410-9431.

[29] Structure shape and stability of nanometric sized particles, Journal of Vacuum Science & Technology B: Microelectronics and Nanometer Structures Processing, Measurement, and Phenomena 19 (2001) 1091-1103.

[30] J.L. Elechiguerra, J. Reyes-Gasga, M.J. Yacaman, The role of twinning in shape evolution of anisotropic noble metal nanostructures, Journal of Materials Chemistry 16 (2006) 3906-3919.

[31] B.L. Smith, J.E. Hutchison, Transformations during Sintering of Small (Dcore < 2 nm) Ligand-Stabilized Gold Nanoparticles: Influence of Ligand Functionality and Core Size, The Journal of Physical Chemistry C 117 (2013) 25127-25137.

[32] R. Fenger, E. Fertitta, H. Kirmse, *et al.*, Size dependent catalysis with CTAB-stabilized gold nanoparticles, Physical Chemistry Chemical Physics 14 (2012) 9343-9349.

[33] S.M. Ansar, C.L. Kitchens, Impact of Gold Nanoparticle Stabilizing Ligands on the Colloidal Catalytic Reduction of 4-Nitrophenol, ACS Catalysis 6 (2016) 5553-5560.

[34] J. Piella, F. Merkoçi, A. Genç, *et al.*, Probing the surface reactivity of nanocrystals by the catalytic degradation of organic dyes: the effect of size, surface chemistry and composition, Journal of Materials Chemistry A 5 (2017) 11917-11929.

Publication 4
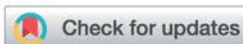
Probing the surface reactivity of nanocrystals by the catalytic degradation of organic dyes: the effect of size, surface chemistry and composition†

Jordi Piella,[ab] Florind Merkoçi,[a] Aziz Genç,[a] Jordi Arbiol, [ID][ac] Neus G. Bastús [ID] [*a] and Victor Puntes [ID] [acd]

We herein present a comprehensive study on how the catalytic performance and reusability of Au nanocrystals (NCs) are affected by systematic variations of crystal size, surface coating and composition. The reductions of different organic dyes (4-nitrophenol, rhodamine B and methylene blue) by borohydride ions were used as model catalytic reactions. The catalytic performance of the Au NCs ranged between 3.6 to 110 nm was found to be dependent on crystal size, indicating that Au surface atoms have a distinct size-dependent reactivity in this reaction. Similarly, the catalytic performance was found to be strongly dependent on the nature of the coating molecule, obtaining lower catalytic activities for molecules strongly bound to the Au surface. Finally, the catalytic performance was found to be dependent on the chemical composition of the NC (Au, Ag, Pt) and the model dye used as a testing system, with the highest degradation rate found for methylene blue, followed by 4-nitrophenol and rhodamine B. We believe that this study provides a better understanding of the catalytic performance of Au NCs upon controlled modifications of the structural and morphological parameters, and a working environment that can be used to facilitate the selection of the optimum NC size. coating molecule and evaluation system for a particular study of interest.

Introduction

Recent advances in the ability to design and develop synthetic strategies for the production of colloidal metal nanocrystals (NCs) with controlled morphologies and well-defined facets and structures allow for the tuning of their physicochemical properties and for optimizing their activity. This unprecedented morphological control is extremely useful in a variety of applications,[1–3] particularly in the case of heterogeneous catalysis, which can benefit from significant enhancements in catalytic activity and/or selectivity along with a significant reduction in the amount of employed material.[4–6] However, most of the catalysts used in industrial applications are still composed of polycrystalline NCs with poorly defined facets and broad size and shape distributions. These NCs of different morphological characteristics present distinct reactivity, attributable to the exposition of different crystallographic facets and fraction of surface atoms, which ultimately affects their performance independently of the catalytic reaction of the study.[7]

In general, the reduction of particle size leads to an increase of catalytic performance due to the larger surface-to-volume ratio of smaller NCs.[8,9] In addition to the fraction of atoms exposed, the performance (activity[10] and selectivity[9,11]) of the catalyst is also determined by the availability and coordination of these atoms. Thus, low coordinated atoms in small NCs may exhibit a much higher catalytic activity than highly coordinated ones due to a greater density of unsaturated atomic steps, ledges, and kinks which can serve as active sites for breaking chemical bonds.[12,13] However, very active surface atoms can also result in NCs being unstable during the course of their catalytic function. NCs have a strong tendency to minimize their total surface energy and, thus, structures with higher surface energies are more prone to surface reconstruction, sintering and aggregation, which may ultimately compromise the long-term catalytic performance and reusability of the catalyst.[7]

Size-dependent catalysis by colloidal metal NCs has been widely studied for different systems, including CO and alcohol oxidation,[14–16] selective hydrogenation[17] and the reduction of hexacyanoferrate(III) ions,[18] 4-nitrophenol[19] and eosin.[20] However, direct relationships between the size and catalytic function are missing or have been difficult to extract since the NCs studied, particularly in the small size regime, were

[a]*Institut Català de Nanociència i Nanotecnologia (ICN2), CSIC, The Barcelona Institute of Science and Technology (BIST), Campus UAB, 08193, Bellaterra, Barcelona, Spain. E-mail: neus.bastus@icn2.cat*

[b]*Universitat Autònoma de Barcelona (UAB), Campus UAB, 08183 Bellaterra, Barcelona, Spain*

[c]*ICREA, Pg. Lluis Companys 23, 08010 Barcelona, Catalonia, Spain*

[d]*Vall d'Hebron Institut de Recerca (VHIR), 08035, Barcelona, Spain*

† Electronic supplementary information (ESI) available. See DOI: 10.1039/c7ta01328k

This journal is © The Royal Society of Chemistry 2017

J. Mater. Chem. A, 2017, 5, 11917–11929 | **11917**

heterogeneous (lack of control of the NC size and comparison of NCs with different surface chemistries) and/or because of the use of model systems dissimilar to the working catalysts. Besides, the presence of the by-products in the reaction mixture, and the synthetic chemical environment in which they were produced (pH, concentration and surfactant) affected the final catalytic activity of NCs.[21] Therefore, an important requirement for comparing the size-dependent catalytic effects is the precise control of NC size and morphology following highly reproducible and robust techniques.

Additionally, an issue that has not been sufficiently addressed is the role of the outer organic shell, *i.e.*, the presence of capping agents normally used to control NC growth and stabilize the NCs against Ostwald ripening and aggregation. These organic ligands exert a "barrier" effect on reagents and products, limiting their access to (adsorption) and removal from (desorption) the catalytic surface, while on the other hand they provide chemical and colloidal stability to the catalyst.[4] Consequently, a compromise between activity and robustness (reusability) may require the use of ligands that cause a decrease in the performance of the catalysts but allow for longer durability.[22] Despite their crucial role in maintaining the stability of NCs, the impact of the ligand shell on both the final catalytic performance and reusability of NCs has been poorly studied,

due in part to the difficulty in producing metal NCs with the same intrinsic parameters (composition, size and crystal structure) while presenting different surface coatings.[23,24]

Herein, we present a comprehensive study on how the catalytic performance and reusability of colloidal dispersions of metal NCs are affected by systematic variations in size, composition, and surface coating using the reduction of organic dyes by borohydride ($NaBH_4$) ions as a model reaction (Scheme 1) (see Fig. S1†). Due to its simplicity and the ease by which it can be monitored using UV-Vis spectroscopic techniques[25] this reaction has emerged as one of the most widely used systems for assessing the catalytic (and photocatalytic) properties of nanostructured materials.[26–28] In particular, it takes place at room temperature only in the presence of the catalyst and has no known side reactions.[27] Therefore, high-precision real-time monitoring is possible by recording successive reductions in the characteristic absorbance maximum of the selected dye. Additionally, when carried out in excess of borohydride, the reaction can be understood in terms of the Langmuir–Hinshelwood (LH) model which allows the quantitative measurement of reaction rates and other kinetic parameters.[29] Furthermore, the use of monodisperse NCs allows estimating their total surface area (specific area) in solution
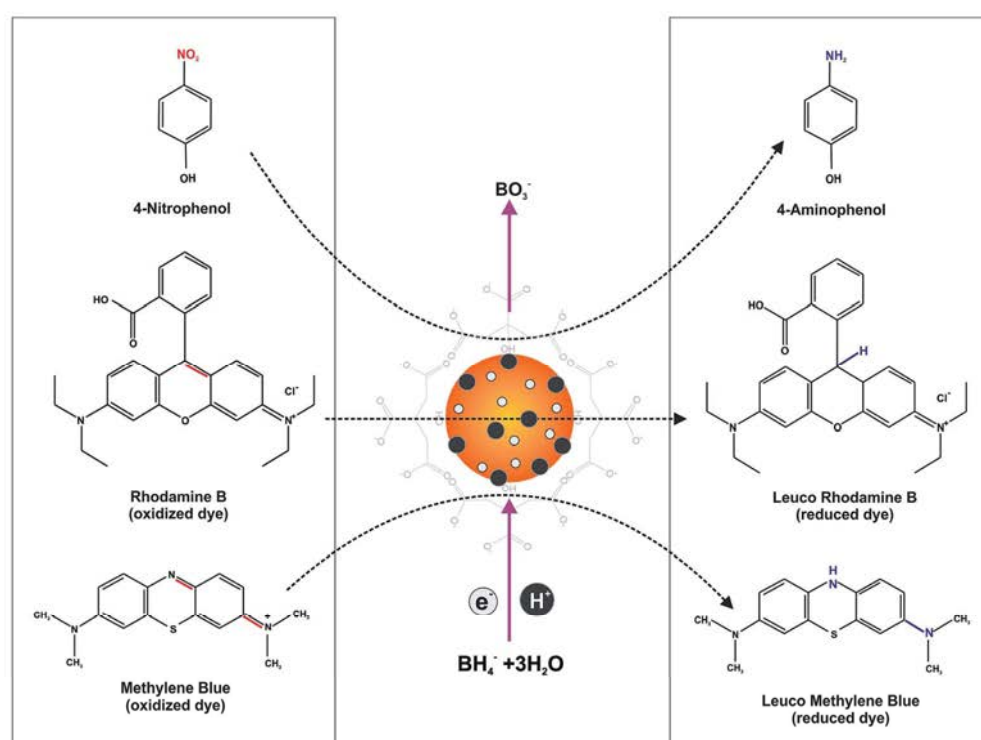
Scheme 1 Mechanism of the catalytic reduction and degradation of dyes used in this study. The catalytic reduction of dyes (4-nitrophenol, rhodamine B and methylene blue) by $NaBH_4$ is an electrochemical process in which the metal NCs have the main role of acting as the electron relay systems, transferring the electrons from the donor (BH_4^-) to the acceptor (dye). BH_4^- ions are adsorbed on and react with the surface of metal NCs, thereby creating active metal hydrides at their surface. At the same time, the dye also adsorbs on the surface of the metal NCs. Then electron transfer takes place between the dyes and BH_4^- through the particle surface. After receiving the electrons, the dye molecules are reduced to 4-aminophenol, leuco methylene blue or leuco rhodamine B.

11918 | *J. Mater. Chem. A*, 2017, 5, 11917–11929

This journal is © The Royal Society of Chemistry 2017

with a high precision, which can be directly used for determining the specific reaction constant per unit of surface area.

Taking advantage of the recent improvements in the colloidal synthesis of noble metal NCs, we have systematically studied these effects on highly monodisperse citrate-stabilized Au NCs of different sizes (from 3.6 to 110 nm).[30,31] Due to the accurate morphological and chemical control of their surface (functionalization), these colloids are extremely interesting candidates for studying the impact of the surface nature of NCs in their final catalytic performance. We start first by analyzing the size-dependent catalytic activity of Au NCs followed by an analysis of how their catalytic performance is affected by modifications of the Au NC surface chemistry. Finally, we extend this study to Ag and Pt NCs, aiming to understand how different materials present different catalytic performances. For completeness, we also evaluate this effect on different dyes in order to facilitate comparison and to evaluate the effects of charge and hydrophilicity of the dye. We believe that this study provides a better understanding of the catalytic performance of Au NCs upon controlled modifications of the structural and morphological parameters, and the working environment, that can be used to facilitate the selection of the optimum NC size, coating molecules and evaluation systems for a particular study of interest.

Results and discussion

Synthesis of gold nanocrystals

Colloidal aqueous solutions of Au NCs were produced following recently reported seeded-growth strategies.[30,31] $HAuCl_4$ was used as an Au precursor and its reduction was achieved by the combined use of two competing reducing agents: sodium citrate (SC) and tannic acid (TA). Au NCs were coated with SC/TA molecules, which provides a negative electrostatic stabilization once adsorbed onto the NC surface, allowing excellent dispersibility in aqueous media and easy post-synthetic functionalization. The growth of seed particles was kinetically controlled by adjusting the temperature of the reaction, the pH, the seed to Au precursor ratio, and the balance between both reducing agents. By controlling these synthetic parameters, successive generations of Au NCs with precisely controlled sizes (from 3.6 to 110 nm) and decreasing concentrations (from $\sim 10^{14}$ NCs per mL to $\sim 10^{10}$ NCs per mL, respectively) were obtained. Representative Transmission Electron Microscopy (TEM) images of selected Au NCs used in this study can be found in Fig. 1, clearly showing their high monodispersity and narrow size distribution, with standard deviations below 10% (see Fig. S2†).

For the deeper investigation of Au NCs and in order to discard facet-dependent effects, we analyzed the morphology and crystal structure of selected NC sizes using high-resolution TEM (HRTEM) and high-angle annular dark field scanning TEM (HAADF-STEM). The results shown in Fig. 2 suggest that Au NCs are faceted multiply twinned structures with decahedral or icosahedral geometry, all of them exposing the same {111} external facets. Interestingly, smaller Au NCs present a rounder decahedral shape while larger sizes have a morphology closer to the ideal decahedron with sharper facets exposed. Finally, very large particles present an icosahedral structure with an increased number of, but identical, {111} exposed facets. On the basis of the presented HRTEM observations, we propose a model to calculate and compare the variation of the ratio of surface active Au atoms with size (see Fig. S3†). The 3D atomic modelling and simulation results can be found in the ESI (Fig. S7–S12†). Although morphological differences are observed, it is possible to conclude that the particular size-dependent catalytic performance obtained is not produced by differences in the crystal structure or the facets exposed by the Au NCs upon variations on their size.
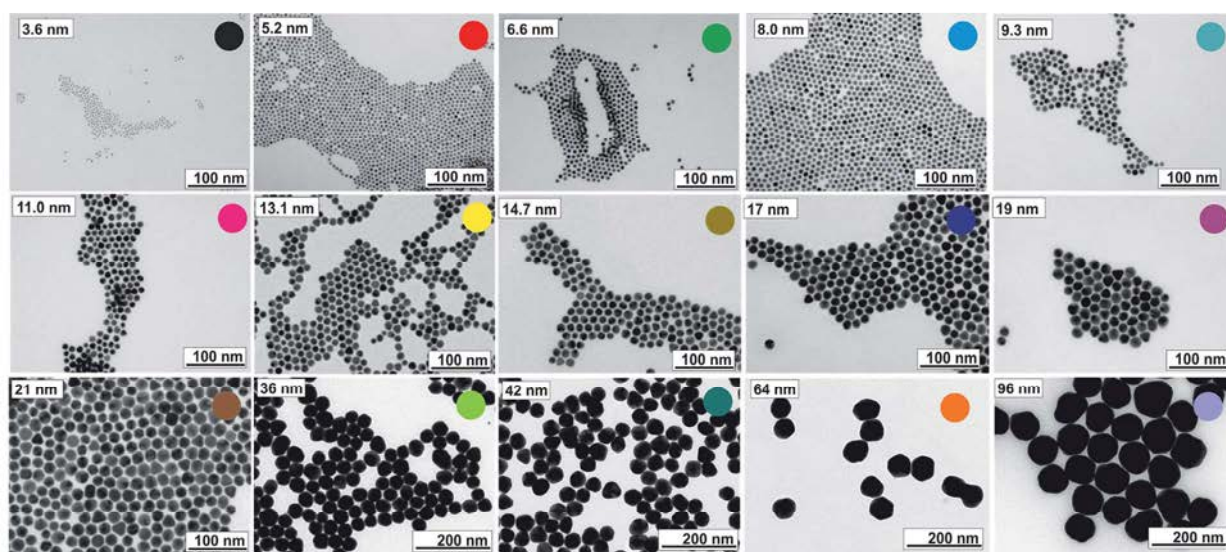

Fig. 1 Representative transmission electron microscopy images of citrate-stabilized Au NCs of selected particles ranging from 3.6 nm to 110 nm. Au NCs of 80.5 nm and 110 nm have been omitted from the figure. Color codes are visual aids corresponding to line plots in later figures.

This journal is © The Royal Society of Chemistry 2017

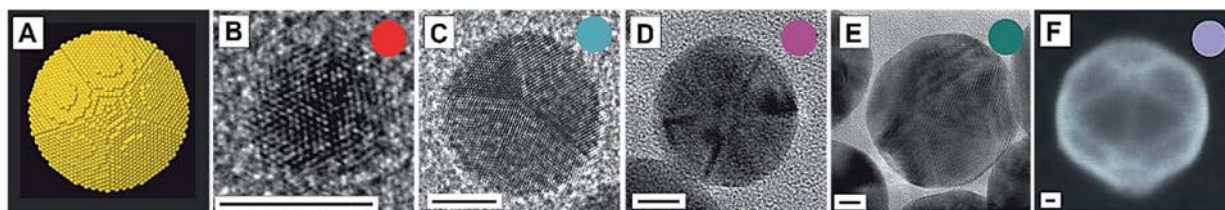J. Mater. Chem. A, 2017, 5, 11917–11929 | 11919

Fig. 2 Representative HRTEM (B–E) and SEM (F) images showing the typical structure of Au NCs of 5.2 nm (B), 9.3 nm (C), 19 nm (D), 42 nm (E) and 96 nm (F) shown in Fig. 1. Au NCs from (B) to (E) show a spheroidal decahedron morphology while (F) shows an icosahedral morphology. The image on the left (A) shows a 5.2 nm diameter 3D atomic simulation of a spheroidal decahedron.[32] Scale bars are 5 nm.

Size-dependent catalytic activity of Au nanocrystals

The catalytic performance of Au NCs of different sizes was assessed for the reduction of 4-nitrophenol (4-NP) to 4-amino-phenol (4-AP) using sodium borohydride ($NaBH_4$) as the reducing agent.[33] The size range from 3.6 to 110 nm was covered by 17 different samples. Catalysis measurements were carried out using aqueous solutions of 4-NP and $NaBH_4$ concentrations of 0.16 mM and 6 mM. Reactants were pipetted into the cuvette in the sequence 4-NP, $NaBH_4$ and then the Au NCs to initiate the reaction. In our experiments, the pH of the solution was maintained at highly alkaline conditions (pH $\sim$ 10), which allows discarding the chemical decomposition of the $NaBH_4$ on the timescale of the catalyzed reaction.[27,34] The total surface area of the NCs in solution was kept constant for the different sizes studied (0.5 cm² mL⁻¹) by controlling the volume of Au NCs added to the reaction mixture. An accurate estimation of the surface area was obtained by considering the size distribution of the Au NCs used (see S2†) and its concentration in solution. Every Au NC set was synthesized at least twice and the catalytic test reaction was repeated in triplicate for each set to ensure reproducibility.

The reduction process of 4-NP to 4-AP was monitored by measuring the temporal evolution of UV-Vis absorption spectra of the reaction mixture (Fig. 3A–F). The initially clear solution of 4-NP rapidly turned yellow immediately after the addition of $NaBH_4$, indicating the formation of 4-nitrophenolate ions (absorbance peak at $\sim$ 400 nm) in the alkaline reducing medium caused by $NaBH_4$.[10,26,35,36] Although the reduction of 4-NP by $NaBH_4$ is a thermodynamically feasible process, it is kinetically restricted and did not occur even after 7 days, with the maximum absorption peak remaining unaltered in the absence of the catalyst.[37] The further addition of Au NCs cata-lyzed the transfer of electrons from BH_4^- to nitrophenolate ions, which was translated into a gradual decrease in the absorbance at 400 nm and the growing of a new absorbance band at 298 nm, associated with the formation of 4-AP. It is worth mentioning that in our working conditions, no optical interference with the absorption band of the Au NCs was observed due to the low spectral overlapping between both signals (Fig. S6†) and the small volume of Au NCs needed to catalyze the reaction (Fig. 3A–F). The presence of isosbestic points in the spectra of the reacting mixtures indicates that no side reactions occur.[38] Importantly, the concentration of the BH_4^- ion greatly exceeded ($\sim$40-times higher) that of 4-NP and

essentially remained constant during the process.[27] Therefore, the reaction followed pseudo-first order kinetics[39] with respect to the concentration of 4-NP. Despite still being a matter of debate,[33] this assumption has been made in previous studies.[19,33,40] Degradation rates are described in terms of the apparent reaction rate constant, k_{app}, determined for each sample from the negative slope of the linear on the $\ln(A/A_0)$ vs. time plot, where A/A_0 is the dye absorbance maximum normalized to its value at the initial time of reaction.[25]

Fig. 3G shows the temporal evolution of the absorbance at 400 nm (4-nitrophenolate peak position) for all the sizes studied. As can be seen, for very small sizes the reduction of 4-NP is very fast, as evidenced by the fact that the absorption profile drops rapidly to zero. As the particle size increases from 5.2 to 8 nm, their catalytic activity slightly decreases. Surprisingly, Au catalysts with sizes between 8 nm and 11 nm are more active for the investigated reaction than the Au NCs with smaller diameters. For larger Au NCs (from 13 to 110 nm), an increase in size is accompanied by a decrease in catalyst activity, on average three times lower than that of the smallest Au NCs studied. The specific reaction rates are given in Fig. 3H and Table 1. k_{app} is highest for the smallest Au NCs studied (k = 0.444 min⁻¹), decreasing with increasing particle size except for the size range between 5.1 and 13.1 nm, where it first dropped, reaching a minimum at 9.3 nm (k = 0.288 min⁻¹), and then increased again (k = 0.408 min⁻¹). This behavior results in an absolute maximum at 3.6 nm, the smallest size herein tested, and a relative maximum at 13.1 nm. In between, Au NCs present a lower performance.

Interestingly, this unexpected non-monotonic behavior was masked when the obtained results were normalized to the elemental Au concentration in each sample (Fig. 3J) or to the total number of NCs in solution (Fig. 3K). Keeping constant the total number of Au atoms in solution, an overall decrease of the catalytic rate with size is observed, which can be explained by considering that the total number of surface Au atoms exposed exponentially decreases as the size of the Au catalyst increases, being much lower for larger Au NCs than for smaller ones.[41,42] However, this decrease is faster than expected if the decrease of catalytic activity was only due to the reduction of the surface to volume ratio. Conversely, when the total number of particles (i.e., particle concentration) was kept constant, an increase of the k_{app} with size is found, arising from the fact that a single, larger particle possesses a higher surface area than a small one.

11920 | J. Mater. Chem. A, 2017, 5, 11917–11929

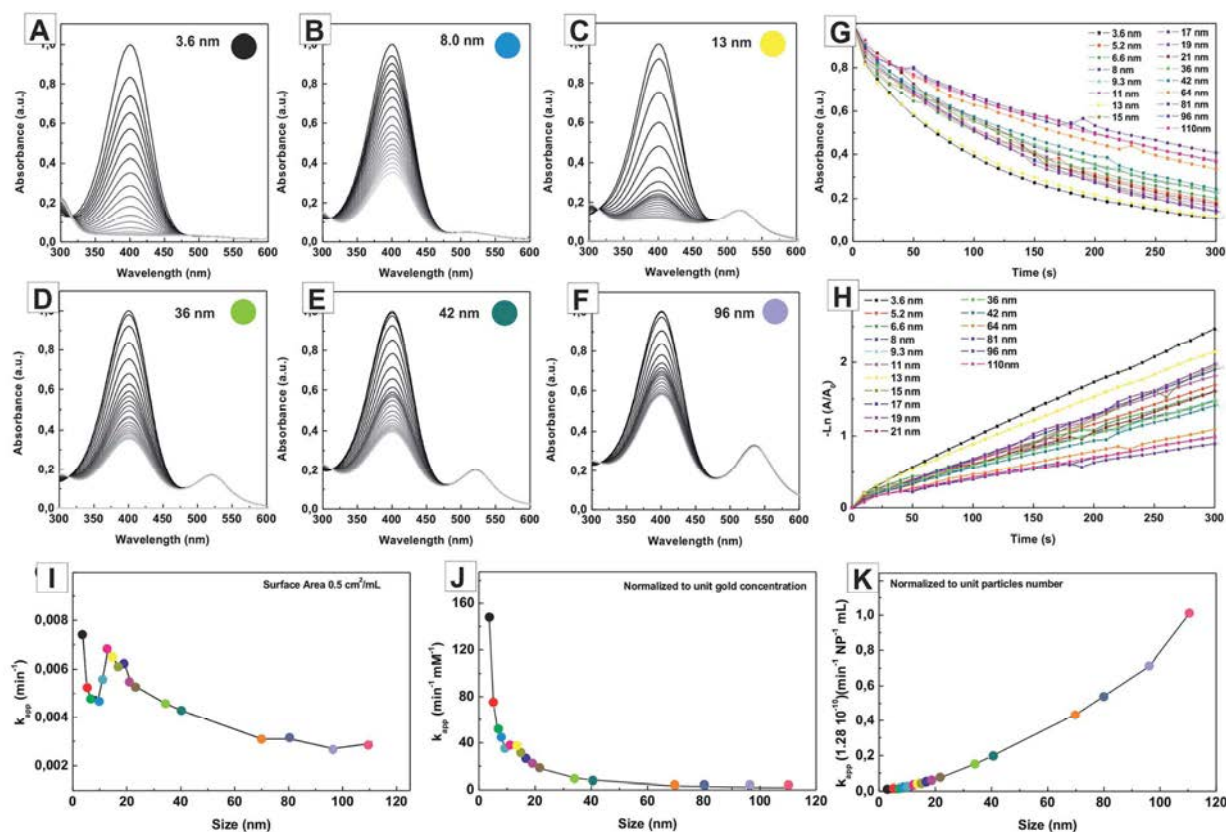This journal is © The Royal Society of Chemistry 2017

- 176 -

Fig. 3 Time-dependent UV-visible spectra for the catalytic reduction of 4-NP by $NaBH_4$ in the presence of Au NCs of selected sizes (A) 3.6 nm, (B) 8.0 nm, (C) 13 nm, (D) 36 nm, (E) 42 nm, (F) 96 nm. Plot of time dependent absorbance at 400 nm (G) and $\ln(A_t/A_0)$ vs. time (H) for the reduction of 4-NP by $NaBH_4$ in the presence of Au NCs of different sizes. Comparative plots of k_{app} were obtained by keeping constant the total surface area of the Au catalysts exposed (I), those normalized to the total Au atoms in solution (J) and particle number (K) for the different Au NC solutions tested. In our working conditions, low spectral overlapping between the absorption band of 4-NP and Au NCs was observed due to the small volumes of Au NCs needed to catalyze the reaction.

Consequently, the exceptional behavior found for the small particle regime (3.6 to 13.1 nm) cannot be observed when normalizing the studies to the total Au concentration or particle number. This indicates that for a proper evaluation of the intrinsic size effects at the nanoscale, the catalytic rates should be compared "per surface area" rather than comparing them "per particle" or "per weight", despite the fact that these parameters are the most commonly used to represent kinetic constants.[19,20]

The size-dependent catalytic activity found in this study indicates that the final catalytic performance is affected by the distinct surface reactivity of the Au NCs. Thus, Au atoms at the surface of small NCs are less coordinated than those of large particles and thus more reactive, nicely accounting for the general increase in their catalytic activity with decreasing sizes.[7,41,42] Unexpectedly, in our study this general trend partially reverts for sizes below 13.1 nm, indicating that small particles are less efficient in their catalytic performance than expected (Fig. 2I). Analogous observations have been reported for similar and dissimilar systems,[9,19,20,43–45] attributing its origin to a combination of factors, including size-dependent charge

transfer properties of the Au catalyst[46,47] and size-dependent chemical interaction between the Au catalyst and the reactant.[19,48] In this regard, it should be kept in mind that, although the catalytic process is well-described by a LH kinetic model, the interaction of the dye with the metal NCs is a complex process greatly determined by the size of the NCs and the nature of the dye. Thus, a lower catalytic performance may be correlated with a less efficient electronic transfer to the catalytic Au site. As discussed by Fenger et al.[19] and further analyzed by others, a minimal Au surface area is required to adsorb planar dyes with its aromatic ring parallel to the surface (at least 6 gold atoms are needed for one 4-NP to adsorb[19]). This binding mode would prefer larger particles that have larger surface terraces. This ineffective binding may lead to a decrease in the catalytic performance that ultimately explains the observed size-dependent catalytic performance. Similarly, the less efficient performance can also be explained by a higher avidity of the small particles to interact with their surrounding environment, particularly with the molecules in their vicinity. Thus, it is widely known that less coordinated atoms tend to form stronger bonds with small molecules, being reported, for instance, on

This journal is © The Royal Society of Chemistry 2017

J. Mater. Chem. A, 2017, 5, 11917–11929 | 11921

Paper

Table 1 Size-dependent catalytic performance of citrate-stabilized gold nanocrystals

	Pseudo first order rate constant					
	Constant surface area		Normalized Au atoms		Normalized particle number	
Size (nm)	k_{app} (min^{-1})	k_{app} ^{a} (size)/k_{app} (3.6 nm)	k_{Au} (min^{-1} mM^{-1})	k_{Au} ^{b} (size)/k_{Au} (3.6 nm)	k_{NC} (min^{-1} NPs^{-1} mL)	k_{NC} ^{c} (size)/k_{NC} (3.5 nm)
3.6 ± 0.4	0.444	1	147.8	1	3.57×10^{-13}	1
5.2 ± 0.8	0.318	0.73	74.2	0.50	5.27×10^{-13}	1.47
6.6 ± 0.6	0.288	0.68	51.4	0.35	7.58×10^{-13}	2.12
8.0 ± 0.8	0.288	0.65	43.9	0.30	1.11×10^{-12}	3.12
9.3 ± 1.0	0.282	0.64	35.6	0.24	1.51×10^{-12}	4.23
11.0 ± 1.0	0.336	0.76	36.6	0.25	2.51×10^{-12}	7.02
13.1 ± 1.1	0.408	0.92	37.8	0.26	4.33×10^{-12}	12.11
14.7 ± 1.2	0.39	0.88	31.8	0.22	5.22×10^{-12}	14.60
17 ± 1.4	0.366	0.82	25.8	0.18	6.80×10^{-12}	19.01
19.3 ± 1.5	0.378	0.85	23.5	0.16	8.31×10^{-12}	23.23
21.4 ± 1.5	0.324	0.73	18.0	0.12	9.27×10^{-12}	25.91
36 ± 3.1	0.276	0.62	9.9	0.07	1.95×10^{-11}	54.56
42.0 ± 3.7	0.258	0.58	8.1	0.05	2.50×10^{-11}	70.07
64.0 ± 6.4	0.186	0.42	3.2	0.02	5.60×10^{-11}	156.56
80.5 ± 6.8	0.186	0.42	2.7	0.02	7.01×10^{-11}	196.06
96.3 ± 8.1	0.162	0.36	2.0	0.01	9.18×10^{-11}	256.42
110.4 ± 8.5	0.174	0.39	1.9	0.01	1.28×10^{-10}	359.66

^{a} k_{app} pseudo first order rate constant at equal total surface area 0.5 cm^2 mL^{-1}. ^{b} k_m pseudo first order rate constant normalized at total mass $k_{Au} = k_{app}/[Au]$. ^{c} k_n pseudo first order rate constant normalized at total number of particles $k_{NC} = k_{app}/[NC]$.

how thiol-terminated ligands adsorb more strongly on small NCs than larger ones.[48] Therefore, as suggested by El-Sayed and co-workers,[44] this stronger adsorption of reactant molecules on small NCs may block the reaction players from reaching the particle surface, resulting in a decrease in the catalytic performance and consequently a lower reaction rate. Finally, another important factor is the colloidal stability and integrity of the Au NCs as the coordination of the surface atoms decreases.[7] This higher morphological instability of small particles is well-known, which is specifically critical at the liquid–solid interphase. Thus, small Au NCs more promptly undergo surface degradation processes such as corrosion[49] and dissolution, as well as aggregation and coalescence. All of these processes significantly alter the surface accessibility of the Au NCs, and therefore their catalytic performance. All of these hypotheses may account for the observed results in the small Au NC regime.

Reusability of catalytic nanocrystals

Robustness and stability are important factors when assessing the overall performance of a catalyst. In our study, size-dependent reusability was investigated by evaluating the repeated use of the Au NCs. The experiments for the degradation of 4-NP were performed six consecutive times, each time using the same Au NCs and a fresh dye solution. Results for two selected sizes, 3.6 nm and 9.3 nm, are shown in Fig. 4. As can be seen in Fig. 4C and D, larger Au NCs show relatively good catalytic activity after 6 reaction cycles which turns into minor variations (<8%) of its reaction rate constant after different cycles. On the contrary, the performance of small Au NCs is compromised after repeated use. Thus, their reaction rate constant decreases 50%, from 0.152 min^{-1} to 0.73 min^{-1}. This

decrease in the efficiency for small Au NCs probably results from their lower structural stability, which may be attributed to their higher curvature radii.

The obtained results evidence the complex role of the surface nature in the evaluation of the overall catalytic performance of Au NCs. Although low-coordinated surface atoms in small NCs exhibit much higher catalytic activity due to a greater density of unsaturated atomic steps,[12] these very active surface atoms may also be responsible for the deactivation of the catalyst. Thus, the small NCs have higher surface energies and hence a strong tendency to minimize their total surface energy, which may be translated into surface reconstruction, sintering and eventually aggregation.[9] Alternatively, as previously discussed, this lower performance can also be ascribed to the stronger adsorption of reactant molecules on small NCs.[44] In this sense, a detailed design and study of the catalyst functionalization of the NCs is of fundamental importance in the development of improved catalysts. As mentioned before, a compromise between activity and reusability may require the use of ligands that cause a decrease in the initial reaction rate but allow a longer durability, passivating the surface and providing robust colloidal stability.

Effect of surface coating

The effect of surface coating was studied by comparing the rates of the 4-NP reduction by NaBH$_4$ catalyzed by identical 3.6 nm Au NCs stabilized with different molecules: hexanoic acid (HA), aminohexanoic acid (AHA), polyethyleneglycol (PEG) of two different lengths (1000 and 3500 MW) and functional group (NH$_2$ and SH), polyvinylpyrrolidone (PVP, 40 KDa), mercaptoundecanoic acid (MUA) and bovine serum albumin (BSA).
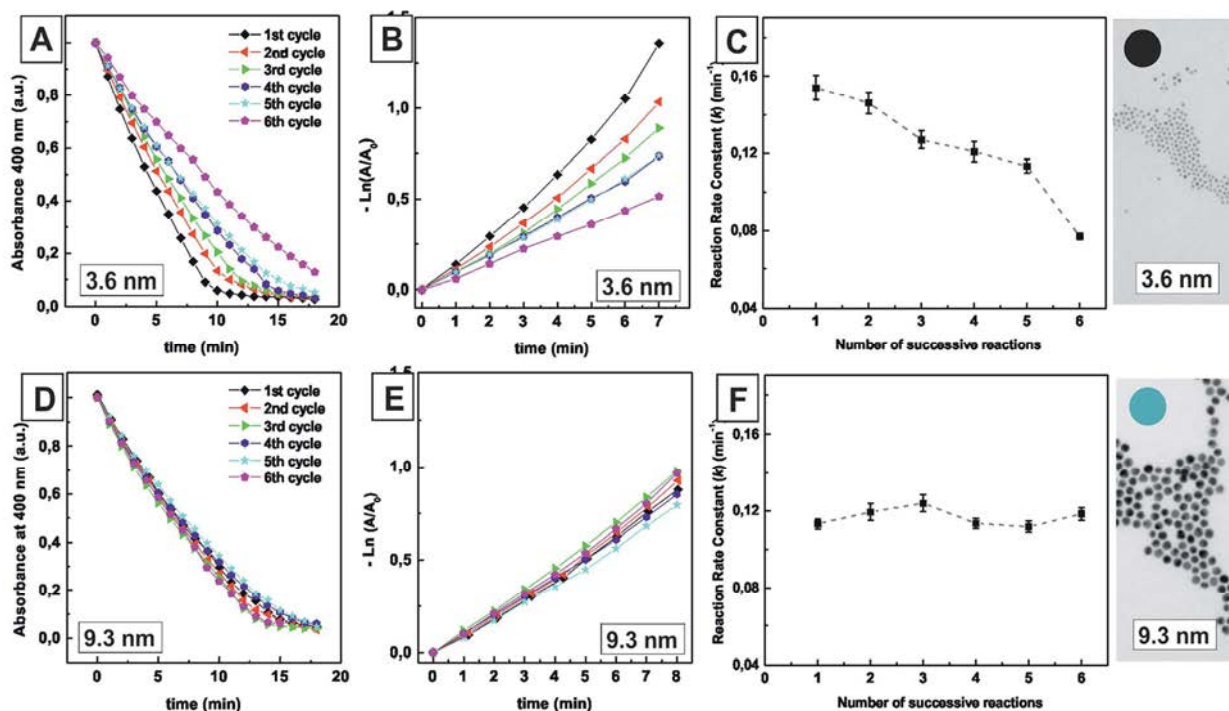
- 178 -

Fig. 4 Evaluation of the reusability of Au NPs of different sizes. Plot of time-dependent absorbance 400 nm (A, D) and $\ln(A_t/A_0)$ vs. time (B, E) for the reduction of 4-NP by $NaBH_4$ in the presence of Au NCs of different sizes: 3.6 nm (A, B) and 9.3 nm (D, E). Comparative plots of k_{app} obtained by keeping constant the total surface area of Au catalysts exposed vs. number of successive reaction cycles for Au NCs of 3.6 nm (C) and 9.3 nm (F).

These ligands were chosen as model molecules due to their wide use and the special interest paid to them in material synthesis and functionalization.[50–53] Ligand exchange was performed by adding known amounts of molecules to Au NC solutions under vigorous stirring. The mixture was allowed to react for 2 to 12 h (depending on the molecule affinity) until no further peak evolution was detected by UV-vis spectroscopy.[54] Functionalized NCs were then centrifuged to remove the excess of unreacted molecules and finally re-dispersed in the same volume of Milli-Q water. Characterization of the Au NCs (see Fig. S4†) shows that neither aggregation nor observable structural or morphological changes took place, indicating that the observed catalytic effects were due to modifications of the NC surface chemistry.

The effect of surface coating in the catalytic performance of Au NCs is summarized in Fig. 5 and Table 2. As can be seen, a distinct decrease of the reduction rate of the dyes is observed after the functionalization of Au NCs with different molecules. Thus, as-synthesized SC/TA-stabilized Au NCs present the highest reaction rate constant, completely catalyzing 4-NP degradation in less than 20 min (Fig. 5A). In contrast, the reduction rate of dyes is decreased to a considerably extent for HA (Fig. 5B), AHA (Fig. 5C), and NH_2-PEG (1000)-coated Au NCs (Fig. 5D) having rate constants 3 times lower than those obtained for as-synthesized Au NCs (Fig. 5I–K). Finally, the functionalization of Au catalysts with MUA (Fig. 5E), PVP-40 (Fig. 5F), BSA (Fig. 5G) and SH-PEG(3500) (Fig. 5H) significantly blocked catalysis after some initial progress. As

a result, the obtained reaction rates are up to 2 orders of magnitude lower than that obtained for the as-synthesized Au NCs (Fig. 5I–K).

The obtained results indicate that the functionalization of Au NCs with different molecules compromise (to some extent) the performance of the catalysts. It is well-assumed that, after functionalization, Au NCs are surrounded by a dense coating layer which acts as a barrier for the reacting molecules, consequently leading to a partial or complete loss of catalytic activity. Interestingly, the extent of this process is determined by the nature of the surfactant layer (degree of density, robustness and hydrophilicity) and can be explained, in a simplified manner, in terms of the physicochemical characteristics (length and anchor group) of the molecule tested. Thus, the catalytic performance depends on the molecule length. Assuming a full surface coverage of the NC, short molecules provide a higher surface accessibility than larger ones, which is translated into higher catalytic performances. This is clearly seen in Fig. 5 where the reduction rate is distinctly slower in SH-PEG(3500) than in MUA. Both molecules present the same anchor group (SH) but different lengths (~7.9 nm vs. ~2.4 nm). Similarly, the catalytic reduction rate is closely related to the nature of the chemical bonding between the molecule and the Au NCs. Thus, strongly bound molecules, such as SH-terminated ones, block more efficiently than weakly bound ones (NH_2 or COOH), the reagents and reaction intermediates reaching the particle surface, thereby acting as a poison to the reaction and decreasing the rate of reaction. This is appreciated when
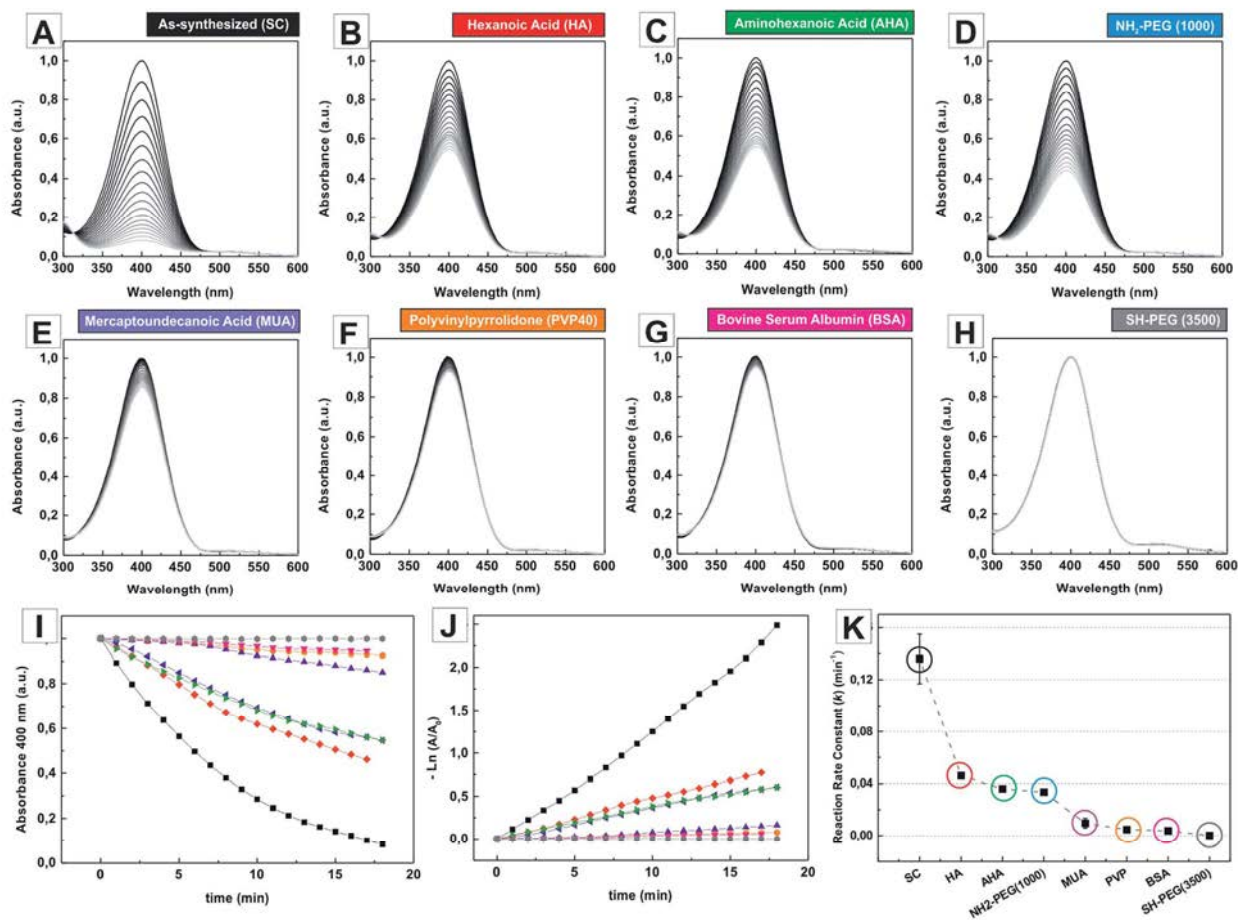
This journal is © The Royal Society of Chemistry 2017

J. Mater. Chem. A, 2017, 5, 11917–11929 | 11923

Journal of Materials Chemistry A

Fig. 5 Influence of surface coating on the catalytic performance of Au NPs. The effect of surface coating was studied by comparing the rates of the 4-NP reduction by NaBH₄ catalyzed by identical 3.6 nm Au NCs stabilized with different molecules: as-synthesized (A), hexanoic acid (B), aminohexanoic acid (C), NH₂-PEG (1000) (D), mercaptoundecanoic acid (E), polyvinylpyrrolidone (F), bovine serum albumin (BSA) (G), and SH-PEG (3500) (H). Plot of time-dependent absorbance at 400 nm (I) and $\ln(A_t/A_0)$ vs. time (J) for the reduction of 4-NP by NaBH₄ in the presence of Au NCs of 3.6 nm after modifications of their surface coating. Comparative plots of k_{app} normalized to surface area vs. functionalization molecule (K).

Table 2 The Effect of the coating molecule on the catalytic performance of 3.6 nm gold nanocrystals[a]

Stabilizer	Pseudo first order rate constant	
	k_{app} (min^{-1})	$k_{app\ (stabilizer)}/k_{app\ (citrate)}$
SC	0.136	1
HA	0.046	0.34
AHA	0.036	0.26
NH₂-PEG (1000)	0.034	0.25
MUA	0.010	0.07
PVP	0.005	0.03
BSA	0.004	0.03
SH-PEG (3500)	0.000	0.00

[a] k_{app} pseudo first order rate constant at equal total surface area.

comparing the catalytic performance of HA, AHA and MUA which differ in the anchor group (*i.e.*, the nature of the chemical bonding, HA (COOH−), AHA (NH₂−) and MUA (SH−)), while their length is similar (∼1.3 nm for HA and AHA and ∼2.4 nm for MUA) and much shorter than that of the other molecules tested (NH₂-PEG(1000), ∼4.3 nm) that present a higher catalytic performance. Other factors affecting the performance of the catalysts are the charge and particular hydrophobicity/hydrophilicity of the molecule. As a result of the electrostatic interaction between the dye and the coating layer, the accessibility of the reacting molecules to the catalyst is more difficult for the dye when the surfactant carries the same charge due to electrostatic repulsion. Consequently, a larger decrease of the reaction rate is observed when the dye and the surfactant carry the same charge, while a smaller reduction of the reaction rate results in the dye and the surfactant being oppositely charged. Besides, the degree of molecule loading density and packaging along with the effectivity of the ligand exchange reaction determine the structure of the coating layer, which ultimately affects the performance of the catalyst.[55]

This surface-dependent reactivity of NCs has been widely reported for similar systems, including Au and Pd NCs coated

Paper
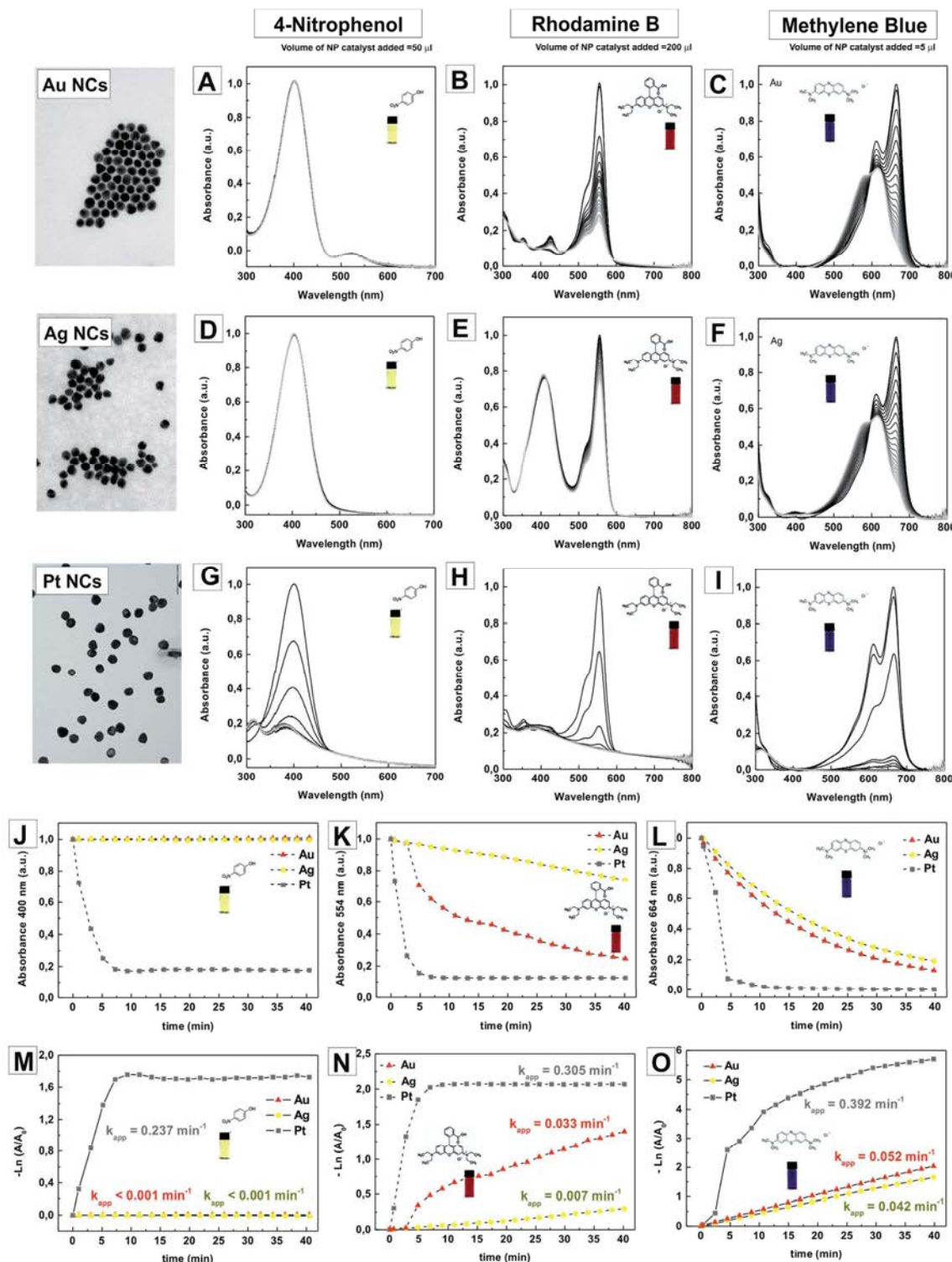
Fig. 6 Influence of the dye on the catalytic performance of Au, Ag and Pt NCs. The effect of the model dye was studied by comparing the reduction rates of 3 model dyes (4-NP, RB and MB) by $NaBH_4$ catalyzed by identical 20 nm Au, Ag and Pt NCs stabilized with polyvinylpyrrolidone (A–I). Plot of time-dependent absorbance at 400 nm (J–L) and $\ln(A_t/A_0)$ vs. time (M–O) for the reduction of 4-NP, RB and MB by $NaBH_4$ in the presence of Au, Ag and Pt NCs of 20 nm after modifications of their surface coating with PVP.

This journal is © The Royal Society of Chemistry 2017

J. Mater. Chem. A, 2017, **5**, 11917–11929 | **11925**

- 181 -

with different organic molecules.[19,23,24,56] An interesting point of these findings is the enhanced catalytic performance found after coating the Au NCs with hexadecyltrimethylammonium bromide (CTAB), widely used in the synthesis of Au NCs.[57–59] In our studies, this synergic effect was discarded when evaluating the catalytic performance of an aqueous solution of CTAB molecules (see Fig. S5†), which showed that the molecules themselves are able to rapidly degrade 4-NP. These results emphasize the important role of the organic ligand in heterogeneous catalysis.[60] Similar controls were performed with all the ligands described in Fig. 5 with the result that catalysis did not occur even after 48 hours.

Effect of dye and nanocrystal composition

Beyond size and surface effects, the catalytic properties of Au NCs depend on the surrounding environment, particularly the model dye used as the testing system. In order to evaluate this influence, different organic dyes with well-defined spectral and electrochemical properties were used as probes. In addition to 4-NP, methylene blue (MB) and rhodamine B (RB) were chosen due to their wide use and their particular absorption profiles.[36] Each of them present a strong absorption signal in the UV-Vis region. 4-NP has a maximum at 400 nm, RB at 554 nm and MB at 664 nm, which may interfere with the optical properties of the colloidal catalysts (see Fig. S6†). The effects of the dye of choice and composition of the metal catalysts were studied by comparing the rates of 4-NP, RhB and MB reduction by NaBH$_4$ catalyzed by Au, Ag and Pt NCs (Fig. 6A–I). Each catalyst solution consisted of ~20 nm PVP-capped NCs with a concentration of 4.2×10^{12} NCs per mL, which allows the size and capping effect to be discarded. Moreover, to properly evaluate the stability of each dye in the presence of each catalyst, the dye concentration was kept constant.

Fig. 6 shows the plot of the normalized decay of absorbance at each dye maximum as a function of time (Fig. 6J–L), together with the negative natural logarithm from which the k_{app} values were obtained (Fig. 6M–O). These values are summarized in Table 3. As can be seen, different concentrations of catalyst were needed to completely degrade each dye (50 μL for 4-NP, 200 μL for RB and 5 μL for MB), suggesting that the reaction rate strongly depends on the dye used but not on the overall response to variation of the catalyst composition. MB appeared to degrade most promptly followed by 4-NP and then RB. As expected, the reaction rate depends on the composition of the catalysts used. In our explored conditions, the reactions catalyzed by Pt are systematically faster than those catalyzed by Au and Ag, independent of the dye. Thus, only 5 μL of the Pt catalyst solution was needed to completely degrade the MB solution (Fig. 6I), whereas Ag (Fig. 6F) and Au (Fig. 6C) showed a similar lower catalytic performance, with Au being slightly higher. Similar tendencies were found when using 4-NP. In this case, the concentration of the Pt catalyst needed to completely degrade the 4-NP (Fig. 6G) solution was 10-fold higher than that with MB (Fig. 6I). It is worth mentioning that, in our working conditions, no optical interferences were observed for Pt (Fig. 6G) or Au (Fig. 6A) due to the low volume of NCs needed to

Table 3 The Effect of the dye on the catalytic performance of 20 nm gold, silver and platinum nanocrystals coated with PVP

	Pseudo first order rate constant	
	k_{app} (min^{-1})	$k_{app\ (metal)}/k_{app\ (Au)}$
4-Nitrophenol		
Au	<0.001	1
Ag	<0.001	1
Pt	0.237	237
Rhodamine B		
Au	0.033	1
Ag	0.007	0.212
Pt	0.305	9.240
Methylene blue		
Au	0.052	1
Ag	0.042	0.807
Pt	0.392	7.538

catalyze the reaction. Conversely, the high absorption signal of Ag NCs (Fig. 6D), with a strong maximum surface plasmon resonance (SPR) band peaking at 400 nm, interferes with the dye signal. All this suggests that the evaluation of the catalytic activity of Ag with 4-NP is not suitable since high quantities of Ag catalysts were needed to complete the reaction, altering the absorbance signal and thereby providing unreliable results due to the difficulties in de-convoluting both signals. Despite Au NCs also contributing with a small absorbance peak at 520 nm, the significantly lower optical intensity does not mask the dye signal and can be practically discarded. Finally, among the three tested dyes, RB was the most difficult to reduce, evidenced by the fact that 200 μL of catalyst solution (40-fold higher than with MB) were needed to catalyze the reaction. As in the previous cases, Pt shows the highest activity (Fig. 6H), followed by Au (Fig. 6B), which is also significantly higher than Ag (Fig. 6E).

Conclusions

Au NCs with sizes ranging from 3.6 to 110 nm and with different functionalization were tested for their efficiency in the catalytic reduction of 3 different dyes (4-NP, RB and MB) with sodium borohydride. The catalytic performance of the Au NCs was found to be dependent on size, indicating that the performance is affected by the distinct surface reactivity of the Au NCs. As expected, the catalytic activity was also found to be strongly dependent on the nature of the coating molecule, with increased catalytic activities for molecules that are weakly coordinated with the Au surface and compromised for molecules that are strongly absorbed. This lower catalytic activity for strongly bound molecules was due to the blocking of the reaction players reaching the particle surface, mediated by the presence of strongly adsorbed molecules, thereby decreasing the rate of the reaction. Finally, the results demonstrated that the catalytic performance of NCs depends on the surrounding

environment, particularly the model dye used as the testing system and the NC chemical composition. The highest activity was found for MB, followed by 4-NP and RB. Besides, the reactions catalyzed by Pt are systematically faster than those catalyzed by Au and Ag, independent of the dye. We believe that this study provides an advance in basic understanding of NC catalytic properties and also a quantification of their response in performance and reusability to controlled modifications of structural, morphological and physicochemical parameters, and the working environment. This knowledge can be used to select the optimum NC size, capping molecule and catalytic evaluation system for a particular study of interest, providing a framework through which the effects of potential system improvements can be assessed.

Experimental methods

Chemicals

Sodium citrate tribasic dihydrate (≥99%), gold(III) chloride trihydrate $HAuCl_4 \cdot 3H_2O$ (99.9% purity), tannic acid (ACS reagent), 4-nitrophenol solution (10 mM), rhodamine B (≥95%), methylene blue, sodium borohydride (99.99%), hexanoic acid (99%), 6-aminohexanoic acid (≥98.5%), 11-mercaptoundecanoic acid (98%), polyvinylpyrrolidone (M_W 40 000), poly(ethylene glycol) 2-aminoethyl ether acetic acid ($M_W \approx 1000$ g mol^{-1}, $n = 22$) (NH$_2$-PEG1000-COOH), poly(ethylene glycol) 2-mercaptoethyl ether acetic acid ($M_W \approx 3500$ g mol^{-1}, $n = 77$) (SH-PEG3500-COOH), 11-mercaptoundecanoic acid and bovine serum albumin (BSA) were purchased from Sigma-Aldrich. All the reagents were used as received without further purification and all the glass material was sterilized and dehydrogenated in an oven prior to use. Milli-Q water was used in the preparation of all the solutions.

Nanocrystals synthesis

Aqueous solutions of citrate-stabilized Au NCs with different sizes (3.6–110 nm) were synthesized according to previously developed seeded-growth methods in our group. Detailed synthetic procedure and full characterization of the resultant solutions can be found in the respective articles.[30,31] Briefly, Au NCs with increasing sizes were obtained from an initial Au NC solution after different sequential steps of growing, consisting of sample dilution plus further addition of the gold precursor. Consequently, the number of particles in the solution decrease as its size increases. In detail, the concentration of small 3.6 nm particles was 10^{14}, which decreased down to 10^{10} NCs per mL for the largest 110 nm particles. All the particles were used within 20 days of their synthesis. A similar seeded-growth strategy was followed to produce the citrate-stabilized Ag NCs.[36] The resultant NCs were purified by centrifugation (10 000g to 18 000g, depending on the size) acid and further redispersed in Milli-Q water or sodium citrate 2.2 mM before sample characterization and ligand exchange experiments. Pt NC surfaces were produced via a galvanic replacement reaction (GRR) using PVP-coated 20 nm Ag NPs as sacrificial templates.[10]

Ligand exchange of nanocrystals

For ligand exchange experiments, aqueous solutions of (i) hexanoic acid (99%), (ii) 6-aminohexanoic acid (≥98.5%), (iii) 11-mercaptoundecanoic acid (98%), (iv) polyvinylpyrrolidone (M_W 40 000), (v) poly(ethylene glycol) 2-aminoethyl ether acetic acid ($M_W \approx 1000$ g mol^{-1}, $n = 22$) (NH$_2$-PEG1000-COOH), (vi) poly(ethylene glycol) 2-mercaptoethyl ether acetic acid ($M_W \approx 3500$ g mol^{-1}, $n = 77$) (SH-PEG3500-COOH), and (vii) bovine serum albumin (BSA) were prepared and added to as-synthesized citrate-stabilized Au NC solutions under vigorous stirring (final concentration 0.5 mM). The mixture was allowed to react for 2 h (SH-PEG3500-COOH, MUA) or 12 h (HA, AHA, PVP40, NH$_2$-PEG1000-COOH, BSA), and the resultant NCs were then centrifuged to remove the excess of unreacted molecules and finally redispersed in the same volume of Milli-Q water.[54]

Characterization

NCs were characterized by transmission electron microscopy (TEM, JEOL 1010) and UV-vis spectroscopy (Shimadzu, 2010). All the 3D atomic models presented in this work have been created by using the Rhodius software.[61,62] The morphological and structural characterizations of the nanocrystals were carried out by high-resolution TEM (HRTEM). HRTEM images were obtained using a FEI Tecnai F20 field-emission gun microscope with a 0.19 nm point-to-point resolution operated at 200 keV.

Catalytic reaction

The standard catalytic test reaction was carried out in 4.5 mL PS-disposable cuvettes. Aqueous solutions of 4-nitrophenol (4-NP), methylene blue (MB) or rhodamine B (RB) (1 mM) were prepared as received. NaBH$_4$ solution (0.1 M, pH = 10.6) was freshly prepared before each set of kinetic trials. Experimentally, 2 mL of Milli-Q water, 30–75 μL of dye solution and 100 μL of NaBH$_4$ solution were sequentially added into a PS-disposable cuvette. Then, an aqueous solution containing the Au NCs (normalized in terms of surface area) was injected into the cuvette to start the reaction. The absorbance of each organic dye was monitored by UV-Vis spectroscopy as a function of time (20 runs, each 60 seconds) in the 300 nm to 800 nm range at room temperature.

Calculation of kinetic rate constants

Apparent kinetic constant rates were obtained according to the first-order rate law in which the intensity of the signal was firstly normalized to the maximum of absorbance of each dye (400 nm, 554 nm and 664 for 4-NP, RB and MB, respectively) and then the negative natural logarithm was plotted as a function of time, where the steepest part of the curve was linearly fitted, the slope of which was considered the apparent rate constant k_{app}. The rate constant is considered apparent because previous work by other groups has shown that the observed rate constant depends on the concentration of NaBH$_4$ as well as on the starting concentration of 4-nitrophenol.[39] Each measurement was performed in triplicate to evaluate its reproducibility.

This journal is © The Royal Society of Chemistry 2017

J. Mater. Chem. A, 2017, 5, 11917–11929 | 11927

Journal of Materials Chemistry A

Paper

Acknowledgements

References

1 N. G. Bastús, E. Gonzalez, J. Esteve, J. Piella, J. Patarroyo, F. Merkoçi and V. Puntes, *Z. Phys. Chem.*, 2015, **229**, 65–83.

2 L. K. Bogart, G. Pourroy, C. J. Murphy, V. Puntes, T. Pellegrino, D. Rosenblum, D. Peer and R. Levy, *ACS Nano*, 2014, **8**, 3107–3122.

3 M. V. Kovalenko, L. Manna, A. Cabot, Z. Hens, D. V. Talapin, C. R. Kagan, V. I. Klimov, A. L. Rogach, P. Reiss, D. J. Milliron, P. Guyot-Sionnnest, G. Konstantatos, W. J. Parak, T. Hyeon, B. A. Korgel, C. B. Murray and W. Heiss, *ACS Nano*, 2015, **9**, 1012–1057.

4 Y. Wu, D. Wang and Y. Li, *Chem. Soc. Rev.*, 2014, **43**, 2112–2124.

5 Y. Xia, H. Yang and C. T. Campbell, *Acc. Chem. Res.*, 2013, **46**, 1671–1672.

6 H.-L. Jiang and Q. Xu, *J. Mater. Chem.*, 2011, **21**, 13705–13725.

7 N. G. Bastús, E. Casals, I. Ojea, M. Varon and V. Puntes, in *The Delivery of Nanoparticles*, ed. A. A. Hashim, InTech, 2012, DOI: 10.5772/35238.

8 M. Haruta, *Catal. Today*, 1997, **36**, 153–166.

9 R. Reske, H. Mistry, F. Behafarid, B. Roldan Cuenya and P. Strasser, *J. Am. Chem. Soc.*, 2014, **136**, 6978–6986.

10 E. Gonzalez, F. Merkoci, R. Arenal, J. Arbiol, J. Esteve, N. G. Bastus and V. Puntes, *J. Mater. Chem. A*, 2016, **4**, 200–208.

11 K. M. Bratlie, H. Lee, K. Komvopoulos, P. Yang and G. A. Somorjai, *Nano Lett.*, 2007, **7**, 3097–3101.

12 Y. Xiong, B. J. Wiley and Y. Xia, *Angew. Chem., Int. Ed.*, 2007, **46**, 7157–7159.

13 M. A. Mahmoud, R. Narayanan and M. A. El-Sayed, *Acc. Chem. Res.*, 2013, **46**, 1795–1805.

14 M. Valden, X. Lai and D. W. Goodman, *Science*, 1998, **281**, 1647–1650.

15 H. Tsunoyama, H. Sakurai, Y. Negishi and T. Tsukuda, *J. Am. Chem. Soc.*, 2005, **127**, 9374–9375.

16 H. Song, R. M. Rioux, J. D. Hoefelmeyer, R. Komor, K. Niesz, M. Grass, P. Yang and G. A. Somorjai, *J. Am. Chem. Soc.*, 2006, **128**, 3027–3037.

17 J. Jia, K. Haraki, J. N. Kondo, K. Domen and K. Tamaru, *J. Phys. Chem. B*, 2000, **104**, 11153–11156.

18 P. L. Freund and M. Spiro, *J. Phys. Chem.*, 1985, **89**, 1074–1077.

19 R. Fenger, E. Fertitta, H. Kirmse, A. F. Thunemann and K. Rademann, *Phys. Chem. Chem. Phys.*, 2012, **14**, 9343–9349.

20 T. K. Sau, A. Pal and T. Pal, *J. Phys. Chem. B*, 2001, **105**, 9266–9272.

21 C. Deraedt, L. Salmon, S. Gatard, R. Ciganda, R. Hernandez, J. Ruiz and D. Astruc, *Chem. Commun.*, 2014, **50**, 14194–14196.

22 D. Astruc, F. Lu and J. R. Aranzaes, *Angew. Chem., Int. Ed.*, 2005, **44**, 7852–7872.

23 Y. Li and M. A. El-Sayed, *J. Phys. Chem. B*, 2001, **105**, 8938–8943.

24 R. Ciganda, N. Li, C. Deraedt, S. Gatard, P. Zhao, L. Salmon, R. Hernandez, J. Ruiz and D. Astruc, *Chem. Commun.*, 2014, **50**, 10126–10129.

25 P. Herves, M. Perez-Lorenzo, L. M. Liz-Marzan, J. Dzubiella, Y. Lu and M. Ballauff, *Chem. Soc. Rev.*, 2012, **41**, 5577–5587.

26 T. Aditya, A. Pal and T. Pal, *Chem. Commun.*, 2015, **51**, 9410–9431.

27 S. Carregal-Romero, J. Peérez-Juste, P. Herveés, L. M. Liz-Marzaán and P. Mulvaney, *Langmuir*, 2009, **26**, 1271–1277.

28 I. K. Konstantinou and T. A. Albanis, *Appl. Catal., B*, 2004, **49**, 1–14.

29 S. Wunder, F. Polzer, Y. Lu, Y. Mei and M. Ballauff, *J. Phys. Chem. C*, 2010, **114**, 8814–8820.

30 N. G. Bastus, J. Comenge and V. Puntes, *Langmuir*, 2011, **27**, 11098–11105.

31 J. Piella, N. G. Bastús and V. Puntes, *Chem. Mater.*, 2016, **28**, 1066–1075.

32 http://gaen.cat/research/295.

33 M. Li and G. Chen, *Nanoscale*, 2013, **5**, 11919–11927.

34 M. Chatenet, F. Micoud, I. Roche and E. Chainet, *Electrochim. Acta*, 2006, **51**, 5459–5467.

35 N. Pradhan, A. Pal and T. Pal, *Langmuir*, 2001, **17**, 1800–1802.

36 N. G. Bastús, F. Merkoçi, J. Piella and V. Puntes, *Chem. Mater.*, 2014, **26**, 2836–2846.

37 A. Gangula, R. Podila, R. M, L. Karanam, C. Janardhana and A. M. Rao, *Langmuir*, 2011, **27**, 15268–15274.

38 Y. Mei, Y. Lu, F. Polzer, M. Ballauff and M. Drechsler, *Chem. Mater.*, 2007, **19**, 1062–1069.

39 S. Wunder, Y. Lu, M. Albrecht and M. Ballauff, *ACS Catal.*, 2011, **1**, 908–916.

40 M. Dasog, W. Hou and R. W. J. Scott, *Chem. Commun.*, 2011, **47**, 8569–8571.

41 S. Panigrahi, S. Basu, S. Praharaj, S. Pande, S. Jana, A. Pal, S. K. Ghosh and T. Pal, *J. Phys. Chem. C*, 2007, **111**, 4596–4605.

42 Y. Mei, G. Sharma, Y. Lu, M. Ballauff, M. Drechsler, T. Irrgang and R. Kempe, *Langmuir*, 2005, **21**, 12229–12234.

43 C. Lin, K. Tao, D. Hua, Z. Ma and S. Zhou, *Molecules*, 2013, **18**, 12609.

44 Y. Li, E. Boone and M. A. El-Sayed, *Langmuir*, 2002, **18**, 4921–4925.

- 184 -

45 L. Yan, Y. Liu, K. Zha, H. Li, L. Shi and D. Zhang, *ACS Appl. Mater. Interfaces*, 2017, **9**, 2581–2593.

46 M. M. Kappes, *Chem. Rev.*, 1988, **88**, 369–389.

47 K. Rademann, B. Kaiser, U. Even and F. Hensel, *Phys. Rev. Lett.*, 1987, **59**, 2319–2321.

48 B. L. Smith and J. E. Hutchison, *J. Phys. Chem. C*, 2013, **117**, 25127–25137.

49 M. Varon, I. Ojea-Jimenez, J. Arbiol, L. Balcells, B. Martinez and V. F. Puntes, *Nanoscale*, 2013, **5**, 2429–2436.

50 A. Yazdi, F. Mercoçi, N. Bastús, I. Imaz, V. Puntes and D. Maspoch, *Catal. Sci. Technol.*, 2016, **6**, 8388–8391.

51 E. Casals, T. Pfaller, A. Duschl, G. J. Oostingh and V. Puntes, *ACS Nano*, 2010, **4**, 3623–3632.

52 T. Yu, J. Zeng, B. Lim and Y. Xia, *Adv. Mater.*, 2011, **22**, 5188–5192.

53 J. Zeng, Q. Zhang, J. Chen and Y. Xia, *Nano Lett.*, 2010, **10**, 30–35.

54 N. G. Bastus, J. Piella and V. Puntes, *Langmuir*, 2016, **32**, 290–300.

55 S. M. Ansar and C. L. Kitchens, *ACS Catal.*, 2016, **6**, 5553–5560.

56 A. Quintanilla, V. C. L. Butselaar-Orthlieb, C. Kwakernaak, W. G. Sloof, M. T. Kreutzer and F. Kapteijn, *J. Catal.*, 2010, **271**, 104–114.

57 N. R. Jana, L. Gearheart and C. J. Murphy, *Langmuir*, 2001, **17**, 6782–6786.

58 N. R. Jana, L. Gearheart and C. J. Murphy, *J. Phys. Chem. B*, 2001, **105**, 4065–4067.

59 J. Pérez-Juste, I. Pastoriza-Santos, L. M. Liz-Marzán and P. Mulvaney, *Coord. Chem. Rev.*, 2005, **249**, 1870–1901.

60 Z. Niu and Y. Li, *Chem. Mater.*, 2013, **26**, 72–83.

61 J. Arbiol, A. Cirera, F. Peiró, A. Cornet, J. R. Morante, J. J. Delgado and J. J. Calvino, *Appl. Phys. Lett.*, 2002, **80**, 329–331.

62 S. Bernal, J. Calvino, M. Cauqui, J. P. Omil, J. Pintado and J. Rodrıguez-Izquierdo, *Appl. Catal., B*, 1998, **16**, 127–138.

This journal is © The Royal Society of Chemistry 2017

J. Mater. Chem. A, 2017, **5**, 11917–11929 | **11929**

Electronic Supplementary Information

Probing the Surface Reactivity of Nanocrystals by the Catalytic Degradation of Organic Dyes: The Effect of Size, Surface Chemistry and Composition.

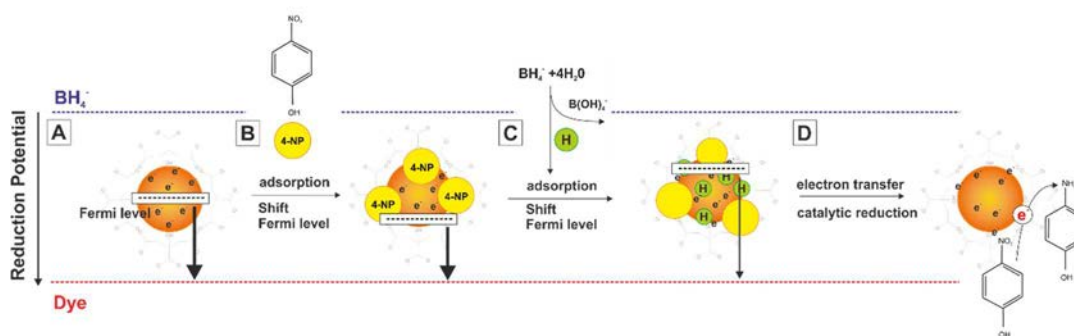Jordi Piella, Florind Merkoçi, Aziz Genç, Jordi Arbiol, Neus G. Bastús and Victor Puntes

Figure S1. Electro-chemical mechanism of catalytic reduction of dyes by metal NCs in the presence of BH_4^- and changes of the Fermi level of metal NCs during the process.

The Fermi potential of the metal NCs can be shifted to positive or to negative potentials by the adsorption of electrophile (dyes) or nucleophile species (BH_4^- ions) respectively. **Figure S1B-C** schematically illustrates the changes of the Fermi level of metal NCs during the catalytic process. Thus, after the adsorption of dyes molecules, the Fermi potential of the metal NCs shift to relatively high values (Fig. S1-B). However, after the addition and further adsorption of BH_4^- ions the Fermi level of the metal NCs decreases (Fig. S1-C) promoting the transfer of electrons from the nucleophile to the dye via the metal NC, driving its reduction to the corresponding reduced forms (Fig. S1-D).

The particular mechanism of the catalytic reduction of the various dyes used in this work can be explained as follows.

Degradation of 4-NP to aminophenol. The catalytic reduction of 4-NP into 4-aminophenol (4-AP) by $NaBH_4$ is an electrochemical process in which the metal NCs have the main role of acting as electron relay systems, transferring the electrons from the donor (BH_4^-) to the acceptor (4-NP). In detail, in the reaction aqueous solution, BH_4^- ions are adsorbed on and react with the surface of metal NCs, thereby creating active metal hydrides at their surface. At the same time, 4-NP also adsorbs on the surface of metal NCs. These two steps are reversible and are fitted into a Langmuir isotherm model. The diffusion of both reactants to the surface of metal NCs and the adsorption/desorption equilibriums of these reactants on the surface is also fast. Therefore, the reduction of 4-NP to corresponding 4-AP occurs in view of the reaction of adsorbed 4-NP with the metal hydrides bound by metal NC surface. A first mechanistic insight was provided by Fritz Haber in the late 1890s using electrochemical methods.[1] From Haber's mechanistic scheme, there are two main paths to get the final products: the direct path and the condensation path. The direct route is a stepwise hydrogenation

1

intermediate product was azobenzene.[2] When formed, 4-AP detaches from the metal NCs surface, the next cycle of new catalytic reduction can be triggered again.

Degradation of MB to Leuco MB and RhB to Leuco RhB. The catalytic reduction of RhB and MB can be also explained by an electrochemical mechanism, where the metal NCs serve as an electron relay system for the oxidant and reductant species. First BH_4^- ions and MB or RhB molecules are adsorbed together onto the surface of the metal NCs. Then electron transfer takes place between the dyes and BH_4^- through particle surface. After receiving the electrons, the dye molecules are reduced to Leuco MB or Leuco RhB.[3]
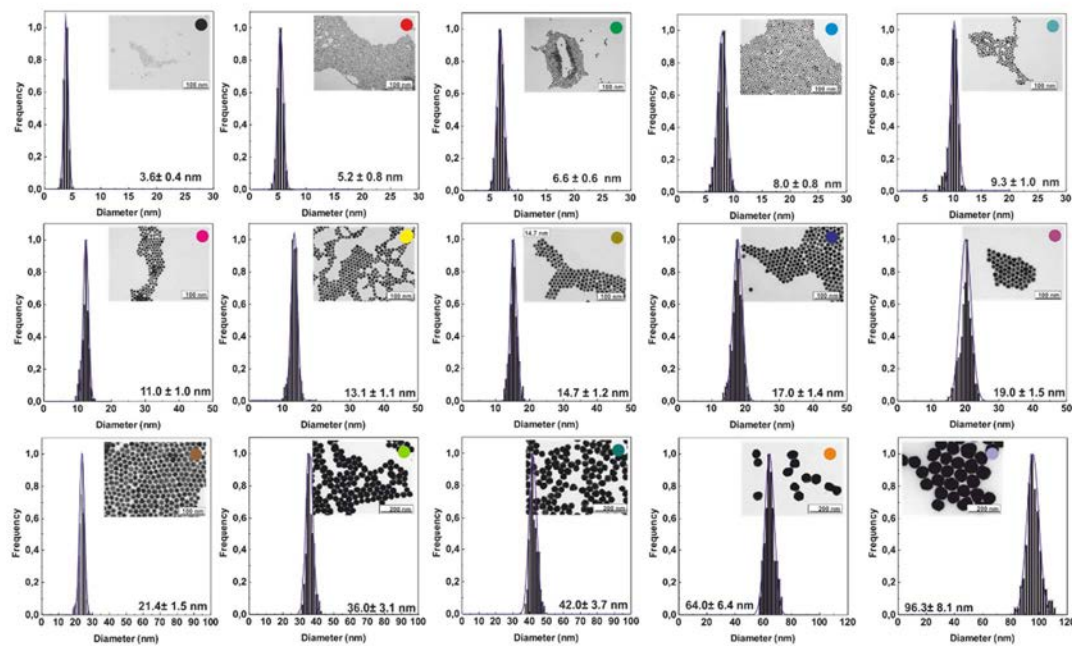

Figure S2. TEM images analysis of Au NPs shown in Figure 1. Au seeds diameter increase from ~3.6 to ~110 nm after different growth steps. At least 1000 NPs were counted for each size.

2
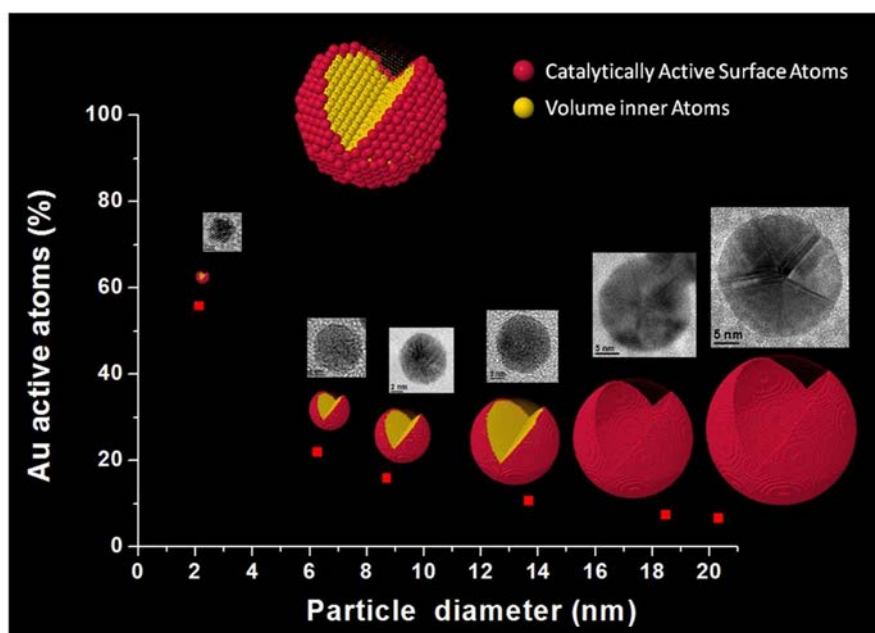
Figure S3. Comparison of the ratio of catalytically active Au atoms for 2, 5, 10, 15, 20 and 30 nm NCs. The ratio of Au active atoms if found to be 55.83%, 21.97%, 15.95%, 10.63%, 7.48% and 6.67%, respectively. Corresponding HRTEM experimental images for all the simulated models are also presented.

Figure S4. Surface coating of Au NPs. UV-Vis spectroscopy of as-synthesized (A), hexanoic acid (B), aminohexanoic acid (C), NH_2-PEG (1000) (D), mercaptoundecanoic acid (E), polyvinylpyrrolidone (F), and bovine serum albumin (BSA) (H) and SH-PEG (3500) (H).

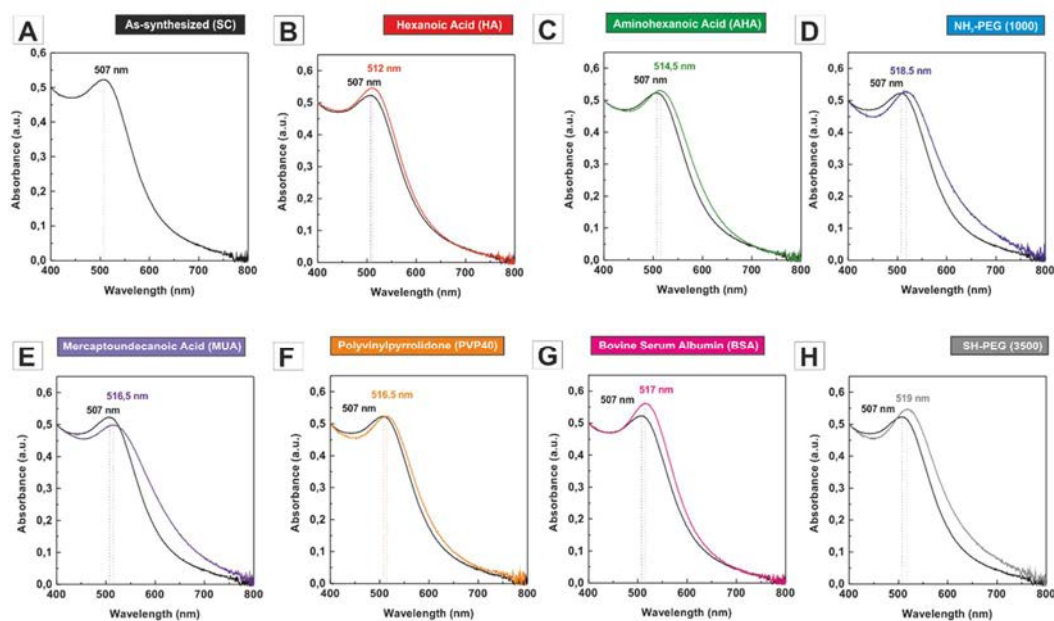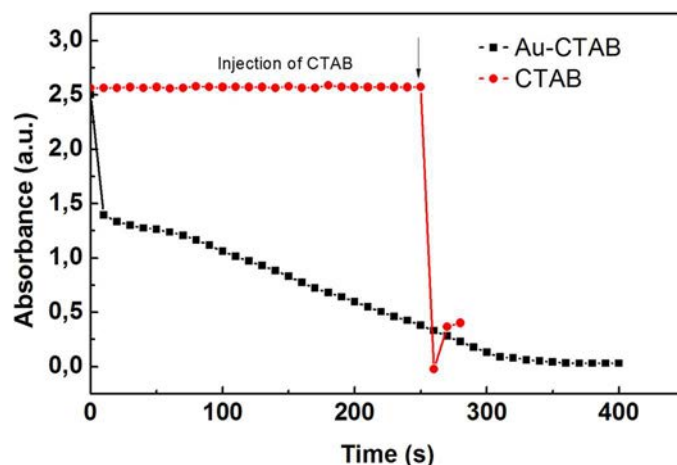**Figure S5.** CTAB degradation of 4-Nitrophenol. The catalytic performance of CTAB was evaluated by added an aqueous solution of CTAB molecules (0.1 mL, 10 mM) into a solution of 4-NP and NaBH4, obtaining that CTAB molecules are able to rapidly degrade 4-NP by themselves. Similarly, the drop observed at short reaction times for CTAB-coated Au NCs can be attributed to the free of bound CTAB molecules.

Figure S6. Optical interference between 4-Nitrophenol, Rhodamine B and Methylene blue and Au NCs of 10 nm (A), 50 nm (B), Ag NCs (C) and Pt NCs (D). In the case of Au and Ag spectra were normalized to the maximum absorption of the dyes.

4

Au NP Modelling and Simulation Studies

Figure S7. HRTEM image of a 2.6 nm decahedron shaped nanoparticle and corresponding power spectrum (FFT) image of the nanoparticle.

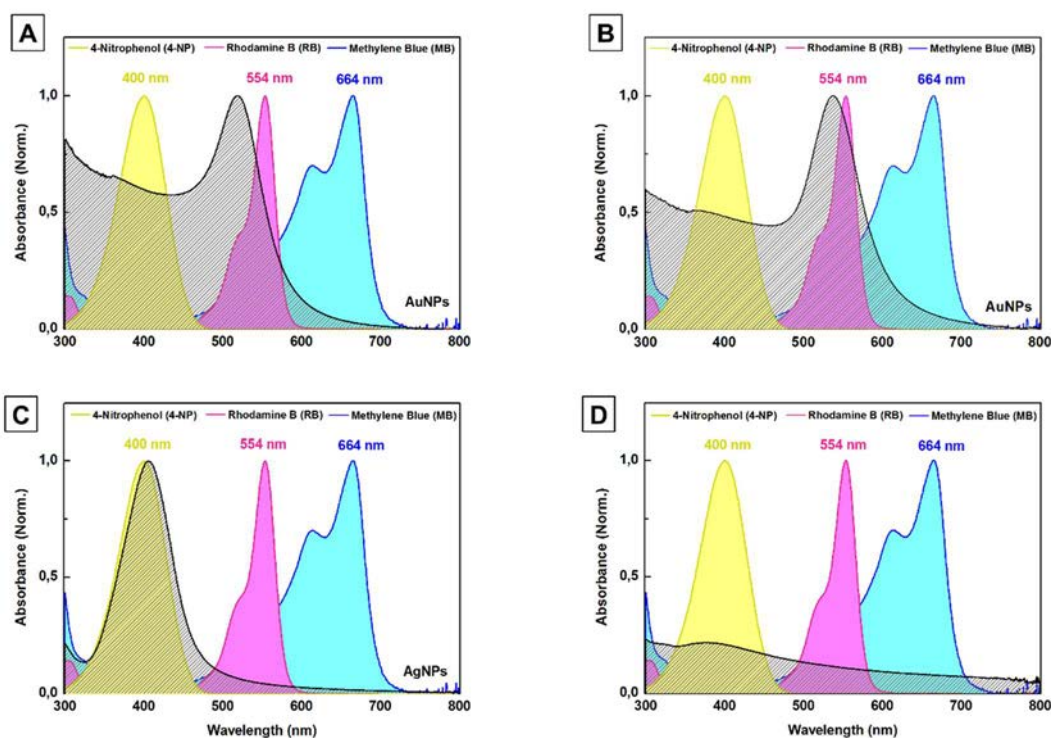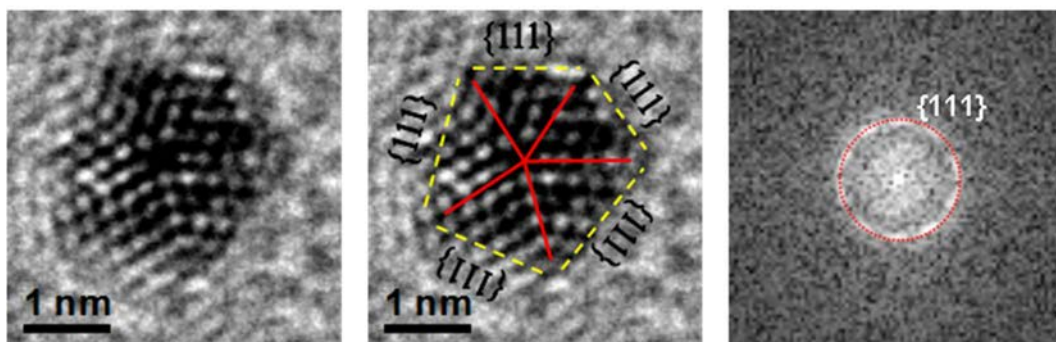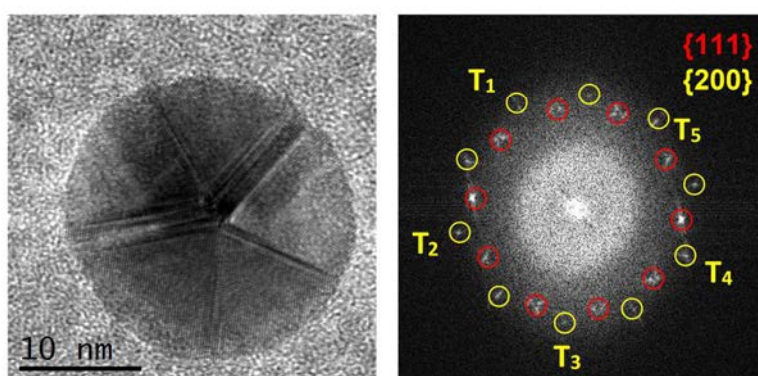**Figure S8.** HRTEM image and corresponding power spectrum (FFT) of a 24.4 nm nanoparticle. Diffraction spots corresponding to {111} and {200} family of planes form a perfect symmetry, which is typical for this kind of decahedrons.[4-6]

On the basis of above presented HRTEM observations, we propose a model of spheroidal decahedron shape particles, which is present in all samples. We must say here, that for bigger nanoparticles the {111} external facets tend to be sharper and the nanoparticles have a morphology closer to the ideal decahedron, losing the spheroidal shape. Regular decahedron shape consists of the merging of 5 {111} faceted tetrahedral.[5, 7, 8] Yet, the theoretical angle between to (111) planes is 70.53° and combination of 5 tetrahedrons to form a decahedron results in a 7.35° gap[7], which must be filled by some form of internal strain such as dislocations and other structural defects.[6, 8] Johnson et al.[8] reports that elastic anisotropy, results in an internal lattice rotation of 4.3°, combined with about 0.6° shear-strain for each tetrahedron accommodate this 7.35° gap in their experimental decahedron shaped Au nanoparticle.

Here, we assume a homogeneous distribution of these strains to form a regular decahedron out of 5 {111} faceted tetrahedra with a rotation angle of 72°.

5
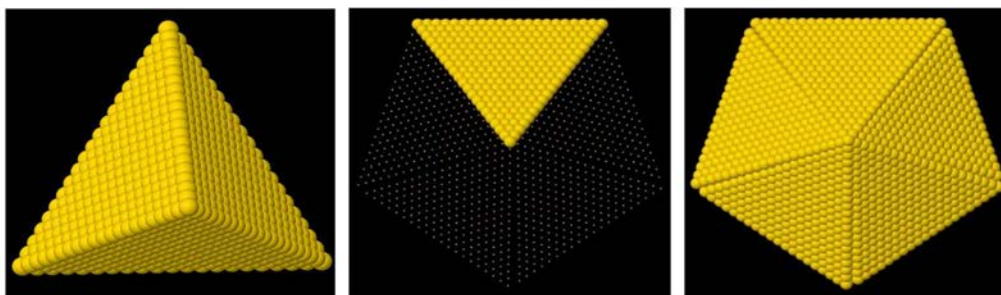
Figure S9. Modeling a regular Au decahedron with a size of 10 nm: (i) creation of a {111} faceted tetrahedron, (ii)-(iii) combination of 5 individual tetrahedra with sequential rotations of 72°.

In Figure S9 we have modeled a regular Au decahedron with a size of 10 nm. Figure S6 shows the stages of this modeling process. However, as can be seen in the above presented HRTEM images, such a model cannot be representative for the present samples. Most of the reported Au decahedral shapes having sizes smaller than 30 nm reveals similar spheroidal behavior[5-7], however, modeling and simulation studies are conducted as if they were perfect decahedrons.[7, 9]

Due to above presented discrepancy between experimentally observed nanoparticles and suggested regular decahedral models, we propose a spheroidal decahedron model, which contains 5 {111} facets but has a spheroidal like structure.
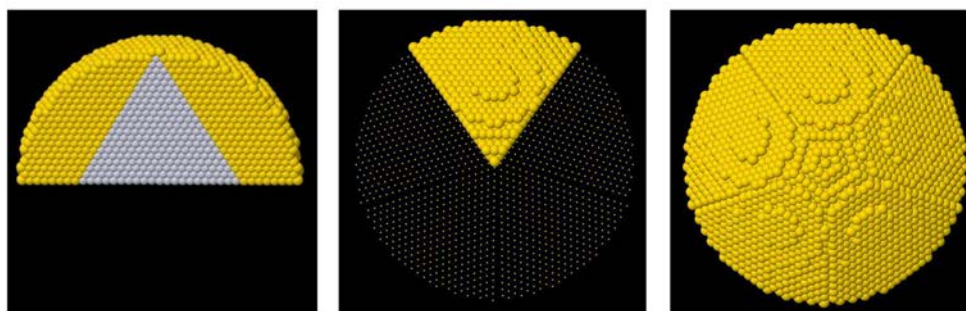
Figure S10. Modeling a spheroidal Au decahedron with a diameter of 10 nm: (i) creation of a {111} faceted spheroidal subunit, (ii)-(iii) combination of 5 individual subunits with sequential rotations of 72°.

Figure S10 shows the steps of the spheroidal decahedron modeling process. First, we have created a {111} faceted segment over a tetrahedron. Then, we merge 5 of them with a sequential rotations of 72° forming a 5 twinned spheroidal decahedral structure.
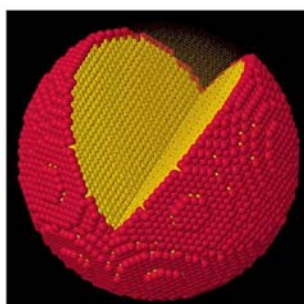
Figure S11. A spheroidal Au decahedron with a diameter of 10 nm, showing the surface active atoms in red.

6

We extended the spheroidal decahedral model and added a shell in order to calculate the ratio of catalytically active surface atoms over volume atoms. Figure S11 shows the catalytically active surface atoms in red and volume atoms in yellow. For the case of 10 nm spheroidal decahedron, total number of atoms is found to be 30245, where 4272 of the total atoms are in the surface. Percent ratio of catalytically active surface Au atoms is 14.12% for this model.

In addition to 10 nm model, we have modeled particles with different sizes such as 1 nm, 2 nm, 4 nm, 6 nm, 8 nm, 12 nm and 15 nm in order to compare the variation of the ratio of surface active Au atoms with size (**Fig. S12**).
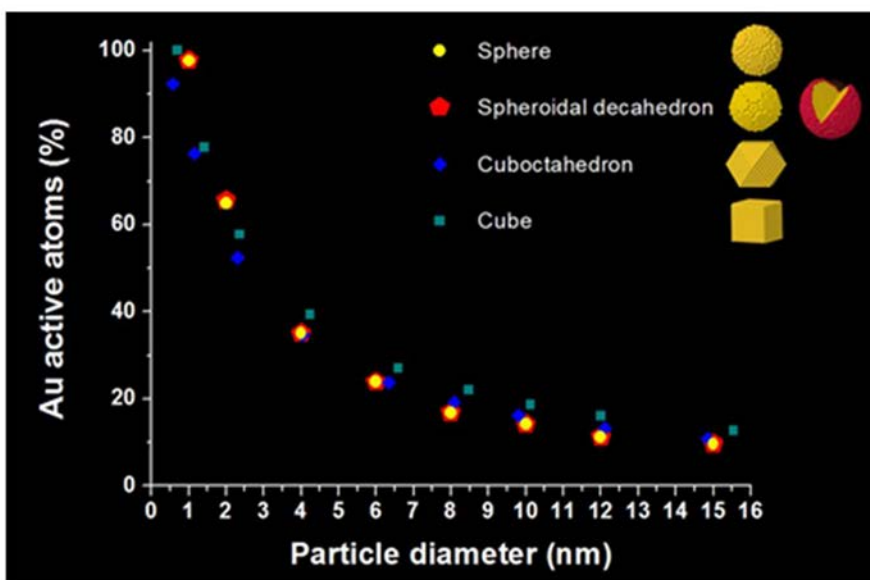
Figure S12. Comparison of the ratio of catalytically active Au atoms with increasing particle diameters for different Au nanostructures such as sphere, spheroidal decahedron, cuboctahedron and cube. The results plotted here have been summarized in an animated video movie that can be reached by following the link in ref [10].

1. F. Haber, *Z. Elektrochem. Angew. Phys. Chem*, 1898, 506-514.
2. Z. Li, X. Xu, X. Jiang, Y. Li, Z. Yu and X. Zhang, *RSC Adv.*, 2015, **5**, 30062-30066.
3. B. R. Ganapuram, M. Alle, R. Dadigala, A. Dasari, V. Maragoni and V. Guttena, *International Nano Letters*, 2015, **5**, 215-222.
4. H. Hofmeister, *Mater. Sci. Forum*, 1999, **312**, 325-332.
5. L.-F. Zhang, L. Wang, S.-L. Zhong, Y.-X. Huang and A.-W. Xu, *Dalton Transactions*, 2012, **41**, 4948-4954.
6. J. L. Elechiguerra, J. Reyes-Gasga and M. J. Yacaman, *J. Mater. Chem.*, 2006, **16**, 3906-3919.
7. C. Y. Yang, *J. Cryst. Growth*, 1979, **47**, 274-282.
8. C. L. Johnson, E. Snoeck, M. Ezcurdia, B. Rodriguez-Gonzalez, I. Pastoriza-Santos, L. M. Liz-Marzan and M. J. Hytch, *Nat Mater*, 2008, **7**, 120-124.
9. Z. W. Wang and R. E. Palmer, *Phys. Rev. Lett.*, 2012, **108**, 245502.
10. http://gaen.cat/research/295

7

Chapter 6:

Size-dependent protein-nanoparticle interactions

One of the most significant alterations of nanoparticles (NPs) in biological media is the formation of a protein corona (PC) as a result of the adsorption of proteins onto the NP's inorganic surface. This process deserves special attention because the proteins forming the 'corona' provide the NP's biological identity and determine the interactions between NPs and the host in living systems. In other words, the protein coating 'expressed' at the NP surface is what is 'read' by cells. In this chapter, the effect of NP size on the kinetics of PC formation on citrate-stabilized Au NPs of different diameters after their incubation in cell culture media is presented. The results were collected in the article entitled *Size-Dependent Protein-Nanoparticle Interactions in Citrate-Stabilizes Gold Nanoparticles: The Emergence of the Protein Corona.*

6.1. Interactions of nanoparticles with biological systems

A deeper understanding of the physical chemistry of inorganic matter when its morphology approaches that of macromolecular biological entities is of paramount importance in order to improve the control and development of these materials. In addition, the safe application of different NPs and NP conjugates in biomedicine (e.g., as tools for therapy and/or diagnosis), their molecular characteristics and their behaviour in biological media are basic parameters to take into account. Surprisingly, despite the rapid development of new methodologies of synthesis and conjugation of NPs, a thorough knowledge of their *in vitro* and *in vivo* behaviour in complex biological systems has not yet been achieved. Blood, lymph, mucus and other biological environments contain a large amount and variety of different molecules, and NPs dispersed in these fluids are sensitive to such environments, being modified by and modifying them [1].

In order to understand the biological effects of NPs, it is worth analysing how NPs and biological systems relate to each other. On one hand, a living cell is connected to the external environment predominantly through proteins. Proteins are macromolecules that have an amphipathic character, possessing polar and nonpolar residues that confers them a 3D structure. They have also a large number of hydrogen bonds and different functional groups (such as thiols, carboxylic acids and amines). These two characteristics allows proteins to interact with almost all the 'foreign' matter they come into contact with. On the other hand, inorganic NPs possess very high surface energy and (intended during functionalization or unintended during NP exposure to the environment) they tend to associate with other particles and molecules that finally become part of the nano-object and determine their interactions with the surrounding environment [2, 3]. Thus, NPs inside living bodies are expected to be immediately coated by proteins and other serum components (unless they have been previously protected with a surfactant). Recently grouped under the name of protein corona (PC), these processes of protein coating are one of the most significant and studied modifications of NPs in physiological media [2-4].

6.2. The nanoparticle protein corona

Already in 2004, it was reported that the presence of proteins in physiological media affects the entry and intracellular localization of NPs in cells, and thus modulates their potential biological effects and toxicity [5]. Later, the formation of a PC on top of the NP surface was observed to control biodistribution, uptake and biological response, transforming them from innocuous to toxic, or vice versa. The increasing number of recent publications covering different aspects of the NP corona reflects the importance of this topic [6, 7]. This is largely because the proteins forming the 'corona' remain associated with the NPs under normal conditions of *in vivo* and *in vitro* exposure, thereby conferring the NPs their biological identity and determining the interactions between NPs and the host. In other words, this corona of proteins 'expressed' at the surface of the particle is what is 'read' by the cells [8].

The formation of a PC on the surface of NPs may improve their stability and biocompatibility, as in the case of the albuminization of potentially toxic drugs [9]. However, it can also entail detrimental effects, e.g. through the depletion of specific proteins or enabling a more intense or more specific interaction with living cells. The depletion of proteins is uncommon as it is difficult for NPs inside blood or organs to reach high enough concentrations for protein depletion. However, the triggering of a more intense or specific response can occur due to avidity effects arising from the close spatial repetition of the same protein if accumulated on a particle surface, or the attachment of specific components of the immune system that can tags the vehicles for phagocytosis [10]. Finally, one should take into consideration that packing of proteins on the NP surface may increase NP robustness against their natural metabolic degradation [11], allowing a deeper penetration into biological systems and possible accumulation in cells or tissues. However, after extended periods of time, the metabolic degradation of the corona is likely and the leaching of ions from the particles may induce toxic effects. Currently, some of these hypotheses are an active field of research.

6.2.1. Time evolution of the nanoparticle protein corona

The formation of the PC is a dynamic process governed by the Vroman effect [12]. In 1962, Leo Vroman reported how the exposure of hydrophobic inorganic powders to

blood plasma resulted in the removal of coagulation factors, and the inorganic surface became more hydrophilic. This result manifested a competitive adsorption hierarchy: the proteins with high mobility arrive first and are replaced by others with lower mobility and higher affinity for the surface, mainly factor V and fibrinogen, in a process that takes up to a few hours. As stated by Slack and Horbett [13], this process is recognized as the general phenomenon governing the competitive adsorption of a complex mixture of proteins (as with serum) to surfaces. Thus, after exposure to cell culture media, NP coating evolves in a time-dependent manner, from a soft PC, a transient agglomeration of proteins on the NP surface, to a hard PC, a dense and permanently attached protein coating [14] (**Figure 6.1**).

Initially, the strongest argument for the irreversibility was that proteins are provided with multiple, although weak, anchor points. However, detailed studies have also suggested other mechanisms. The work of Alaeddine and Nygren demonstrated that, contrary to what might be suspected, proteins do not distribute on surfaces randomly [15]. Instead, once the first proteins are attached, an initial cluster of proteins forms around these, thereby stabilizing them, and this mechanism is repeated until the entire surface is covered. This, and other attempts to explain the irreversibility of the process of protein adsorption to inorganic surfaces, suggests that the initial attachment of a protein to a surface is followed by a series of movements and/or rearrangements to make the interaction more stable. Once clustered, the movement of one implies the movement of many. Therefore, not only protein–surface affinity, but also mechanisms such as molecular relaxation time or spreading (related to the interaction time), and crowding effects have been identified as factors determining complete adsorption [16].

Accordingly, these entire interfacial processes take place when NPs are dispersed in biological media, such as when injected into veins as drug delivery vehicles or incubated with cells in *in vitro* studies. While these processes are analogous to the interaction of serum components with medical implants, there are some differences. Unlike implants, NPs are not a fixed substrate and move quickly in solution; they have similar dimensions to proteins and possess high radii of curvature that change the accessibility to their inorganic surfaces. All these effects may modify the kinetics of an encounter between the NP surface and proteins, the mechanisms of attachment and the biological outcome.
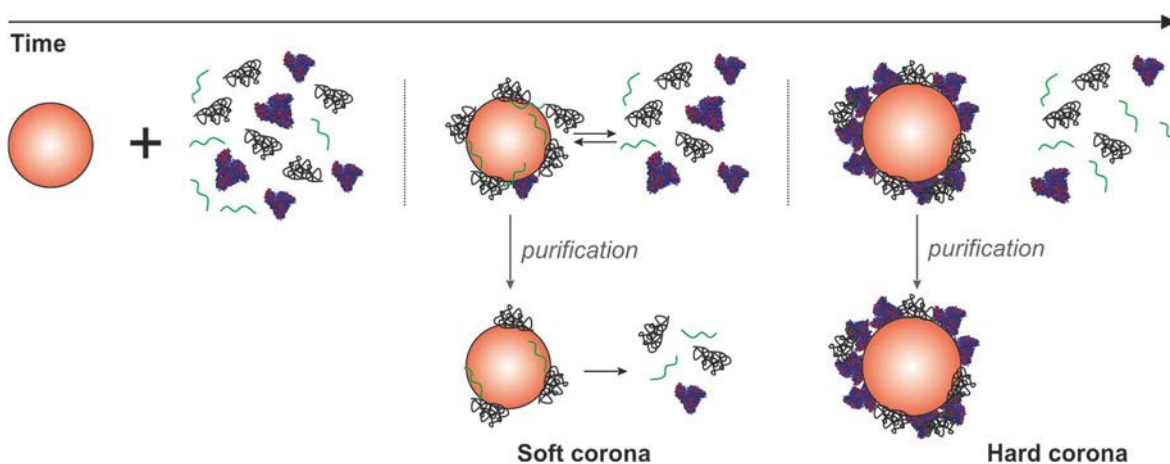
Figure 6.1. Kinetics of the formation of the nanoparticle protein corona. The process of protein adsorption in biological media evolves from a soft corona composed by weakly bound proteins in equilibrium with the proteins in the medium to an irreversible corona composed by strongly attached proteins that are no longer in equilibrium with their in-solution counterparts.

6.2.2. Factors affecting the protein corona formation

PC formation is time, serum and NP (size and surface) dependent [3, 17]. Hydrophobicity and surface charge have historically been the factors taken into account to explain protein adsorption onto inorganic surfaces. This is illustrated by the work of Prime and Whitesides using self-assembled monolayers (SAMs) on Au films [18]. These SAMs consisted of alkyl chains with different terminal groups, where the more hydrophobic the surface the greater the degree of protein adsorption. In a later study [19], the binding of bovine serum albumin (BSA) to Au surfaces modified by alkyl thiol SAMs was found to decrease in the following order of terminal groups: $C_6H_5OH > CH_3 > COO^- > NH_3^+ > OH^- >$ oligoethylene oxide. Together with hydrophilicity, charge has also been shown to play a key role in the interaction with proteins due to electrostatic interactions. It was observed by Norde and Lyklema that there was a higher adsorption of positively charged proteins onto negatively charged polystyrene surfaces and vice versa [20]. Currently, different examples of the role of NP hydrophobicity and surface charge on PC formation can be found in the literature [21-24].

Affinities of different proteins for the same surface are different [22]. Therefore, the formation and evolution of the PC on NPs is affected by the composition of biological fluids. The PC resulting from incubation of NPs in blood plasma, which contains fibrinogen, is substantially different to the PC found after NP incubation in blood serum, which is free from that protein. As an example, Deng *et al.* [25] found fibrinogen as the

major blood plasma protein bound to Au NPs while Casals *et al.* [14], using blood serum, found albumin as the main component of the PC also formed around Au NPs. Not only can the protein content influence the formation of the PC but also the physiological buffer used to prepare the cCCM with the same type of serum. Maiorano *et al.* studied protein adsorption onto Au NPs of different sizes upon incubation with DMEM-high glucose and Roswell Park Memorial Institute-1640 medium supplemented with fetal bovine serum [26]. Results revealed that DMEM exhibits a large time-dependent PC formation while Roswell Park Memorial Institute medium represents dissimilar kinetics with a reduced PC composition.

As regards to the conformation proteins attached to the NPs, methods of immunoassay in the solid phase have been quite successful in identifying their tertiary structure [27-29]. Additionally, as pointed out by Norde [30] and later confirmed in by us [14, 31], the thickness of the adsorbed protein layer is usually close to the native protein size. This indicates that some parts of the proteins adsorbed on the NPs maintain their active structure, since their denaturation and aggregation after losing their tertiary structure is well known. However, there is no consensus regarding the maintenance of the protein tertiary structure after adsorption. Partial unfolding of proteins adsorbed on a surface has been described in several studies [32, 33]. For instance, it has been reported how adsorption of proteins onto SiO_2 NPs is followed by irreversible protein conformational changes, ultimately leading to a molten-globule-like state [34-36]. In another study using Au NPs of approximately 90 nm in diameter, Zhang *et al.* observed that proteins at the NP surfaces were partially unfolded resulting in stable protein–NP assemblies [33]. Remarkably, in all of these experiments, neither protein nor NP aggregation was observed, indicating the stability of the NP–protein complexes. The model closest to reality seems to be a mixture of protein conformational states on a surface; the proteins arriving first may lose their original conformation and be denatured, while the proteins arriving last have no room for denaturation, thus maintaining their native structure [37].

The majority of previous studies regarding protein adsorption have been performed on larger and polymeric NPs in the order of 100s of nanometers, whereas fewer have addressed NPs in the small size range. PC formation studies in the case of inorganic NPs smaller than a few tens of nanometers have been carried out on metallic NPs (Au [14,

38-40], Ag [38, 41] and FePt [42]), metal oxide NPs (SiO_2 [25, 43], Fe_3O_4, CoO and CeO_2 [38], TiO_2 [25, 44] and ZnO [25]), and quantum dots (CdSe [45, 46] and CdSe/ZnS [42]). These NPs have diameters similar to the proteins found in serum (**Figure 6.2**) and it has been observed that they can easily escape from opsonization and from the reticuloendothelial system [10]. In addition, a new generation of diagnostic and therapeutic devices, based on such small engineered metal and oxide NPs is proposed for *in vivo* applications [47, 48].
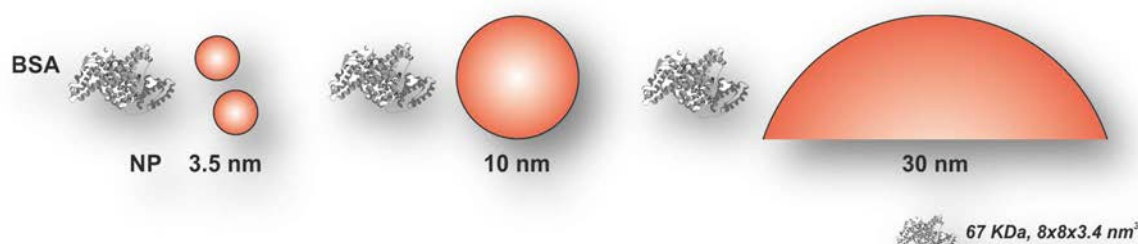
Figure 6.2. Relative size of nanoparticles and proteins. Comparison between the size of a BSA protein and the size of NPs with different diameters (3.5, 10 and 30 nm). The hydrodynamic diameter of BSA is about 6-7 nm [49].

It is assumed that the radii of curvature of NPs with different sizes will influence the competitive adsorption of proteins in complex biological fluids, such as blood plasma. In the literature, it has been described that for large particles (100s of nanometers in diameter) there is no size effect on the PC formation [43, 46]. For smaller sizes, Dobrovolskaia *et al.* [39] observed that the increase of the hydrodynamic diameter (HD) before and after NP incubation in human plasma was similar (~45 nm) for the 30-nm and the 50-nm Au NPs but with large differences in their protein binding profiles. For instance, 30-nm Au NPs bonded a greater range of proteins (almost two-fold more different proteins) than 50-nm Au NPs. In both cases, albumin, apolipoprotein, immunoglobulins, complement and fibrinogen were the most abundantly bound species. In another study, Casals *et al.* [14] noticed significant differences in the PC formation between Au NPs of 15 and 4 nm in cCCM. Au NPs of 15 nm mean diameter showed a hard PC with full coverage by serum proteins while Au NPs of 4 nm showed a partially formed PC. These data suggest that Au NPs with sizes similar, or even larger, to the most abundant serum proteins (6-7 nm) assemble an ordered hard PC with time, while Au NPs smaller than proteins accommodate fewer proteins at their surface. These results indicate

the complexity of the process of PC formation around NPs with sizes similar to the proteins and, probably, different outcomes must be expected for NPs with different sizes regarding the amount and organization of the adsorbed proteins.

In the present chapter, the kinetics of the nanoparticle PC formation on citrate-stabilized Au NPs of different diameters (3.5-150 nm) after their incubation in DMEM supplemented with fetal bovine serum (FBS) is presented. The aim of this study was to gain insights into how NP size affects the interactions between NPs and proteins. The study required application of the knowledge acquired previously during the thesis. For example, the synthesis of highly monodisperse metal NPs described in **Chapters 2** was used to produce the Au NPs, while their optical properties studied in **Chapter 4** were used to monitor protein adsorption. Finally, the experiments were performed following the recommendations exposed in **Appendix A**. These results can be found in the last article of this thesis entitled: *Size-Dependent Protein-Nanoparticle Interactions in Citrate-Stabilizes Gold Nanoparticles: The Emergence of the Protein Corona* (**Publication 5**).

6.3. Results: Size-dependent protein-nanoparticle interactions in citrate-stabilized gold nanoparticles

6.3.1. Exposure of gold nanoparticles to cell culture medium

Before studding the equilibrium between NPs and proteins in solution, it is important to develop an accurate protocol for the exposure of NPs to the biological media. Many of the original synthesis methods yield NPs that are not colloidally stable under conditions present in biological fluids. In particular, inorganic NPs are naturally colloidally unstable and prone to agglomeration because they attract each other by van der Waals forces (see **Chapter 1**). To stabilize them in a solvent, i.e., to keep them dispersed, requires a repulsive force. In the case of electrostatically stabilized NPs dispersed in biological media, the concentration of salts, a major constituent of most biological fluids, and the presence of highly aggregative divalent ions such as Ca^{2+} may screen the surface charge of the NPs and induce their aggregation. This phenomenon is often unnoticed since proteins in the media cover the NPs via PC formation, conferring them with steric
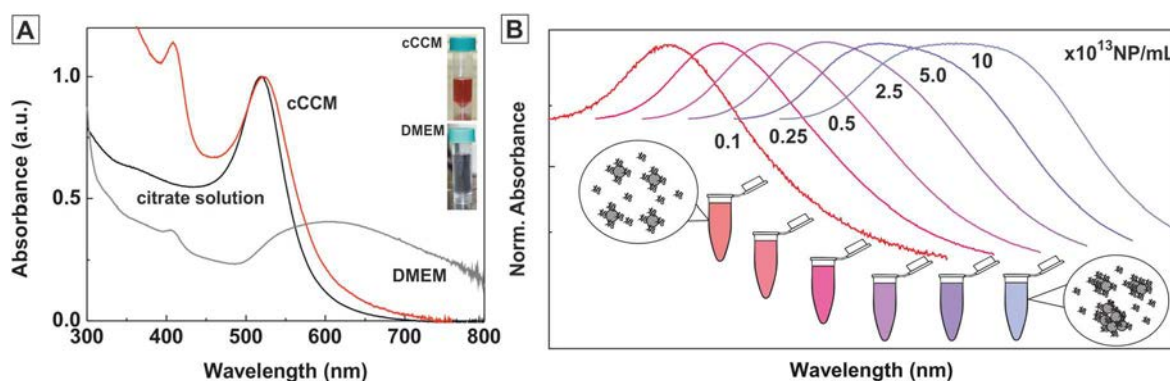
Figure 6.3. Stability of nanoparticles in cell culture media. (A) Extinction spectra of Au NPs of 10 nm dispersed in DMEM (grey line) and in DMEM supplemented with 10% FBS (red line). The high ionic strength of DMEM resulted in particle aggregations in the absence of proteins. This aggregation was traduced in a broadening and damping of the extinction peak of the particles. (B) Extinction spectra of the Au NPs dispersed in cCCM at different particle concentrations. At high concentrations, Au NPs aggregated even in the presence of proteins. In all cases, 1 mL of a solution containing different concentrations of Au NPs was added to a 9 mL medium solution.

stability. However, because high concentrations of NPs are required for *in vivo* and *in vitro* applications, the PC may be insufficient to guarantee NP stability.

To illustrate this point, the stability of citrate-stabilized Au NPs dispersed in complete cell culture media (cCCM) was evaluated at different NP concentrations (**Figure 6.3**). DMEM supplemented with 10% fetal bovine serum (FBS) was used as a reference medium. FBS is a complex fluid that contains more than 3700 different proteins with up to 12 orders of magnitude in their concentrations, with albumin being the most abundant (>50 % w/w of total proteins) and the one expected to be the fastest to reach the surface of the NPs. For the studies, different solutions containing increasing concentrations of Au NPs were mixed with cCCM at a ratio of 1:10 v/v and the peak position of the localized surface plasmon resonance (LSPR) was measured by UV-vis spectroscopy. Aggregation of Au NPs is known to broaden and shift the LSPR band to longer wavelengths and to increase scattering in the 600-800 nm range [50]. First, the stabilizing role of the proteins was confirmed since all Au NPs aggregated when they were incubated in DMEM not supplemented with FBS (**Figure 6.3A**). Conversely, in the presence of FBS, the colloidal stability of the Au NPs was dependent on their concentration (**Figure 6.3B**). At low concentrations, Au NPs remained perfectly stable when dispersed in cCCM while at high concentrations, Au NPs aggregated and these aggregates where later stabilized by the proteins of the medium, reaching a final and stable size after a few minutes. Because protein concentration in cCCM is largely above

the highest concentration of Au NPs used in the experiments, in the order of 10^{14} NP/mL, aggregation was likely due to kinetic issues: high NP concentrations promoted contact between NPs before proteins had the chance to be adsorbed onto their surface and confer them with steric stability. Conversely, at low NP concentrations, they became coated with proteins before having the chance to get in contact.

It is worth noting that the methodology followed for the exposure of the Au NPs played a relevant role in the observed results. Later observations showed that if a low volume of high concentrated Au NPs was added to a large volume of cCCM, Au NPs aggregated rapidly, even though the final mixture had a low NP concentration. On the other hand, if the Au NPs were previously diluted in water and then added to cCCm to reach the same final concentration, stability was improved. These results supports the idea that in most experiments, the limit of stability of NPs dispersed in physiological media is determined by the way NPs are exposed to the medium rather than due to the final concentration of the different components (proteins and NPs). In this regard, all experiments on PC formation were carried out far below the limit of stability for the described protocol, thus ensuring that all NPs remained stable during exposure to cCCM. Interestingly, this limit was dependent on NP size, an issue that is discussed in more detail in the related publication (**Publication 5**).

6.3.2. Characterization techniques

A combination of UV-vis spectroscopy, DLS and z-potential was chosen to monitor the formation of PC on the Au NPs. DLS is useful for determining the hydrodynamic diameter of colloidal particles and conjugates, i.e. the diameter of the sphere with the same Brownian motion as the analysed particle. However, despite the simplicity of DLS measurements, a broad range of results is often obtained with a lack of reproducibility, especially when the refractive index of the material approaches that of water, as it is for very small particles. Moreover, the interference caused by free proteins in solutions can lead to multiple peaks if the sample is not purified, in particular for particles with similar sizes (DLS signal scales with d^6, thus free proteins of 6-7 nm does not interfere with the signal of particles larger than 30 nm NPs). For this reason, DLS measurements were performed in combination with other techniques. For instance, in the case of Au NPs, the evolution of the NP surface charge towards the value of the serum measured by
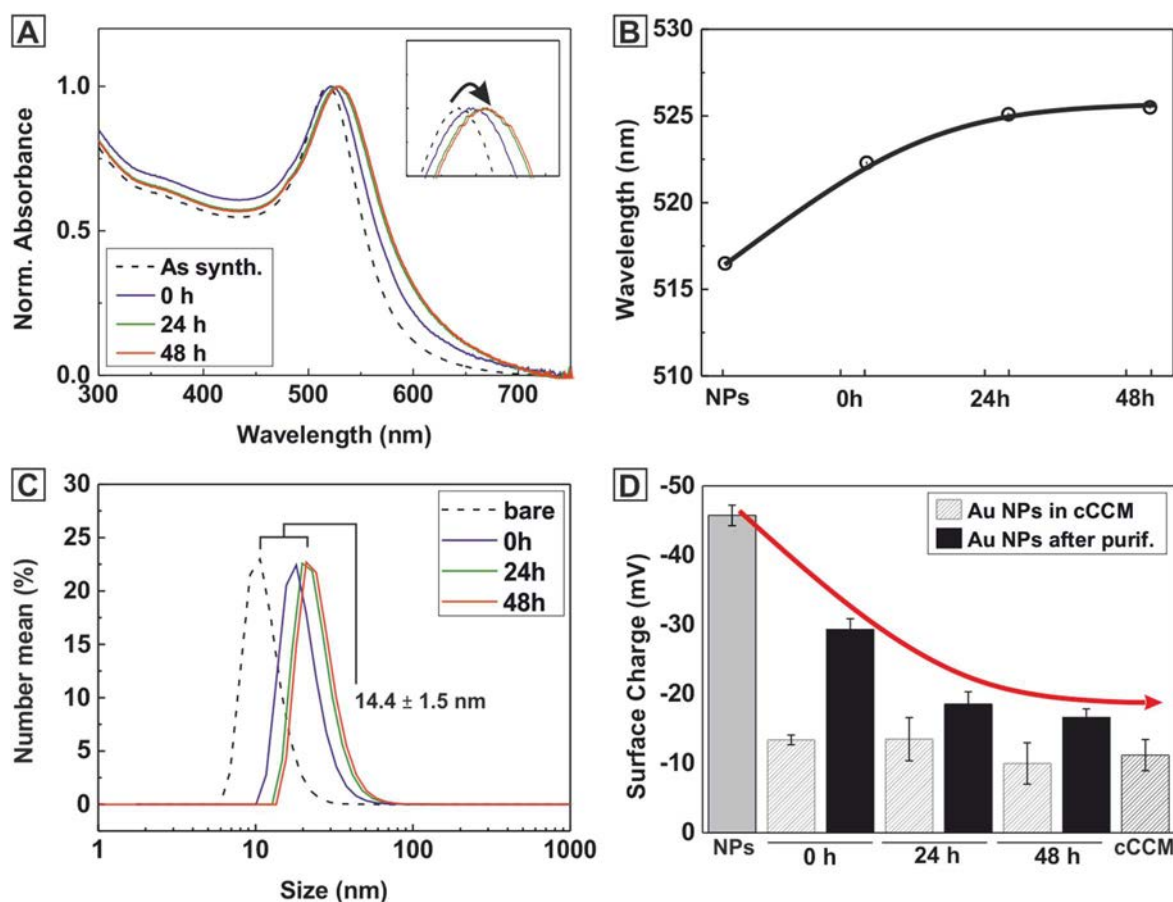
Figure 6.4. Characterization of the nanoparticle protein corona. (A) Time-evolution extinction spectra of 10 nm Au NPs after their incubation in DMEM with 10% FBS. (B) Position of the extinction peak. (C) Hydrodynamic diameter measured by DLS and expressed in number mean. (D) Time-evolution of the surface charge measured by z-potential. Unless indicated, Au NPs in cell medium were purified by centrifugation and dispersed in a 2 mM citrate solution for characterization.

z-potential, the red-shift of the surface LSPR band as a consequence of a shift in the refractive index at the surface of the NPs due to the presence of proteins and the increase of the hydrodynamic diameter measured by DLS were used to track the evolution of the PC formation (**Figure 6.4**). In general, UV-vis spectroscopy is less susceptible to interferences from small aggregates and free proteins in solution than DLS, while z-potential gives more accurate information regarding the density of the protein packaging.

The purification of NPs from the media is a prerequisite in most studies related to PC formation, particularly for DLS and z-potential measurements. Purification consists of separating the NPs with proteins strongly attached to their surface from the excess of free or weakly bound proteins. In our case, this was done by means of centrifugation, e.g. 20 min. at 16.000 *g* for Au NPs of 10 nm (a speed at which NPs precipitate but proteins stay in solution due to their very low density) followed by resuspension of the

Au NPs in protein-free media, that is, either in their original solvent or in pure water. After adjusting the centrifugation speed for each NP size, no aggregation of the Au NPs was observed during precipitation due to the protective effect of the PC enabling a good redispersion of the NPs. Indeed, centrifugation is a commonly used purification technique to separate NP from free proteins [51].

6.3.3. Size-dependent evolution of the nanoparticle protein corona

Figures 6.4 summarizes the results of PC formation onto the surface of 10 nm Au NPs. First, a red shift of the LSPR peak of the NPs was observed after incubation in cCCM. It is known that proteins adsorbed at the surface of the NPs may changes the dielectric constant around NPs, which shifts the position of the LSRP peaks (see **Chapter 5**). For example, the wavelength of the maximum LSPR signal was initially 516.5 nm in the as-synthesized 10 nm Au NPs and moved to 522.3 nm at short incubation times and to 525.5 nm at longer cCCM incubation times (**Figure 6.4B**). Preservation of the initial shape and intensity of the LSPR peak further revealed that this shift in the peak position was not due to aggregation. A similar trend was observed when the diameter of the particles was analysed with DLS, as it increased from 10.9 nm in the as-synthesized NPs to 21.8 nm at short incubation times and 25.3 nm at longer incubation times (**Figure 6.4C**). Consistent with the red-shift and the increase of the hydrodynamic diameter, an increase in surface charge, from -45.8 to -16.7 mV (average value of proteins) was also observed. Since this charge itself is not high enough to prevent NPs from aggregation (it should be at least ±30 mV), it further verified that the stability of the NPs in physiological conditions was mediated by the steric repulsions between the absorbed proteins rather than via electrostatic repulsion as before incubation.

Concerning the particle size (3.5-150 nm), most of the differences were observed in respect of the kinetics and extent of the PC formation (**Figure 6.5**). DLS and z-potential analyses of the different NPs after incubation and purification show that the smaller NPs (<5 nm) did not obtain a stable PC, and the original values of surface charge and DLS almost recovered after all the studied incubation times (UV-vis was less sensitive in this respects). Despite the smaller degree of coating, these NPs showed long-term colloidal stability. This is consistent with the formation of a corona with a low
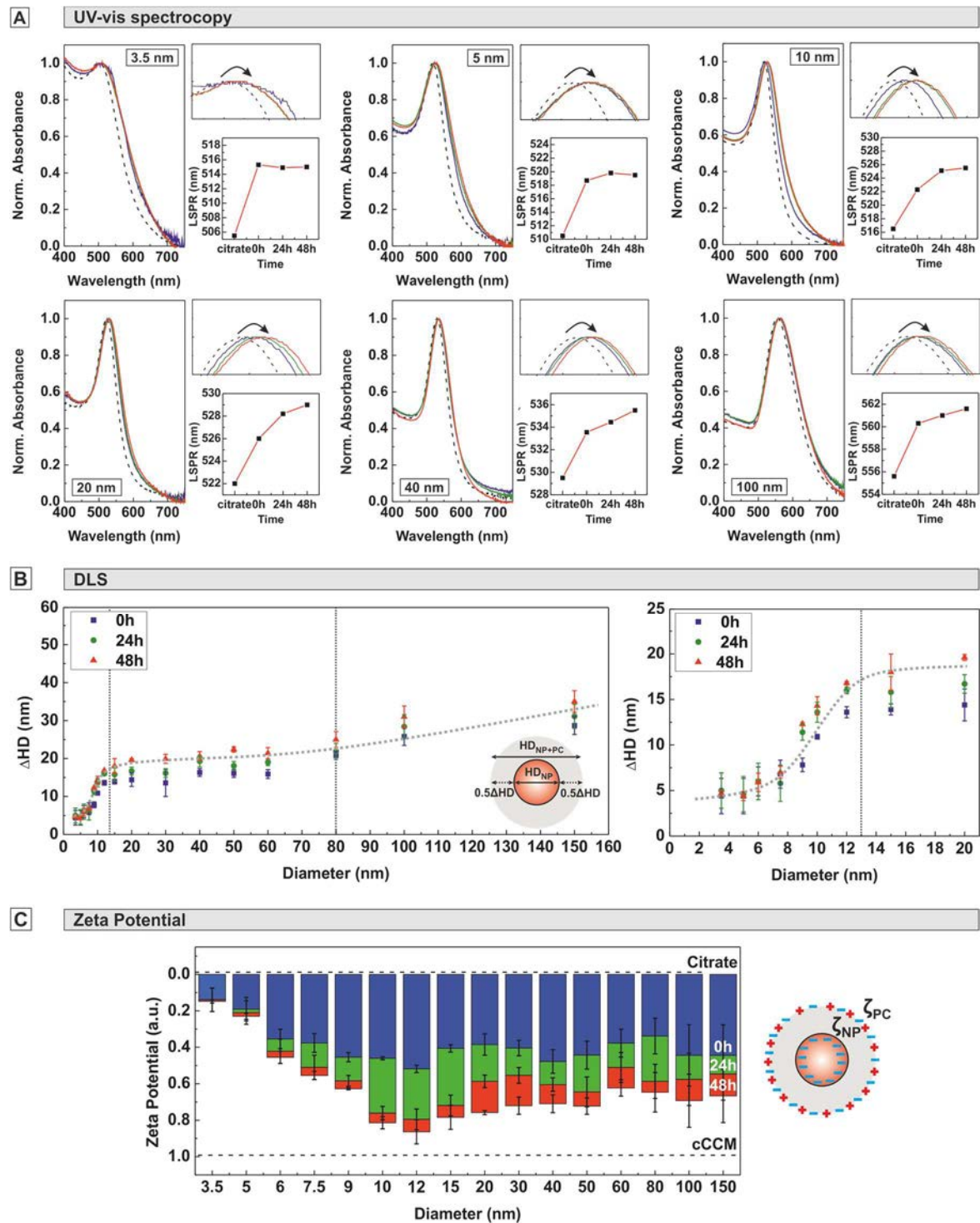
Figure 6.5. Characterization of the nanoparticle protein corona on gold nanoparticles with different diameters. (A) Time-evolution extinction spectra of the Au NPs after different incubation times. (B) Thickness of the PC measured by DLS. (C) Time-evolution of the surface charge measured by z-potential. Au NPs in cCCM (DMEM with 10% FBS) were purified by centrifugation and dispersed in a solution of 2.2 mM of citrate for a proper characterization.

packing density. For example, a particle of 3.5-4 nm can hardy accommodate two BSA proteins at the surface, which is not enough for cooperative protein effects. Conversely, for Au NPs between 12 and 50 nm, a stable PC was formed with the NPs reaching almost the same surface charge of the proteins. Additionally, the increase in the hydrodynamic size of the NP after incubation was 10-20 nm. This corresponds to a 5-10 nm thick corona, which would fit with a single layer of BSA molecules (albumin can be considered as a 8 x 8 x 3.4 nm^3 object) [49]. Finally, in the case of Au NPs larger than 80 nm, PC formation appeared similar to the 10 nm Au NPs at the beginning, but it extended to longer times and the final increase in the hydrodynamic diameter was significantly larger compared to the smaller, probably due to the formation of a multi-layered corona composed of two or three layers of proteins. This would be consistent with the fact that, as the NP surface approached to a flat surface, proteins directly adsorbed experienced larger conformational changes and expose core regions from which other proteins can be assembled.

Based on these results, three different regimes of temporal evolution were identified (**Figure 6.6**): incomplete corona or NP-Protein complexes (<12 nm), a full PC composed of a monolayer of proteins (12-80 nm) and a multi-layered PC (>80 nm). These three regimes were also observed when BSA was used instead of cCCM, indicating that in a complex mixture of proteins, BSA is probably a relevant component of the PC formed on citrate-stabilized Au NPs.
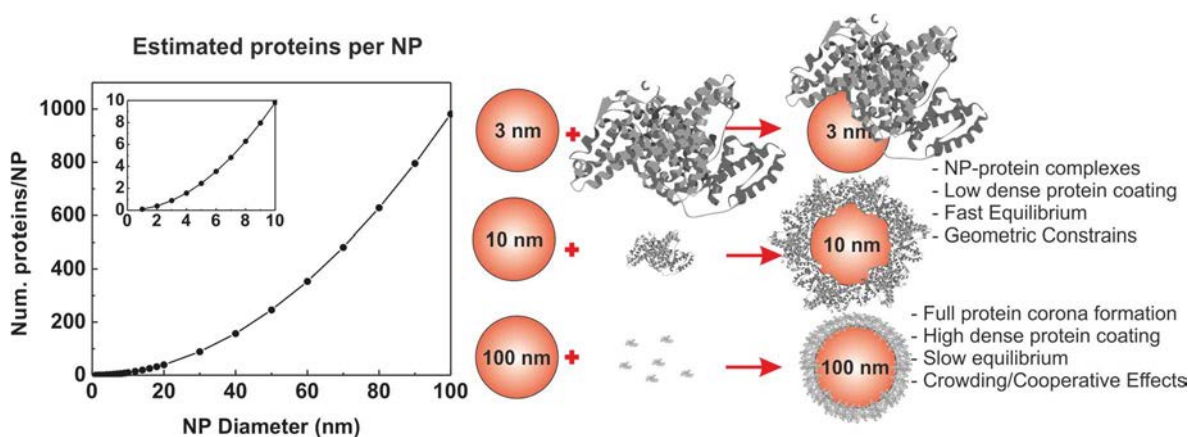
Figure 6.6. Schematic representation of the formation of a hard protein corona in citrate-stabilized gold nanoparticles of different sizes. Estimation of proteins per NPs was calculated based on the size of BSA according to [49].

6.4. Conclusions

In the present chapter, a combination of UV-visible spectroscopy, DLS and z-potential measurements were used to elucidate the kinetics of PC formation on citrate-stabilized Au NPs of different diameters after their incubation in cell culture media. The results agree with the formation of a size-dependent PC that can be divided into three different regimes: incomplete PC for Au NPs with diameters similar, or even lower, than most abundant proteins; a full PC composed of a monolayer of proteins for Au NP with sizes between 12-80 nm and a multi-layered PC for very large NPs (>80 nm) with near flat surfaces. A deeper analysis of this process can be found in the related **Publication 5**. In this regard, a comprehensive knowledge of PC formation is essential to understand NP-induced effects on biological systems.

6.5. References

[1] E. Casals*, et al.*, Reactivity of inorganic nanoparticles in biological environments: insights into nanotoxicity mechanisms, Journal of Physics D: Applied Physics 45 (2012) 443001.

[2] E. Casals, V.F. Puntes, Inorganic nanoparticle biomolecular corona: formation, evolution and biological impact, Nanomedicine 7 (2012) 1917-1930.

[3] V.H. Nguyen, B.-J. Lee, Protein corona: a new approach for nanomedicine design, International Journal of Nanomedicine 12 (2017) 3137-3151.

[4] F. Barbero*, et al.*, Formation of the Protein Corona: The Interface between Nanoparticles and the Immune System, Seminars in Immunology 34 (2017) 52-60.

[5] J. REJMAN*, et al.*, Size-dependent internalization of particles via the pathways of clathrin- and caveolae-mediated endocytosis, Biochemical Journal 377 (2004) 159-169.

[6] S. Tenzer*, et al.*, Rapid formation of plasma protein corona critically affects nanoparticle pathophysiology, Nature Nanotechnology 8 (2013) 772.

[7] C.D. Walkey*, et al.*, Protein Corona Fingerprinting Predicts the Cellular Interaction of Gold and Silver Nanoparticles, ACS Nano 8 (2014) 2439-2455.

[8] I. Lynch*, et al.*, What does the cell see?, Nature Nanotechnology 4 (2009) 546.

[9] J. Cortes, C. Saura, Nanoparticle albumin-bound (nab™)-paclitaxel: improving efficacy and tolerability by targeted drug delivery in metastatic breast cancer, European Journal of Cancer Supplements 8 (2010) 1-10.

[10] P. Victor, Nanoparticle Interaction with Biomolecules: How it Shapes the Nano-Effects on Immunity, Current Bionanotechnology (Discontinued) 2 (2016) 11-19.

[11] S. Goy-López*, et al.*, Physicochemical Characteristics of Protein–NP Bioconjugates: The Role of Particle Curvature and Solution Conditions on Human Serum Albumin Conformation and Fibrillogenesis Inhibition, Langmuir 28 (2012) 9113-9126.

[12] L. Vroman, Effect of absorbed proteins on the wettability of hydrophilic and hydrophobic solids, Nature 196 (1962) 476-477.

[13] S.M. Slack, T.A. Horbett, The Vroman Effect, Proteins at Interfaces II, American Chemical Society1995, pp. 112-128.

[14] E. Casals*, et al.*, Time Evolution of the Nanoparticle Protein Corona, ACS Nano 4 (2010) 3623-3632.

[15] S. Alaeddine, H. Nygren, Logarithmic Growth of Protein Films, Proteins at Interfaces II, American Chemical Society1995, pp. 41-51.

[16] J.L. Brash, T.A. Horbett, Proteins at Interfaces, Proteins at Interfaces II, American Chemical Society1995, pp. 1-23.

[17] C.D. Walkey*, et al.*, Nanoparticle Size and Surface Chemistry Determine Serum Protein Adsorption and Macrophage Uptake, Journal of the American Chemical Society 134 (2012) 2139-2147.

[18] K.L. Prime, G.M. Whitesides, SELF-ASSEMBLED ORGANIC MONOLAYERS - MODEL SYSTEMS FOR STUDYING ADSORPTION OF PROTEINS AT SURFACES, Science 252 (1991) 1164-1167.

[19] V. Silin*, et al.*, SPR Studies of the Nonspecific Adsorption Kinetics of Human IgG and BSA on Gold Surfaces Modified by Self-Assembled Monolayers (SAMs), Journal of Colloid and Interface Science 185 (1997) 94-103.

[20] W. Norde, J. Lyklema, Why proteins prefer interfaces, Journal of biomaterials science. Polymer edition 2 (1991) 183-202.

[21] M.S. Ehrenberg*, et al.*, The influence of protein adsorption on nanoparticle association with cultured endothelial cells, Biomaterials 30 (2009) 603-610.

[22] T. Cedervall*, et al.*, Understanding the nanoparticle–protein corona using methods to quantify exchange rates and affinities of proteins for nanoparticles, Proceedings of the National Academy of Sciences 104 (2007) 2050-2055.

[23] K. Saha*, et al.*, Regulation of Macrophage Recognition through the Interplay of Nanoparticle Surface Functionality and Protein Corona, ACS Nano 10 (2016) 4421-4430.

[24] S.H. Brewer, *et al.*, Probing BSA Binding to Citrate-Coated Gold Nanoparticles and Surfaces, Langmuir 21 (2005) 9303-9307.

[25] J.D. Zhou, *et al.*, Differential plasma protein binding to metal oxide nanoparticles, Nanotechnology 20 (2009) 455101.

[26] G. Maiorano, *et al.*, Effects of Cell Culture Media on the Dynamic Formation of Protein−Nanoparticle Complexes and Influence on the Cellular Response, ACS Nano 4 (2010) 7481-7491.

[27] Y. Xing, L. Dai, Nanodiamonds for nanomedicine, Nanomedicine 4 (2009) 207-218.

[28] X. Liu, *et al.*, A One-Step Homogeneous Immunoassay for Cancer Biomarker Detection Using Gold Nanoparticle Probes Coupled with Dynamic Light Scattering, Journal of the American Chemical Society 130 (2008) 2780-2782.

[29] L.R. Hirsch, *et al.*, A Whole Blood Immunoassay Using Gold Nanoshells, Analytical Chemistry 75 (2003) 2377-2381.

[30] W. Norde, Adsorption of proteins from solution at the solid-liquid interface, Advances in Colloid and Interface Science 25 (1986) 267-340.

[31] J. Piella, *et al.*, Size-Dependent Protein–Nanoparticle Interactions in Citrate-Stabilized Gold Nanoparticles: The Emergence of the Protein Corona, Bioconjugate Chemistry 28 (2017) 88-97.

[32] P. Roach, *et al.*, Interpretation of Protein Adsorption: Surface-Induced Conformational Changes, Journal of the American Chemical Society 127 (2005) 8168-8173.

[33] D. Zhang, *et al.*, Gold Nanoparticles Can Induce the Formation of Protein-based Aggregates at Physiological pH, Nano Letters 9 (2009) 666-671.

[34] P. Billsten, *et al.*, Adsorption to silica nanoparticles of human carbonic anhydrase II and truncated forms induce a molten-globule-like structure, FEBS Letters 402 (1997) 67-72.

[35] M. Lundqvist, *et al.*, Transient Interaction with Nanoparticles "Freezes" a Protein in an Ensemble of Metastable Near-Native Conformations, Biochemistry 44 (2005) 10093-10099.

[36] M. Karlsson, *et al.*, Adsorption of Human Carbonic Anhydrase II Variants to Silica Nanoparticles Occur Stepwise: Binding Is Followed by Successive Conformational Changes to a Molten-Globule-like State, Langmuir 16 (2000) 8470-8479.

[37] L. Fei, S. Perrett, Effect of Nanoparticles on Protein Folding and Fibrillogenesis, International Journal of Molecular Sciences 10 (2009) 646-655.

[38] E. Casals, *et al.*, Hardening of the Nanoparticle–Protein Corona in Metal (Au, Ag) and Oxide (Fe3O4, CoO, and CeO2) Nanoparticles, Small 7 (2011) 3479-3486.

[39] M.A. Dobrovolskaia, *et al.*, Interaction of colloidal gold nanoparticles with human blood: effects on particle size and analysis of plasma protein binding profiles, Nanomedicine: Nanotechnology, Biology and Medicine 5 106-117.

[40] S.H.D.P. Lacerda, *et al.*, Interaction of Gold Nanoparticles with Common Human Blood Proteins, ACS Nano 4 (2010) 365-379.

[41] J.S. Gebauer, *et al.*, Impact of the Nanoparticle–Protein Corona on Colloidal Stability and Protein Structure, Langmuir 28 (2012) 9673-9679.

[42] C. Röcker, *et al.*, A quantitative fluorescence study of protein monolayer formation on colloidal nanoparticles, Nature Nanotechnology 4 (2009) 577.

[43] D. Walczyk, *et al.*, What the Cell "Sees" in Bionanoscience, Journal of the American Chemical Society 132 (2010) 5761-5768.

[44] Z. Ji, *et al.*, Dispersion and Stability Optimization of TiO2 Nanoparticles in Cell Culture Media, Environmental Science & Technology 44 (2010) 7309-7314.

[45] B. Sahoo, *et al.*, Spontaneous formation of a protein corona prevents the loss of quantum dot fluorescence in physiological buffers, Chemical Physics Letters 445 (2007) 217-220.

[46] A.M. Derfus, *et al.*, Probing the Cytotoxicity of Semiconductor Quantum Dots, Nano Letters 4 (2004) 11-18.

[47] V. Puntes, Design and pharmacokinetical aspects for the use of inorganic nanoparticles in radiomedicine, The British Journal of Radiology 89 (2016) 20150210.

[48] E. Casals, *et al.*, Intrinsic and Extrinsic Properties Affecting Innate Immune Responses to Nanoparticles: The Case of Cerium Oxide, Frontiers in Immunology 8 (2017) 970.

[49] S. Dominguez-Medina, *et al.*, In Situ Measurement of Bovine Serum Albumin Interaction with Gold Nanospheres, Langmuir 28 (2012) 9131-9139.

[50] J.M. Zook*, et al.*, Measuring Agglomerate Size Distribution and Dependence of Localized Surface Plasmon Resonance Absorbance on Gold Nanoparticle Agglomerate Size Using Analytical Ultracentrifugation, ACS Nano 5 (2011) 8070-8079.
[51] M.P. Monopoli*, et al.*, Physical−Chemical Aspects of Protein Corona: Relevance to in Vitro and in Vivo Biological Impacts of Nanoparticles, Journal of the American Chemical Society 133 (2011) 2525-2534.

Publication 5

BC Bioconjugate Chemistry

Size-Dependent Protein−Nanoparticle Interactions in Citrate-Stabilized Gold Nanoparticles: The Emergence of the Protein Corona

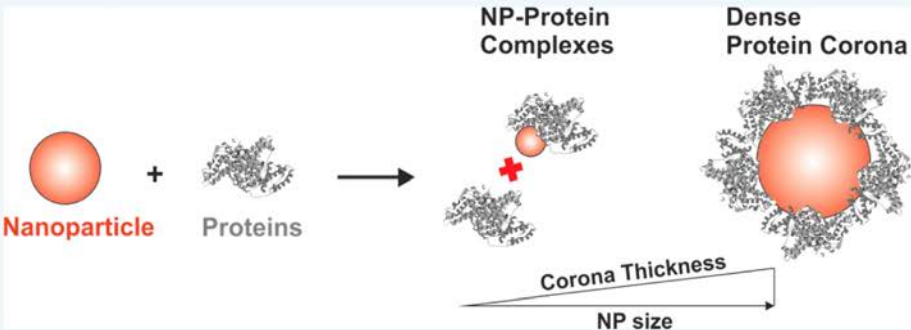Jordi Piella,[†,‡] Neus G. Bastús,[†] and Víctor Puntes[*,†,§,||]

[†]Institut Català de Nanociència i Nanotecnologia (ICN2), CSIC and The Barcelona Institute of Science and Technology (BIST), Campus UAB, 08193, Bellaterra, Barcelona, Spain

[‡]Universitat Autònoma de Barcelona (UAB), Campus UAB, 08193 Bellaterra, Barcelona, Spain

[§]Institució Catalana de Recerca i Estudis Avançats (ICREA), P. Lluís Companys 23, 08010 Barcelona, Spain

[||]Vall d'Hebron Institut de Recerca (VHIR), 08035, Barcelona, Spain

S *Supporting Information*

ABSTRACT: Surface modifications of highly monodisperse citrate-stabilized gold nanoparticles (AuNPs) with sizes ranging from 3.5 to 150 nm after their exposure to cell culture media supplemented with fetal bovine serum were studied and characterized by the combined use of UV−vis spectroscopy, dynamic light scattering, and zeta potential measurements. In all the tested AuNPs, a dynamic process of protein adsorption was observed, evolving toward the formation of an irreversible hard protein coating known as Protein Corona. Interestingly, the thickness and density of this protein coating were strongly dependent on the particle size, making it possible to identify different transition regimes as the size of the particles increased: (i) NP-protein complexes (or incomplete corona), (ii) the formation of a near-single dense protein corona layer, and (iii) the formation of a multilayer corona. In addition, the different temporal patterns in the evolution of the protein coating came about more quickly for small particles than for the larger ones, further revealing the significant role that size plays in the kinetics of this process. Since the biological identity of the NPs is ultimately determined by the protein corona and different NP−biological interactions take place at different time scales, these results are relevant to biological and toxicological studies.

◼ INTRODUCTION

Noble metal nanoparticles (NPs) are among the most widely used nanomaterials in biomedicine because of their outstanding optical, electromagnetic, and photothermal properties. These unique properties, together with the high reactivity of the NPs and their affinity for binding many different (bio)molecules, make them attractive candidates in a wide variety of uses and applications including delivery, diagnostics, and therapy.[1,2] However, despite the rapid development of strategies for particle design and functionalization, relatively little is known about their in vitro and in vivo behavior in complex biological systems.[3]

The ability to integrate NPs in biological systems ultimately relies on the fundamental understanding of the interaction of these inorganic NPs with biological fluids.[4−6] A large number of biological fluids (plasma serum or otherwise) are complex aqueous media composed of electrolytes, proteins, lipids, and

metabolites, able to adsorb (by electrostatic, hydrophobic, van der Waals, and dispersive forces) onto the surfaces of the NPs forming a protein dense coating known as Protein Corona (PC),[7−11] a phenomena extensively studied previously in implants.[12] The PC shields the original surface properties of the NPs acting as a "complex" surfactant, and alters their size and composition providing the NPs with a new biological identity.[10,13,14] This corona is what is ultimately "seen" by cells, and critically determines the physiological response and interaction of the NPs with living systems, including cellular uptake, circulation lifetime, signaling, biodistribution, therapeutic effects, and toxicity.[15−21]

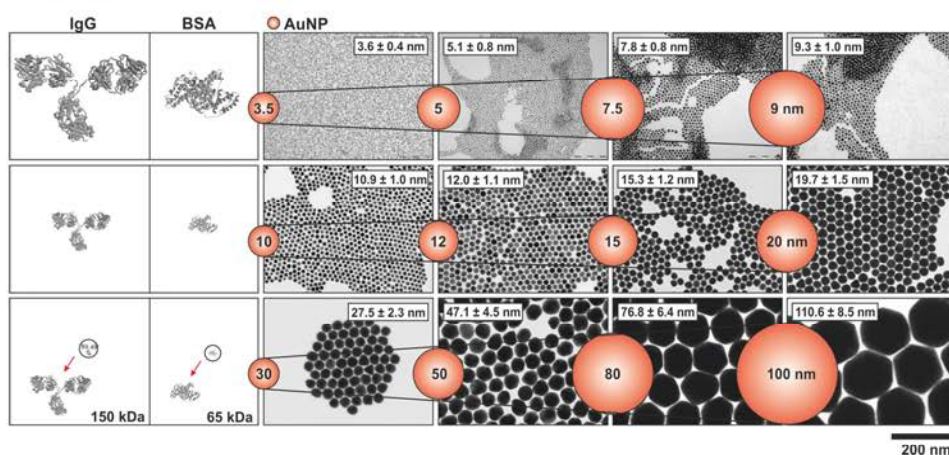**Bioconjugate Chemistry**　　　　　　　　　　　　　　　　　　　　　　　　　　　　　Article

Figure 1. Representative TEM images of citrate-stabilized AuNPs of selected sizes used in this study. The relative difference in size between AuNPs and proteins has been compared by choosing BSA (65 kDa) and IgG (150 kDa), the two most abundant protein in serum, as model proteins. The inset spheres represent the size of the AuNPs while the model proteins are schematically drawn in the column on the left. The smallest AuNPs (3.6 nm) cannot accommodate more than 1–2 proteins while AuNPs larger than 30 nm can accommodate hundreds of them on their surfaces.

The composition, structure, and kinetics of the PC formation depends on (i) the specific characteristics of the biological environments in which NPs are dispersed, especially protein composition[22] and concentration;[16,23] (ii) the physicochemical features of the dispersed material, such as NP chemical composition,[24] morphology,[7,25,26] surface charge (functional groups),[16,27] and hydrophobicity;[7,28] and (iii) the exposure time, which directly correlates with the relative abundance of proteins and the different protein-NP binding constants (Vroman's effect).[24,27,29] Among these parameters, the morphology of the NPs relating to size and shape has been suggested to play an important role. Due to surface curvature effects,[30] molecules tend to adopt different conformations on top of NPs as compared to flat surfaces indicating different protein-binding affinities, giving rise to variation of the structure of PC according to the size of the NPs.[31] Pioneering studies were performed by Cerdervall et al.[7,32] who investigated the role of surface curvature in copolymer NPs of 70 and 200 nm after their dispersion in plasma, and further studies were later extended to other sizes and compositions including AuNPs,[22,33–35] AgNPs,[20] polystyrene NPs,[36–38] SiO$_2$,[14,15,25,36] metal oxide NPs,[24,39,40] and polymer-coated FePt and CdSe/ZnS.[41] Although all of the authors reported consistent results, it was often difficult to separate the effect of NP size from other physicochemical aspects, such as particle composition and surface chemistry. Some of them found that particle size and surface curvature influences the amount of bound protein and (to a lesser extent) the identity of these proteins.[15,25,32] In contrast, other studies reported significant qualitative size-dependent changes in protein adsorption.[40] So far, the underlying mechanism explaining size-dependent protein–particle specific interaction is not yet resolved. Moreover, in all these studies the diameter of the tested NPs was above that of most abundant serum proteins (6–12 nm). As a result, changes in the PC of NPs of a similar or even smaller size than proteins were not addressed. In this regard, only a few studies have provided data on this size regime, including AuNPs (2 nm,15 nm),[16,22] CdSe/ZnS (9–11 nm),[42] and FePt (10 nm).[41]

Little is known about the PC formation of NPs when they are smaller than most of the proteins themselves, with subsequent lack of knowledge of their biological consequences.

Smaller NPs present some features that make them very attractive for biomedical applications: they are less prone to opsonization and have substantially longer lifetimes in the bloodstream, in such a way that a particle as small as 10 nm would not significantly activate the immune system.[43,44] They also have faster biodegradation (e.g., dissolution) together with excretion profiles which may avoid unwanted bioaccumulation.[45] Moreover, the small size of the NP may affect the PC formation process. Thus, when NPs have sizes similar to (or even smaller than) those of proteins it may be difficult to form a compact corona since the number of proteins at the surface of the particle is too small for a crowding cooperative effect to be achieved.[24,46] Conversely, as the size of the particles becomes larger, it may be possible for a proper full-density protein corona to develop.

Taking advantage of the recent improvements in the synthesis of sub-10 nm AuNPs,[47,48] we have studied the formation of PC on highly monodisperse citrate-stabilized AuNPs of different sizes (from 3.5 to 150 nm) after their exposure to cell culture media (CCM) supplemented with fetal bovine serum (FBS). By the combined use of UV–vis spectroscopy, dynamic light scattering, and zeta potential, a dynamic process of protein adsorption has been identified and characterized for all the tested particles, leading to the formation of an irreversible coating that mediates the colloidal stability of the AuNPs in the physiological medium. Interestingly, the thickness (and compactness) of this protein coating was strongly determined by the size of the NPs being possible to identify a transition regime from AuNP-complexes (or spare corona) in which the thickness of the corona was smaller than that expected for a single protein layer (AuNPs ≤ 12 nm), to the formation of a full corona composed by a dense protein monolayer for AuNPs sizes from 12 to 80 nm. Finally, for very large particles (>80 nm), an additional regime could be identified in which a multilayered corona composed of 2–3 protein layers, similar to that reported in flat surfaces, seemed to be favored.[49]

■ RESULTS AND DISCUSSION

The protein adsorption process was studied by incubating citrate-stabilized AuNPs for 48 h at 37 °C in complete cell
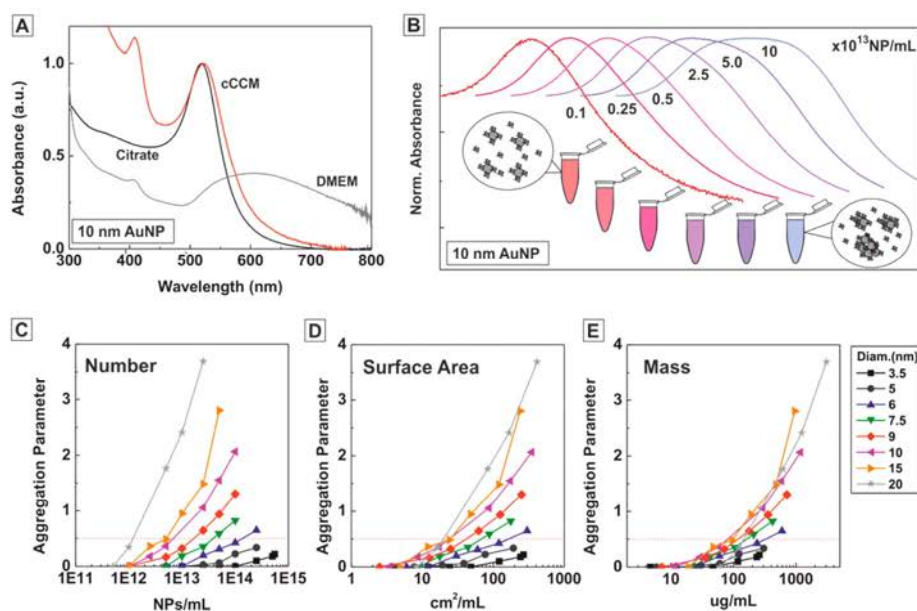
Bioconjugate Chemistry

Figure 2. Optimization of exposure conditions. (A) UV−vis spectra of AuNPs in different media. AuNPs aggregate in DMEM, even at low particle concentration, while they remain stable in cCCM. (B) Normalized UV−vis spectra of AuNPs in cCCM at different concentrations. The changes in the LSPR band indicate that AuNPs aggregate in cCCM when were exposed to the medium at high concentration while their stability was not compromised at low concentration. (C−E) Experimentally measured aggregation parameter of AuNPs of different sizes after their exposure to cCCM at increasing NP concentrations. Results are normalized by particle number (NPs/mL) (C), total particle surface area (cm^2/mL) (D), and total mass of Au atoms (μg/mL) (E). In all cases 1 mL of a solution of AuNPs 10× concentrated with respect to the desired concentration was added to 9 mL of the medium and rapidly mixed for a couple of minutes before being left undisturbed for 1 h under mild stirring.

culture media (cCCM); composed of Dulbecco's Modified Eagle Medium (DMEM) supplemented with 10% of fetal bovine serum (FBS). Highly monodisperse citrate-stabilized AuNPs with sizes ranging from 3.5 to 150 nm were synthesized following recently reported kinetically controlled seeded-growth approaches.[47,48] Citrate is a biocompatible reducer commonly used in the synthesis of AuNPs which provides a negative electrostatic stabilization once adsorbed on the NP surface. Besides, different from other surfactants that hinder the formation of the PC, i.e., polyethylene glycol (PEG),[26,50,51] the citrate layer is easily replaced, allowing the spontaneous adsorption of proteins under normal conditions of in vitro and in vivo exposure.[50,52] Moreover, FBS is a biological fluid that contains more than 3700 different proteins, with 12 orders of magnitude difference in their relative concentrations.[7] Among all proteins in serum, albumin represents the most abundant fraction and accounts for ~60% in mass of the total proteins in solution (1 mM), with globulins the second most abundant (~40%) and all the rest representing less than 1%.[52] With this in mind, in Figure 1 the relative size of the particles used in this study is compared to proteins, using bovine serum albumin (BSA) and Immunoglobulin G (IgG) as model proteins.

For the study of the PC formation, it is important to previously select the proper exposure condition of the AuNPs in cCCM. cCCM is a high ionic strength medium in which the stability of citrate-coated AuNPs is strongly compromised due to the screening of the electrostatic repulsion between particles by the high concentration of charges in solution. This process is evidenced when performing exposure experiments in DMEM media (Figure 2A), where the immediate aggregation of 10 nm AuNPs is clearly observed by UV−vis spectroscopy.[53] Thus, in the absence of serum proteins, the localized surface plasmon

resonance (LSPR) band of the particles rapidly vanishes, red-shifts, and broadens, and a new band between 600 and 800 nm emerges, which can be univocally ascribed to the coupling of the plasmon modes of individual NPs when they come into contact.[52,54]

In the presence of proteins (fixed at the level of standard in vitro studies), particle concentration is the main driver for aggregation. Stability conditions of 10 nm AuNPs in cCCM were initially studied by exposing the same volume (1 mL) of particles of adjusted concentrations (from 10^{12} NP/mL to 10^{15} NP/mL) to an equal volume of cCCM (9 mL), thus keeping the concentration of proteins constant (Figure 2B). The extent of aggregation was systematically quantified from UV−vis spectra, by calculating the aggregation parameter (AP) according to Lévy et al.[54] after 1 h of exposure. AP values higher than 0.5 indicated significant aggregation. It is important to note that the LSPR peak and the calculation of this parameter were not affected by the presence of free protein in solution, since proteins absorb at wavelengths far lower than the characteristic AuNPs band. For the selected NP-protein exposure conditions, AuNPs were stable in cCCM at a low concentration of 2.5×10^{12} NPs/mL while they formed aggregates when the concentration was increased above 2.5×10^{13} NPs/mL. Since the concentration of proteins in the media does not represent a limiting factor (in all conditions the amount of proteins in solution is largely above that needed to fully cover all available NP surface), the aggregation is likely due to kinetic factors when mixing both solutions. That is, NPs destabilize and aggregate before proteins succeed in protecting their surfaces.

When the NP and the protein solutions are mixed, two different kinetic processes are competing at the same time: (i) the destabilization (and further aggregation) of the NPs

Bioconjugate Chemistry   `Article`

Table 1. Physicochemical Characterization of AuNPs before and after Exposure to cCCM for 48 h and Further Purified

target size (nm)	citrate				cCCM		
	diameter TEM (nm)	diameter DLS (nm)	ζ-potential (mV)	LSPR maximum (nm)	diameter DLS (nm)	ζ-potential (mV)	LSPR maximum (nm)
3.5	3.6 ± 0.4	5.5 ± 1.2	−36.8 ± 8.7	505.5	10.2 ± 3.9	−32.8 ± 5.1	515.0
5	5.1 ± 0.8	6.6 ± 1.4	−37.2 ± 14.3	510.5	11.0 ± 3.6	−31.0 ± 7.8	519.5
6	6.2 ± 0.6	7.4 ± 1.6	−39.6 ± 11.1	513.0	13.3 ± 3.2	−26.1 ± 4.3	522.5
7.5	7.8 ± 0.8	9.1 ± 1.9	−42.6 ± 8.6	515.0	16.1 ± 4.3	−24.5 ± 6.2	523.5
9	9.3 ± 1.0	10.3 ± 2.2	−43.6 ± 19.8	516.0	22.6 ± 4.1	−22.5 ± 5.1	524.0
10	10.9 ± 1.0	10.9 ± 3.4	−45.8 ± 14.6	516.5	25.2 ± 5.3	−16.7 ± 5.3	525.5
12	12.0 ± 1.1	12.9 ± 2.7	−42.9 ± 16.4	516.5	29.7 ± 6.9	−16.5 ± 4.8	524.0
15	15.3 ± 1.2	16.4 ± 3.5	−42.9 ± 17.3	518.5	34.4 ± 8.3	−17.1 ± 4.6	527.0
20	19.7 ± 1.5	23.3 ± 4.8	−46.9 ± 15.6	522.0	42.9 ± 9.3	−18.9 ± 6.5	529.0
30	27.5 ± 2.3	32.0 ± 6.2	−48.3 ± 22.8	526.0	51.9 ± 11.9	−20.7 ± 5.9	532.0
40	42.0 ± 3.7	41.8 ± 8.2	−45.7 ± 23.4	529.5	62.4 ± 13.0	−20.9 ± 6.8	535.5
50	47.1 ± 4.5	47.4 ± 11.8	−45.7 ± 17.8	533.0	69.8 ± 15.2	−19.9 ± 7.4	539.0
60	58.3 ± 4.6	55.8 ± 14.6	−42.8 ± 15.6	536.5	77.2 ± 19.3	−25.1 ± 6.6	542.5
80	76.8 ± 6.4	77.5 ± 16.6	−50.2 ± 22.8	546.5	106.5 ± 29.1	−24.2 ± 6.6	553.0
100	110.6 ± 8.5	106.6 ± 34.1	−44.2 ± 14.5	556.5	137.6 ± 43.4	−20.5 ± 8.2	561.3
150	149.1 ± 11.9	139.3 ± 40.8	−44.1 ± 15.2	586.0	174.3 ± 57.5	−21.4 ± 7.4	597.5

promoted by the high ionic strength of the media in which they are dispersed and (ii) the stabilization of the NP surface against aggregation via protein adsorption. Thus, if the formation of a protective protein layer is faster than the characteristic time of destabilization (that is the time needed by two individual "bare" particles to bind to each other), then the resultant colloidal solution will remain stable. Conversely, the sample will destabilize and (partially or totally) agglomerate, forming aggregates immediately coated by proteins that will progressively sediment.[55] Based on the obtained results, it becomes clear that these two processes take place in the same time scale. For completeness, stability conditions were additionally evaluated for particles of different sizes (3.5 to 20 nm) and the results were normalized to (1) the total number of NPs in solution (Figure 2C), (2) the total surface area exposed by the NPs (Figure 2D), and (3) the total gold mass in each sample (Figure 2E), with it being possible to observe that curves hardly converge in any case. Only when the results were normalized to the total gold mass in each sample did they become comparable, which suggests that, in excess of free proteins, the aggregation of the particles is not exclusively determined by the probability of collisions of two individual particles but may be affected by additional parameters. Interestingly, small particles appear to be slightly more stable than large ones and thus are able to reach higher concentrations. This could be related to faster protein coating or a faster dispersion of the NP due to increased Brownian motion as size decreases. Consequently, stability conditions depend on both the characteristics of the AuNPs and the ratio between the NPs and protein concentration in the media.

Considering these results, we adjusted the concentration of AuNPs, from ∼10^{13} NPs/mL for the smallest particles (3.5 nm) to ∼10^9 NP/mL for the largest ones (150 nm), to be low enough to promote the formation of a protein layer before the characteristic time of destabilization. It is worth mentioning that these studies show how the exposure of NP to physiological media is concentration dependent and how dispersion of highly concentrated NP samples in these media (as i.v. injection or high NP dose toxicology studies) may be challenging.

Protein adsorption profile is a kinetic process in which a "soft protein corona" composed of loosely bound proteins in equilibrium with the free proteins in solution initially forms and evolves slowly toward an irreversible "hard protein corona" consisting of tightly bound proteins that do not readily desorb.[24] In this process, the proteins adsorb/desorb and rearrange at the surface of the particle, leading to the hardening of the corona, a process that determines the final identity of the particle. In this stable (hard) conformation of the protein corona, crowding/cooperative effects between attached proteins are a key factor: once the protein layer is formed, the incorporation of a new protein implies the rearrangement of many, which is translated into a highly stable PC. This process takes about 48 h in the case of AuNPs that end up having a permanent PC that does not detach from the surface when NPs are redispersed in protein-free media.[27] To obtain a PC hardening profile, the NP has to be purified from the exposure media to remove the unbound and loosely bound proteins, which is indeed a critical step. Purification of the AuNPs was performed by centrifugation followed by subsequent dispersion in protein-free aqueous solution after a proper optimization of the process. Additionally, the number of purification steps was determined to be at least 2. Otherwise, the presence of unbounded free proteins was directly translated into bimodal size distributions in dynamic light scattering (DLS) measurements, in particular for the small nanoparticles (more details can be found in the SI).

The size-dependent evolution of the hardening of the protein corona was analyzed by UV−vis spectroscopy, DLS, and zeta potential measurements of purified samples. This combination of characterization techniques provides a remarkably robust analysis of the interaction between the proteins and the NPs in the colloidal state,[27] bypassing complex postprocessing steps and/or avoiding chemical labeling strategies, such as luminescent or radioactive labeling, usually needed for protein detection. As observed in Table 1, important changes in the physicochemical properties of the purified AuNPs after exposure to cCCM are identified. The LSPR band of the AuNPs systematically red-shifts which can be ascribed to the change of the refractive index at the vicinity of the particles,[56] and it is consistent with the spontaneous binding of media
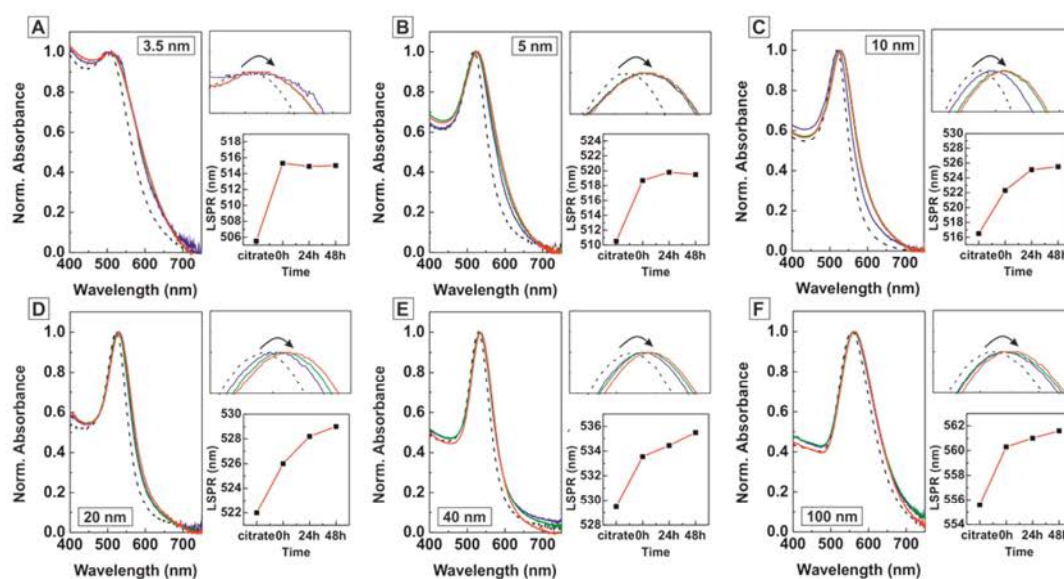
Bioconjugate Chemistry

Figure 3. UV–vis characterization of purified AuNPs of selected sizes after their exposure to cCCM for different times: (A) 3.5 nm, (B) 5 nm, (C) 10 nm, (D) 20 nm, (E) 40 nm, (F) 100 nm. UV–vis spectra before (dotted-line) and after their exposure at different times (blue t < 30 min, green t = 24 h, red t = 48 h).
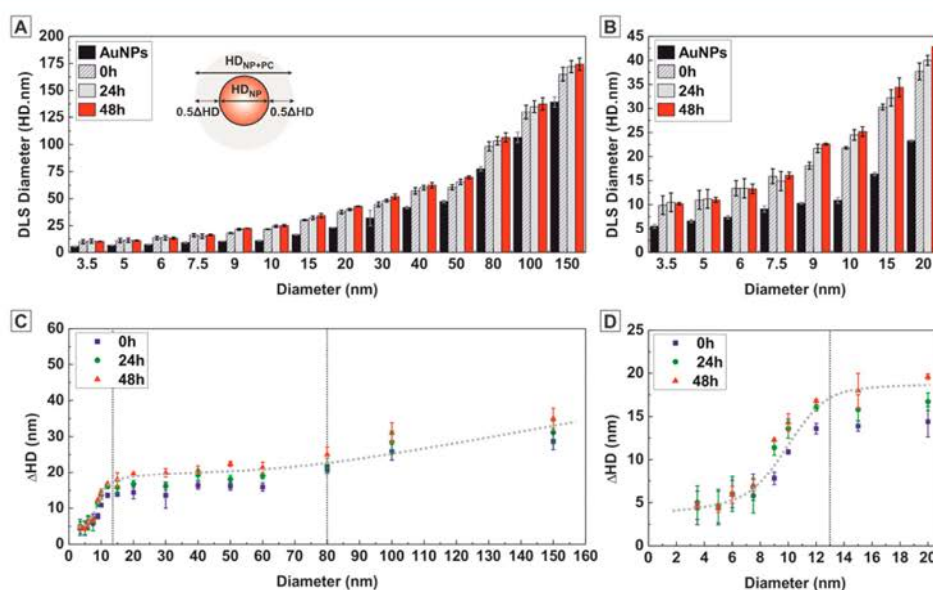

Figure 4. Hydrodynamic diameter (HD) measured by DLS of purified AuNPs of different sizes after their exposure to cCCM for different times. (A) HD obtained by DLS for particles between 3.5 and 150 nm and (B) detailed for particles between 3.5 and 20 nm. (C,D) Respective increases in the HD showing doubling of the corona thickness. Straight lines indicate different tendencies in the resultant protein corona.

proteins.[27,51] The shift is clearly observed within minutes and it takes 24–48 h to reach a stationary value, indicating a dynamic process of hardening of the protein corona, reaching a constant value faster for small particles than for the large ones (Figure 3). The extent of the red-shift also depends on particle size being $\Delta\lambda \approx 9$ nm for the smallest AuNPs (3.5 nm) and $\Delta\lambda \approx 6$ nm for the largest ones (150 nm). However, this cannot be directly correlated with the thickness and density of the protein layer since particles of different sizes present different sensitivity toward similar modifications of the surrounding environment (thickness, refractive index, and chemical anchoring).[56] The absence of absorbance peaks at longer wavelengths is further

evidence that under optimized conditions the AuNPs remain stable and well-dispersed in cCCM for all the sizes under study.[54]

DLS was used for an in-depth study of the PC and to determine variations in the hydrodynamic diameter (HD) of the samples. Obtained results are summarized in Table 1 and Figure 4, where it can be seen how the HD of the AuNPs systematically increases after their exposure to cCCM, which is associated with the direct adsorption of the proteins onto the surface of the NPs (Figure 4A,B). This increase strongly depends on the NP size and can be directly correlated with the thickness of the PC (thickness = 1/2 ΔHD) (Figure 4C,D).

Thus, for small 3.5 nm AuNPs a protein layer of ~2.5 nm in thickness is observed (ΔHD ~ 5 nm). As the size of the particles progressively increases the protein coating becomes thicker, reaching a rather constant value of 8–10 nm (ΔHD from 16 to 20 nm) for AuNPs from 12 to 80 nm. Finally, for particles larger than 80 nm, the thickness of the corona seems to be even larger, obtaining an increase of 15–16 nm in thickness (ΔHD from 30 to 32 nm).

Considering the results obtained earlier and assuming that albumin (65 kDa, HD ~ 6–7 nm) and other high-molecular-mass (>65 kDa) proteins[13] have been extensively found as the major constituents of the PC, it is reasonable to identify three different regimes: (i) small size regime, where the particles are smaller than mentioned proteins, and the thickness of the PC is thinner than that of a single layer of proteins; (ii) medium size regime, where the size of the particles starts to be significantly larger than of the proteins, and where the obtained thickness of the PC supports the overall formation of a single layer of proteins; and (iii) large size regime, where the size of the particles is much larger than that of proteins, approaching a flat surface, and where the obtained PC thickness suggests the formation of a multilayer of proteins. It is worth noting that despite the PC not being completely developed in the small AuNP regime; it is robust and provides enough stability to prevent them from aggregation.

Similar evidence was obtained by zeta potential measurements used to assess the changes in particle surface charge after exposure to cCCM. Thus, concomitant with the observed red-shift of the LSPR position and the increase of the NP size measured by DLS, a drop in absolute surface charge of the particles toward the average value of the medium proteins was systematically observed. It accounts for the progressive screening of the negatively charged citrate-metal surface by the coating protein layer, which provides a long-term colloidal stability to the AuNPs in biological media. Interestingly, here again, zeta potential results depend on AuNP size (Figure 5A), changing from −40 mV (citrate) to −30 mV for the smallest particles, and to −(15–20) mV for larger particles after protein coating. These results supports the previous idea that proteins are unable to form a dense layer on the surface of very small AuNPs, while a proper protein corona is formed in the large ones, either by a single dense protein layer or a multilayered coating. Since the surface charge itself is not high enough to prevent NPs from electrostatic aggregation (an absolute value of 30 mV is usually considered a limit for particle stability), these results are further evidence that the stability of the NPs is mediated by steric repulsion provided by proteins (which stay in their native state[27]) rather than via the former electrostatic repulsion provided by citrate.

As previously observed by UV–vis spectroscopy, time-dependent DLS and zeta potential results confirm the kinetic evolution of a hard protein corona and its dependence on particle size (Figures 4 and 5), being faster (24 h) for smaller sizes than for larger ones (48 h). These results suggest that particle size plays a critical role in both the kinetics and the thickness of the protein layer: the smaller the particle, the faster the kinetic evolution and the thinner (incomplete) the protein layer.

Based on these results, there seems to be a size limit below which a complete PC cannot fully develop. Presumably, this can be related to geometric constraints or other effects (crowding, cooperative effects) that could be a subject of further studies. As described by Nygren and Alaeddine,[57] and contrary to what
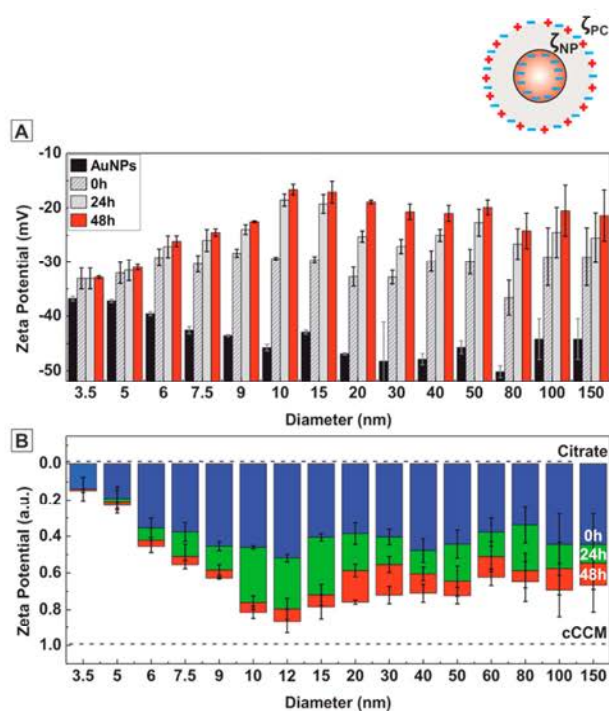

Figure 5. Zeta potential of purified AuNPs of different sizes after their exposure to cCCM for different times. (A) Absolute values of zeta potential measurements and (B) relative values in which 0 represents the surface charge of the citrate coated particles and 1 the charge of the proteins. The size-dependent protein corona evolution is clearly observed; where small particles present the most negative charge after exposure as a consequence of not forming a dense layer. For large particles, zeta potential is closer to that of the proteins indicating the formation of a denser layer.

might be expected, proteins do not distribute on surfaces randomly. Instead, once the first proteins are attached they serve as nucleation centers for the deposition on new ones, thereby stabilizing them, and this mechanism is repeated until the entire surface is filled. These and other attempts to explain the irreversibility of this process seem to have in common that the initial attachment of a protein to a surface is followed by a series of movements and/or rearrangements to make the interaction more stable, ultimately resulting in an irreversible attachment. These processes appear to be restricted when the particles become very small and their surface is limited to very few proteins per NP (Figure 6). On the other hand, the formation of a hard protein corona composed of more than one layer of proteins is a plausible explanation for larger particles. In this case, when approaching flat surfaces, proteins are subjected to larger conformational changes upon adsorption leading to multiple protein adsorptions. Thus, the increase in the corona thickness of the larger particles with respect to the smaller particles could be related to this effect along with the appearance of defects on the first protein layer docking other proteins (Figure 6). However, it remains unknown whether particle size determines the nature of the PC only quantitatively (the number of proteins attached) or also in a qualitatively way (the composition of proteins).[15]

In order to see whether and how obtained results can be extrapolated to other systems we studied the PC formation in the presence of pure albumin. Considering the high abundance
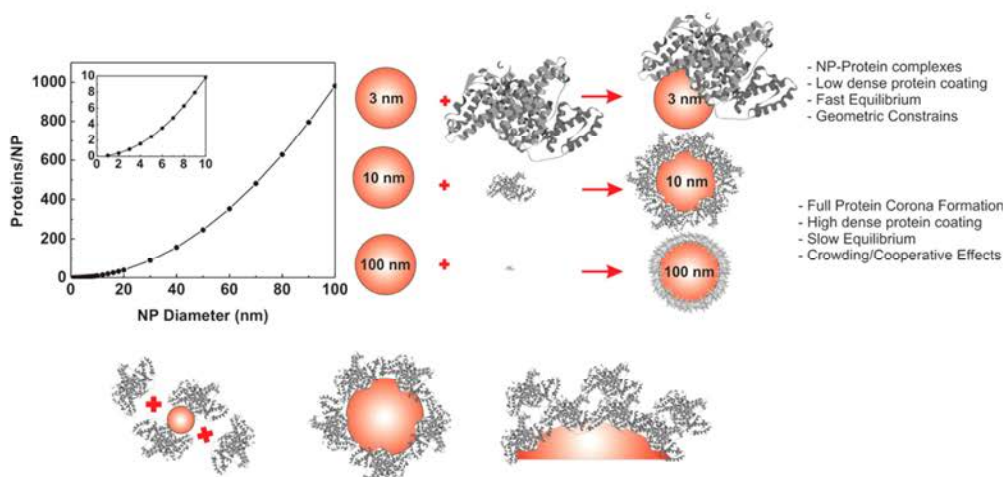
Figure 6. Representative scheme of the formation process of a hard protein corona in citrate-stabilized AuNPs of different sizes. (i) NP−protein complexes (or incomplete coating), (ii) the formation of a single dense protein corona layer, and (iii) the formation of a multilayer corona. Graphic on the left details the number of proteins that can attach on the surface of the NP as a single monolayer. Calculations has been performed based on the size of BSA chosen as model protein (see SI).

of albumin in serum (represents ∼60% of the total mass serum proteins), its high affinity for many different surfaces, and low specificity, albumin is known to be one of the main components of the protein corona when AuNPs, and other NPs, are exposed to serum or blood plasma.[15,25] Indeed, this high affinity of albumin for gold surfaces has been widely proven, resulting in the spontaneous formation of a dense and tightly bound albumin-rich coating in a process usually known as albuminization.[41,49,51,58,59] With the aim to elucidate whether the albuminization of the particles showed similar size dependent effects to those observed in the PC formation by serum proteins, analogous experiments were performed by exposing the particles to a BSA in phosphate buffer solution. The obtained results are summarized in Table 2, confirming the formation of an irreversible BSA coating layer onto all the citrate-stabilized AuNPs after 48 h of exposure. BSA adsorption did not induce colloidal aggregation of the NPs, comparable to

that given by FBS serum proteins in cCCM. This further indicates that the BSA preserves their native state and do not undergo denaturalization. The obtained results are in general agreement with those observed in the case of cCCM, suggesting that BSA is unable to form a proper corona for the very small particles while a single layer or multilayer is formed on larger ones. Slight differences observed between FBS and BSA may account for the presence of other proteins in combination with BSA. Briefly, the differences in the shift of the LSPR position (smaller in the case of BSA than FBS) along with the variations of the HD and surface charge observed by DLS and zeta potential (smaller in the case of BSA than FBS) suggest that the presence of pure BSA may lead to the formation of a more structured, and consequently thinner, layer.

■ CONCLUSIONS

The optimization of exposure conditions (stability and purification) allowed us the study of the protein corona in citrate-stabilized AuNPs of different sizes. The proper combination of UV−vis spectroscopy, DLS, and zeta potential measurements has been proven as a potential tool to describe qualitatively the protein corona formation on the surface of AuNPs. These techniques need to be discussed together in order to avoid misleading interpretations. For example, the largest red-shift in the LSPR, measured by UV−vis, is observed for the smallest particles, while DLS measurements show that these small particles form the thinnest corona. On the other hand, UV−vis spectroscopy and zeta potential do not predict the formation of a multilayer protein coating while DLS allows characterization of this process. Finally, all three techniques are effective in monitoring kinetic protein adsorption profiles. As a result we observed how both the kinetics of protein corona hardening and the characteristics of the protein corona are particle size-dependent, despite the question of debate remaining whether particle size determines the PC not only quantitatively but also in a qualitatively way.

The obtained results present relevant biological consequences as different NP−biological interactions take place at different time scales. Thus, tightly associated proteins may

Table 2. Physicochemical Characterization of AuNPs before and after Exposure to BSA for 48 h and Further Purified

target size (nm)	BSA		
	diameter DLS (nm)	ζ-potential (mV)	LSPR maximum (nm)
3.5	9.6 ± 1.6	−30.7 ± 7.3	513.5
5	10.6 ± 1.7	−29.5 ± 6.8	518.0
6	12.6 ± 2.5	−27.7 ± 4.5	520.0
7.5	14.9 ± 3.4	−23.5 ± 6.1	522.5
9	19.8 ± 4.4	−23.5 ± 4.7	522.5
10	22.2 ± 5.1	−18.5 ± 4.4	523.0
12	22.3 ± 5.2	−20.8 ± 5.2	522.5
15	29.6 ± 6.7	−21.9 ± 5.1	524.5
20	34.8 ± 7.8	−19.7 ± 6.8	527.5
30	44.4 ± 10.8	−21.8 ± 7.4	531.0
40	56.1 ± 11.0	−25.1 ± 6.6	534.0
50	60.9 ± 13.2	−22.2 ± 5.3	536.5
60	69.5 ± 19.3	−23.4 ± 5.9	540.5
80	98.3 ± 19.1	−25.2 ± 6.1	550.5
100	135.6 ± 35.4	−22.5 ± 7.7	560.5
150	159.1 ± 53.2	−24.6 ± 7.6	594.0

stay adherent to the particle when the particle is endocytosed from the extracellular fluid to an intracellular location, whereas proteins with a fast exchange rate are replaced by intracellular proteins during or after such a transfer. As a result, the same NP can give different biological responses depending on the portal of entry, history, and preincubation in serum among others, thereby illustrating the importance of the study of size-dependences of the protein corona in a biological environment.

■ EXPERIMENTAL SECTION

Chemicals. Sodium citrate tribasic dihydrate (≥99%) and gold(III) chloride trihydrate $HAuCl_4 \cdot 3H_2O$ (99.9% purity) were purchased from Sigma-Aldrich. Fetal Bovine Serum, FBS (research grade, sterile filtered), and Dulbecco's Modified Eagle Medium, DMEM (with 1000 mg/mL glucose and sodium bicarbonate, whiteout L-glutamine, sodium pyruvate, and phenol red, liquid, sterile-filtered), were purchased from Sigma. All reagents were used as received without further purification and all glass material was sterilized and dehydrogenated in an oven prior to use. Milli-Q water was used in the preparation of all solutions.

Nanoparticle Synthesis. Aqueous solutions of citrate-stabilized AuNPs with different sizes (3.5−150 nm) were synthesized according to the previously developed seeded-growth method in our group. Detailed synthetic procedure and full characterization of the resultant solutions can be found in the respective articles.[47,48] Briefly, AuNPs with increasing sizes were obtained from an initial AuNP solution after different sequential steps of growth, consisting of sample dilution plus further addition of gold precursor. This means that the number of particles in the solution decreases as the size increases. Consequently, the concentration of smallest particles was $\sim 10^{14}$, which decreased down to $\sim 10^{10}$ for the largest 150 nm particles. All the particles were used within 20 days after synthesis. The use of aged particles may result in increased experimental variability, since after a large period of time the stability of the particles may be compromised by the degradation of the surfactant.

Exposure to Cell Culture Media. Complete cell culture medium (cCCM) consisted of DMEM supplemented with 10% of FBS. AuNPs and cCMM were mixed (1:10 by volume) and placed in an incubator at 37 °C for different incubation times. As a result, the final concentration of AuNPs was that of the synthesis divided by the dilution factor: $\sim 10^{13}$ NP/mL for the smallest particles and $\sim 10^9$ for the largest particles (approximately 0.05 mM of Au). At these working concentrations, AuNPs were stable throughout the experiments and the number of proteins in larger excess with respect to the available particle surface area. After incubation, the samples were centrifuged between 2000 and 35 000 g for 10−20 min. (the larger the size, the lower the speed) to remove the excess of unbound or loosely bound proteins on the NP surfaces followed by resuspension in the particle original medium (sodium citrate 2.2 mM). Any possible aggregated fraction resulting from the centrifugation process was removed by filtering the samples with a 200-nm-pore-size cellulose acetate membrane. In the case in which the AuNPs solution needed to be concentrated with respect to the synthesis concentration, such as for stability tests, a regenerated cellulose centrifugal filter (Millipore 10KDa) was used.

Physicochemical Characterization of the NPs and NPs-Protein Corona. AuNPs and the time evolution of their coating by proteins were characterized before and after exposure to cCCM using different techniques. The proper combination of these techniques has been used in other similar studies by our group[27] and proven to be reliable when performed with adequate controls.

TEM. Diameter of the synthesized particles was obtained from analysis of TEM images acquired with a JEOL 10101 electron microscope operating at an accelerating voltage of 80 kV. Samples were prepared by drop-casting 10 μL of the sample on a carbon-coated copper TEM grid and left to dry at room temperature. At least 500 particles from different regions of the grid were counted. In order to avoid aggregation of the particles during TEM grid preparation they were previously conjugated with 11-mercaptoundecanoic acid.

UV−vis Spectroscopy. UV−vis spectra were acquired with a Shimadzu UV-2400 spectrophotometer. 1 mL of sample was placed in a plastic cuvette, and spectral analysis was performed in the 300−800 nm range at room temperature. AuNPs exhibit a characteristic absorbance peak in this region, the so-called localized surface plasmon resonance (LSPR) band. The LSPR position is sensitive to the surrounding of the NPs at the molecular level, and therefore the changes in the close environment of the NPs (such as the protein adsorption) can be investigated using this technique. Water was taken as the reference for all samples.

DLS and Zeta Potentia Measurements. The hydrodynamic size and surface charge of the AuNPs before and after incubation in cCCM were determined by Dynamic Light Scattering (number mean) and Laser Doppler Anemometry, respectively, using a Zetasizer Nano ZS instrument equipped with a light source wavelength of 532 nm and a fixed scattering angle of 173°. Aliquots (0.8 mL) of the colloidal NP solutions were placed into specific plastic cuvettes and the software was arranged with the parameters of refractive index and adsorption coefficient of gold, and solvent viscosity of water at 25 °C. Each value was the average of at least 3 independent measurements.

■ ASSOCIATED CONTENT

ⓢ Supporting Information

The Supporting Information is available free of charge on the ACS Publications website at DOI: 10.1021/acs.bioconj-chem.6b00575.

> Full characterization of the cell culture media by UV−vis spectroscopy, dynamic light scattering and zeta potential, verification of the excess of proteins compared to the surface area of the nanoparticles, and detailed purification steps of the particles (PDF)

■ AUTHOR INFORMATION

Corresponding Author

*E-mail: victor.puntes@icn2.cat.

ORCID ⊙

Neus G. Bastús: 0000-0002-3144-7986

Notes

The authors declare no competing financial interest.

■ ACKNOWLEDGMENTS

Bioconjugate Chemistry   Article

■ REFERENCES

(1) Sperling, R. A., Rivera Gil, P., Zhang, F., Zanella, M., and Parak, W. J. (2008) Biological applications of gold nanoparticles. *Chem. Soc. Rev. 37*, 1896–1908.

(2) Ghosh, P., Han, G., De, M., Kim, C. K., and Rotello, V. M. (2008) Gold nanoparticles in delivery applications. *Adv. Drug Delivery Rev. 60*, 1307–15.

(3) Krug, H. F. (2014) Nanosafety Research-Are We on the Right Track? *Angew. Chem., Int. Ed. 53*, 12304–12319.

(4) Nel, A. E., Madler, L., Velegol, D., Xia, T., Hoek, E. M., Somasundaran, P., Klaessig, F., Castranova, V., and Thompson, M. (2009) Understanding biophysicochemical interactions at the nano-bio interface. *Nat. Mater. 8*, 543–57.

(5) Moyano, D. F., and Rotello, V. M. (2011) Nano Meets Biology: Structure and Function at the Nanoparticle Interface. *Langmuir 27*, 10376–10385.

(6) Saptarshi, S. R., Duschl, A., and Lopata, A. L. (2013) Interaction of nanoparticles with proteins: relation to bio-reactivity of the nanoparticle. *J. Nanobiotechnol. 11*, 26.

(7) Cedervall, T., Lynch, I., Lindman, S., Berggard, T., Thulin, E., Nilsson, H., Dawson, K. A., and Linse, S. (2007) Understanding the nanoparticle-protein corona using methods to quantify exchange rates and affinities of proteins for nanoparticles. *Proc. Natl. Acad. Sci. U. S. A. 104*, 2050–2055.

(8) Walkey, C. D., Olsen, J. B., Song, F., Liu, R., Guo, H., Olsen, D. W. H., Cohen, Y., Emili, A., and Chan, W. C. W. (2014) Protein Corona Fingerprinting Predicts the Cellular Interaction of Gold and Silver Nanoparticles. *ACS Nano 8*, 2439–2455.

(9) Hamad-Schifferli, K. (2015) Exploiting the novel properties of protein coronas: emerging applications in nanomedicine. *Nanomedicine 10*, 1663–1674.

(10) Casals, E., and Puntes, V. F. (2012) Inorganic nanoparticle biomolecular corona: formation, evolution and biological impact. *Nanomedicine (London, U. K.) 7*, 1917–30.

(11) Mahmoudi, M., Lynch, I., Ejtehadi, M. R., Monopoli, M. P., Bombelli, F. B., and Laurent, S. (2011) Protein−Nanoparticle Interactions: Opportunities and Challenges. *Chem. Rev. 111*, 5610–5637.

(12) Wilson, C. J., Clegg, R. E., Leavesley, D. I., and Pearcy, M. J. (2005) Mediation of biomaterial-cell interactions by adsorbed proteins: a review. *Tissue Eng. 11*, 1–18.

(13) Monopoli, M. P., Aberg, C., Salvati, A., and Dawson, K. A. (2012) Biomolecular coronas provide the biological identity of nanosized materials. *Nat. Nanotechnol. 7*, 779–786.

(14) Walczyk, D., Bombelli, F. B., Monopoli, M. P., Lynch, I., and Dawson, K. A. (2010) What the Cell "Sees" in Bionanoscience. *J. Am. Chem. Soc. 132*, 5761–5768.

(15) Tenzer, S., Docter, D., Kuharev, J., Musyanovych, A., Fetz, V., Hecht, R., Schlenk, F., Fischer, D., Kiouptsi, K., Reinhardt, C., et al. (2013) Rapid formation of plasma protein corona critically affects nanoparticle pathophysiology. *Nat. Nanotechnol. 8*, 772–U1000.

(16) Saha, K., Rahimi, M., Yazdani, M., Kim, S. T., Moyano, D. F., Hou, S., Das, R., Mout, R., Rezaee, F., Mahmoudi, M., et al. (2016) Regulation of Macrophage Recognition through the Interplay of Nanoparticle Surface Functionality and Protein Corona. *ACS Nano 10*, 4421–4430.

(17) Salvati, A., Pitek, A. S., Monopoli, M. P., Prapainop, K., Bombelli, F. B., Hristov, D. R., Kelly, P. M., Aberg, C., Mahon, E., and Dawson, K. A. (2013) Transferrin-functionalized nanoparticles lose their targeting capabilities when a biomolecule corona adsorbs on the surface. *Nat. Nanotechnol. 8*, 137–143.

(18) Jiang, Y., Wang, M., Hardie, J., Tonga, G. Y., Ray, M., Xu, Q. B., and Rotello, V. M. (2016) Chemically Engineered Nanoparticle-Protein Interface for Real-Time Cellular Oxidative Stress Monitoring. *Small 12*, 3775–3779.

(19) Corbo, C., Molinaro, R., Parodi, A., Furman, N. E. T., Salvatore, F., and Tasciotti, E. (2016) The impact of nanoparticle protein corona on cytotoxicity, immunotoxicity and target drug delivery. *Nanomedicine 11*, 81–100.

(20) Miclaus, T., Beer, C., Chevallier, J., Scavenius, C., Bochenkov, V. E., Enghild, J. J., and Sutherland, D. S. (2016) Dynamic protein coronas revealed as a modulator of silver nanoparticle sulphidation in vitro. *Nat. Commun. 7*, 11770.

(21) Saha, K., Moyano, D. F., and Rotello, V. M. (2014) Protein coronas suppress the hemolytic activity of hydrophilic and hydrophobic nanoparticles. *Mater. Horiz. 1*, 102–105.

(22) Maiorano, G., Sabella, S., Sorce, B., Brunetti, V., Malvindi, M. A., Cingolani, R., and Pompa, P. P. (2010) Effects of Cell Culture Media on the Dynamic Formation of Protein−Nanoparticle Complexes and Influence on the Cellular Response. *ACS Nano 4*, 7481–7491.

(23) Monopoli, M. P., Walczyk, D., Campbell, A., Elia, G., Lynch, I., Baldelli Bombelli, F., and Dawson, K. A. (2011) Physical−Chemical Aspects of Protein Corona: Relevance to in Vitro and in Vivo Biological Impacts of Nanoparticles. *J. Am. Chem. Soc. 133*, 2525–2534.

(24) Casals, E., Pfaller, T., Duschl, A., Oostingh, G. J., and Puntes, V. F. (2011) Hardening of the Nanoparticle-Protein Corona in Metal (Au, Ag) and Oxide (Fe3O4, CoO, and CeO2) Nanoparticles. *Small 7*, 3479–3486.

(25) Tenzer, S., Docter, D., Rosfa, S., Wlodarski, A., Kuharev, J., Rekik, A., Knauer, S. K., Bantz, C., Nawroth, T., Bier, C., et al. (2011) Nanoparticle Size Is a Critical Physicochemical Determinant of the Human Blood Plasma Corona: A Comprehensive Quantitative Proteomic Analysis. *ACS Nano 5*, 7155–7167.

(26) Walkey, C. D., Olsen, J. B., Guo, H., Emili, A., and Chan, W. C. W. (2012) Nanoparticle Size and Surface Chemistry Determine Serum Protein Adsorption and Macrophage Uptake. *J. Am. Chem. Soc. 134*, 2139–2147.

(27) Casals, E., Pfaller, T., Duschl, A., Oostingh, G. J., and Puntes, V. (2010) Time Evolution of the Nanoparticle Protein Corona. *ACS Nano 4*, 3623–3632.

(28) Gessner, A., Waicz, R., Lieske, A., Paulke, B. R., Mader, K., and Muller, R. H. (2000) Nanoparticles with decreasing surface hydrophobicities: influence on plasma protein adsorption. *Int. J. Pharm. 196*, 245–249.

(29) Slack, S. M., and Horbett, T. A. (1995) The Vroman Effect, in *Proteins at Interfaces II*, pp 112–128, American Chemical Society.

(30) Hill, H. D., Millstone, J. E., Banholzer, M. J., and Mirkin, C. A. (2009) The Role Radius of Curvature Plays in Thiolated Oligonucleotide Loading on Gold Nanoparticles. *ACS Nano 3*, 418–424.

(31) Walkey, C. D., and Chan, W. C. W. (2012) Understanding and controlling the interaction of nanomaterials with proteins in a physiological environment. *Chem. Soc. Rev. 41*, 2780–2799.

(32) Cedervall, T., Lynch, I., Foy, M., Berggard, T., Donnelly, S. C., Cagney, G., Linse, S., and Dawson, K. A. (2007) Detailed identification of plasma proteins adsorbed on copolymer nanoparticles. *Angew. Chem., Int. Ed. 46*, 5754–5756.

(33) Dobrovolskaia, M. A., Patri, A. K., Zheng, J., Clogston, J. D., Ayub, N., Aggarwal, P., Neun, B. W., Hall, J. B., and McNeil, S. E. (2009) Interaction of colloidal gold nanoparticles with human blood: effects on particle size and analysis of plasma protein binding profiles. *Nanomedicine 5*, 106–117.

(34) Mahmoudi, M., Lohse, S. E., Murphy, C. J., Fathizadeh, A., Montazeri, A., and Suslick, K. S. (2014) Variation of Protein Corona Composition of Gold Nanoparticles Following Plasmonic Heating. *Nano Lett. 14*, 6–12.

(35) Deng, Z. J., Liang, M. T., Toth, I., Monteiro, M., and Minchin, R. F. (2012) Plasma protein binding of positively and negatively charged polymer-coated gold nanoparticles elicits different biological responses. *Nanotoxicology 7*, 314–322.

(36) Lundqvist, M., Stigler, J., Elia, G., Lynch, I., Cedervall, T., and Dawson, K. A. (2008) Nanoparticle size and surface properties determine the protein corona with possible implications for biological impacts. *Proc. Natl. Acad. Sci. U. S. A. 105*, 14265–14270.

(37) Ehrenberg, M. S., Friedman, A. E., Finkelstein, J. N., Oberdorster, G., and McGrath, J. L. (2009) The influence of protein adsorption on nanoparticle association with cultured endothelial cells. *Biomaterials 30*, 603–610.

(38) Gessner, A., Lieske, A., Paulke, B. R., and Muller, R. H. (2003) Functional groups on polystyrene model nanoparticles: Influence on protein adsorption. *J. Biomed. Mater. Res., Part A 65*, 319–326.

(39) Sund, J., Alenius, H., Vippola, M., Savolainen, K., and Puustinen, A. (2011) Proteomic Characterization of Engineered Nanomaterial-Protein Interactions in Relation to Surface Reactivity. *ACS Nano 5*, 4300–4309.

(40) Deng, Z. J., Mortimer, G., Schiller, T., Musumeci, A., Martin, D., and Minchin, R. F. (2009) Differential plasma protein binding to metal oxide nanoparticles. *Nanotechnology 20*, 455101.

(41) Roecker, C., Poetzl, M., Zhang, F., Parak, W. J., and Nienhaus, G. U. (2009) A quantitative fluorescence study of protein monolayer formation on colloidal nanoparticles. *Nat. Nanotechnol. 4*, 577–580.

(42) Treuel, L., Brandholt, S., Maffre, P., Wiegele, S., Shang, L., and Nienhaus, G. U. (2014) Impact of Protein Modification on the Protein Corona on Nanoparticles and Nanoparticle-Cell Interactions. *ACS Nano 8*, 503–513.

(43) Bastus, N. G., Sanchez-Tillo, E., Pujals, S., Farrera, C., Lopez, C., Giralt, E., Celada, A., Lloberas, J., and Puntes, V. (2009) Homogeneous conjugation of peptides onto gold nanoparticles enhances macrophage response. *ACS Nano 3*, 1335–44.

(44) Banerjee, T., Mitra, S., Singh, A. K., Sharma, R. K., and Maitra, A. (2002) Preparation, characterization and biodistribution of ultrafine chitosan nanoparticles. *Int. J. Pharm. 243*, 93–105.

(45) Choi, H. S., Liu, W., Misra, P., Tanaka, E., Zimmer, J. P., Ipe, B. I., Bawendi, M. G., and Frangioni, J. V. (2007) Renal clearance of quantum dots. *Nat. Biotechnol. 25*, 1165–1170.

(46) Gebauer, J. S., Malissek, M., Simon, S., Knauer, S. K., Maskos, M., Stauber, R. H., Peukert, W., and Treuel, L. (2012) Impact of the Nanoparticle–Protein Corona on Colloidal Stability and Protein Structure. *Langmuir 28*, 9673–9679.

(47) Piella, J., Bastús, N. G., and Puntes, V. (2016) Size-Controlled Synthesis of Sub-10-nanometer Citrate-Stabilized Gold Nanoparticles and Related Optical Properties. *Chem. Mater. 28*, 1066–1075.

(48) Bastús, N. G., Comenge, J., and Puntes, V. F. (2011) Kinetically Controlled Seeded Growth Synthesis of Citrate-Stabilized Gold Nanoparticles of up to 200 nm: Size Focusing versus Ostwald Ripening. *Langmuir 27*, 11098–11105.

(49) Goy-López, S., Juárez, J., Alatorre-Meda, M., Casals, E., Puntes, V. F., Taboada, P., and Mosquera, V. (2012) Physicochemical Characteristics of Protein–NP Bioconjugates: The Role of Particle Curvature and Solution Conditions on Human Serum Albumin Conformation and Fibrillogenesis Inhibition. *Langmuir 28*, 9113–9126.

(50) Comenge, J., and Puntes, V. (2015) Role of PEG Conformation in Mixed Layers: From Protein Corona Substrate to Steric Stabilization Avoiding Protein Adsorption. *Science Open Research 2015 (3)*, 1–10.

(51) Dominguez-Medina, S., McDonough, S., Swanglap, P., Landes, C. F., and Link, S. (2012) In Situ Measurement of Bovine Serum Albumin Interaction with Gold Nanospheres. *Langmuir 28*, 9131–9139.

(52) Casals, E., Pfaller, T., Duschl, A., Oostingh, G. J., and Puntes, V. (2010) Time evolution of the nanoparticle protein corona. *ACS Nano 4*, 3623–32.

(53) Saha, K., Agasti, S. S., Kim, C., Li, X., and Rotello, V. M. (2012) Gold Nanoparticles in Chemical and Biological Sensing. *Chem. Rev. 112*, 2739–2779.

(54) Lévy, R., Thanh, N. T. K., Doty, R. C., Hussain, I., Nichols, R. J., Schiffrin, D. J., Brust, M., and Fernig, D. G. (2004) Rational and Combinatorial Design of Peptide Capping Ligands for Gold Nanoparticles. *J. Am. Chem. Soc. 126*, 10076–10084.

(55) Zook, J. M., MacCuspie, R. I., Locascio, L. E., Halter, M. D., and Elliott, J. T. (2011) Stable nanoparticle aggregates/agglomerates of different sizes and the effect of their size on hemolytic cytotoxicity. *Nanotoxicology 5*, 517–530.

(56) Bastús, N. G., Piella, J., and Puntes, V. (2016) Quantifying the Sensitivity of Multipolar (Dipolar, Quadrupolar, and Octapolar) Surface Plasmon Resonances in Silver Nanoparticles: The Effect of Size, Composition, and Surface Coating. *Langmuir 32*, 290.

(57) Alaeddine, S., and Nygren, H. (1995) Logarithmic Growth of Protein Films, in *Proteins at Interfaces II*, pp 41–51, American Chemical Society.

(58) Tsai, D.-H., DelRio, F. W., Keene, A. M., Tyner, K. M., MacCuspie, R. I., Cho, T. J., Zachariah, M. R., and Hackley, V. A. (2011) Adsorption and Conformation of Serum Albumin Protein on Gold Nanoparticles Investigated Using Dimensional Measurements and in Situ Spectroscopic Methods. *Langmuir 27*, 2464–2477.

(59) Brewer, S. H., Glomm, W. R., Johnson, M. C., Knag, M. K., and Franzen, S. (2005) Probing BSA Binding to Citrate-Coated Gold Nanoparticles and Surfaces. *Langmuir 21*, 9303–9307.

Supporting information for:

Size-dependent Protein-Nanoparticle Interactions in Citrate-stabilized Gold Nanoparticles: The Emergence of the Protein Corona.

Jordi Piella, Neus G. Bastús and Víctor Puntes

Table of Contents

1

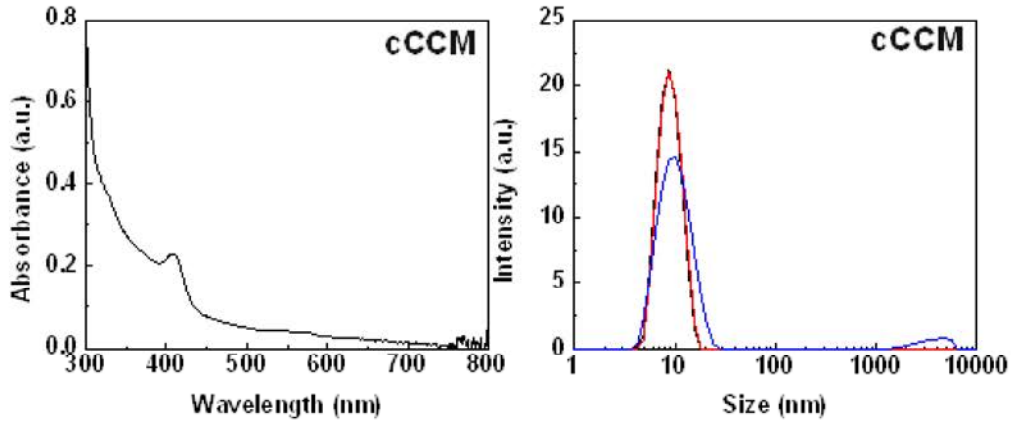## 1. Characterization of complete cell culture media (cCCM)

Figure S1. Characterization of complete cell culture media (cCCM): DMEM supplemented with 10% of FBS. UV-vis spectrum (left) shows a strong absorbance in the region below 500 nm, while almost no absorbance is observed above this value, where the Localized Surface Plasmon Resonance peak characteristic of the AuNPs is usually located. Dynamic light scattering plot (DLS) (right) of the cCCM displaying an intense peak in the region between 5 and 15 nm attributed to the proteins. This peak may overlap with the AuNPs peak if they have not been previously purified. Finally, the zeta potential of the cCCM results in -11.2 ± 0.9 mV which is characteristic of the slightly negative charge of most of the proteins.

2. Excess of proteins in cCCM compared to the total surface area of AuNPs

For a specific colloidal solution of AuNPs, the average NP diameter ($\bar{D}$), average NP surface area ($\bar{S}$) and average NP mass ($\bar{M}$) can be calculated from the size distribution obtained by TEM analysis:

$$\bar{D}\left(\frac{cm^2}{NP}\right) = \frac{\sum D_n{}^2}{n} \tag{1}$$

$$\bar{S}\left(\frac{cm^2}{NP}\right) = \frac{\pi}{4}\frac{\sum D_n{}^2}{n} \tag{2}$$

$$\bar{M}\left(\frac{mols}{NP}\right) = \bar{V}_{NP}\delta M_W = \frac{4}{3}\frac{\sum\left(\frac{D_n}{2}\right)^3}{n}\delta M_W \tag{3}$$

where n and D_n are the number and diameter of the particles that has been counted by TEM (at least 500 NPs are needed for a representative population), δ is the density of gold, 19.3 g/mL,

2

and M_w the molecular weight, MW 197. Notice that a common error is to calculate $\bar{S}$ and $\bar{M}$ from $\bar{D}$ (the polydispersity degree of the particles is erroneously omitted in this case). Finally, the concentration of gold (C_{Au}), obtained either from the concentration of precursor used in the synthesis of the particles and the yield of the reaction or by ICP-MS, can be translated to the number of NPs and the surface area in solution as follow:

$$number\ of\ NPs\ \left(\frac{NP}{L}\right) = concentration\ of\ Au\ (M) \cdot \frac{1}{\bar{M}} \left(\frac{mol}{NP}\right)^{-1} \quad (4)$$

$$surface\ area\ \left(\frac{cm^2}{L}\right) = number\ of\ NP \left(\frac{NP}{L}\right) \cdot \bar{S} \left(\frac{cm^2}{NP}\right) \quad (5)$$

The total surface area in a standard synthesis procedure range from 2 to 30 cm^2/mL, which corresponds to ~10^9 NPs/mL for the larger particles (150 nm) and to ~10^{13} for the smallest ones (3.5 nm).

On the other hand, the total number of proteins in cCCM is at least three orders of magnitude larger than that of the particles in solution. The total surface area they can cover upon adsorption on a surface is the result of multiplying their cross section (CS) for their concentration (C):

$$area_{proteins}\ \left(\frac{cm^2}{L}\right) = \Sigma \left(C_{protein} \cdot CS_{protein}\right) \quad (6)$$

For example, the triangular CS of the BSA in the folded conformation has been previously estimated to be 32 nm^2 = 32·10^{-14} cm^2 while their concentration in the cCMM is around 6·10^{16} (0.1 mM). This represents enough BSA in the cCCM to cover a total area of 19300 (cm^2/mL); at least more than 5 10^2 times higher than that needed to fully surround the AuNPs surface in solution. Thus, it is reasonable to consider the number of proteins in the cCCM largely in excess with respect to the AuNPs, even if more than one layer of proteins is adsorbed on the surface of the particles, and the fraction depleted from the medium upon adsorption insignificant.

3

3. Number of washing steps for a proper DLS characterization

cCCM free of NPs gives a background peak in the range of 5-15 nm by DLS (see section 1), which is comparable to the hydrodynamic size of the small AuNPs used in the experiments here presented. Consequently, interferences from the unbounded proteins in solution when measuring the hydrodynamic size of the AuNPs by DLS is something that should not be ruled out if the particles has not been previously washed and dispersed in a solution free of proteins.

The interferences that free proteins in solution may induce to the DLS measurements[1] can be estimated from their respective abilities to scatter light assuming Rayleigh scattering properties, in which scattering intensity of a specific molecule is proportional to its number in solution (N) and its size raised to the six power (D^6):

$$I \propto \varepsilon\, N\, D^6 \tag{7}$$

where ε is the refractive index for each molecule. The relative contributions of the unbounded proteins with respect to the AuNPs can be then quantified by defining a dimensionless parameter (γ) as follow:

$$\gamma = \frac{I_{NP}}{I_p} = \frac{\varepsilon_{NP} N_{NP} D_{NP}{}^6}{\sum \varepsilon_P N_P D_P{}^6} = \frac{0.47 N_{NP} D_{NP}{}^6}{\sum \varepsilon_P N_P D_P{}^6} \tag{8}$$

where the refractive index for AuNP is $\varepsilon_{NP} = 0.47$, while the ε_P is ~ 1.5 for proteins. Previous studies with BSA have demonstrated that γ should be at least > 0.1 to avoid the contributions of free proteins in the DLS measurements.[1]

In this regard, rough calculations based on the approximate BSA concentration in cCCM ($6\cdot10^{16}$ NP/mL, HD 7 nm and $\varepsilon_P = 1.447$), demonstrated that $\gamma \ll 0.1$ for AuNPs of 3.6 nm in the range of concentration here working (10^{13} NP/mL) and at least 2 cycles of washing were needed to avoid the contribution of unbound proteins (note that each washing step consist on replacing 980 uL of supernatant from a 1000 uL of solution decreasing the concentration of proteins in

4

solution by a factor of 50x). Indeed, based on the previous approximation the concentration of these particles should be in the range of $1 \cdot 10^{18}$ to be properly measured in cCCM without requiring any washing step. On the other hand, γ already approach to that of 0.1 for AuNP of 60 nm at any concentration larger than $4 \cdot 10^{10}$, which is in the range of working concentration in our experiments. In agreement with that, DLS plot showed monomodal curves even in the absence of any washing steps for large NPs (Figure S2-S3).

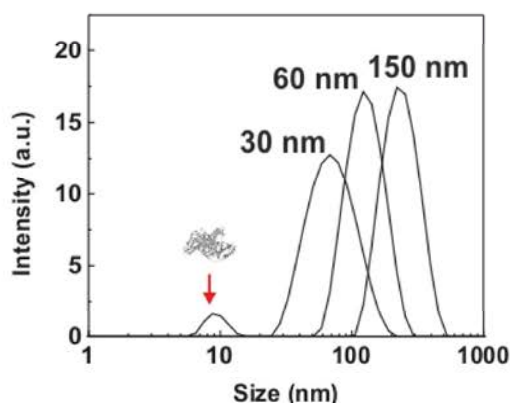**Figure S2. DLS plot of AuNPs measured in cCCM without purification of the particles.** Particles of 60 nm and 150 nm show a monomodal curve, while particle of 30 nm, and below, present a bimodal curve due to interferences from unbound proteins in the medium.
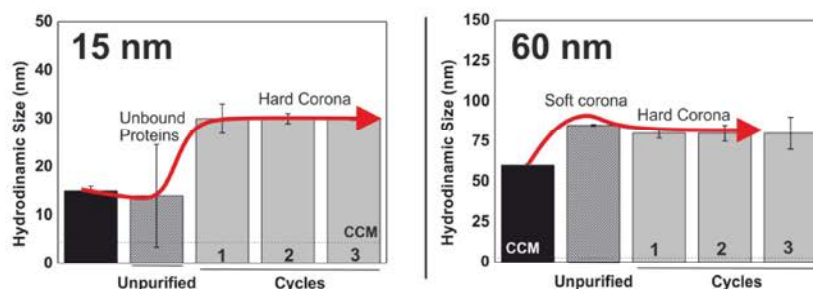

Figure S3. Number of cycles needed to reach stationary values. Small particles need at least 2 cycles, while larger particles only one.

5

4. Maximum number of proteins per NP considering a monolayer coating

The theoretical available number of binding sites for a monolayer coverage of proteins (considering BSA as a model protein) on AuNP with a diameter (D) is estimated by dividing the surface area of the NP by the triangular cross section of the folded BSA (32 nm^2): [2]

$$\frac{BSA}{NP} = \frac{CS_{BSA}}{\pi D^2} = \frac{32}{\pi D^2} \tag{9}$$

References

(1)   Tsai, D.-H., DelRio, F. W., Keene, A. M., Tyner, K. M., MacCuspie, R. I., Cho, T. J., Zachariah, M. R., and Hackley, V. A. (2011) Adsorption and Conformation of Serum Albumin Protein on Gold Nanoparticles Investigated Using Dimensional Measurements and in Situ Spectroscopic Methods. *Langmuir 27*, 2464-2477.

(2)   Dominguez-Medina, S., McDonough, S., Swanglap, P., Landes, C. F., and Link, S. (2012) In Situ Measurement of Bovine Serum Albumin Interaction with Gold Nanospheres. *Langmuir 28*, 9131-9139.

6

Appendix A:

Towards reproducible testing of nanoparticles: sources of variability

In order to fulfil future expectations, especially for medical or investigation purposes, attention must be paid to the preparation and characterization of nanomaterials in order to improve reproducibility. In this chapter, the main drawbacks associated with the synthesis, characterization and handling of NPs are discussed along with some recommendations on how to obtain reliable and reproducible results.

A.1. Introduction

During the past two decades, improvements in both synthetic routes and characterization methods have enabled the use of nanoparticles (NPs) in highly complex biological assessments for both nanomedical research and nanospecific toxicity (see Chapter 1). However, even for stable and monodisperse NP solutions, experimental results have shown large discrepancies between assays performed across different laboratories [1]. This lack in consistency could be related to either variations in particle preparation or post synthetic processing, which has led to calls for increased harmonisation and minimum characterization to validate nanomedical and nanotoxicological research [2]. In the development of novel nanocatalytic platforms similar guidelines apply, where to understand catalytic performance of nanomaterials a sound knowledge of NP structure and surface state is required. Given the many recognised potential advantages of NPs in the fields of medicine and materials, there is currently a debate among experts concerning the need for improving reproducibility, including more accuracy in reporting of reliable and systematic results alongside adequate physical characterization [3-5].

There are several reasons why complete reproducibility has not been achieved in the field of nanotechnology, despite the inherent desire of most research groups to perform high-quality research [6-8]. First, NPs require specific preparation and analysis methods that are new to some disciplines and researchers. Second, because of the multidisciplinary nature of the field, not every research team has access to the range of characterization tools needed to obtain potentially important information. Third, nanoscience and nanotechnology still suffer from gaps between disciplines, particularly in biological contexts where the effect of NPs are typically investigated using relatively undefined samples, with large polydispersity, limited colloidal stability and unknown chemistry. The widespread definition of NPs, which ranges from suspended ultrafine particles to engineered supported nanomaterials, further confounds this problem.

The following section examines the main challenges associated with the synthesis, characterization and handling of colloidal NPs along with some recommendations on how to obtain reliable and reproducible results. This knowledge has been gained and implemented during research for the present thesis and associated publications.

A.2. Nanoparticle synthesis

The core of NP research starts with controlled synthesis. Traditionally, in wet chemistry, synthetic processes have been designed to work at high concentrations, where environmental alterations and fluctuations are less critical. However, at high concentrations, colloidal NPs are unstable and their morphological control challenging. Therefore, NPs are usually synthetized at low concentrations [9]. Under these conditions, three main parameters have been identified as critical in achieving reproducibility: (i) reaction time, (ii) thermal gradients, and (iii) mass gradients.

A.2.1. Reaction time

The formation processes of monodisperse NPs mainly experience two stages: the nucleation, aggregation of atoms to form thermodynamically stable small clusters (i.e., nuclei), followed by growth of these clusters by atom addition [10] (see Chapter 3). In the early stages of this process, the conversion yield is rather low and a mixture of small NPs and a fraction of polycrystalline shapeless particle-complexes are usually detected in solution. A clear example is the synthesis of colloidal Au NPs by the well-known Turkevich method, in which the solution turns first to dark purple before acquiring the typical ruby red color, what indicates the formation of different intermediate complexes [11]. Polydispersity of the primary formed NPs is also relatively high at this point since particle size distribution has not yet been refined by the subsequent growth process, the so called *size-focusing* process [12]. However, once the reaction has finished, if it is overextended, Ostwald Ripening, interparticle growth and other related processes may start to deteriorate the morphology and size distribution of the NPs, the so called *defocusing* process [12]. Moreover, degradation of the stabilizer at high temperatures for prolonged times may also result in a fraction of aggregates. Hence, stopping the reaction at the right point, either by precipitating the NPs out of the solution or by quickly decreasing the temperature, is critical in achieving reproducibility. In this regard, in all the synthesis developed during the thesis (see **Chapters 2** and **3**), the NP formation process was carefully monitored along different reaction times.

A common mistake when determining reaction time is to assume that it has a constant value. It should not be forgotten that time is just an empirical tool used to

estimate the state of the NPs. The reaction will not always finish at the same time as there are so many variables involved, especially when syntheses are performed in different laboratories and by different researchers. For example, in Catalunya, laboratories are quite cold because they are air conditioned, while in Norway they are quite hot because they are heated even in summer. Stopping the reaction based on the properties of the NPs has been proven to cause much less variability than when based on timing. This is especially relevant in the synthesis of anisotropic structures that tend to be thermodynamically unstable. For example, in the synthesis of silver cubes, overcooking the solution results in their transformation to polyhedral shapes and finally to spheres [13]. In this regard, the formation of metal NPs can be quickly monitored *in-situ* according, for example, to their chromatic and plasmonic properties, and the formation of quantum dots by virtue of their fluorescence.

Finally, the transition time, which can be defined as the time taken to move the NPS from reactive to "non-reactive" conditions, is another important point usually ignored in the synthesis. During these intermediate conditions, NPs continue evolving and thus the time they remain in transition conditions will impact their final state. In order to reduce variability, practices that are often considered trivial and usually unreported in the protocols should be carefully reported, for example, specifying whether the temperature was reduced by disconnecting the heater or immersing the sample in ice; or whether the sample was purified by centrifugation (fast) or dialysis (slow).

A.2.2. Thermal and mass gradients

Other synthetic considerations, owing to coupled thermodynamically and kinetically controlled processes in play during NP formation, include thermal and mass gradients.

Thermal gradients: Temperature (together with monomer concentration and surface free energy) has the largest effect on the nucleation rate of NPs [10]. High temperatures tend to increase the nucleation rate and the formation of a large number of small NPs while low temperature promotes growth over nucleation resulting in a lower number of larger NPs. Therefore, temperature regulators are commonly used for size and size dispersion control in many syntheses (see chapter 3 and 4). However, for the same reason, inhomogeneity and fluctuations in the temperature may induce internal variations

in the nucleation rate that can ultimately increase sample polydispersity. In this respect, syntheses performed in small volumes, where most of the sample is near to the edges of the reactor vessel, tend to be poorly reproducible due to their high susceptibility to thermal fluctuations. Similarly, an inefficient heater may increase thermal fluctuations and non-reproducibility. As a result, syntheses should be performed under a powerful heating source, at a high stirring rate and in an optimal reactor to ensure a homogeneous and constant temperature throughout the volume. The heater needs to be able to respond quickly to temperature changes and the thermal conductivity of the reactor vessel should also be considered because reduction-decomposition-nucleation reactions are normally endothermic and heat absorption varies during synthesis. Of course, this not apply if the synthesis is performed at room temperature.

Mass gradients: Similar principles to those discussed for temperature also apply to monomer concentration. Inhomogeneities in monomer concentration and mass gradients can induce internal variations in the nucleation rate of NPs that will eventually increase sample polydispersity. Therefore, a high stirring rate of the reaction mixture is desirable in order to facilitate good homogenization of reagents and reduce mass gradients. Particularly critical is the method of adding the precursor solution to the reaction solution when nucleation is faster than solute homogeneization, (burst nucleation at high temperature). In these cases, a fast injection tends to advantage nucleation, resulting in a high number of small NPs, while a slow injection promotes growth over nucleation, since the degree of supersaturation remains at low values, which results in a fewer number of larger NPs for similar reaction yields. Similarly, the effect of injecting a small volume of a highly concentrated precursor solution will be different from that of a large volume of a diluted one. The mixing conditions and the way the reagents are added are certainly some of the most relevant factors in the synthesis of colloidal NPs but are still often ignored and poorly described in most of the reported protocols.

The above considerations are in line with the results obtained after scaling up various synthetic protocols in our laboratories, where the higher thermal inertia of large volumes combined with turbulent stirring and a less fraction of the sample in the boundaries of the reactor were considered the most plausible reasons for enhanced reproducibility (**Figure A.1**). At this point, however, one faces a hypothetical contradiction. The synthesis of monodisperse NPs has been designed on the basis of a

burst nucleation, for which a fast conversion rate is required. As a consequence, in most of the described protocols the formation of NPs is on the same or shorter time scale than that required for mixing the reagents, especially if they are in large volumes. Typically, injecting 10 mL of a precursor solution into the reaction solution requires times in the order of tens of seconds. Nucleation, however, starts after only a few seconds and, as a result, syntheses based on burst nucleation performed in batch reactors are difficult to scale beyond certain volumes (above 10's L). To overcome these limitations, synthetic strategies should seek monodispersity through thermodynamics rather than with kinetics, or use microfluidic reactors, which are an interesting alternative [14].
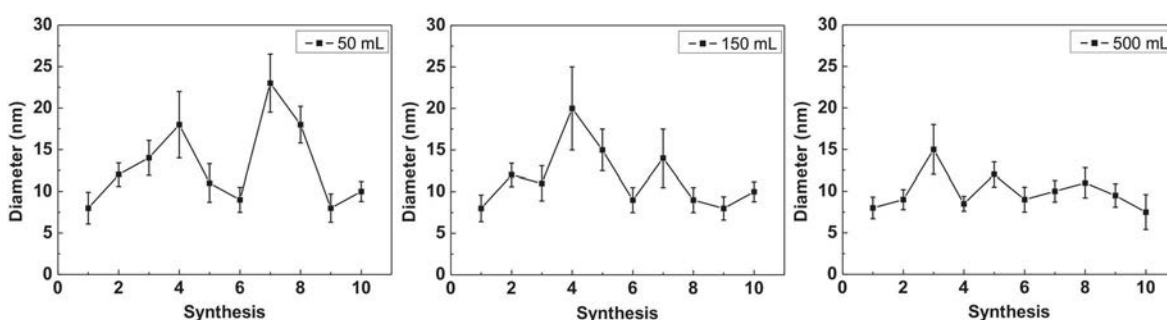

Figure A.1. Effect of reaction volume in the colloidal synthesis of nanoparticles. Mean size of citrate-stabilized Au NP seeds obtained following Bastús *et al.* protocol [15]. The protocol was scaled to different reaction volumes while all other parameters were kept constant. The reproducibility of the synthesis improved as the reaction volume increased in the studied range. Error bars indicate the size standard deviation from mean diameter.

A.2.3. Other general considerations

Apart from the previously discussed parameters, there are other general considerations in the synthesis of NPs that should not be forgotten in the search for reproducibility. For example, it is already known that some NPs can easily oxidize (see Chapter 1) and thus work under inert atmosphere is required. In fact, it is commonly mentioned in the experimental section of published papers whether the experiments was done under controlled atmosphere or not. However, what is often ignored in liquid phase syntheses is that solvent can also be affected by the atmosphere. For example, water, once out of the purification system, is no longer of "pure grade" as it absorbs oxygen and carbon dioxide that can cause changes in pH and oxidativity in a temperature and concentration dependent manner. IN this context, water, which is the most widely used analytical laboratory reagent, is probably the least well-characterized.

Emphasis should also be given to the impurities, cross contamination, the choice of the recipient and the cleaning of glassware [16]. Hopefully, variability of NPs synthetized "in the same" way will soon be reduced and protocoled in such a manner that production of these materials will become simple and robust as needed for development because, if reproducibility cannot be controlled, the future of e.g. nanomedicine will be in jeopardy. For now, it is responsibility of nanotechnologists to ensure that the protocols they develop are described in such detail that they can be reproduced and the resulting products are properly characterized.

A.3. Characterization techniques

Reproducibility and characterization are, in fact, two facets of the same issue, namely that the products of typical NP syntheses are a polydisperse collection of sizes and morphologies.[17] Polydispersity introduces difficulties in characterization, i.e. how many particles must be counted for statistical significance? And also in the definition of reproducible syntheses, i.e. which is more important, mean size or polydispersity? Research articles that neglect this facet of nanomaterials, and focus instead of reporting an average idealized particle, further confound the problem. When the distribution is provided, it typically does so with the assumption that the NPs conform to a symmetric Gaussian distribution. This assumption simplifies reporting by allowing for two parameters, the mean size and the standard deviation, to describe an entire size distribution, but relevant information is still missed. In order to properly characterize a set of NPs and avoid inconsistencies, the number of particles counted and detailed size distribution should always be included. Indeed, this is becoming a requirement in scientific journals such as *Chemical Communications* or *Nature Nano*.

At this point, however, a relevant issue arises when trying to measure the size distribution of the NPs. Different techniques may show different sensitivities to particle size [18]. Some of them, such as DLS, are more sensitive to large sizes, deviating the distribution to larger particles. Others techniques, such as XRD, tends to more easily detect the small particles since the full with at half maximum of the diffraction peaks increases with decreasing crystalline size. Similarly, an aggregate of particles with the same hydrodynamic size of a large single particle cannot be differentiated by DLS, but

these two nanostructures may present different optical signatures and show distinctive absorption bands that can be easily measured by UV-vis spectroscopy (**Figure A.2**). In this regard, a combination of corroborative and complementary characterization techniques is probably the best way to proceed. It is good practice to utilize techniques that describe both individual NPs as well as measuring bulk properties.
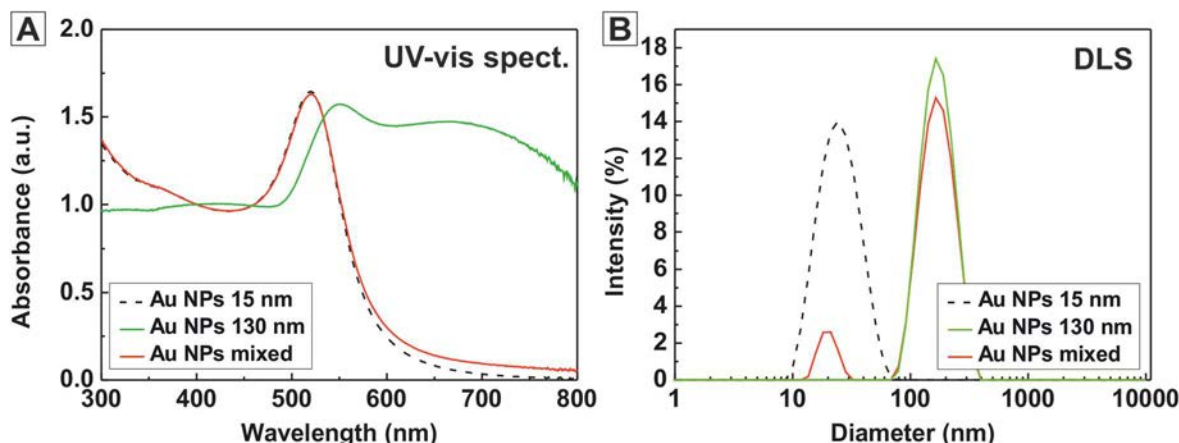

Figure A.2. Sensitivity of characterization techniques to particle size. (A) UV-vis spectra and (B) DLS measurements of solutions containing Au NPs of 15 nm, 130 nm and a mixture of both particles (98 % of 10 nm and 2 % of 130 nm by number). In contrast to the UV-vis spectroscopy, the DLS is strongly affected by the presence of a small fraction of large particles.

Another problem associated with characterization is that most of the techniques require energies that are roughly equal or even higher than those associated with the chemical stability of NPs [16]. One of the consequences is that NPs can be easily damaged during analysis. NPs have been observed to melt when exposed to an electron beam (e.g. Au NPs) [19], change oxidation state upon x-ray or electron beam irradiation (e.g. ceria NPs) [20] or sputter at enhanced rates (e.g. Pt NPs) [21]. A clear example of sample damage is found in **Chapter 2** of the present thesis. During TEM characterization of citrate stabilized sub-10 nm Au NPs, UV-vis spectroscopy showed a surface plasmon peak characteristic of small spherical Au NPs, while TEM images showed large aggregates and shapeless like particles. It took several attempts to demonstrate that the NPs were in fact highly monodisperse and perfectly stable in solution but that they had coalesced during TEM analysis due to electronic beam damage.

These and many other observations highlight the ease with which nanomaterials in various forms can be damaged during analysis, and how the extent of this damage is specific to the type of NPs. In addition, many characterization techniques require the

placing of samples in environments and forms (powder) that differ from those in which they are normally found (colloidal dispersion). This can alter the NPs and must be considered as part of the analysis [16, 17]. Last but not least, NPs are usually synthetized at diluted conditions (µg to mg) and the amount needed for a specific analysis (mg of g) may not be easy to collect in all cases.

A.4. Storage, transport and pre-testing preparation of nanoparticles

Because of their intrinsic instability (summarized in the Gibbs Thomson effect), NPs are susceptible to structural transformations, corrosion, oxidation, dissolving, aggregation and coalesce, which all can happen relatively fast. As a result, their properties and characteristics frequently alters with time, a process often called "aging" [22] (see for example **Chapter 3 Figure 3.7**). This time dependence can be influenced by the synthetic process, exposure to light, temperature, humidity and other aspects of sample environment. It is clear, for example, that the characterization of NPs a month or even weeks before application or use may not provide useful information, unless the reliability of the information is confirmed. Although this might seems a daunting challenge, the effect of "aging" can be substantially reduced under the right conditions. Understanding the changes a particle will undergo particular environmental conditions is useful for determining the time frame and handling requirements for a specific experiment. This was particularly important when comparing the optical, catalytically and surface properties of Au and Ag NPs of various sizes in Chapters 4-6. Additionally, keeping and reporting detailed records of the date of synthesis, storage time, conditions, and times of analysis may facilitate the understanding of similarities and differences between studies.

In this sense, and owing to the high susceptibility of NPs to the environment, samples should not be stored in a master batch, from which small aliquots are taken out when required. The repeated opening of the master batch is undesirable and can be a source of contamination. It is suggested, instead, to prepare and store the NPs in several small, pre-cleaned vials. This will minimize repeated exposure of the entire sample to the external environment. If NPs are susceptible to surface oxidation or surfactant degradation, once exposed to the environment, the remaining sample should be discarded and not stored again.

Issues associated with sample preparation also apply here. The scientific community is currently concerned about the critical role that sub products from the NP synthesis have on the final result [23]. For this reason, a purification post-processing step will be mandatory in the future for most NPs. Depending on when this purification step is done, right after synthesis or just before using them, the evolution of the NPs during this period can be different, thereby producing non-reproducible results. It is worth remembering that there is always a percentage of precursor not converted during the synthesis that is in chemical equilibrium with the NPs. When purifying the sample, this equilibrium is displaced and thus NPs may start to dissolve. In this regards, if most of the precursor has been consumed, keeping the NPs in the reaction media has been probed to help in their preservation [24]. As already mentioned, the reason is that while species from the reaction can affect later experiments, they also play an important role in the equilibrium and stability of the NPs in solution.

Finally, transformations and stability of the NPs in the working media during the time frame of the experiment should also be assessed. A clear example of this is found in **Chapter 6**, during incubation of Au NPs in cell culture media and must include the way the NPs are exposed to the media [25] (**Figure A.3**). It is important to realize that nanomaterials in general and NPs in particular may change in some ways if their local environment changes during incorporation into a biological system, or they are released to the environment. A well-defined dispersing protocol and monitoring of the particles in the working media should be mandatory to understand variability.
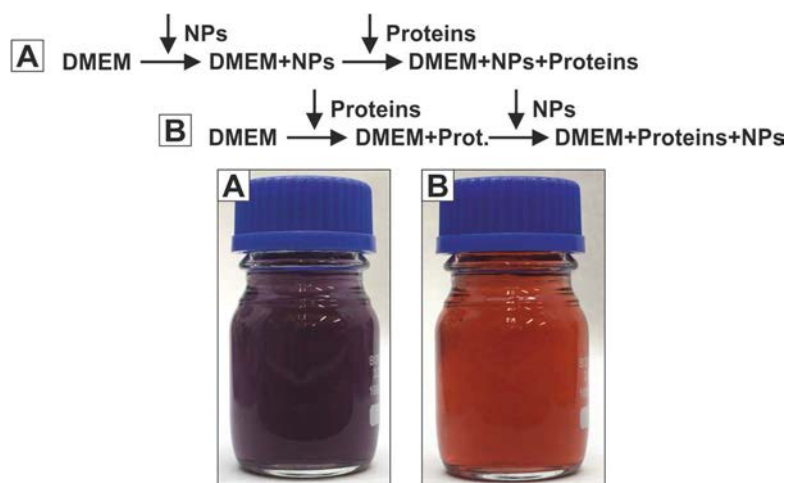

Figure A.3. Effect of the nanoparticle exposure conditions. Sequence of addition were: (A) Proteins to a solution containing DMEM and Au NPs. (B) Au NPs to a solution containing DMEM and proteins.

A.5. Conclusions

Several examples described in this section have illustrated the main drawbacks associated with NP synthesis, characterization and handling. Despite these challenges, it is important to empathise that the use of NPs has led to significant scientific and technological developments. The point is that in order to fulfil future expectations, especially for medical or investigation purposes, attention must be paid to the preparation and characterization of nanomaterials in order to improve reproducibility. In this respect, NPs should not be accepted unless they are accompanied with an accurate description of how and when they were synthetized, how and for how long they were stored, when they were characterized and which post-processing protocol was followed. In this way, the history of NPs can be maintained and possible similarities and sources of differences can be tracked if they are identified.

A.6. References

[1] Join the dialogue, Nature Nanotechnology 7 (2012) 545.

[2] F. Schrurs, D. Lison, Focusing the research efforts, Nature Nanotechnology 7 (2012) 546.

[3] G. Ozin, Nanochemistry Reproducibility, Advanced Science Newshttps://www.advancedsciencenews.com/nanochemistry-reproducibility/, 2013.

[4] A. Tropsha, *et al.*, Reproducibility, sharing and progress in nanomaterial databases, Nature Nanotechnology 12 (2017) 1111.

[5] Joining the reproducibility initiative, Nature Nanotechnology 9 (2014) 949.

[6] D. Langevin, *et al.*, Inter-laboratory comparison of nanoparticle size measurements using dynamic light scattering and differential centrifugal sedimentation, NanoImpact 10 (2018) 97-107.

[7] S. Mulhopt, *et al.*, Characterization of Nanoparticle Batch-To-Batch Variability, Nanomaterials (Basel, Switzerland) 8 (2018).

[8] G.J. Oostingh, *et al.*, Problems and challenges in the development and validation of human cell-based assays to determine nanoparticle-induced immunomodulatory effects, Particle and fibre toxicology 8 (2011) 8.

[9] P. Jongnam, *et al.*, Synthesis of Monodisperse Spherical Nanocrystals, Angewandte Chemie International Edition 46 (2007) 4630-4660.

[10] N.T.K. Thanh, *et al.*, Mechanisms of Nucleation and Growth of Nanoparticles in Solution, Chemical Reviews 114 (2014) 7610-7630.

[11] I. Ojea-Jimenez, *et al.*, Small Gold Nanoparticles Synthesized with Sodium Citrate and Heavy Water: Insights into the Reaction Mechanism, Journal of Physical Chemistry C 114 (2010) 1800-1804.

[12] X.G. Peng, *et al.*, Kinetics of II-VI and III-V colloidal semiconductor nanocrystal growth: "Focusing" of size distributions, Journal of the American Chemical Society 120 (1998) 5343-5344.

[13] Y. Wang, *et al.*, Synthesis of Ag Nanocubes 18–32 nm in Edge Length: The Effects of Polyol on Reduction Kinetics, Size Control, and Reproducibility, Journal of the American Chemical Society 135 (2013) 1941-1951.

[14] Z. Lei, X. Younan, Scaling up the Production of Colloidal Nanocrystals: Should We Increase or Decrease the Reaction Volume?, Advanced Materials 26 (2014) 2600-2606.

[15] N.G. Bastús, *et al.*, Kinetically Controlled Seeded Growth Synthesis of Citrate-Stabilized Gold Nanoparticles of up to 200 nm: Size Focusing versus Ostwald Ripening, Langmuir 27 (2011) 11098-11105.

[16] D.R. Baer, *et al.*, Surface characterization of nanomaterials and nanoparticles: Important needs and challenging opportunities, Journal of Vacuum Science & Technology. A, Vacuum, surfaces, and films : an official journal of the American Vacuum Society 31 (2013) 050820.

[17] E.J. Cho, *et al.*, Nanoparticle Characterization: State of the Art, Challenges, and Emerging Technologies, Molecular Pharmaceutics 10 (2013) 2093-2110.

[18] C.M. Hoo, *et al.*, A comparison of atomic force microscopy (AFM) and dynamic light scattering (DLS) methods to characterize nanoparticle size distributions, Journal of Nanoparticle Research 10 (2008) 89-96.

[19] Y. Chen, *et al.*, Sintering of Passivated Gold Nanoparticles under the Electron Beam, Langmuir 22 (2006) 2851-2855.

[20] F. Zhang, *et al.*, Cerium oxidation state in ceria nanoparticles studied with X-ray photoelectron spectroscopy and absorption near edge spectroscopy, Surface Science 563 (2004) 74-82.

[21] M.A. Asoro, *et al.*, Coalescence and sintering of Pt nanoparticles: in situ observation by aberration-corrected HAADF STEM, Nanotechnology 21 (2010) 025701.

[22] E. Izak-Nau, *et al.*, Impact of storage conditions and storage time on silver nanoparticles' physicochemical properties and implications for their biological effects, Rsc Advances 5 (2015) 84172-84185.

[23] A.M. Alkilany, C.J. Murphy, Toxicity and cellular uptake of gold nanoparticles: what we have learned so far?, Journal of Nanoparticle Research 12 (2010) 2313-2333.

[24] E. Casals, REACTIVITY AND IMPACT OF INORGANIC NANOPARTICLES IN BIOLOGICAL ENVIRONMENTS: BUILDING UP NANOSAFETY, BIOQUIMICA Y BIOLOGIA MOLECULAR, Universidad Autónoma de Barcelona, 2012.

[25] S. Rubio, Increasing the resolution at the nanobiointerface with engineering inorganic nanoparticles, Departament de Bioquímica i Biologia Molecular, Universitat Autònoma de Barcelona, 2016, pp. 214.

List of Publications

Articles published during the doctoral studies:

I. Ojea-Jiménez, <u>J. Piella</u>, T. L. Nguyen, A. Bestetti, A. D. Ryan and V. Puntes, Stability of polymer encapsulated quantum dots in cell culture media, *Journal of Physics: Conference Series* **2013**, *429*, 012009.

<u>J. Piella</u>, N.G. Bastús, E. Casals and V. Puntes, Characterizing Nanoparticles Reactivity: Structuer-Photocatalytic Activity Relationship, *Journal of Physics: Conference Series* **2013**, *429*, 012040.

N.G. Bastús, F. Merkoçi, <u>J. Piella</u> and V. Puntes, Synthesis of Highly Monodisperse Citrate-Stabilized Silver Nanoparticles of up to 200 nm: Kinetic Control and Catalytic Properties, *Chemistry of Materials* **2014**, *26*, 2836-2846.

C. Ichedef, F. Simonelli, U. Holzwarth, **J. Piella**, V. Puntes, *et al.*, Radiochemical syntheis of ^{105g}Ag-labelled silver nanoparticles, *Journal of Nanoparticle Research* **2014**, *13*, 2073.

N.G. Bastús, E. Gonzalez, J. Esteve, <u>J. Piella</u>, V. Puntes, et al., Exploring new synthetic strategies for the production of advanced complex inorganic nanocrystals, *Zeitshrift fur Physikalische Chemier* **2014**, *229,* 63-83.

<u>J. Piella</u>, N.G. Bastús and V. Puntes, Size-Controlled Synthesis of Sub-10-nanometer Citrate-Stabilized Gold Nanoparticles and Related Optical Properties, *Chemistry of Materials* **2016**, *28,* 1066-1075.

N.G. Bastús, <u>J. Piella</u> and V. Puntes, Quantifying the Sensitivity of Multipolar (Dipolar, Quadrupolar, and Octapolar) Surface Plasmon Resonances in Silver Nanoparticles: The Effect of Size, Composition, and Surface Coating, *Langmuir* **2016**, *32,* 290-300.

S. Makama, <u>J. Piella</u>, A. Undas, W.J. Dimmers, R. Peters, V. Puntes and N.W. van der Brink, Properties of silver nanoparticles influencing their uptake in and toxicity to the earthworm Lumbricus rubellus following exposure in soli, *Environmentaol Pollutoion* **2016***, 218*, 870-878.

S. Deville, B. Baré, <u>J. Piella</u>, K. Tirez, P. Hoet, M. P. Monopoli, K. A. Dawson, V. Puntes and I. Nelissen, Interaction of gold nanoparticles and nickel(II) sulfate affects dendritic cell maturation, *Nanotoxicology* **2016**, *10*, 1395-1403.

S. Kensei, K. Murali, Á. Czéh, <u>J. Piella</u>, V. Puntes, E. Madarász, Enhanced detection with spectral imaging fluorescence microscopy reveals tissue- and cell.type-specific compartimentalization of surface-modified polystirene nanoparticles, *Journal of Nanotoxicology* **2016**, *14,* 55.

<u>J. Piella</u>, F. Merkoçi, A. Genç, J. Arbiol, N.G. Bastús and V. Puntes, Probing the surface reactivity of nanocrystals by the catalytic degradation of organic dyes: the effect of size, surface chemistry and composition, *Journal of Materials Chemistry A* **2017**, *5*,11917-11929.

<u>J. Piella</u>, N. G. Bastús and V. Puntes, Size-Dependent Protein-Nanoparticle Interactions in Citrate-Stabilized Gold Nanoparticles: The Emergence of the Protein Corona, *Bioconjugate chemistry* **2017**, *28,* 88-97.

E. Casals, M. F. Gusta, <u>J. Piella</u>, G. Casals, W. Jimenez and V. Puntes, Intrinsic and Extrinsic Properties Affecting Innate Immun Responses to Nanoparticles: The Case of Cerium Oxide, *Frontiers in Inmunology* **2017**, *8*, 970.

F. Barbero, L. Russo, M. Vitali, <u>J. Piella</u>, V. Puntes, et al., Formation of the protein corona: the interface between nanoparticles and the immune system, *Seminars in Immunology* **2017**, *34*, 52-60.

<u>J. Piella</u>, N.G. Bastús and V. Puntes, Modelling the Optical Responses of Nobel Metal Nanoparticles Subjected to Physicochemical Transformations in Physiological Environtments: Aggregation, Dissolution and Oxidation, *Zeitshrift fur Physikalische Chemier* **2017**, *231*, 33-50.

R.A. Sperlinga, L. García-Fernández, I. Ojea-Jiménez, <u>J. Piella</u>, N.G. Bastús and V. Puntes, One-Pot Synthesis of Cationic Gold Nanoparticles by Differential Reduction, *Zeitshrift fur Physikalische Chemier* **2017**, *231*, 7-18.

S. Makama, S.K. Kloet, <u>J. Piella</u>, V. Puntes, N.W. van der Brink, *et al.*, Effects of systematic variation in size and surface coating of silver nanoparticles on their in vitro toxicity to macrophage RAW 264.7 cells, *Toxicological Sciences* **2018**, *162*, 79-88.

J. Mülhop, <u>J. Piella</u>, V. Puntes, *et al.*, Characterization of Nanoparticle Batch-To-Batch Variability, *Nanomaterials (Basel)* **2018**, *8,* 311.

L. Russo, F. Merkoçi, J. Patarroyo, <u>J. Piella</u>, A. Merkoçi, N. G. Bastús and V. Puntes, Time- and Size-Resolved Plasmonic Evolution with nm Resolution of Galvanic Replacement Reaction in AuAg Nanoshells Synthesis, *Chemistry of Materials* **2018**, *30*, 5098–5107.